이학박사 학위논문

Thermal Phase Fluctuations in a Quasi-2D Bose-Einstein Condensate

준 이차원 보즈-아인슈타인 응집체에서 일어나는 열적 위상 요동

2014년 2월

서울대학교 대학원

물리 · 천문 학부

최 재 윤

Thermal Phase Fluctuations in a Quasi-2D Bose-Einstein Condensate

준 이차원 보즈-아인슈타인 응집체에서 일어나는 열적 위상 요동

지도교수 신 용 일

이 논문을 이학박사 학위 논문으로 제출함

2013년 11월

서울대학교 대학원

물리 · 천문 학부

최 재 윤

최재윤의 박사 학위 논문을 인준함

2013년 12월

위 원 장	제 원 호	(인)
부위원장	신 용 일	(인)
위 원	강 병 남	(인)
위 원	민 홍 기	(인)
위 원	문 종 철	(인)

Thermal Phase Fluctuations in a Quasi-2D Bose-Einstein Condensate

by

Jae-yoon Choi, B.S.

Dissertation

Presented to the Faculty of the Graduate School of

Seoul National University

in Partial Fulfillment

of the Requirements

for the Degree of

Doctor of Philosophy

Seoul National University

Feburary 2014

Abstract

Thermal Phase Fluctuations in a Quasi-2D Bose-Einstein Condensate

Jae-yoon Choi
Department of Physics and Astronomy
The Graduate School
Seoul National University

Quantum gases are well isolated, highly controllable, and defect-free systems which can simulate many body quantum phenomena that have been studied in condensed matter systems. To study two-dimensional superfluid, we have developed an experimental apparatus that can produce Bose-Einstein condensates (BEC) of ^{23}Na atoms. The apparatus can generate a pure condensate of 10^7 atoms in an optically plugged magnetic quadrupole trap within 17 s.

The Berezinskii-Kosterlitz-Thouless (BKT) theory provides a general framework of the superfluid phase transition in two dimension, which does not involve spontaneous symmetry breaking and emergence of an order parameter below a critical temperature. Instead, it is the formation of vortex pairs with opposite circulations below the critical temperature that mediates the superfluid phase transition. Recently, it has been demonstrated that degenerate Bose gases confined in highly oblate harmonic potentials undergo the BKT phase transition. This thesis focuses on our experimental research on thermal phase fluctuations (i.e., long-wavelength phonons and vortex pairs) in the superfluid

phase of trapped quasi-2D BECs. We have developed a quantitative probe to measure phase fluctuations in the 2D superfluid by free expansion, where the phase fluctuations in the sample were revealed as density modulations in the course of expansion. The power spectrum of the density fluctuations showed an oscillatory shape and the scaling behavior of the peak positions could be understood as a Talbot effect in matter waves. Employing this method, we demonstrated the thermal origin of phase fluctuations. We also investigated relaxation dynamics of nonequilibrium states of the quasi-2D system using the power spectrum.

Thermally excited vortex pairs are the characteristic feature of the 2D superfluid. The quantized vortices are conventionally observed by a density-depleted core after expanding a trapped sample. The method, however, cannot be applied to the 2D sample because the density modulations after free expansion lower the vortex core visibility. We enhanced the core visibility by radial compression of the sample before the expansion so the phonon modes in the 2D sample were relaxed in a 3D environment. Measuring vortex distributions, we revealed the pairing feature by spatial correlations of the vortex positions. We also studied BKT-BEC crossover phenomena in a finite-size sample trapped in a quasi-2D harmonic potential by investigating the vortex profiles at various temperatures.

Condensates of atoms have an internal spin structure so they can host various kinds of topological excitations. The two-dimensional Skyrmion is one of the topological spin textures in the anti-ferromagnetic spinor condensate and

we imprinted the structure using the magnetic field sweep technique.

The 2D Skyrmion spin texture has a finite Berry curvature because of the non-coplanar spin configuration. We studied a geometric Hall effect, with condensates trapped in a harmonic potential with the Skyrmion spin texture. Under a linear driving of the spin texture, we observed a condensate dipole motion resonantly developed into a circular motion, which demonstrates the existence of an effective Lorentz force.

Keywords : Bose-Einstein condensation, Berezinskii-Kosterlitz-Thouless phase transition, thermal phase fluctuations, quantum vortex, Skyrmion, Berry phase.

Student number : 2009-20433

Contents

List of Tables

List of Figures

Chapter 1

Introduction

The indistinguishability of identical particles such as electrons, protons, and atoms is the core of quantum statical mechanics and all particles in nature must fall into one of these two categories [1]

1. Particles with half-odd-integer spin (1/2, 3/2 ...) are described by the anti-symmetric wave function. Such particles are called *Fermion* and satisfy Fermi-Dirac statics.

2. Particles with integer spin (0, 1 ...) are described by the symmetric wave function. Such particles are called *Boson* and satisfy Bose-Einstein statics.

The profound difference of two types of particles leads to a completely different ground state at zero temperature. Fermionic particles stack up from the lowest energy level because of the anti-symmetric wave function, whereas, Bosonic particles fully occupy the same ground state with the symmetric wave function.

In particular, the ground state of Bose particles can be described by a macroscopically occupied single wave function, called Bose-Einstein condensates, and show a dissipiationless superflow of mass in ^{4}He [2, 3] and charge current in superconductor [4, 5].

A new era of Bose-Einstein condensation (BEC) was initiated in 1995, after the realization of BEC in dilute atomic gases [6, 7]. The condensates of atomic gases can provide unprecedented opportunities to test many-body quantum theory because of its weak interaction, ultra-clean and well isolation from the environment. Moreover, well controlled experimental techniques for manipulating and detecting atomic states allow more direct access to a desired quantum state. Indeed, novel properties of BEC such as phase coherence [8], superfluidity, and quantized vortex state [9–11] were observed soon after the discovery. In 2001, Carl Wieman, Eric Cornell, and Wolfgang Ketterle were awarded the Nobel Prize for Physics for *the achievement of Bose-Einstein condensation in dilute gases of alkali atoms, and for early fundamental studies of the properties of the condensate* [12].

Now with the realization of degenerate gases of Fermionic atoms [13, 14], the quantum gases have successfully demonstrated numerous many body quantum phenomena [15] which were traditionally studied in the condensed matter system and high energy physics. In this respect, the cold atom system is highly recognized as one of the strongest candidates for the universal quantum simulator, envisioned by Feynman [16]. Several astonishing achievements and prospects of the quantum gas system are as follows.

Ultracold quantum gases were loaded into a periodic optical potential to simulate the Hubbard model [17]. For Bose condensates, quantum phase transition from superfluid to Mott insulating phase was clearly observed by dramatic changes of the phase coherence, which was measured by the interference Bragg peak [18]. Loading Fermionic atoms into the optical lattice, metal to Mott insulating phase transition was also demonstrated by measuring the compressibility of the sample [19, 20].

The Feshbach resonance [21] can tune the strength of atom-atom interaction more than several orders of magnitude by external magnetic field. This allowed scientists to explore the BEC-BCS [22, 23] crossover in a degenerate Fermi gas, which provided better understandings about superfluidity at two different regime. Moreover, the thermodynamic properties and the equation of state at the unitary regime (the interaction between atoms diverges) were measured [24–27] with high precision [28] through density distribution. Those results would provide useful discrimination of various theoretical methods [29].

Finally, the cold atoms can be extended to synthesis exotic solid state materials, such as topological insulator and Majonara fermion, through laser light dressing [30, 31]. Recent studies show that the atom-light interaction could generate Rashba and Dresselhaus spin-orbit interaction [32–34] and light-assisted tunneling in optical lattice could realize a fractal band structure, the Hofstadter butterfly [35], because of a huge magnetic flux in a lattice site [36, 37]. Recently, the Hofstadter [38] and the Harper [39] Hamiltonian have been realized in the optical lattice and the interesting topological state of matter could be observed

in the near future.

1.1 Bose-Einstein condensates of dilute gases

One of the simplest but intuitive descriptions of the Bose-Einstein condensation is the formation of gigantic matter wave [40]. In quantum mechanics, a particle can be described by a localized wave packet with its size $\lambda_{\mathrm{dB}} = h/\sqrt{2\pi m k_B T}$, where h is Plank constant, m is atomic mass, and k_B is Boltzmann constant. At high temperature, the thermal wave length is much shorter than the inter-particle spacing d and each atom in a box can be considered as a ballistic ball. As we lower the temperature, however, the size of thermal wave λ_{dB} increases and can be comparable to the inter-particle distance. Then, the thermal wave starts to overlap because of the indistinguishability and finally become a macroscopic gigantic matter wave, BEC, below a certain temperature. This pictorial description quite well explains the condensation except the concept of a saturation of excited state. When we calculate the number of excited state at a given temperature, it has an upper bound N_s and therefore rest number of particles that exceeds the saturation atom number would be remained in the ground state.

The generalized criterion for the BEC is suggested by Penrose and Onsager [41], which is written as

$$\lim_{|x-y|\to\infty} \langle \hat{\psi}^\dagger(x)\hat{\psi}(y)\rangle = f^*(x)f(y), \tag{1.1}$$

where $f(x)$ is some non-zero function. C. N. Yang developed the idea [42] and

showed that new thermodynamic properties of Bosons or Fermions can be explained by the *off-diagonal long range order* of the density matrix.

The condensate wave function can be described by mean field theory which deals the inter-particle interaction as the averaged interaction energy from the other particles. In the mean field description, the wave function of the N-particle system can be represented by single particle wave function $\psi(\mathbf{r}_i)$

$$\Psi(\mathbf{r}_1, \mathbf{r}_2, \ldots, \mathbf{r}_N) = \prod_{i=1}^{N} \psi(\mathbf{r}_i), \tag{1.2}$$

and we can write the Hamiltonian in a low energy limit [43]

$$H = \sum_{i=1}^{N} \left[-\frac{\hbar^2}{2m}\nabla_i^2 + V(\mathbf{r}_i) \right] + U_0 \sum_{i<j} \delta(\mathbf{r}_i - \mathbf{r}_j), \tag{1.3}$$

where $V(x)$ is external potential and $U_0 = \frac{4\pi a_s \hbar^2}{m}$ is the effective interaction strength described by s-wave scattering length a_s. The physical origin of the contact interaction[1] is van der Waals interaction and the total energy E of the system is given by

$$E = N \int d\mathbf{r} \left[\frac{\hbar^2}{2m}|\nabla\psi(\mathbf{r})|^2 + V(r)|\psi(\mathbf{r})|^2 + \frac{(N-1)}{2}U_0|\psi(\mathbf{r})|^4 \right]. \tag{1.4}$$

Introducing the condensate wave function $\psi(\mathbf{r}) = \sqrt{N}\psi(\mathbf{r})$ and minimizing the energy E with the constrainment of fixed number of particles $\int d\mathbf{r}\psi(\mathbf{r}) = N$, we a get non-linear schrödinger equation, which is called Gross-Pitaevskii equation

$$-\frac{\hbar^2}{2m}\nabla^2\psi(\mathbf{r}) + V(\mathbf{r})\psi(\mathbf{r}) + U_0|\psi(\mathbf{r})|^2\psi(\mathbf{r}) = \mu\psi(\mathbf{r}), \tag{1.5}$$

[1]Three-body interaction is neglected because of its dilutees.

where $\mu = \partial E/\partial N$ is chemical potential of the system.

If the kinetic energy is much smaller than other energies, we can neglect the first gradient term in the Gross-Pitaevskii equation,

$$(V(\mathbf{r}) + U_0|\psi(\mathbf{r})|^2)\psi(\mathbf{r}) = \mu\psi(\mathbf{r}). \tag{1.6}$$

Then the solution of the equation is

$$n(\mathbf{r}) = |\psi(\mathbf{r})|^2 = (\mu - V(\mathbf{r}))/U_0, \tag{1.7}$$

where the boundary condition is $\psi(\mathbf{r}) = 0$ for the right hand side become negative. This approximation is called Tomas-Fermi approximation and well describes the condensate density distribution confined in a harmonic potential.

In the opposite limit, where the kinetic energy could not be neglected, gives us important length scale. Consider condensates trapped in a uniform box potential. Since the wave function cannot exist outside of the box, one can consider the condensate wave function would start from 0 at the boundary and grow up to a finite value after a distance ξ from the boundary. The distance is called healing length and determined by competition between kinetic energy and interaction energy

$$\frac{\hbar^2}{2m\xi^2} = U_0 n, \tag{1.8}$$

or

$$\xi = \sqrt{\frac{\hbar^2}{2mnU_0}} = \frac{1}{\sqrt{8\pi n a_s}}. \tag{1.9}$$

The healing length of the condensate is ~ 1 μm, which much larger than that of the liquid He ~ 10 nm. This dramatically different length scale allows more accessible environment to image the spatial variance of the wave function.

1.2 Outline of the thesis

This thesis is organized as follows. In Chapter 2, experimental apparatus for generation of a large number of BEC for sodium (^{23}Na) atoms are introduced, which is composed of a laser system, vacuum system, and control system. Chapter 3 describes experimental procedures for obtaining Bose-Einstein condensates of atomic gases in a magnetic quadrupole trap. By sweeping radio-frequency to the trapped atoms, we obtained a pure condensate of 10^7 atoms within 17 s. A non-adiabatic spin flip near the magnetic field center was suppressed by creating an optical barrier near the trap center. We also present qualitative understandings of the evaporation process from the simple rate equation of atom number and temperature.

Chapter 4 focuses on thermal phase fluctuations (i.e., long-wavelength phonons and vortices) in the superfluid phase of quasi-2D BECs. After introducing the Berezinskii-Kosterlitz-Thouless (BKT) theory of atomic system, optical setup for the quasi-two dimensional potential is described. The major advantage of our sample is of its large size so we can probe thermal phase fluctuations in 2D by simply expanding the gas. Remarkably, the phase fluctuations were revealed by the density modulations and its power spectrums were used to measure the strength of the phase fluctuations in a trapped gas. The spectrum strength was shown to decrease as we lower the temperature, which demonstrated the thermal origin of the phase fluctuations. Moreover, we observed quantized vortices in the superfluid regime by density-depleted core after enhancing the vortex core visi-

bility. The observed vortices were shown to have a two-point correlation, which was strong evidence of the BKT vortex pairs. From the vortex profile at various temperatures, we investigated crossover phenomena from BKT phase to BEC phase, which was characterized by the presence of vortices, in a trapped Bose gases.

The two-dimensional superfluid of the atomic system can become more interesting when the spin degree of freedom is considered. Because of the additional spin vector, the BKT phase transition could be mediated by another type of topological excitation such as half-quantum vortex and Skyrmions in polar condensates [44–46]. Before studying the two-dimensional spinor Bose gas, we artificially created the Skyrmion spin textures in the pancake shape condensate. Chapter 5 introduces a topological excitation in a $F = 1$ spinor condensates, where 2D Skyrmion spin texture can be topologically stable in the polar phase. We present a spin rotation method for creating the Skyrmion configuration of spin vectors in a harmonic potential both in ferromagnetic and polar phase of the spinor condensate.

Chapter 6 describes the general formula of a gauge field for neutral atoms caused by a magnetic quadrupole field. The gauge field forms a magnetic monopole structure with 4π of total flux for spin-1 atoms. We studied a geometric Hall effect with a spin-polarized condensate trapped in an oblate potential, where a rigid Skyrmion spin texture is imposed by the magnetic quadrupole field. Under translational oscillations of the spin texture, the condensate resonantly developed a circular motion in a harmonic trap, demonstrating the

existence of an effective Lorentz force.

Finally, Chapter 7 outlines several remarks, perspectives of this work, and outlooks. Experimental work described in this thesis is based on discussions that *our group* made and related publications are attached at the end of this thesis.

Bibliography

[1] W. Pauli, Phys. Rev. **58**, 716 (1940).

[2] P. Kapitza, Nature **141**, 74 (1938).

[3] J. F. Allen and A. D. Misener, Nature **141**, 75 (1938).

[4] H. K. Onnes, Commun. Phys. Lab. Univ. Leiden **12**, 120 (1911).

[5] J. Bardeen, L. N. Cooper, and J. R. Schrieffer, Phys. Rev. **108**, 1175 (1957).

[6] M. H. Anderson, J. R. Ensher, M. R. Metthews, C. E. Wieman, and E. A. Cornell, Science **269**, 198 (1995).

[7] K. B. Davis, M. -O. Mewes, M. R. Andrews, N. J. van Druten, D. S. Dufree, D. M. Kurn, and W. Ketterle, Phys. Rev. Lett. **75**, 3969 (1995).

[8] M. R. Andrews, C. G. Townsend, H. -J. Miesenr, D. S. Dufee, D. M. Kurn, and W. Ketterle, Science **275**, 637 (1997).

[9] M. R. Matthews, B. P. Anderson, P. J. Haljan, D. S. Hall, C. E. Wieman, and E. A. Cornell, Phys. Rev. Lett. **83**, 2498 (1999).

[10] K. W. Madison, F. Chevy, W. Wohlleben, and J. Dalibard, Phys. Rev. Lett. **84**, 806 (2000).

[11] J. R. Abo-Shaeer, C. Raman, J. M. Vogels, and W. Ketterle, Science **292**, 496 (2001).

[12] The Nobel Prize in Physics 2001; http://www.nobel.se/physics/laureates/2001/.

[13] B. DeMarco and D. S. Jin, Science **285**, 1703 (1999).

[14] K. M. O'Hara, S. R. Granade, M. E. Gehm, T. A. Savard, S. Bali, C. Freed, and J. E. Thomas, Phys. Rev. Lett. **82**, 4204 (2011).

[15] I. Bloch, J. Dalibard, and W. Zwerger, Rev. Mod. Phys. **80**, 885 (2008).

[16] R. P. Feynman, Int. J. Theor. Phys. **21**, 467 (1982).

[17] J. Hubbard, Proc. R. Soc. Lond. A **276**, 238 (1963).

[18] M. Greiner, O. Mandel, T. Esslinger, T. W. Hänsch, and I. Bloch, Nature **415**, 39 (2002).

[19] R. Jördens, N. Strohmaier, K. Günter, H. Moritz, and T. Esslinger, Nature **455**, 204 (2008).

[20] U. Schneider, L. Hackermüller, S. Will, Th. Best, I. Bloch, T. A. Costi, R. W. Helmes, D. Rasch, and A. Rosch, Science **322**, 1520 (2008).

[21] C. Chin, R. Grimm, P. Julienne, and E. Tiesinga, Rev. Mod. Phys. **82**, 1225 (2010).

[22] M. W. Zwierlein, J. R. Abo-shaeer, A. Schorptzel, C. H. Schunk, and W. Ketterle, Nature **435**, 1047 (2005).

[23] M. W. Zwierlein, A. Schirotzek, C. H. Schunk, W. Ketterle, Science **311**, 492 (2006).

[24] Y. Shin, C. H. Schunk, A. Schirotzek, W. ketterle, Nature **451**, 689 (2008).

[25] M. Horikoshi, S. Nakajima, M. Ueda, and T. Mukaiyama, Science **327**, 442 (2010).

[26] N. Navon, S. Nascimbène, F. Chevy, and C. Salomon, Science **328**, 729 (2010).

[27] S. Nascimbène, N. Navon, K. Jiang, F. Chevy, and C. Salomon, Nature **463**, 1057 (2010).

[28] M. J. H. Ku, A. T. Sommer, L. W. Cheuk, and M. W. Zwierlein, Science **335**, 563 (2012).

[29] I. Bloch, J. Dalibard, and S. Nascimbène, Nat. Phys. **8**, 267 (2012).

[30] J. Dalibard, F. Gerbier, G. Juzeliunas, and P. Öhberg, Rev. Mod. Phys. **83**, 1523 (2011).

[31] V. Galitski and I. B. Spielman, Nature **494**, 49 (2013).

[32] Y. J. Lin, R. L. Compton, K. Jiménez-García, J. V. Porto, and I. B. Spielman, Nature **462**, 628 (2009).

[33] Y. J. Lin, K. Jiménez-García, and I. B. Spielman, Nature **471**, 83 (2011).

[34] D. L. Cambell, K. Jiménez-García,and I. B. Spielman, Phys. Rev. A **84**, 095302 (2012).

[35] D. R. Hofstadter, Phys. Rev. B **14**, 2239 (1976).

[36] D. Jaksch and P. Zoller, New J. Phys. **5**, 56 (2003).

[37] F. Gerbier and J. Dalibard, New J. Phys. **12**, 033007 (2010).

[38] M. Aidelsburger, M. Atala, M. Lohse, J. T. Barreiro, B. Paredes, and I. Bloch, Phys. Rev. Lett. **111**, 185301 (2013).

[39] H. Miyake, G. A. Siviloglou, C. J. Kennedy, W. C. Burton, and W. Ketterle, Phys. Rev. Lett. **111**, 185302 (2013).

[40] W, Ketterle, Rev. Mod. Phys. **74**, 1131 (2002).

[41] O. Penrose and L. Onsager, Phys. Rev. **104**, 576 (1956).

[42] C. N. Yang, Rev. Mod. Phys. **34**, 694 (1962).

[43] C. J. Pethick and H. Smith *Bose-Einstein Condensation in Dilute Gases* (Cambridge University Press, 2002).

[44] S. Mukerjee, C. Xu, and J. E. Moore, Phys. Rev. Lett. **97**, 120406 (2006).

[45] V. Pietilä, T. P. Simula, M. Möttönen, Phys. Rev. A **81**, 033616 (2010).

[46] A. J. A. James and A. Lamacraft, Phys. Rev. Lett. **106**, 140402 (2011).

Chapter 2

Experimental setup

For producing quantum degenerate gases, numerous cooling techniques [1] have been invented and persistent efforts have been made to develop more reliable and simpler methods [2]. As a result of the research, ultracold atoms of new species [3–7] have been realized recently, offering a unique opportunity for studying noble quantum phenomena. A common strategy for obtaining the quantum gases are based on laser cooling of atomic vapor followed by evaporative cooling in a conservative potential such as magnetic or optical dipole trap.

In this chapter, I would introduce experimental apparatus for making condensates of ^{23}Na atoms. A pure Bose-Einstein condensate of 10^7 number of atoms can be produced in 17 s by evaporative cooling in an optically plugged magnetic quadrupole trap. The machine consists of laser system for cooling and trapping atomic vapor, vacuum system for evaporative cooling in the magnetic potential, and control system for manipulating cold atoms. Related results are

reported in the following publication.

- Jae-yoon Choi, Myoung-sun Heo, and Yong-il Shin. *"Experimental apparatus for producing large ^{23}Na Bose-Einstein condensates"* Journal of the Korean Physical Society **59**, 211 (2011).

2.1 Laser system

Resonant laser light is essential tool for cooling and trapping atomic vapor, which is a first step before reaching the quantum degenerate regime. When the atom absorbs a resonant photon, it becomes an excited state with its momentum changed by the amount of absorbed photon momentum. Since the direction of photons emitted by the excited state atoms are random, a successive absorption and emission of the resonant laser light could impart a net force to the atoms in the direction of light propagation. More comprehensive description can be found in Ref. [1, 8]. In typical experiment, 600 K atomic gases need to cool down to several hundred μK by the laser cooling. Since the photon recoil momentum is only few cm/s, about 10^5 number of photons are required for slowing down the atom. In this respect, laser cooling works efficiently when we take a cycling transition line, where an excited state of atoms return to its original ground state after the emission of photon.

For sodium atoms, the transition line that excites $^3S_{1/2}$ $|F = 2\rangle$ ground state into $^3P_{3/2}$ $|F' = 3\rangle$ excited state is the optimal cooling transition line, where F and F' are the total angular momenta of the ground and the excited

hyperfine states, respectively [Fig. 2.1]. Some atoms in the $|F' = 3\rangle$ state, however, can be relaxed to $|F' = 2\rangle$ states, which means that atoms in $|F' = 3\rangle$ state can decay into $|F = 1\rangle$ state via the relaxation channel. Since, the $|F = 1\rangle$ state cannot see the cooling transition line, one need to repump the atoms in the dark state back into $|F = 2\rangle$ state so they could see the cooling laser. This can be achieved by shining another repumping transition line which excites ${}^3S_{1/2}$ $|F = 1\rangle$ ground state into ${}^3P_{3/2}$ $|F' = 2\rangle$ excited state. Therefore, two transition lines are required for the laser cooling. The Table 2.1 presents laser beam power and detuning for the experiments.

	Transition line	Detuning (MHz)	Power (mW)
MOT	F=2 $\rightarrow$ F′=3	-15	70
Slower	F=2 $\rightarrow$ F′=3	-700	55
Repump	F=1 $\rightarrow$ F′=2	-10	15
F=1 probe	F=1 $\rightarrow$ F′=2	0	0.3

Table 2.1: Experimental parameters for cooling and imaging atoms.

A 1.8 W laser beam at the frequency of the sodium D_2 line is generated from a dye laser system (Matisse DS, Sirah, Germany) by pumping with a 8 W, 532-nm laser light (Millennia Pro 15, Spectra-Physics) and experimental setup for the laser cooling is shown in Fig. 2.2 (see appendix A for detail optics layout). The repumping and imaging lights for the $|F = 1\rangle \rightarrow |F' = 2\rangle$ transition are derived using a single 1.7-GHz, high-frequency acousto-optic modulator (AOM) (TEF-1700-100-589, Brimrose Corp., USA) with a diffraction efficiency of $\approx$ 25%. The slowing light is phase-modulated at 1.7 GHz with an EOM (4421-M,

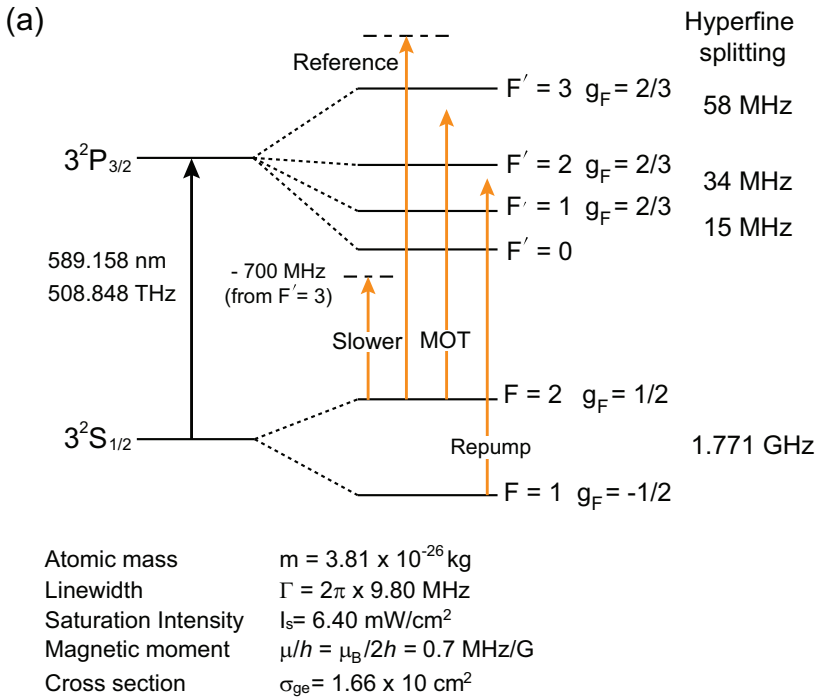

Figure 2.1: (a) Sodium energy level for D_2 transition and various frequencies of lights are displayed by the yellow arrows. Physical properties of sodium atoms are written below the level diagram. Transition strength of the sodium D_2 line is displayed with (b) σ^+ and (c) π polarization.

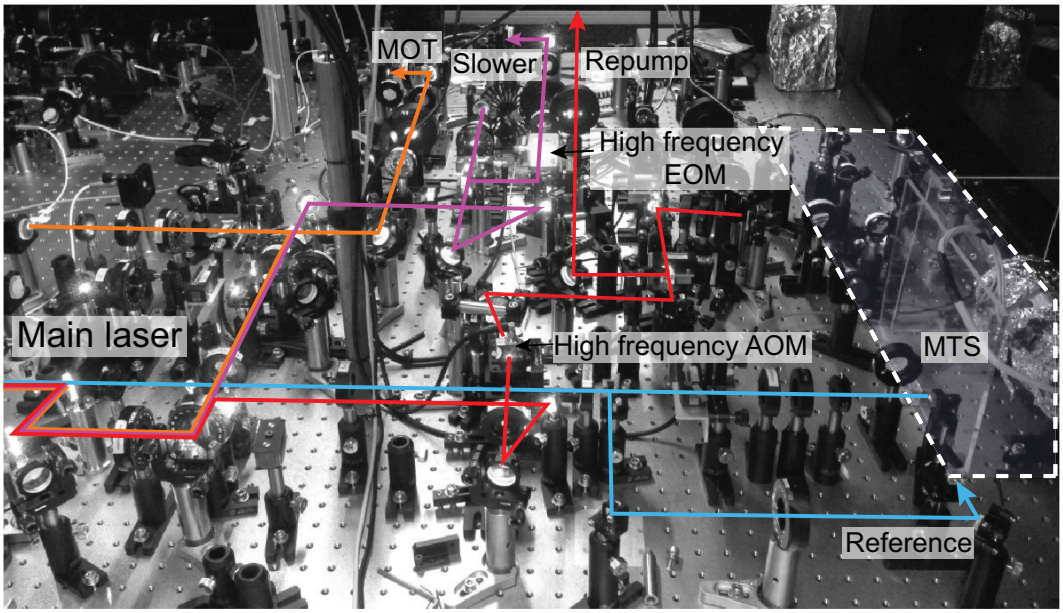

Figure 2.2: A 589-nm yellow light is generated from a main laser and split by acoustic optical modulators (AOM). Most of the AOMs are set up in double pass configuration and all light except the repumping light are fiber coupled to main chamber.

New Focus), transferring 10% of the total power into the first-order sidebands so that atoms can be continuously decelerated. Most AOMs are set up in a double-pass configuration to facilitate frequency tuning and shuttering of light. Diffraction efficiency of the double pass AOM is more than 50%. All the light except the repumping light is delivered to the experiment table via single-mode optical fibers (P3-460B-FC, Thorlabs) to clean beam modes and to enhance the beam pointing stability. The typical fiber coupling efficiency is above 60 %.

The laser frequency is stabilized to an external reference cavity, whose long-term drift is locked using modulation transfer spectroscopy of a sodium vapor cell, where we use a homemade 30-MHz electro-optic modulator (EOM) [9].

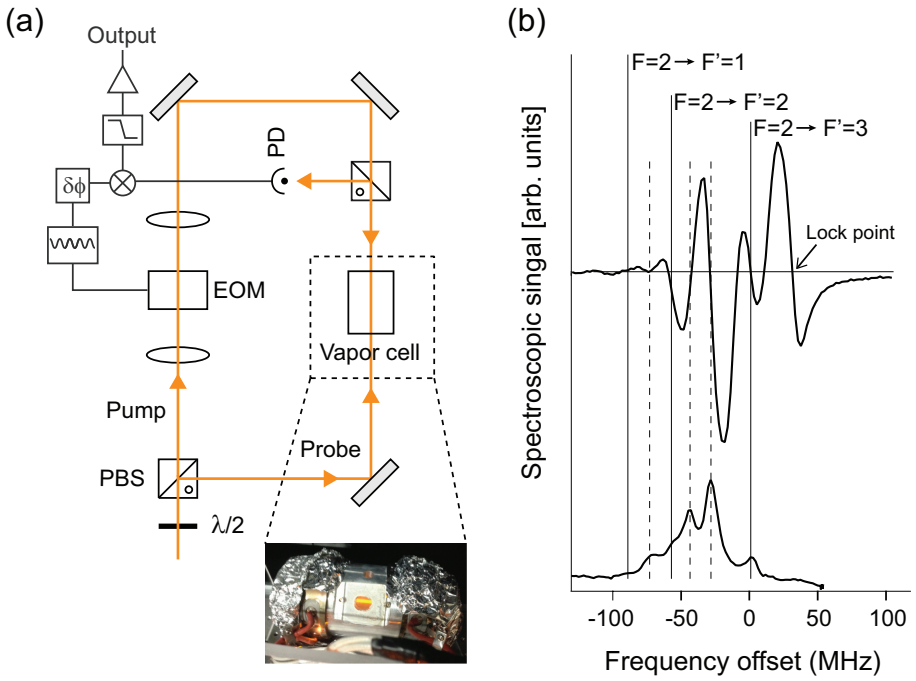

Figure 2.3: (a) Schematic layout of frequency lock with modulation transfer spectroscopy. Inset figure represents sodium vapor cell. (b) Modulation transfer spectroscopy (top) and saturation absorption spectroscopy (bottom) of sodium. Solid and dash vertical lines indicate optical transitions and their crossovers, respectively. The laser frequency is locked using the zero-crossing point on the blue side of the $|F = 2\rangle \rightarrow |F' = 3\rangle$ transition in modulation transfer spectroscopy.

The reference sodium vapor cell is purchased from Thorlabs (GC25075-NA) and temperature of the glass cell is maintained at 90 °C. Doppler absorption signal of the cooling transition line is 40 %. The life time of sodium vapor cell is about 2 years. The homemade EOM consists of non-linear crystal $LiTaO_3$ and LC resonance circuit for imposing oscillating voltages at the crystal. The observed spectroscopy signal and its setup is shown in Fig. 2.3.

Probe beam passing through the vapor cell is detected at the photo diode and amplified (SRS) signal is mixed (ZX05-1L+, Minicircuits CO) with 30MHz local oscillator (ZOS-50, Minicircuits CO). Adjusting the offset phase (JSPHS-32+, Minicircuits CO), we could obtain quadrature phase of error signal. The lock point is chosen at the zero-crossing point on the blue side of the $|F = 2\rangle \rightarrow |F' = 3\rangle$ cooling transition. The laser linewidth is estimated to be less than 200 kHz, much smaller than the natural linewidth $\Gamma = 9.8$ MHz of the D_2 line. The spectroscopy signal is improved after we replace the homemade EOM with the one made by Photonics Technology, UK (EOM-01-10-U), where the modulation frequency is 10 MHz. The locking scheme is very stable and the frequency lock is broken only one or two times in a day.

In the experiment, far-detuned laser light is also used for making potential barrier or deep well. A part of the output of the 532-nm pump laser is allocated for an optical plug (see appendix A), and a 5-W Ytterbium fiber laser at 1070 nm (YLR-5-LP, IPG Photonics) is used to form an optical dipole trap. Experimental setups for the plug beam and optical dipole trap are described in the following chapters.

2.2 Condensate machine

Schematic diagram of the condensate machine[1] is shown in Fig. 2.4, which can generate large number of condensates of atoms rapidly. We adapt zero-crossing Zeeman slower for the high atom flux in the main chamber and bucket shape window flanges at the top and bottom of main chamber are helpful to obtain high-resolution image because of the large optical access. Each vacuum part is well secured to a non magnetic optical table (Kintics System Inc., USA).

Here is the brief summaries of major events in the process of making condensate machine. In the October 2009, we assembled the machine part by part and ultra-high vacuum was achieved at the main chamber 3 months after the baking process. The Laser system was completed at the March 2010 and we captured the sodium atoms in the magneto-optical-trap at the May 2010. About one month later, 14 June 2010, the first condensates sodium atoms were generated in the machine, which is indeed *the fast production of Bose-Einstein condensates.*

2.2.1 Oven chamber

A well collimated sodium atomic beam, propagating into the main chamber, is produced in the oven chamber. The chamber consists of 4 main parts: atom cup, nozzle, cold plate, and differential pump tube. The atom cup is a half nipple flange and we load two or three ampules each containing 5 g of sodium. Heating

[1]Most of vacuum components of condensate machine are designed by Yong-il Shin (my supervisor).

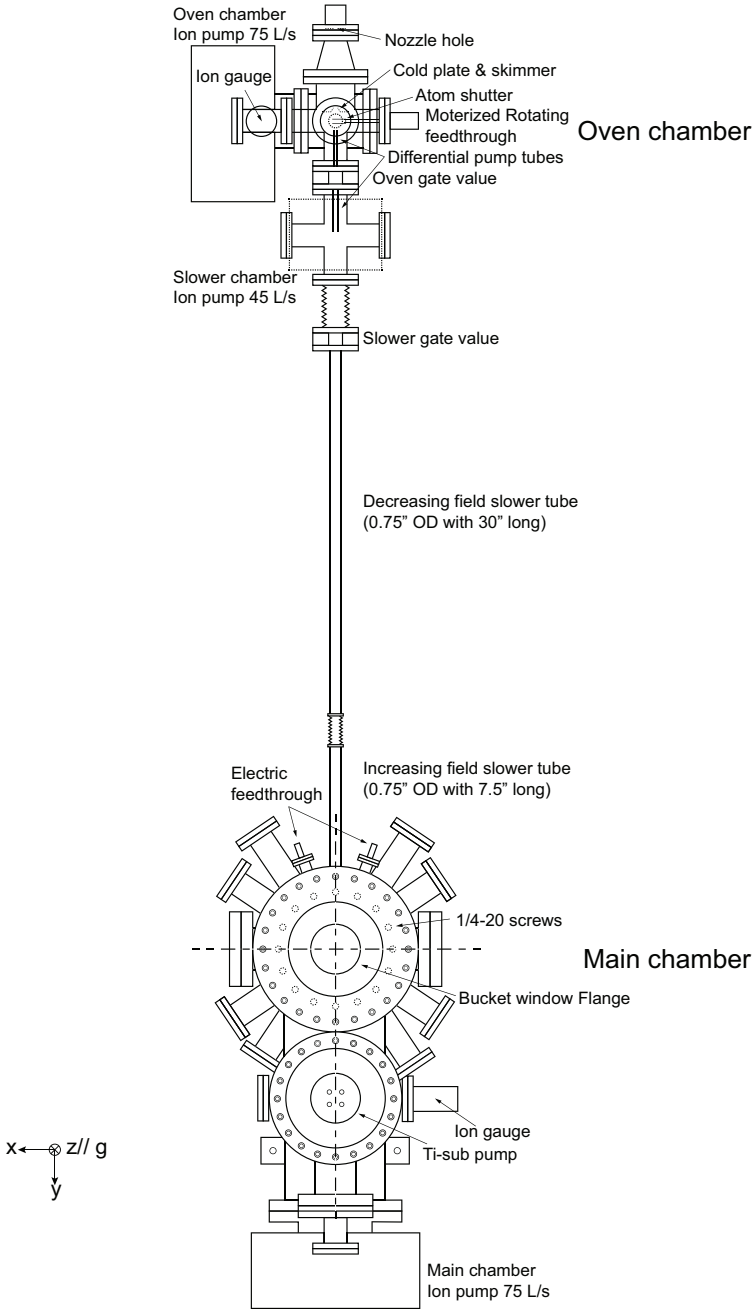

Figure 2.4: Schematic drawings of our condensate apparatus. It consists of oven chamber, Zeeman slower tube and main chamber and all of the vacuum systems are built up onto a non-magnetic optical table. Detail description would be discussed in the text.

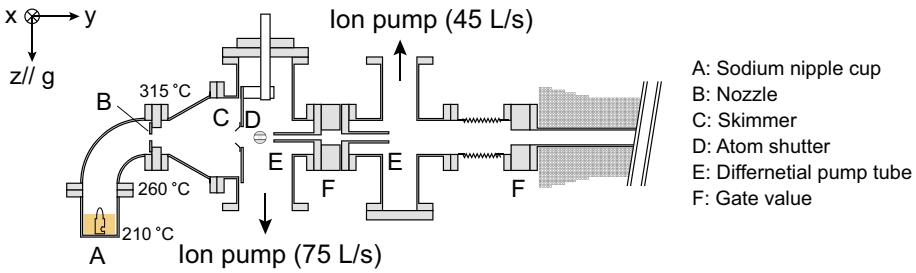

Figure 2.5: Cross-sectional diagram of the oven chamber. A sodium atomic beam is generated from the oven and propagates into the main chamber through the Zeeman slower tube. The oven temperatures are displayed with operating condition and atom shutter rotates 45° to block the atomic beam.

the cup to 210 °C by band heater, sodium gas is generated with 2.7×10^{-4} Torr vapor pressure. The vapor effuses out of a 4-mm diameter nozzle, which is maintained at 315 °C, resulting 740 m/s mean velocity[2]. Since the atomic beam passing through the nozzle still have large transverse velocity, we place copper slug with 0.6" OD to collect the spreading atom. The L-shape of the skimmer helps to minimize the clogging of the hole. Finally, well collimated atomic source is made by passing through the differential pump tube, which is 2.5" length with 0.18"-0.25" inner diameter.

The long tube can also balance pressure difference from oven chamber to the slower chamber. The conductance of the tube for air at room temperature is $C = 121\ m/s \times \frac{d^3}{l}$, where d and l are the diameter and the length of the tube respectively. Because of low conductance of the long tube (~ 0.02), more than two order of magnitude different pressure can be maintained.

[2]The mean velocity takes the formula $\sqrt{\frac{8k_BT}{\pi m}}$, where k_B is Boltzmann constatn, T is temperature, and m is sodium mass.

The atomic source is switched on and off by the atom shutter that opens or blocks the atomic beam path. It is a ball-valve-type shutter installed on a rotational feedthrough, and the shutter's motion is precisely controlled by using a stepping motor. The range of the rotational motion is set to be less than 50 degrees to prolong the feedthrough lifetime. The shutter is closed within 200 ms. The distance from the nozzle to the center of the main chamber is $\simeq 1.7$ m, and the atom flux into the main chamber is estimated to be about 3.0×10^{11} atoms/s.

2.2.2 Zeeman slower

The atomic beam is decelerated after they pass through the Zeeman slower tube, where a laser light propagates in opposite to the atomic beam direction. The slowering laser is red detuned to the cycling transition because of the doppler shift from directional atomic beam. Note that the decrease of atomic velocity also effects the doppler shift, so the resonant condition would be broke down only after a few cycle. Applying a constant magnetic field, however, the Zeeman energy shift can compensate the doppler shift changes, so the atomic velocity can be continuously decreased by the constant photon scattering force, . We can write the condition for the Zeeman slowing as $\omega_L = \omega_a - kv(z) + \mu B(z)/\hbar$, where z is the atomic beam propagating direction, ω_L is laser frequency, ω_a is cooing transition line, k is wave vector of the photon, and μ is magnetic moment of the atoms. Then the desired magnetic field distribution can be expressed with some experimental parameters. When initial velocity v_0 atoms are stopped at a distance L under the maximal scattering force, $ma_{\max} = \frac{\hbar k\Gamma}{2}$, the velocity

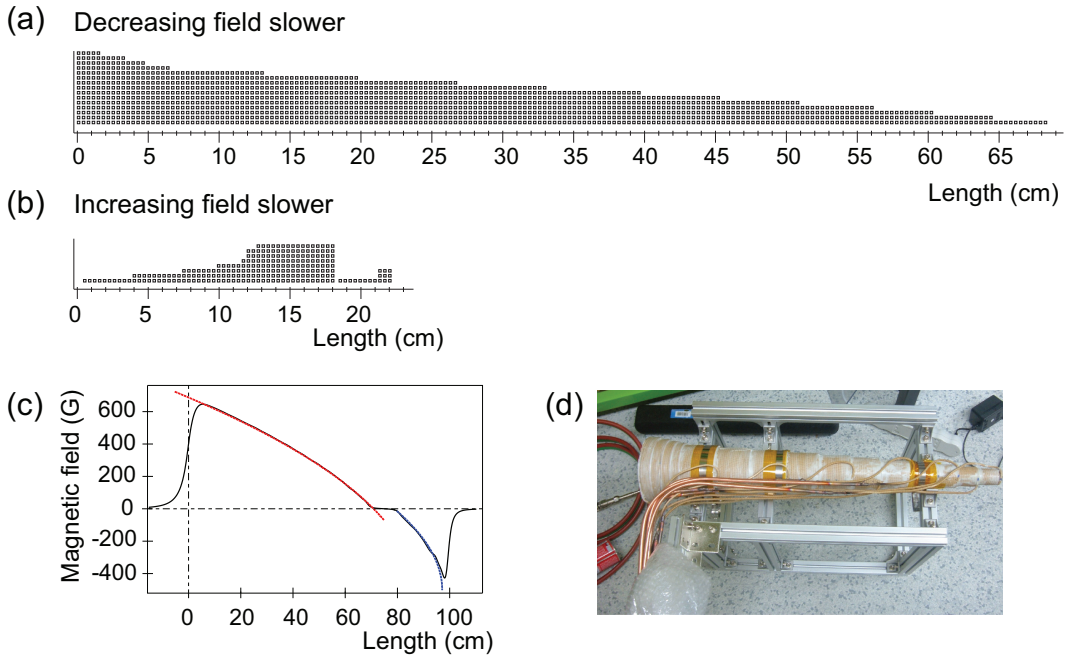

Figure 2.6: Half-cut side view of slower solenoid. (a) Decreasing field part and (b) increasing field part. (c) Estimated profiles of magnetic field generated from the coils. Red and blue curves represent a magnetic field obtained at the half of maximum deceleration. (d) Photo of decreasing field slower secured by aluminum frame.

distribution is $v(z) = v_0\sqrt{1-\frac{z}{L}}$ and the magnetic field profile is given by

$$B(z) = (B_i - B_f)\sqrt{1-\frac{z}{L}} + B_f \tag{2.1}$$

, where the magnetic field is B_i at $z = 0$ and B_f at $z = L$. The initial magnetic field strength is determined by target capture velocity of atoms, v_c, and laser detuning $\delta_L = \omega_L - \omega_a$.

In our experiment, target capture velocity is 950 m/s and slowing laser beam is 700 MHz red-detuned so its magnetic field changes from 650 to -480 G over 1 m, even at half of the maximum deceleration. The magnetic field is generated by using three tapered solenoids [Fig. 2.6]: one for the decreasing part (16 A) and two for the increasing part (15 A and 79 A). The last part of increasing field slower is 2 layer so the magnetic field rapidly drops so minimize residual magnetic field at the main chamber. Since polarity of slower laser is changed as the magnetic field changes its direction, atoms need to rempump from $m_F = -2$ state to $m_F = 2$ state in order to continue the laser cooling at the increasing field part. The two slower part is joined by 7 cm bellow and it repump atoms into cycling transition under the field direction changes.

The solenoids are wound on 1"-diameter brass pipes with 1/8" square hollow copper tubes (copper alloy 102, Daglas insulated) and are cemented with non-magnetic high temperature (150°) epoxy (Duralco NM25, Contronics Corp., USA). Cooling water flows through 1/16" square inner holes, and the wire resistivity is $\leq$ 2.6 mΩ/m. A compensation coil is placed on the other side of the main chamber to cancel the slower field at the center of the main

chamber. The residual field gradient is estimated to be < 1 G/cm along the y-direction. All currents flowing into the slower coils and compensate coil are simultaneously switched by using one insulated-gate bipolar transistor (IGBT) module.

2.2.3 Main chamber

Sample preparation and measurement are performed in the main chamber, which is displayed in Fig. 2.7. This chamber is constructed of polished 304 stainless steel, with a helium mass spectrometer tested and electropolished for UHV service (Sharon Vacuum Co. Inc., USA). The center experiment zone with twelve viewports is connected to a pumping body through a 6" $\times$ 4" rectangular tube. The pumping body is equipped with a 75-L/s ion pump (75S-DI-6S-SC, Gamma Vacuum) and a Ti-sublimation pump (P/N9160050, Varian Inc). The recessed bucket flanges on the top and the bottom of the main chamber feature non-magnetic window pipes with 50-mm-diameter clearance (UKAEA Fusion Special Technique Group, UK), providing a large numerical aperture of ≈ 0.5, which is beneficial to high-resolution imaging. All the view port windows are AR coated on both sides for 532, 589, 670 and 1064 nm.

A pair of magnetic coil sets are secured around the window pipes. Each quadrupole and Feshbach coil are wound by 36 turns with square copper tubing. The quadrupole and Feshbach coil pairs generate a field gradient of 1.5 G/(cm A) and a uniform field of 4.5 G/A along the z-axis. Since a strong magnetic field would be generated along the vertical z-axis, we mount the whole vacuum sys-

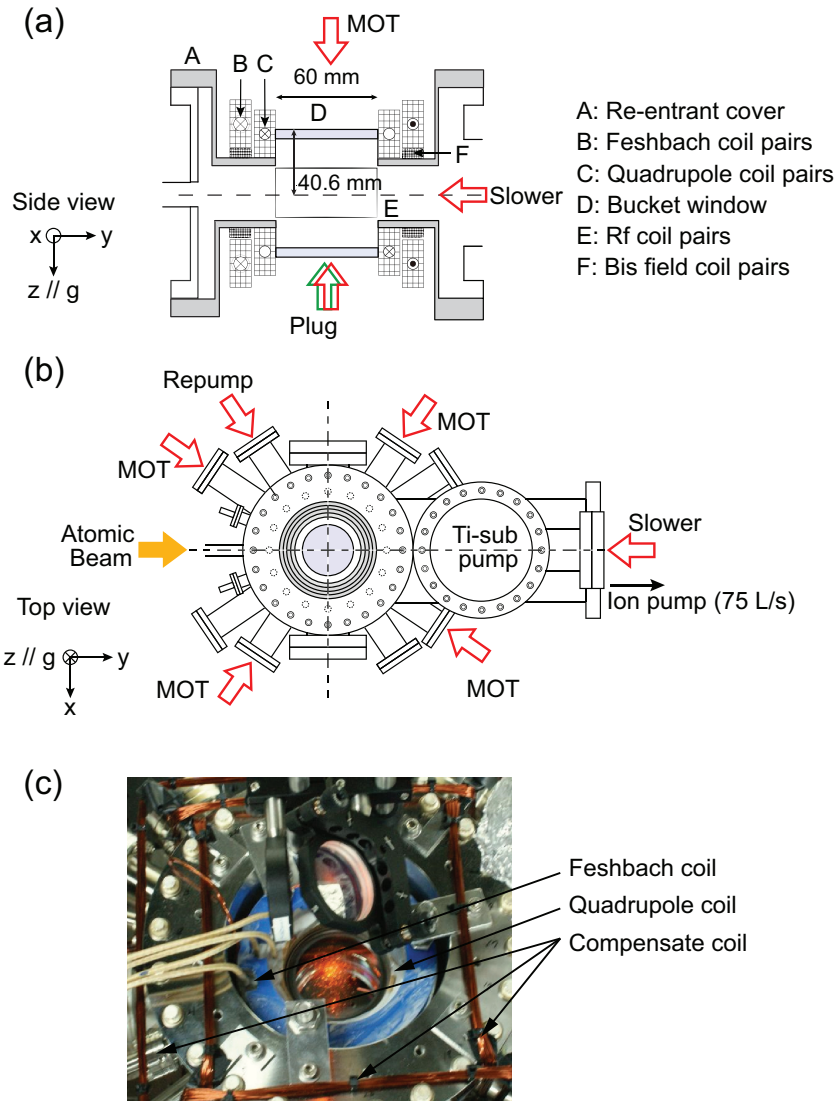

Figure 2.7: (a) Side and (b) top view of main chamber. Recessed bucket windows with 60-mm diameter clearance are mounted above and below the main vacuum chamber. A pair of 36-turn water-cooled coils are secured chamber's center. Radio-frequency evaporation coils are placed inside the vacuum chamber. A plug beam is aligned wi the axial direction of the magnetic field. (c) A photo of main chamber in bird's eye view. Feshbach coil pairs and quadrupole coil pairs are attached to taflon frame fixed by non-magnetic epoxy.

tem on a nonmagnetic optical table (Kinetic Systems Inc., USA) to suppress field reflection. The flow rate of cooling water through a 12-m-long quadrupole coil tube was 250 ml/s at a 22-bar water pressure, so a current of 580 A would increase the temperature of the cooling water by less than 10°C. Two pairs of rectangular coils of UHV-compatible kapton wires are mounted inside the chamber for rf evaporation and are connected via electric feedthroughs. The stray magnetic field, including the earth's field, is compensated for by using three pairs of magnetic coils surrounding the chamber.

In order to precisely align the atomic beam line to the center of the main chamber, the decreasing part of the slower and the oven assembly are secured on independent adjustable supports and are connected with flexible bellows. Direct visual inspection of the beam line alignment was performed before installing the sodium cup.

2.2.4 Vacuum

Since background collisions heat up the cold atoms, the ultra-high vacuum (UHV) condition is critical for efficient evaporation cooling and manipulating quantum gas. Usually the oven chamber records the highest pressure up to 10^{-8} Torr because of the atomic vapor and therefore we place two differential pumping tubes in series between the oven and the slower by using a long tube for the slower (inner diameters of $5-6$ mm). At a typical running condition, the pressures in the oven, the slower and the main chamber are low 10^{-9}, high 10^{-11} Torr and below 10^{-11} Torr, respectively. Pressure readings are taken from

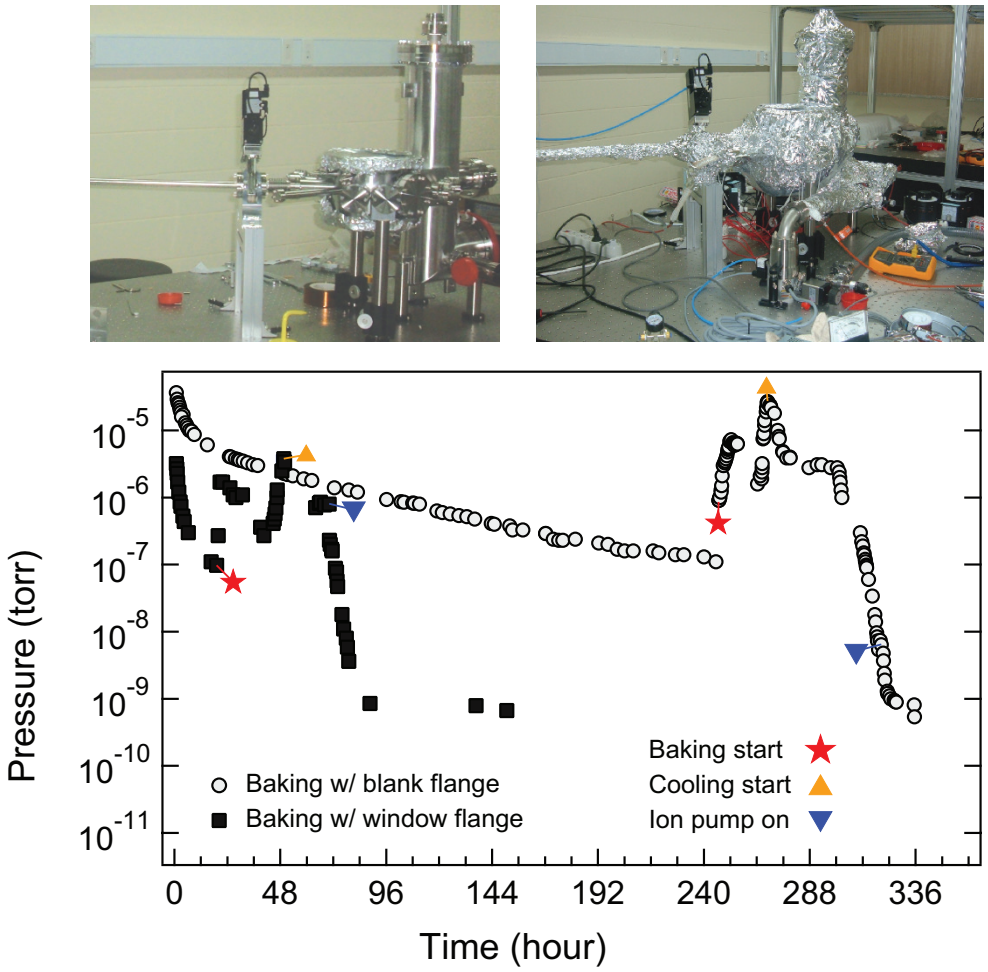

Figure 2.8: Pressure of main chamber read by ion gauge during the baking process. The circle symbol is pressure variance during baking with blank flanges are attached. After replacing the blanks with window flanges, we rebake the chamber (Solid square). Inset photos represent assembled main chamber with blank flanges and baking process.

the ion pumps.

Fig. 2.8 shows variations of the main chamber pressure during bakeout. We first bake the stainless-steel vacuum chamber at 250 °C with blank metal flanges are attached at the view port[3]. Temperature was raised by 10 °C in an hour, minimizing temperature gradient of the chambers while keeping the hottest part to be the ion pumps (75 L/s). The ion pump was turned on after degassing the ion pump and we decreased temperature of the main chamber uniformly. The decreasing rate is 3.75 °C/hour and about one order of magnitude pressure (torr) was lowered as the temperature cool down by 60 °C. Two days later, we obtained mid 10^{-10} Torr at room temperature.

Then we mildly rebaked the main chamber at 150 °C for couple of days with all the blank components were replaced by view ports and coils for the slower. After cooling the machine at room temperature, the pressure read 10^{-10} Torr [Fig. 2.8]. Finally, pressure below 10^{-11} Torr was achieved at the main chamber after Ti-sublimation pumping. The pump consist of four Ti-sub filaments and working range is below 10^{-7} Torr. When a current flows into the filament, the substance would be evaporated by the resistance heating. Its surrounding chamber walls would be coated by the thin film of Ti and hence reduces the pressure of the chamber. Typical condition for the sublimation is 4.7 V - 48 A flows at 10 to 20 minute and the chamber is heating up during the Ti-sub pumping so we turn off ion pump. At least 2 hours is required to cool down the machine and we were able to obtain UHV, below 10^{-11} Torr, which

[3]Glass windows and gate valves are the high temperature fragile components.

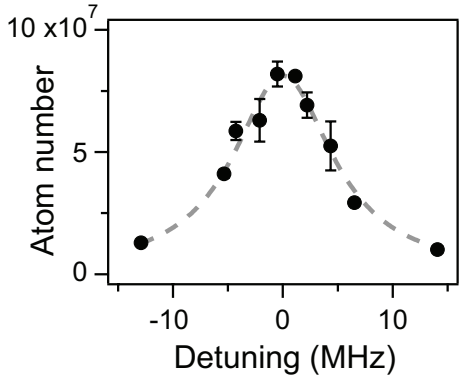

Figure 2.9: Atom number at different imaging laser frequency. Each data point is average value of three experimental realization and error bar indicate standard deviation. Dashed line is Lorentzian curve fit to the data, where the obtained linewidth is 11.1 MHz (natural linewidth of sodium atoms is 9.8 MHz).

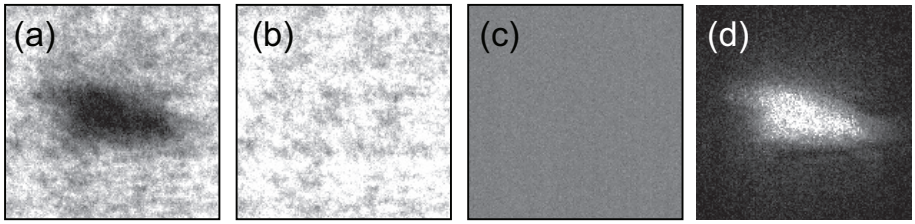

Figure 2.10: For imaging construction three images are required. (a) Raw image of atoms, (b) image of photons without atoms, and (c) image without laser light. These images are processed to get optical density image (d).

was also reflected in the increases of lifetime of atoms in magnetic trap.

2.2.5 Imaging setup

The atom number and the temperature of atom clouds were determined from absorption images of the samples. A 50-μs pulse of imaging light, resonant on the $|F = 1, m_F = -1\rangle \rightarrow |F' = 2, m_F = -2\rangle$ transition[4], was applied in the

[4]We can fine the resonance condition by varying the imaging beam frequency, see Fig. 2.9.

z-direction, and the spatial distribution of the imaging light was captured with a CCD camera (pixelfly qe, Cooke Corp.). The probe light was σ-polarized, and a small magnetic bias field was applied along the direction of light propagation. The density distribution, $\tilde{n}(x, y)$, integrated along the line of sight (z-axis) was obtained from three consecutive images [Fig. 2.10]: the first with atoms, $I_1(x, y)$, the second without atoms, $I_2(x, y)$, and the last dark image without light, $I_3(x, y)$,

$$\tilde{n}(x, y) = \int n(x, y, z)dz = -\sigma_0^{-1} \ln(\frac{I_1 - I_3}{I_2 - I_3}), \tag{2.2}$$

where $\sigma_0 = 3\lambda^2/4\pi$ (λ=589 nm) is the resonant cross section. The total atom number is given by integrating $\tilde{n}(x, y)$ over the whole area, and the temperature is determined from the Gaussian width of the spatial distribution of the atoms (described in chapter 3). The above equation is valid when the probe beam intensity is in a linear regime and atomic density is sufficiently low enough to avoid unreliable range of the CCD. To resolve high atomic density region, we use saturation absorption imaging technique [12, 13] In-trap absorption images were used for aligning the plug beam and for magnetic field compensation.

2.2.6 Control system

For manipulating cold atoms, precise control of electronic signal is essential. Fortunately, the software program *Word Generator* (WG) developed by A. Keshet can fulfill the requirements and our research group appreciate for the control software. The the software and operation manual can be downloaded from the

website [14] and its working principles are described in Ref [15].

For controllable outputs, we purchase commercial output cards: Two digital cards (PCI-6534, National Instruments) provide the 64 channel digital outputs and two analog 8 channel cards (PCI-6713, National Instruments) provide the 16 analog outputs. Theses four cards and a GPIB cards are mounted in a PCI chassis, which is connected to standard PC. Timing of the digital and analog cards is controlled by one of the PCI cards, within 2 μs resolution. Using the variable frequency clock generated by FPGA (XEM3001, Opal Kelly), we can avoid redundant buffers. The GPIB bus directly controlled frequency and amplitude our function generator (N5181A, Agilent). The analog channels provide voltage from -10 V to $+10$ V with 5 mV resolution maximum output current is about 20 mA. The digital channels can provide 0 or 5 V and all of the output channels are buffered through opto-isolator (TLP-250, TOSHIBA) and follower circuit in order to reduce possible electric shock from a device. The TTL timing is controlled within 500 ns.

2.3 Magneto-optical trap

2.3.1 Dark-MOT

We adopt the dark magneto-optical trap (MOT) scheme to increase the atom density in a MOT [11]. By simply blocking the central part of the repumping beam, one can reduce the re-radiation pressure at the core of a MOT, enabling

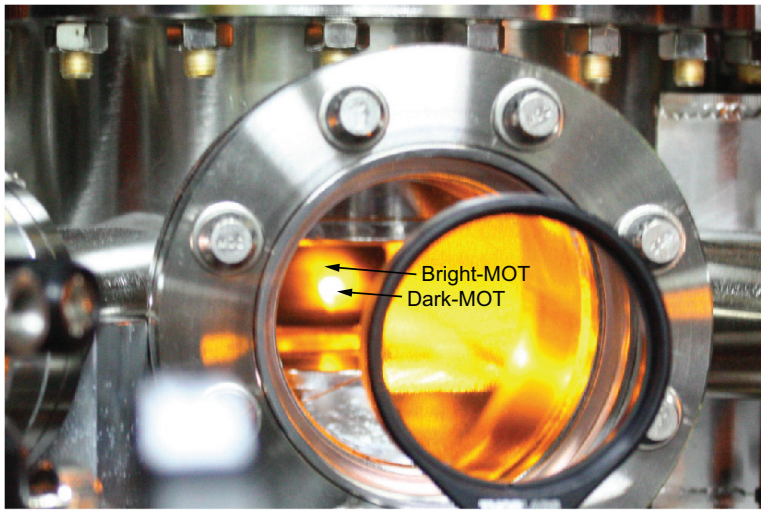

Figure 2.11: A photo of atoms captured in the dark-MOT. Due to the spontaneous emission of light, the core of dark-MOT is still bright. The flares around the dark-MOT, where the repumping light is passing through, is the bright MOT.

more atoms to be collected in the $|F = 1\rangle$ hyperfine state at higher density.

Our trapping, slowing, and repumping beams have $1/e^2$ beam diameters of ≈ 2.5 cm. The frequencies of the trapping and the slowing beams are 15 MHz and 700 MHz red-detuned to the $|F = 2\rangle \rightarrow |F' = 3\rangle$ transition, respectively, and that of the repumping beam is 10 MHz red-detuned to the $|F = 1\rangle \rightarrow |F' = 2\rangle$ transition. The trapping beam powers for all six beams are 10 mW and the total power of the repumping beam was 15 mW, where the 1-cm-diameter center part was blocked to implement a dark MOT. A 55-mW slowing beam was aligned to the atomic beam line and focused to the oven nozzle. We observed that the MOT performance for BEC production was deteriorated with a higher slowing beam power, which might be attributed to the induced

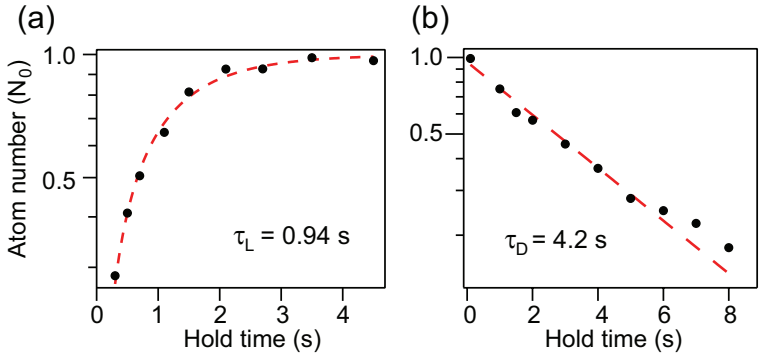

Figure 2.12: Loading and decay of atoms in the dark magneto-optical trap. (a) Loading rate and (b) decay rate of the MOT is measured by atoms number, which is normalized by the stead state number. Dashed line is exponential curve fit to the data $1 - e^{-t/\tau_L}$ for (a) and e^{-t/τ_D} for (b), which gives τ_L=0.94 s and τ_D =4.2 s, respectively.

AC stark shift ($\approx$ 1 MHz). The quadrupole field gradient along the z-direction B_q was 7.5 G/cm. The loading time and the lifetime of our dark MOT were 0.94 s and 4.2 s, respectively [Fig 2.12]. In typical experimental runs, more than 10^{10} atoms were collected within a 3 s loading. In a bright MOT, i.e., one with an unblocked, bare repumping beam, the number of trapped atoms was reduced by a factor of 50.

2.3.2 Aligning the dark-MOT

Obtaining high density with low temperature MOT is crucial for making Bose-Einstein condensate. This section would briefly introduce some basic principles that I follows for obtaining good MOT. Once the bright MOT is shown up at the main chamber, residual magnetic field can be compensated by shimming coils around the main chamber. The insensitive movements of center position at

various magnetic quadrupole field gradient can be a reference for field compensation. For the optical alignment, balance the beam power in each MOT beam and check out the polarization by making checker composed of $\lambda/4$ waveplate and polarizer. The 2D-MOT, which is made by blocking one axis of the MOT beam, can be a good guide for optimal beam alignment. Inserting the dark-spot into the repumping beam path, you can see the round core of dark-MOT. Unfortunately, visual inspection of dark-MOT shape does not always generate the condensates after evaporation cooling in a magnetic trap. For a fine tuning of the dark-MOT, imaging the number of atoms trapped in the magnetic trap and maximizing the number by MOT beam twig is very tedious but solid way to get condensate.

Bibliography

[1] H. Metcalf and P. van der Straten, Phys. Rep. **244**, 203 (1994).

[2] S. Stellmer, B. Pasquiou, R. Grimm, and F. Schreck, Phys. Rev. Lett. **110**, 263003 (2013).

[3] Y. Takasu, K. Maki, K. Komori, T. Takano, K. Honda, M. Kumakura, T. Yabuzaki, and Y. Takahashi, Phys. Rev. Lett. **91**, 040404 (2003).

[4] A. Griesmaier, J. Werner, S. Hensler, J. Stuhler, and T. Pfau, Phys. Rev. Lett. **94**, 160401 (2005).

[5] S. Kraft, F. Vogt, O. Appel, F. Riehle, and U. Sterr, Phys. Rev. Lett. **103**, 130401 (2009).

[6] M. Lu, N Q. Burdick, S. H. Youn, and B. L. Lev, Phys. Rev. Lett. **107**, 190401 (2011).

[7] K. Aikawa, A. Frisch, M. Mark, S. Baier, A. Rietzler, R. Grimm, and F. Ferlaino, Phys. Rev. Lett. **108**, 210401 (2012).

[8] E. Arimondo, W. D. Phillips, and F. Strumia, *International School of Physics, Enrico Fermi, Course CXNIII* (North-Holland, Amsterdam, 1992).

[9] D. J. McCarron, S. A. King and S. L. Cornish, Meas. Sci. Technol. **19**, 105601 (2008).

[10] J. F. O'Hanlon, *A User's Guide to Vacuum Technology* (Wiley, NewYork, 1989).

[11] W. Ketterle, K. B. Davis, M. Joffe, A. Martin, and D. E. Pritchard, Phys. Rev. Lett. **70**, 2253 (1993).

[12] G. Reinaudi, T. Lahaye, Z. Wang, and D. Guery-Odelin, Optics Letters, **32**, 3143 (2007).

[13] W. J. Kwon, J. Choi, and Y. Shin, J. Korean. Phys. Soc. **61**, 1970 (2012).

[14] A. Keshet, *The Cicero Word Generator*,

http://github.com/akeshet/Cicero-Word-Generator (2012).

[15] A. Keshet and W. Ketterle, arXiv.1208.2007

Chapter 3

Evaporative cooling to Bose-Einstein condensates

Evaporation is a familiar phenomenon in our daily life and has been regarded as the powerful and exclusive method for obtaining quantum degenerate gases, such as Bose-Einstein condensation of atomic gas [1, 2]. Evaporative cooling of neutral atoms relies on selective removal of particles having an higher energy than the average energy [3], where remaining atoms would be cool down after rethermalization. Thus, efficient evaporation cooling requires fast rethermalization and a conservative environment that could minimize undesired atom loss, heating due to inelastic collisions and background collisions.

This chapter describes the evaporation process that generates large number Bose-Einstein condensates of sodium atoms. Measuring the heating rate and loss rate of atoms in an optically plugged magnetic quadrupole trap, we could

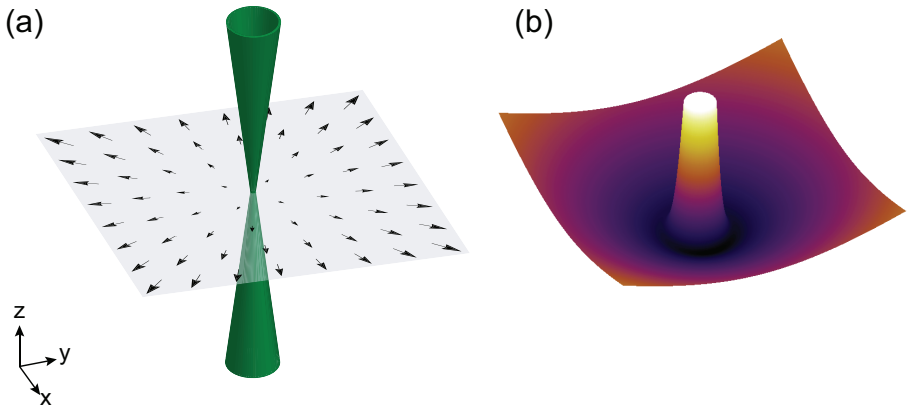

Figure 3.1: (a) Schematic diagram of optical plugging. The magnetic quadrupole field is displayed by vector in the x-y plane and green laser light is focused at the magnetic quadrupole field center. (b) Shape of plugged magnetic potential in the $z = 0$ plane.

understand the cooling path toward the Bose-Einstein condensates quantitatively. The results are reported in the following publication.

- Myoung-sun Heo, Jae-yoon Choi, and Yong-il Shin. *"Fast production of large ^{23}Na Bose-Einstein condensates in an optically plugged magnetic quadrupole trap"* Physical Review A **83**, 013622 (2011).

3.1 Optically plugged magnetic quadrupole trap

A magnetic quadrupole trap provides sufficient conditions for evaporative cooling of neutral atoms. Applying a radio-frequency wave to trapped atoms, we can selectively manipulate the trapped atomic spin state into anti-trapping spin state. The quadrupole trap also has a large volume and the magnetic field can be generated by simple coil configuration, coaxial coils with opposite current, of-

fering large optical access to a sample. The magnetic quadrupole field direction is given by

$$\mathbf{B}_{\text{quad}} = B_q(\frac{x}{2}, \frac{y}{2}, -z), \tag{3.1}$$

where B_q is axial field gradient. Because of the linear trap geometry, it provides more tight confinement than harmonic trap, which is better for rapid evaporation [4].

Despite the benefits of magnetic quadrupole trap, however, a spin state near the trap center can be non-adiabatically flipped into anti-trapping state because of the low Larmor frequency. This atom loss is a significant drawback of the magnetic quadrupole trap since the atom loss leads to heat up the sample, setting a limit for maximum phase-space density. In our group, the atom loss could be highly suppressed by imposing potential barrier near the zero-field center so the non-adiabatic spin flip probability is reduced.

The additional potential barrier can be made by focusing off-resonant laser light near the magnetic trap center [Fig. 3.1]. The optical potential is induced by interaction between induced electric dipole moment of atom and the external field, which can be also understood by time-independent perturbation theory [5]. For simplicity, we assume two level atom without degeneracy. When the interacting Hamiltonian is $H_1 = -\mu\mathbf{E}$, $\mu = -e\mathbf{r}$ is electric dipole moment, second-order energy shift ΔE_i of unperturbed state E_{0i} (in view of dressed state)

is

$$\Delta E_i = \sum_{i \neq j} \frac{|\langle j|H_1|j\rangle|^2}{E_{0i} - E_{0j}}. \tag{3.2}$$

The level shift of the ground and excited state is simplifies to

$$\Delta E_g = -\frac{|\langle e|\mu|g\rangle|^2}{\delta}|E|^2 = -\frac{3\pi c^2}{2\omega_0^3}\frac{\Gamma}{\delta}I, \tag{3.3}$$

$$\Delta E_i = +\frac{|\langle e|\mu|g\rangle|^2}{\delta}|E|^2 = +\frac{3\pi c^2}{2\omega_0^3}\frac{\Gamma}{\delta}I, \tag{3.4}$$

where δ is laser detuning, Γ is the natural linewidth $\frac{\omega_0^3}{3\pi\epsilon_0\hbar c^2}$, and I is intensity of laser light. Since the difference of level shift between the ground state and excited state ($\Delta E = \Delta E_i - \Delta E_g = \frac{3\pi c^2}{\omega_0^3}\frac{\Gamma}{\delta}I$) proportional to the intensity of light, laser beam with gaussian profile can exert forces to the atoms.

In the experiments, optical plugging is performed by focusing a blue-detuned 532-nm laser beam near the zero of the magnetic field. The plug beam propagates along the z direction with a beam waist of $w \simeq 45$ μm, providing a repulsive potential barrier of $U_p = k_B \times 90$ μK with 1.7 W, where k_B is the Boltzmann constant. Improving the beam pointing stability, we use a fiber to deliver green light close to the main chamber[1]. The position stability of the optical plug was ≈ 5 μm and optical setup for the plug beam is displayed in the appendix A.

The effective potential of the optically plugged magnetic trap is

$$U(\mathbf{r}) = \mu B_q \sqrt{\frac{(x^2+y^2)}{4} + z^2} + U_p e^{-\frac{(x+d)^2+y^2}{2w^2}}, \tag{3.5}$$

where $\mu = \mu_B/2$ (μ_B is the Bohr magneton) is the magnetic moment of the atom, U_p and w are the potential height and the beam waist of the optical plug,

[1]The fiber lifetime is more than 1 year with 50% of coupling efficiency.

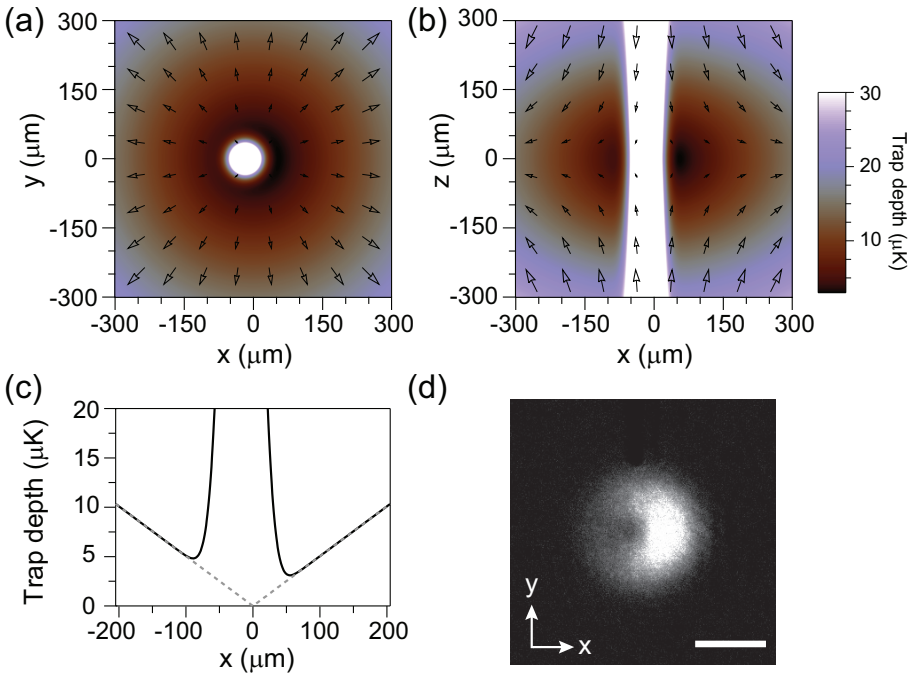

Figure 3.2: Contour plots of potential trap depth in the (a) x-y plane and (b) z-x plane at $B_q = 30$ G/cm. The magnetic field direction is displayed by the vector in the contour. (c) Radial potential at the $z = 0$ plane with(solid) and without(dashed) the optical barrier. (d) Atoms in the optically plugged quadrupole trap is imaged after 8 ms expansion. Scale bar represents 500 μm.

respectively, d is the offset of the plug beam from the magnetic field's center, m is the mass of the atom. Here, the beam focusing is assumed to be preserved along the axial direction since the Rayleigh length $\pi w^2/\lambda \approx 12\ mm$ is larger than the sample size. The contour plot of the plugged trap is shown in Figure 3.2 within our typical final condition B_q =30 G/cm, $d = 17\ \mu$m and $w \simeq 45\ \mu$m and trapping frequencies are estimated to be $(f_x, f_y, f_x) \approx (210, 55, 110)$ Hz.

When the plug beam has circular shape and placed at the center of magnetic trap, the plugged trap has azimuthal symmetry, forming a ring trap. Despite the interesting researches on about persistent mass flow in the ring trap, it is desirable to break this symmetry to make large number of condensate. In the previous experiments, the symmetry is broken by applying plug beam in the transverse direction [2] or using elliptic beam [6]. In our group, we simply displaced the plug beam from the zero-field center by $\simeq 17\ \mu$m in the x direction. We found that a slight misalignment, smaller than the beam waist, is effectively helpful to get condensate without significantly reducing the plugging effect.

3.2 Bose-Einstein condensation

3.2.1 Radio frequency-induced evaporative cooling

For radio frequency-induced evaporation, the laser-cooled atoms are transferred to the magnetic trap by increasing current flows of quadrupole coils and turning off the cooling laser. The trapped atoms are in $|F = 1, m_F = -1\rangle$ state and

evaporation process is started by linear radio frequency sweep from 30 to 2 MHz in 12 s and then to 0.1 MHz in another 2 s [Fig. 3.3(a)].

Before the detail description of evaporation process in the magnetic potential, I would introduce several methods for measuring a temperature. Neglecting the inter-atomic interaction, the density distribution of Bosonic atoms $n_{th}(\mathbf{r})$ in a potential $U(\mathbf{r})$ is

$$n_{th}(\mathbf{r}) = \frac{1}{\lambda_{dB}^3} g_{3/2}(z(\mathbf{r})), \tag{3.6}$$

where $\lambda_{dB} = h/\sqrt{2\pi m k_B T}$, $z(\mathbf{r}) = \exp(\frac{\mu - U(\mathbf{r})}{k_B T})$, μ is chemical potential, and $g_{3/2}(z)$ is the Bose function defined by $g_\nu(z) = \sum_{i=1} z^i / i^\nu$. The higher order term of z in the Bose function reflects the quantum statics and it can be approximated to z at the low density regime. Therefore, the density profile at the outer wings of trap could be simplified into $n_{th} = \frac{1}{\lambda_{dB}^3} z \propto \exp(-\frac{U(r)}{k_B T})$ and the temperature of atomic gas confined in the potential can be obtained by exponential fit.

The temperature of trapped atoms can be also measured from time-of-flight (TOF) image. If the atomic gases expand ballistically during the time-of-flight, atoms at starting position $\mathbf{r}_i$ and momentum $\mathbf{p}$ would arrive at $\mathbf{r} = \mathbf{r}_i + \mathbf{p} t_e / m$ after a expansion time t_e. Then, density profile $n_{\mathrm{tof}}(\mathbf{r}, t_e)$ after the expansion is

$$n_{\mathrm{tof}}(\mathbf{r}, t_e) = \frac{1}{h^3} \int d^3\mathbf{r} d^3\mathbf{p} \frac{1}{e^{-(\mu - H(\mathbf{r}_i, \mathbf{p}))/k_B T} - 1} \delta^3(\mathbf{r} - \mathbf{r}_i - \frac{\mathbf{p}}{m} t_e). \tag{3.7}$$

When the atoms are trapped in harmonic potential, $U = \frac{1}{2} m(\omega_x x^2 + \omega_y y^2 + \omega_z z^2)$,

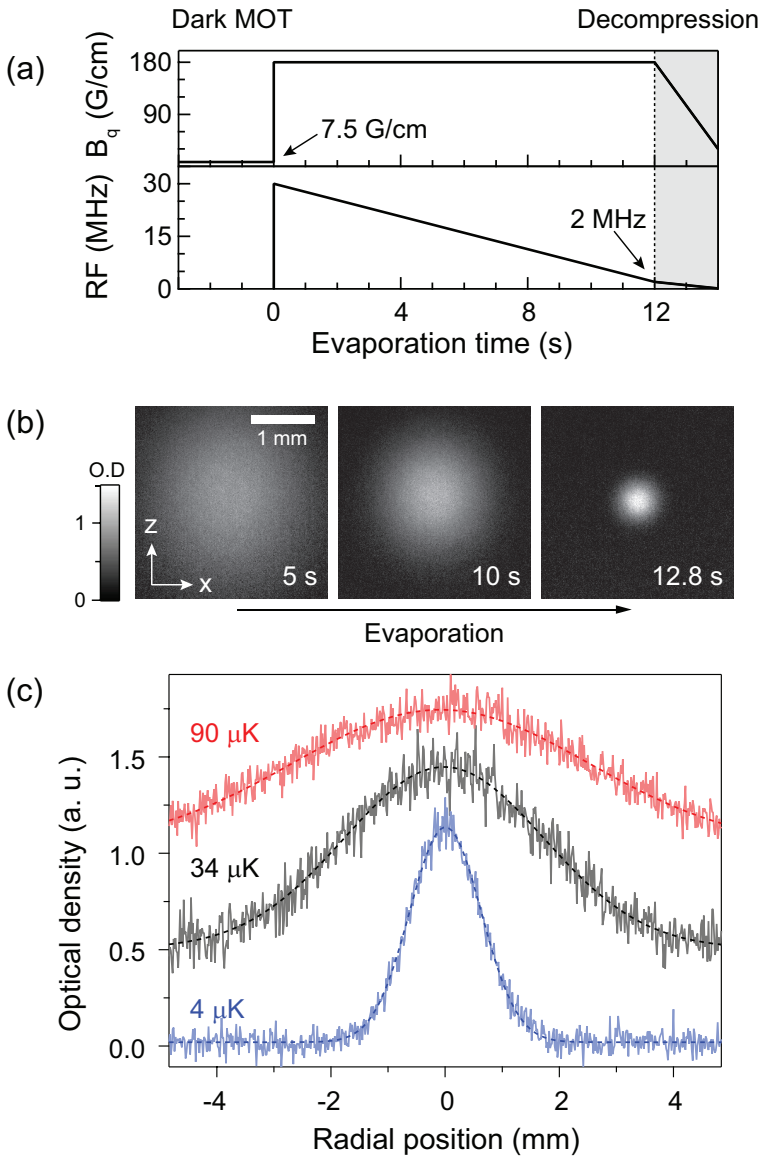

Figure 3.3: (a) Experimental sequence for rf-induced evaporative cooling. (b) Optical density images during evaporation with 24 ms of time-of-flight expansion. (c) Atomic density profiles along the cloud center are displayed for each evaporation time. Red line for 5 s, black line for 10 s, and blue line for 12.8 s. The dashed lines are Gaussian curves fit to the density distribution and temperatures could be obtained from the curve fitting.

the density distribution is

$$n_{\mathrm{tof}}(\mathbf{r}, t_e) = \frac{1}{\lambda_{dB}^3} \prod_{i=x,y,z} \left(\frac{1}{1+\omega_i^2 t^2} \right) g_{3/2} \left(\exp \left[\frac{\mu - \sum_{i=x,y,z} \frac{i^2 \omega_i^2}{1+\omega_i^2 t^2}}{k_B T} \right] \right). \quad (3.8)$$

Again, the density profile at the outer regime along the i-th direction follows gaussian shape with w_i of thermal width and therefore, we can relate the temperature of atomic gas with the trap frequency and gaussian width of atomic density distribution after the expansion time:

$$k_B T = \frac{m}{2} \left(\frac{\omega_i^2}{1+\omega_i^2 t^2} w_i^2 \right). \quad (3.9)$$

Note that when the expansion time is sufficiently long ($t_e \gg \omega_x^{-1}, \omega_y^{-1}, \omega_z^{-1}$) enough that initial position could be ignored, the expression is simplified to

$$n_{\mathrm{tof}}(\mathbf{r}, t_e) = \frac{1}{\lambda_{dB}^3} \frac{1}{\omega_x \omega_y \omega_z t_e^3} g_{3/2}(e^{(\mu - \frac{mr^2}{2t_e^2})/k_B T}), \quad (3.10)$$

where $r^2 = x^2 + y^2 + z^2$. It implies that the cloud shape become isotropic and thermal width of spatial wing is independent of the trapping potential but only related to the expansion time and temperature. We usually obtain the temperature of trapped sample by the long time-of-flight image that has isotropic density distribution [Fig. 3.3(b)].

Figure 3.3(c) shows the horizontal cross section view and we can see that the thermal width is decreased as the evaporation cooling proceeded. In the last 2 s of evaporation, the quadrupole field gradient B_q was ramp down from 180 to 30 G/cm. The decompression process is necessary to achieve a large condensate by reducing inelastic losses caused by high atom density, such as three-body

recombinations. Moreover, adiabatic decompression lower the temperature so effect of optical plug beam is effectively enhanced.

The time evolution of atom number and temperature during the evaporation was determined from absorption images taken after 16 ms of time of flight [Fig. 3.4]. Peak density n and collision time τ are estimated as $n = N/[32\pi(k_BT/\mu B_q)^3]$ and $\tau^{-1} = \sqrt{2}\sigma\bar{v}$, respectively, ignoring gravity and the plug potential. $\sigma = 8\pi a^2$ is the elastic collision cross section, where scattering length $a = 52a_0$ (a_0 is the Bohr radius) and $\bar{v} = (8k_BT/\pi m)^{1/2}$ is the average thermal velocity. The truncation parameter η is defined as $\eta = (h\nu_{rf} - U_0)/k_BT$, where U_0 is the potential at the trap bottom and $U_0/h \simeq$320 KHz at 180 G/cm and $\simeq$70 KHz at 30 G/cm. Runaway evaporation was achieved with increasing collision rate τ^{-1}. When the decompression stated, the peak density was estimated to be $\sim 10^{14}/cm^3$. η smoothly increased from 6 to 9 before the decompression.

The evaporation in a bare quadrupole trap was also investigated without the plug beam. Fig 3.5 shows the evaporation trajectories in the N-T (atom number-temperature) and N-D (atom number-phase space density) planes. At $T < 20$ μK, the plugging effect becomes noticeable from the deviation between the evaporation curves with and without plugging. The maximum phase-space density was about 5×10^{-2} in an unplugged quadrupole trap.

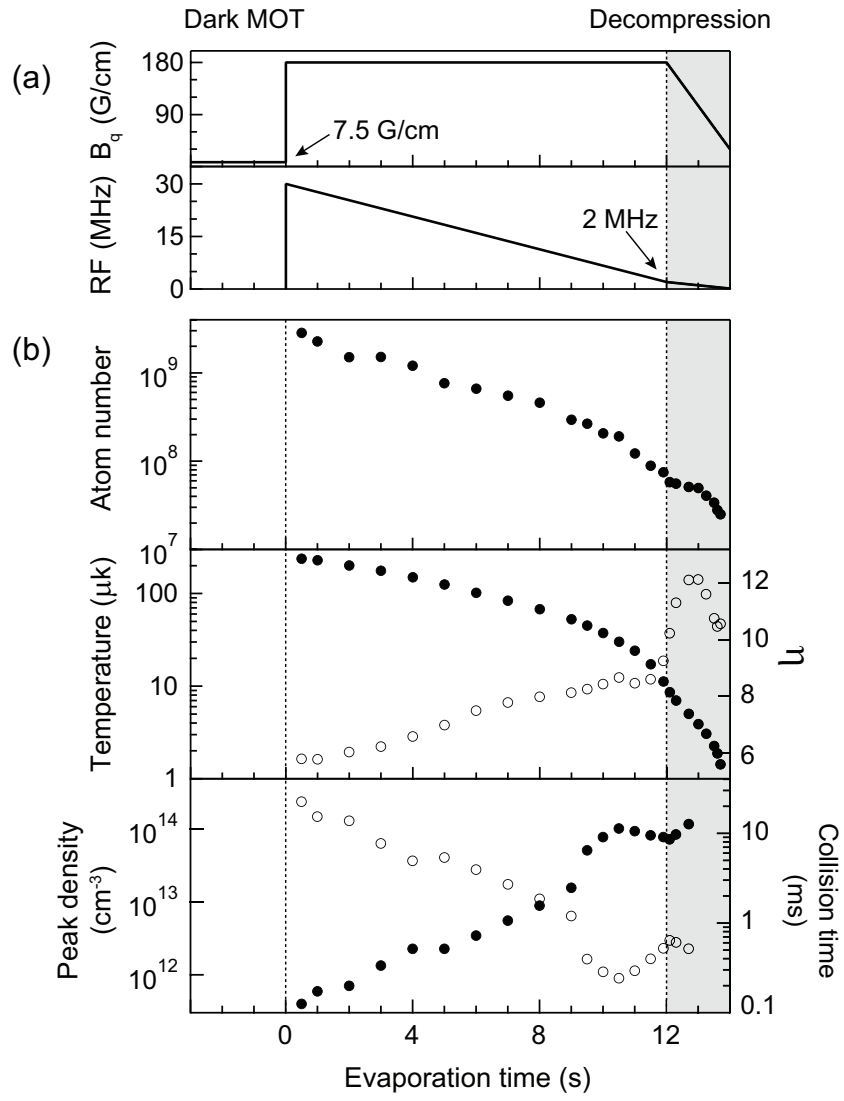

Figure 3.4: Experimental sequence for BEC production, which consists of dark MOT, rf evaporation, and trap decompression. (a) Field gradient and radio frequency. (b) Time evolution of atom number, temperature, truncation parameter η, peak density, and collision time. The decompression phase is indicated with a grey zone.

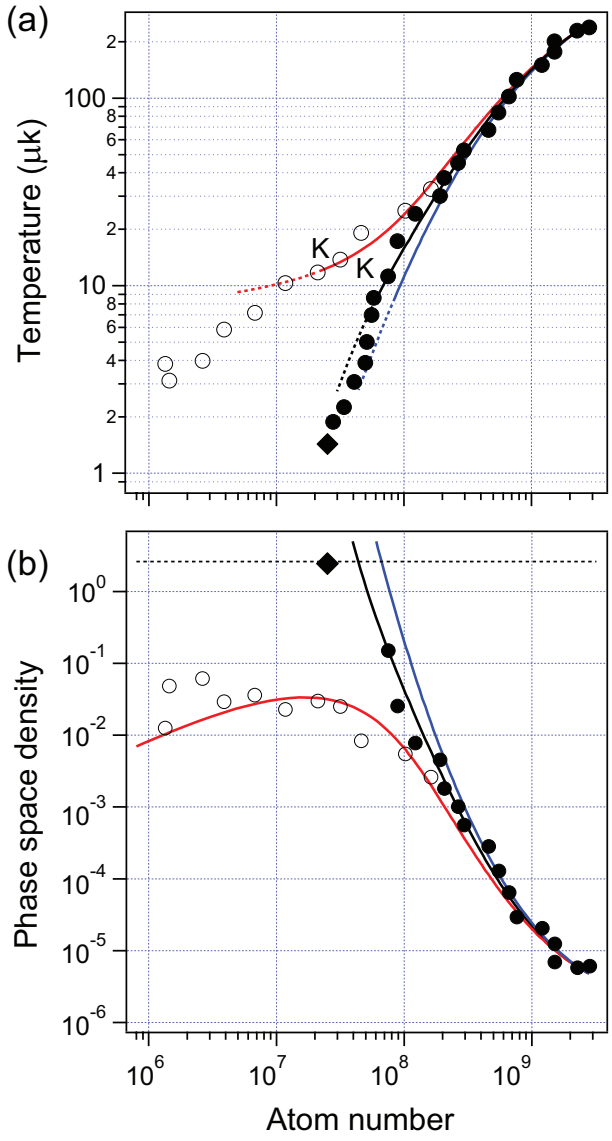

Figure 3.5: Evaporation trajectory. (a) Temperature versus atom number. (b) Peak phase-space density versus atom number. Data points at 11.9 s (before decompression) are marked with K's. The onset of condensation is observed at 13.7 s in a plugged trap from the bimodal momentum distribution (see inset). The black diamond indicates the transition point. The solid lines are from numerical simulation with a plug (black), no plug (light grey, red online), and no loss (dark grey, blue online). The dashed lines are the evolution after 12 s

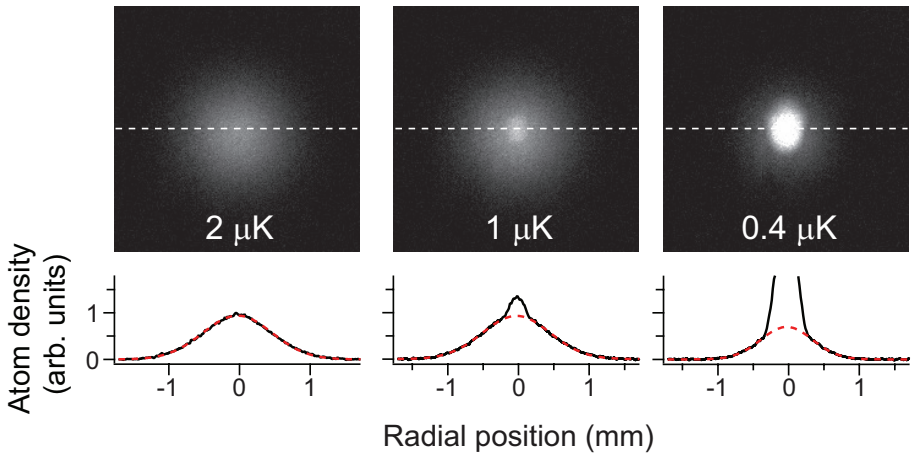

Figure 3.6: Bose-Einstein condensation. Absorption images taken after a time-of-flight of 24 ms (top) and the atom density distribution along the center dashed lines (bottom). The red dashed lines are Gaussian curves fit to the outer thermal wings. Below a critical temperature, the condensate fraction increases with clear bimodality of the momentum distribution of atoms.

3.2.2 Producing Bose-Eisntein condensates

Bose-Einstein condensation of sodium atoms has been generated after 13.7 s of evaporation in the plugged magnetic potential. The signature of condensate is a bimodal momentum distribution [Fig. 3.6], which can be obtained by 24 ms TOF absorption image. After such a long TOF, thermal gas will display a broad Gaussian distribution because of the finite temperature, while the condensate atoms are zero momentum state. Therefore, the shadow image after long TOF should display the two different state of atom.

For large sample size, we optimized the displacement of the optical plug at $d \simeq 17\ \mu$m, less than half of its beam waist [Fig. 3.7]. At the phase transition, the atom number and the critical temperature were $N_c = 2.5 \times 10^7$ and $T_c = 1.4\ \mu$K,

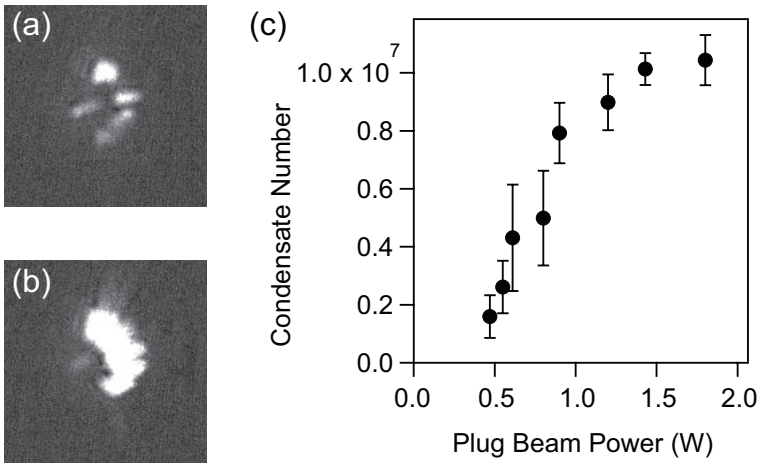

Figure 3.7: (a) Absorption image of BEC after 8 ms time-of-flight when the green plug beam is aligned at the trap center. (b) Same experiment with the $d = 17$ μm offset from the center. Atom numbers in the images are 10^6 and 4×10^6, respectively. (c) Condensate number versus plug power. Each point is averaged over three separate runs of the experiment.

respectively. The critical temperature of an ideal gas in a 3D harmonic trap is given as $k_B T_c' = 0.94\ h\bar{f} N_c^{1/3}$ [2], where $\bar{f}$ is the geometric mean of the trap frequencies. From the local curvatures of our trapping potential, we estimate $\bar{f}$=108 Hz, leading to $T_c' = 1.4$ μK, which is in agreement with our observation. After a full evaporation of 14 s, a quasipure condensate of 1.0×10^7 atoms was generated. The condensate lifetime in a plugged magnetic trap was over 10 s with an additional decompression to $B_q = 15$ G/cm.

The minimum plug beam power for making a condensate of $> 10^6$ atoms was $\sim$0.4 W for the 14 s of evaporation and we could minimize the evaporation time to 8 s to observe a condensate. Note that we could produce fragmented small condensates containing $< 10^6$ atoms with a centered optical plug [Fig. 3.7], i.e., $d \approx 0$ μm, due to an imperfection in the plug beam profile.

3.3 Characterizing evaporation process

3.3.1 Rate equations for atom number and temperature

A simple model can characterize the rf-induced evaporation process which is well described in ref. [3]. When spin-flip atom has $\varepsilon_e k_B T$ average energy, we can write rate equation for the total energy as $\dot{E} = \varepsilon_e k_B T \dot{N}$ from the energy conservation. When $E = N\varepsilon k_B T$ is the total energy of the system with the average energy of a trapped atom $\varepsilon k_B T$, we can derive a simple relation between the temperature and the atom number,

$$\frac{\dot{T}}{T} = (\frac{\varepsilon_e}{\varepsilon} - 1)\frac{\dot{N}}{N}. \tag{3.11}$$

This equation can be also expressed by two coupled rate equations of atom number and temperature,

$$\frac{\dot{N}}{N} = -\Gamma_e \tag{3.12}$$

$$\frac{\dot{T}}{T} = -(\frac{\varepsilon_e}{\varepsilon} - 1)\Gamma_e, \tag{3.13}$$

where Γ_e is evaporation loss rate.

In the experiment, however, atom loss and heating process also caused by background collisions and non-adiabatic spin flip, so our evaporation curve in Fig. 3.5 could be understood by studying those effects. In the following section, experimental studies on the spin fliped atom loss and numerical simulation of the evaporation curve would be discussed.

3.3.2 Suppression of the non-adiabatic spin flip

Measuring the loss and heating rate of a thermal gas for various temperature with and without plug at $B_q = 180$ G/cm, we can quantitatively understand the effect of the non-adiabatic atom loss. The initial temperature of thermal gas was controlled by the final rf-values. Varying the holding times in the magnetic trap, the atom number and temperature were determined. The rf field was turned off after the sample preparation in order to exclude the evaporation effects. In Ref [8], a rf field was applied to main tain a constant temperature. In our experiments, however, nonmonotonic behavior of the temperature is observed probably because of initially cooling and then heating. Without the rf, we observed that the temperature almost linearly increases with a small acceleration and the number decay rate decreases slowly. The initial loss and heating rate were determined from an exponential fit and a linear fit, respectively, to the data points with temperatures lower than 120% of the initial temperature [Fig. 3.8].

The Majorana loss rate Γ_m in a quadrupole trap is proposed to scale as $\Gamma_m \propto \hbar/m(\mu B_q/k_B T)^2$ [7] and our fit dashed line in Fig 3.9 with $CT^{-2} + \Gamma_b$ yield to $C = 139(3)\ \mu K^2/s$ and $\Gamma_b = 0.013(7)s^{-1}$, where Γ_b is the background loss rate (corresponding to a lifetime of 75 s). This result suggests $\Gamma_m = 0.14\hbar/m(\mu B_q/k_B T)^2$ and we found the proportionality constant is much smaller than the valuse of 0.87 [7] and 0.58 [8] in previous experiments with ^{87}Rb atoms, which is beyond the simple model.

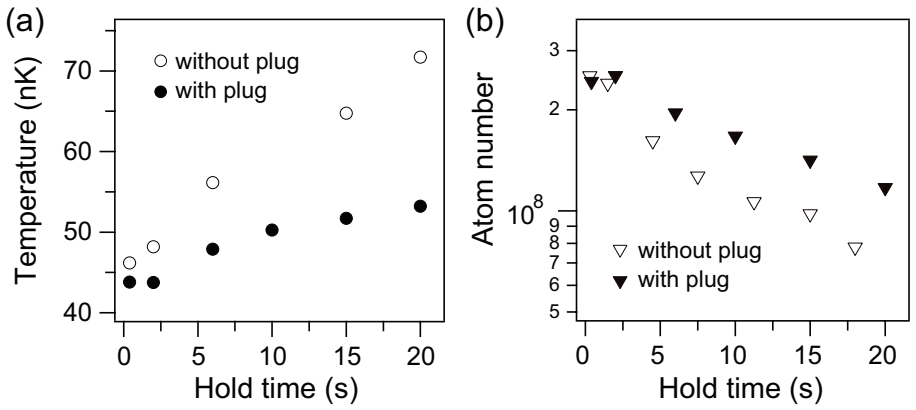

Figure 3.8: (a) Temperature variation as a function of hold times in magnetic quadrupole trap with 180 G/cm field gradient with (solid circle) and without (open circle) optical barrier. (b) Atom numbers measurement in the magnetic trap with (solid triangle) and without (open triangle) the optical plug.

A spin flip happens when the spin of a moving atom cannot adiabatically follow the field orientation, so the flipping probability of an atom at a given position is fully determined by the local field strength, its gradient, and the velocity distribution of the atom, i.e., temperature. Therefore, the plugging effect is a consequence of the density suppression due to the optical repulsive potential in the low-field, spin-flipping region. Including a Boltzmann density suppression factor, the reduced loss rate would be given as

$$\Gamma_m^{plug} = \Gamma_m f \exp(-U^*/k_B T), \tag{3.14}$$

where U^* is the characteristic potential of the plug and f is a factor depending on the details of the plug beam, such as shape, position, and power. Figure 3.9 (a) shows that this model nicely fits to our data with $C'T^{-2}\exp(-U^*/k_BT) + \Gamma_b$, where $U^* = k_B \times 25(1)\mu$K and $C' = 97(6)\mu K^2/s (f \simeq 0.7)$. Note that U^* is

consistent with the deviation point in the $N - T$ evaporation trajectories and close to the potential at the trap bottom $U_0 \simeq k_B \times 15\ \mu$K. In our experiment, the collision rate was approximately 10^3 times faster than the loss rate, validating the thermal equilibrium assumption.

We characterized the heating effect of the Majorana loss with determination of the average loss energy of a spin flipped atom $\varepsilon_m k_B T$. Our measurements show that ε_m has a very weak temperature dependence, slightly increasing at low temperatures, with an average value of 2.8, which is less than $\varepsilon = 4.5$ for a linear trap ($\delta = 3$) [Fig. 3.9(b)]. Remarkably, we observe that ε_m is not affected by the optical plug in the temperature range of 10–100 μK. This is somewhat surprising because the average energy of a lost atom should increase in the presence of the plug due to the repulsive optical potential. We estimate that the effective increment in the average loss energy would be $U^* - U_0 \simeq k_B \times 10\ \mu$K with respect to the trap bottom, and it might be observable at lower temperatures.

3.3.3 Numerical simulation of the evaporation process

In this section, we numerically study the dynamics of the evaporation process in the optically plugged quadrupole trap. Including only three loss processes (background collision, rf evaporation, and the Majorana spin flip), the rate

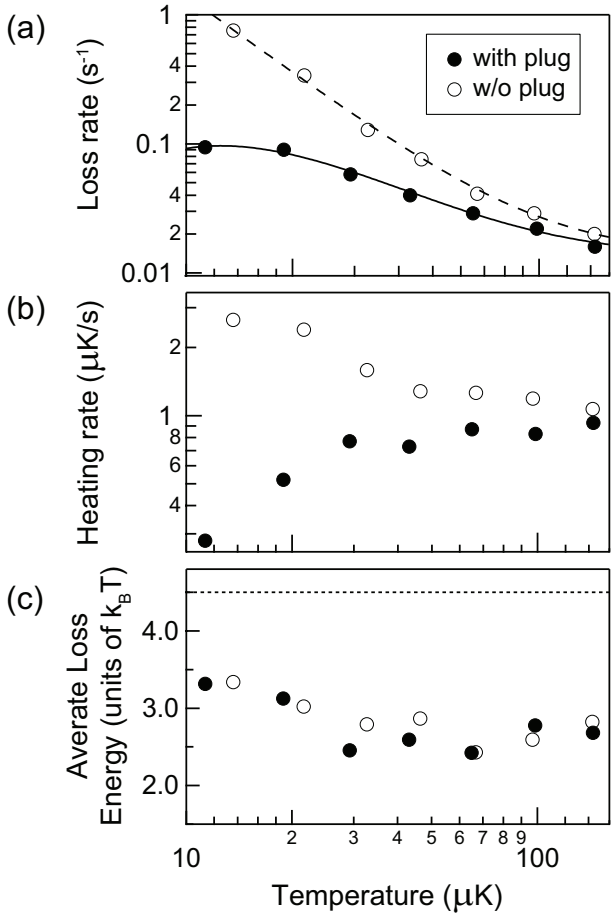

Figure 3.9: Majorana loss in a magnetic quadrupole trap. (a) Loss rates and (b) heating rates for various temperature at the field gradient $B_q = 180$ G/cm. Solid curves are fits to the data with a loss model, Eq. (3.14) (see text for detail). (c) Average energy of a lost atom due to the Majorana spin flip. The dot line indicates the average energy of an atom in a linear trap.

equations for the atom number N and temperature T are given as

$$\frac{\dot{N}}{N} = -\Gamma_b - \Gamma_e - \Gamma_m, \tag{3.15}$$

$$\frac{\dot{T}}{T} = -(\frac{\varepsilon_e}{\varepsilon} - 1)\Gamma_e - (\frac{\varepsilon_m}{\varepsilon} - 1)\Gamma_m, \tag{3.16}$$

where Γ_e is the evaporation loss rate and $\varepsilon_e = \eta + \kappa$ is the average energy of an evaporated atom in $k_B T$. The first term in Eq. (3.16) corresponds to the cooling from evaporation. We assume that the background collision loss occurs equally to all trapped atoms, thus not affecting the temperature.

The simulation for our experiment was performed under the following conditions: $N(0) = N_i$ and $T(0) = T_i$ at $t = 0$ s, $\nu_{rf}(t) = (30 - 7t/3)$ MHz, $\eta = h\nu_{rf}/k_B T$, Γ_b=0.013/s, and $\varepsilon_e = 0.28$. The Majorana loss rate is parameterized with the plug beam power P as $\Gamma_m = C(1 - aP)T^{-2}\exp(-bP/T)$, where $C = 139\ \mu K^2/s, a = 0.176/W$, and $b = 1.48\ \mu K/W$. For three-dimensional (3D) evaporation in a linear trap ($\delta = 3$), standard evaporation theory gives [9] $\Gamma_e^{\text{theroy}} = n\sigma\bar{v}e^{-\eta}[\eta P(\frac{9}{2},\eta) - \frac{11}{2}P(\frac{11}{2},\eta)]/P(\frac{9}{2},\eta)^2$ and $\kappa = 1 - P(\frac{13}{2},\eta)/[\eta P(\frac{9}{2},\eta) - \frac{11}{2},\eta]$, respectively, where $P(a,\eta) = \frac{1}{\Gamma(a)}\int_0^\eta dt\ t^{a-1}e^t$ is the incomplete gamma function and $n = n_0 P(\frac{9}{2},\eta)$. However, the observed evaporation speed was almost 2 times faster than the theoretical value. This result is quite surprising because the theoretical estimation accounts for the maximum 3D evaporation, and it is worthy of further investigation. We empirically set $\Gamma_e = 1.95\Gamma_e^{\text{theory}}$ theory in our simulation. The simulated evaporation trajectories are presented with the experiment data in Fig. 3.5. The trap decompression is not included in our simulation, so the trajectories deviate from the data points after 12 s.

Bibliography

[1] M. H. Anderson, J. R. Ensher, M. R. Matthews, C. E. Wieman, and E. A. Cornell, Science **269**, 198 (1995).

[2] K. B. Davis, M. O. Mewes, M. R. Andrews, N. J. van Druten, D. S. Dufee, D. M. kurn, and W. Ketterle, Phys. Rev. Lett. **75**, 3969 (1995).

[3] W. Ketterle and N. J. van Druten, Adv. At. Mol. Opt. Phys. **37**, 181 (1996).

[4] H. Metcalf and P. van der Straten, Phys. Rep. **244**, 203 (1994).

[5] R. Grimm, M. Weidemüller, and Yu. B. Ovchinnikov,

Adv. At. Mol. Opt. Phys. **42**, 95 (2000).

[6] D. S. Naik and C. Raman, Phys. Rev. A **71**, 033617 (2005).

[7] W. Petrich, M. H. Anderson, J. R. Ensher, and E. A. Cornell, Phys. Rev. Lett. **74**, 3352 (1995).

[8] Y. J. Lin, A. R. Perry, R. L. Compton, I. B. Spielman, and J. V. Porto, Phys. Rev. A **79**, 063631 (2009).

[9] O. J. Luiten, M. W. Reynord, and J. T. M. Walraven, Phys. Rev. A **53**, 381 (1996).

Chapter 4

Phase fluctuations in a two-dimensional Bose gas

In the previous chapter, the experimental apparatus and procedure for making Bose-Einstein condensates of atomic gases are described. One of the most striking phenomena of the condensate is a dissipationless mass flow, called superfluidity. The superfluid behavior was first discovered at 1937 by Kapitza [1], Allen, and Misener [2] in liquid a Helium-4 and it was London [3] who related superfluid and BEC by pointing out that the superfluid critical temperature can be roughly estimated by the condensate critical temperature. Later on, theoretical [4–7] and experimental efforts [8,9] uncover the nature of superfluidity in the ^{4}He that moving object cannot excite quasi-particles of the condensates below a critical velocity because a two body interaction can modify energy-momentum dispersion curve [7]. The historical review of superfluid and Bose-Einstein con-

densation is well described in the References [10, 11].

Things become more interesting in two dimension. Due to the enhancement role of the thermal phase fluctuations, a long-range order cannot be established in two dimension [12,13] so BEC cannot exist in two-dimensional Bose gas at a finite temperature. Now we may conclude that there is no superfluidity in 2D because the thermal fluctuation destroys condensates. However, there is indeed a superfluid to normal fluid phase transition in a thin film of Helium-4 [14] and can be explained by the Berezinskii-Kosteriltz-Thouless (BKT) theory [15, 16]. This chapter describes experimental studies of two dimensional physics with atomic system in the superfluid regime and the results are published in the following reports.

- Jae-yoon Choi, Sang Won Seo, Woo Jin Kwon, and Yong-il Shin. *"Probing phase fluctuations in a 2D degenerate Bose gas by free expansion"* Physical Review Letters **109**, 125301 (2012).

- Jae-yoon Choi, Sang Won Seo, and Yong-il Shin. *"Observation of thermally activated vortex pairs in a Quasi-2D Bose gas"* Physical Review Letters **110**, 175302 (2013).

4.1 Phase transition in two dimensional Bose system

4.1.1 Absence of Bose-Einstein condensation

Ideal Bose particles in a 2D Box potential is one of the textbook example that shows the absence of condensates. According to the Bose statics, the excited number of particles N_e at given temperature T is

$$N_e = \int_0^\infty d\epsilon \; g(\epsilon) \frac{1}{e^{\beta(\epsilon-\mu)} - 1}, \tag{4.1}$$

where $g(\epsilon)$ is density of state for energy $\epsilon = \hbar^2 k^2/2m$, $\beta = 1/k_B T$, and μ is chemical potential. Since the density of state $g(\epsilon) = \frac{mL^2}{2\pi\hbar^2}$ for a uniform system with its size L, the integral becomes

$$N_e = L^2\lambda^2 \int_0^\infty \; d(\beta\epsilon) \frac{1}{z^{-1}e^{\beta\epsilon} - 1} = -\ln(1-z), \tag{4.2}$$

where $\lambda = h/\sqrt{2\pi m k_B T}$ is mean thermal wavelength and $z = e^{\beta\mu}$ is fugacity. Because the integral has the logarithm dependence of fugacity, which is unbounded function, excited number of particle cannot be saturated in 2D and therefore no Bose condensation.

Interacting Bose gas in a harmonic potential also does not undergo the condensation. Though the harmonic potential can change the density of state[1] and form BEC with ideal particles, a repulsive interaction between the particles

[1]The radial trapping frequencies need to much smaller than the condensate critical temperature, $\omega_{x,y} \ll k_B T_c$.

effectively lowers the trap confinements and prevents the formation of condensates.

When a two-body contact interaction between particles is g and trapping potential is $V(r) = \frac{m\omega^2 r^2}{2}$, the mean field density profile is

$$\begin{aligned} n_{\rm mf}(r) &= \int d\epsilon \frac{g(\epsilon)}{e^{\beta(-\mu+V_{\rm eff}(r))}e^{\beta\epsilon}-1} \\ &= -\frac{1}{\lambda^2}\ln(1-e^{\beta(\mu-V_{\rm eff}(r))}), \end{aligned} \tag{4.3}$$

where $V_{\rm eff}(r) = m\omega^2 r^2/2 + 2gn_{\rm mf}(r)$ is the effective potential energy. From the self-consistent relation of the density distribution, the effective trapping frequency $\omega_{\rm eff}$ at the trap center in the $\mu \to 2gn_{\rm mf}(r)$ limit is

$$\begin{aligned} \omega_{\rm eff}^2 &= \omega^2 + \frac{2g}{m}\frac{\partial^2 n_{\rm mf(r)}}{\partial r^2}|_{r=0} \\ &\approx \omega^2 \frac{mg\beta}{\pi}(2gn_{\rm mf}(0)-\mu), \end{aligned} \tag{4.4}$$

so the potential become arbitrary flat due to the interaction and thus BEC would not be developed [17].

As a matter of fact, the absence of condensates in 2D can be understood as an example of the Mermin-Wagner-Hohenberg [12, 13] theorem (*In one and two dimensions, the continuous symmetries cannot be spontaneously broken at finite temperature in systems with sufficiently short-range interactions*). Therefore, the state of matter cannot be described with the order parameter or the onset of off-diagonal long range order in low dimension because of the long-wave length fluctuations. Naturallty, the criteria for BEC [18] $\lim_{\mathbf{r}-\mathbf{r}'\to\infty}\langle\hat{\Psi}^\dagger(r)\hat{\Psi}(r')\rangle \neq 0$ would not be satisfied.

4.1.2 Berezinskii-Kosteriltz-Thouless phase transition

Despite the absence of long-range order and BEC, however, an interacting 2D Bose gas can show superfluidity. This is pointed out by Berezinskii-Kosteriltz-Thouless (BKT) [15, 16] and can be understood by studying two dimensional XY model. The model Hamiltonian is

$$\begin{aligned} H_{\mathrm{XY}} &= -J \sum_{i,j} S_i \cdot S_j \\ &= -J \sum_{i,j} \cos(\theta_i - \theta_j), \end{aligned} \tag{4.5}$$

where J is coupling constant and S_i is spin direction at lattice site i with angle θ_i.

Berezinskii [15] first showed the existence of phase transition in 2D by calculating spin correlation $\langle S_i \cdot S_j \rangle$ both at low and high temperature limit of the model Hamiltonian. The spin correlation function at low temperature limit decays algebraically over the spin separation, $|i-j|^{-T/2\pi J}$, while it decreases exponentially, $e^{|i-j|/\xi}$ with $\xi = 1/\ln(2T/J)$, at high temperature. At the low temperature regime, he also argued that the system has a rigidity of long-wavelength spin wave (spin stiffness) so requires finite energy to distort the spin direction. Though the microscopic mechanism for the phase transition was not described in his work, the complete different form of correlation function implies those two phases are different states of matter and one can assure that there must be a phase transition in two dimension.

A new concept of topological order was introduced by Kosteriltz and

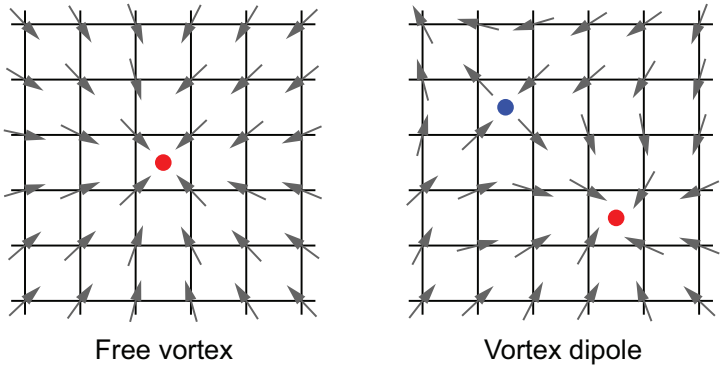

Figure 4.1: Free vortex (left) and Vortex dipole (right) spin configuration in the two dimensional XY model. The red(blue) circle represents counter clockwise(clockwise) rotating vortex core.

Thouless [16] by noting a phase singularity [Fig. 4.1], called vortices, could mediate the phase transition. They argued that the thermally excited vortices would form a bounded pairs with opposite circulation below a critical temperature T_c but can proliferate all over the sample, destroying the phase stiffness. The notion of *topological order* comes from the distinct topological property of the two phases. Since, the size of vortex pairs below the critical temperature is small compare to the sample size, its topological property is equivalent to the uniform phase. When the vortices spread over the entire sample, however, it has lots of singular points and obviously it is topologically distinct from uniform phase.

They also gave insightful free energy argument for estimating the critical

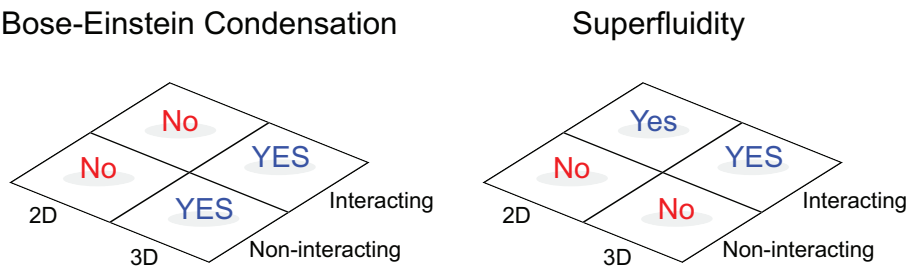

Figure 4.2: Dependence of the Bose-Einstein condensation (left) and superfluidity (right) on the physical dimension of system and presence interaction.

temperature. The energy E_v and entropy S_v of single vortices is

$$E_v = \int_a^L dr 2\pi r \frac{1}{2}\frac{J}{r^2} \sim \pi J \ln(\frac{L}{a}), \tag{4.6}$$
$$S_v = k_B \ln(\frac{L^2}{a^2}) = 2k_B \ln(\frac{L}{a}),$$

where a is vortex core size and L is system size. Therefore the free energy cost for exciting single vortex is $\Delta F = (\pi J - 2k_B T)\ln(\frac{L}{a})$, so when the temperature is higher than critical temperature, $T_c = \frac{\pi J}{2k_B}$, vortex excitation is preferred. The estimated critical point was coincided with the result obtained from renormalization group analysis and universal jump of the superfluid density in ^{4}He was predicted in Ref. [19].

In the Helium system, strong interaction inhibits density fluctuations and kinetic part of the Hamiltonian can be approximated to the 2D XY model, where phase of the wave function plays the spin vector. As a result, though the thermal fluctuations prohibit the perfect phase coherence, still phase stiffness exists to show superfluidity. Figure 4.2 summarize the possibility of condensate and superfluidity depends on the presence of interaction and physical dimension

of the system.

4.1.3 Weakly interacting Bose gas in two dimension

Ultracold atomic gases trapped in a quasi-two dimensional harmonic potential could provide a clean and well-controlled platform for studying the BKT mechanism. When the temperature and interaction energy of the gas is much smaller than the excitation energy of a harmonic potential in z direction ($\hbar\omega_z$), $k_B T, \mu \ll \hbar\omega_z$, axial wave function would be frozen to the ground state of harmonic trap[2] so the wave function has only radial degree of freedom. This condition can be satisfied by highly anisotropic harmonic trap which has one stronger confinement in z direction than the other two directions x and y. For a Bosonic atoms, aspect ratio $\omega_z/\omega_{x,y}$ of 100 can fulfill the qausi-two dimensional condition.

The highly anisotropic harmonic trap also modifies the interacting Hamiltonian of the system. In three dimension, the scattering amplitude $f(k)$ in the low energy limit ($k \to 0$) is represented by s-wave scattering length a_s [20] and interacting Hamiltonian $V(r)$ of dilute gases is approximated by point contact interaction

$$V(\mathbf{r}) = \frac{4\pi\hbar^2 a_s}{m}\delta^3(\mathbf{r}) = g_{3\mathrm{D}}\delta^3(\mathbf{r}). \tag{4.7}$$

In two dimension, however, since scattering amplitude is obtained by the asymptotic wave function defined in the x-y plane [21, 22], the two dimensional scat-

[2]The ground state wave function is $\phi_z(z) = \frac{1}{\pi l_z^{2\,1/4}} e^{-z^2/2l_z^2}$ with oscillator length $l_z = \sqrt{\hbar/m\omega_z}$.

tering amplitude and interaction coupling constant $g_{2\mathrm{D}}$ is also modified and can be written

$$f(\epsilon) = \frac{2\sqrt{2\pi}}{l_z/a_s + (1/\sqrt{2\pi}(\ln(B\hbar\omega/\pi\epsilon)))}, \tag{4.8}$$
$$g_{2\mathrm{D}} = \frac{4\pi\hbar^2}{m}\frac{1}{\sqrt{2\pi}l_z/a_s + \ln(B\hbar\omega/\pi\epsilon)},$$

where $B \approx 0.915$ [22] and ϵ is energy of system. The logarithmic term in the denominator could be neglected for a weakly interacting case and interaction strength is simplified to $g_{2\mathrm{D}} = \frac{4\pi\hbar^2}{m}\frac{a_s}{\sqrt{2\pi}l_z}$. Therefore, the Hamiltonian of two dimensional Bose gas in a weakly interacting case is

$$\hat{H} = \int d^2\mathbf{r}\hat{\Psi}^\dagger(\mathbf{r})(-\frac{\hbar^2\nabla_{\mathbf{r}}^2}{2m})\hat{\Psi}(\mathbf{r}) + \frac{\hbar^2 g_0}{2m}\int d^2\mathbf{r}\hat{\Psi}^\dagger(\mathbf{r})\hat{\Psi}^\dagger(\mathbf{r})\hat{\Psi}(\mathbf{r})\hat{\Psi}(\mathbf{r}), \tag{4.9}$$

where $\nabla_r^2 = \partial_x^2 + \partial_y^2$ and $g_0 = \sqrt{8\pi}a_s/l_z$ is dimensionless quantity. In typical experiments, interaction strength is in a weakly interacting regime $g_0 = 0.1 \sim 0.01$ but one can also explore the strongly interacting regime by Feshbach resonance [24] or loading atoms in optical lattice [25].

The superfluid critical temperature of the trapped gases could be obtained from the universal relation

$$n_s\lambda^2 = 4, \tag{4.10}$$

where n_s is superfluid density. In the cold atom system, however, extracting the superfluid density from total density of sample is a challenging problem and only recently the superfluid fraction is measured in strongly interacting Fermi gas [23]. Theoretical efforts in analytic and numerical studies [26, 27] predicts

the critical condition in terms of total atomic density n_c at the trap center and is written by

$$n_c = \frac{mT}{2\pi\hbar^2} \ln(\frac{C}{g_0}), \tag{4.11}$$

where $C \approx 380$ obtained by Monte-Carlo simulation of classical-field $|\psi|^4$ model [27].

Experimental studies with 2D atomic Bose gases have demonstrated that the BKT mechanism is valid in a finite-size trapped sample [24, 28–34], presenting a new system for studying of 2D physics. From matter-wave interference of multiple layer of two-dimensional Bose gas [28, 29], superfluid to normal phase transition can be observed by the changes of first order correlation function $g_1(r)$ from algebraic to exponential curve across the critical temperature [29]. And the microscopic picture BKT phase transition is well supported by a dislocation of interference fringes [28, 29] near the critical temperature [30]. Moreover, *in situ* density and momentum distributions of trapped samples reveals thermodynamic properties of 2D Bose gas, the scale invariance of the equation of state [24, 31] and presence of a presuperfluid regime [32–34]. Recently, superfluid behavior of 2D sample is demonstrated by measuring critical velocity for heating up the two-dimensional superfluid [35].

Our research interest is the nature of superfluid in 2D and we try to answer the following questions. Can we measure the phase fluctuation in the superfluid and observe its thermal dependency? How can we detect the vortex pairs in the superfluid phase more directly?

4.2 Qausi-two dimensional degenerate Bose gas

4.2.1 Optical dipole trap

Our experiments are carried out with pancake shape condensates trapped in high aspect ratio (1:110) optical potential. A single optical sheet potential is formed by focusing the 1064-nm laser (YLR-5LP, IPG photonics) beam with a $1/e^2$ beam waist of 1.9 mm(17 μm) in the $y(z)$-direction. Schematic diagram of the optics layout for the dipole trap is shown in Fig. 4.3. Each beam waist at the sample position is controlled by two cylindrical lens pair sets, where weak(tight) confinement is provided by horizontal(vertical) direction cylindrical lens pair. For side imaging setup the 1"dichroic mirror (DMSP-1000, Thorlabs) is inserted at the IR-beam path. Characterization of the optical dipole trap is done by measuring $1/e^2$ beam waist by beam profiler (BP209-VIS/M, Thorlabs) and trapping frequencies $\omega_x(\omega_y)$ along the $x(y)$ direction. Inducing a dipole motion of condensates by the magnetic quadrupole field, we measure the radial trapping frequencies $\omega_x = 2\pi \times 3.5$ Hz($\omega_y = 2\pi \times 4.6$ Hz) at 2.7 W of laser beam. From the measurements, the axial trap frequency can be estimated to $\omega_z = 2\pi \times 430$ Hz.

4.2.2 Preparing degnerate Bose gas

Preparing degenerate Bose gases of ^{23}Na atoms in the single pancake-shape optical trap, thermal atoms in the $|F = 1, m_F = -1\rangle$ state are loaded from a plugged magnetic trap in order to avoid perturbation from the repulsive barrier. Evaporative cooling is applied by reducing the trap depth to get the degener-

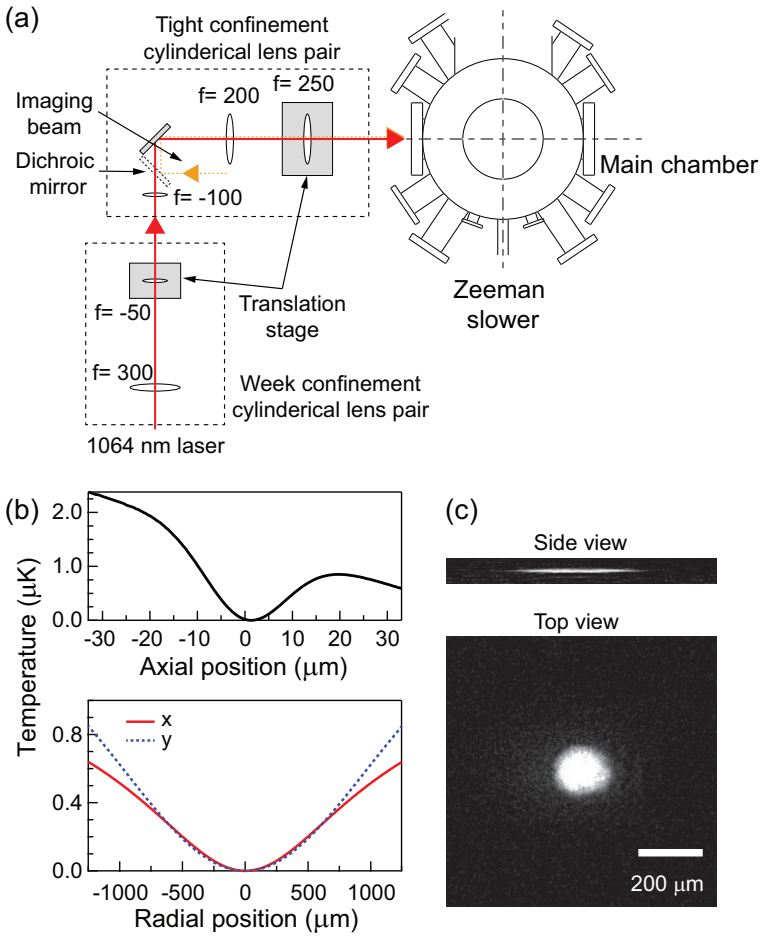

Figure 4.3: (a) Experimental setup for quasi-2D harmonic potential. Far detuned 1064 nm laser beam is deformed into optical sheet beam by two sets of cylindrical lens pairs. Dichroic mirror is inserted to have side view of trapped sample. (b) The trap depth at the potential minima is plotted by temperature scale in the x-z plane and x-y plane. (c) Atomic density images at the side view and top view.

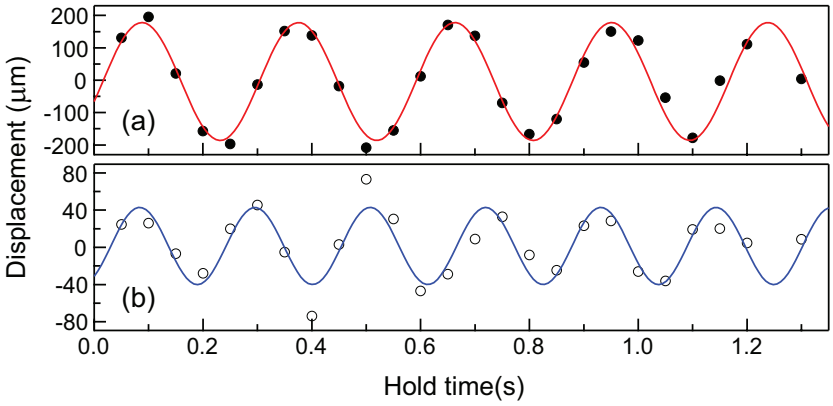

Figure 4.4: Dipole oscillation of condensates in the (a) x-direction and (b) y-direction. Sinusoidal curve fit to the data and the oscillation frequencies are $\omega_x = 2\pi \times 3.5$ Hz and $\omega_y = 2\pi \times 4.6$ Hz, respectively.

ate sample and the cooling procedure is intentionally set to be slow over 15 s [Fig. 4.5], ensuring thermal equilibrium[3]. The sample temperature is controlled by the final trap depth in the evaporation, resulting in $6 \sim 9 \times 10^5$ number of atoms with $20 \sim 70$ nK. Finally, the optical trap depth ramps up and the trapping frequencies $(\omega_x, \omega_y, \omega_z) = 2\pi \times (3.0,\ 3.9,\ 370)$ Hz. In the Thomas-Fermi (TF) approximation, the chemical potential is about $h \times$ 260 Hz and TF radii are $(R_x, R_y) \approx (140, 125)\ \mu$m. The dimensionless interaction strength $\tilde{g} = \sqrt{8\pi} a_s / a_z$ =0.013. Since the tight confinement energy is stronger than the mean-field interaction energy so could explore two dimensional physics. Note that the sample is quasi-two dimensional since $\hbar\omega_z \approx 20$ nK and thermal population along the axial direction could not be negligible, which should be considered for estimating the critical temperature.

For atoms in a two-dimensional harmonic potential with its trap fre-

[3]The lifetime in the optical trap is over 40 s.

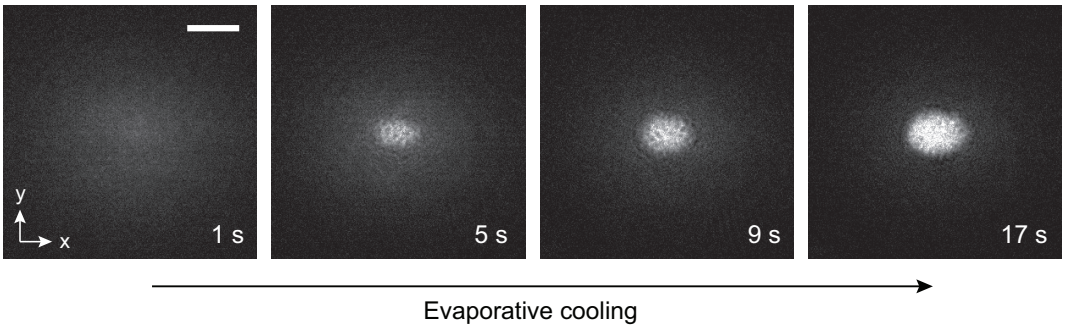

Figure 4.5: Optical density images of degenerate Bose gas in the dipole trap. As we increases the hold time, which is marked at the bottom of each images, atoms are cool down because of the finite trap depth and quasi-2D BEC emerges at the trap center. The scale bar in the figure represents 200 μm and each images are taken after 17 ms time-of-flight.

quencies are ω_x and ω_y, the superfluid critical temperature T_{BKT} is related by a condensate critical temperature of ideal gases [17]:

$$\frac{T_{\mathrm{BKT}}}{T_{\mathrm{BEC}}^{2D}} \simeq (1 + \frac{3\tilde{g}}{\pi^3} \ln \frac{380}{\tilde{g}})^{-1/2}, \tag{4.12}$$

where $T_{\mathrm{BEC}}^{2D} = \frac{\sqrt{6N}\hbar}{\pi k_B}\omega_x\omega_y$.

Because of a finite axial trap frequency, however, thermal population along the axial direction reduces the number of ground state atoms in z-direction, which effectively lowers the critical temperature for Bose-Einstein condensation in the quasi-two dimensional harmonic trap. Considering the axial population [36], we can obtain the quasi-2D condensate temperature of ideal Bose gas by

$$N = \frac{k_B^2 T^2}{\hbar^2 \omega_x \omega_y} \sum_{\nu=0}^{\infty} F_2(\nu \frac{\hbar\omega_z}{k_B T}), \tag{4.13}$$

where $F_2(z)$ is the polylogarithm of order 2. For our small $\tilde{g} = 0.013$, the BKT critical temperature $T_{\mathrm{BKT}} \approx 0.99\ T_{\mathrm{BEC}} = 75$ nK for 10^6 number of atoms with

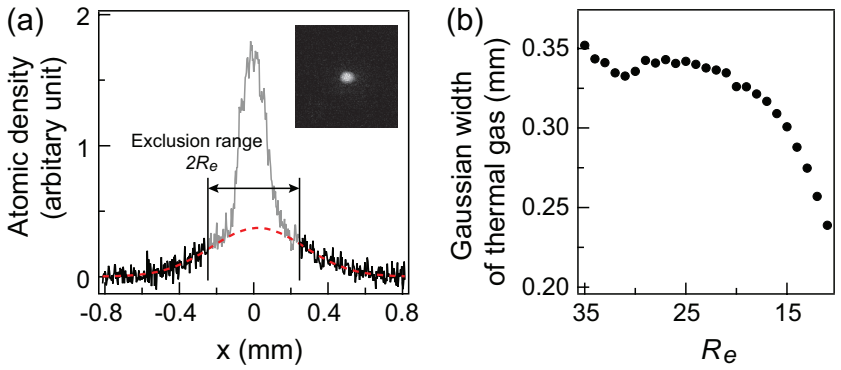

Figure 4.6: Temperature of quasi-2D Bose gas is obtained by gaussian fit to the thermal wings. (a) Integrated cross section of outer thermal regime is obtained by excluding central high density regime with its range $2R_e$. Inset figure is the optical density image of the 17 ms time-of-flight. (b) Gaussian width of the thermal wing as a function of exclusion range R_e. The unit of R_e is 6.45 μm.

$\omega_z = 2\pi \times 370$ Hz.

In the experiment, we measure the temperature of the qausi-2D Bose gas from a Gaussian fit to the outer thermal wings as shown in Fig 4.6(a). From the integrated cross section view $n(x) = \int n(x, y)\, dy$, the Gaussian width of thermal wing is plotted by changing the fitting range and temperature is obtained from the relation

$$T = \frac{m}{2k_B}\left(\frac{\omega_x^2}{1 + (\omega_x t_e)^2} x_{th}^2\right), \tag{4.14}$$

where x_{th} is averaged gaussian thermal width in a relatively plateau region before the bending shape is appeared [Fig 4.6(b)].

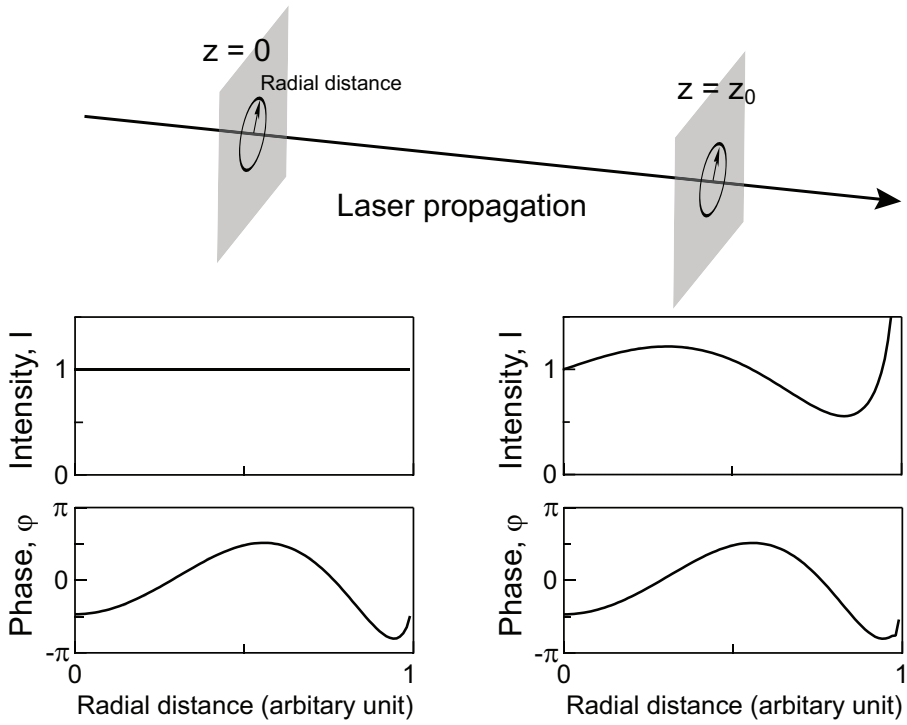

Figure 4.7: Modulation of light intensity along the z-direction. When the phase of electric field has inhomogeneous distribution at the $z = 0$ plane, intensity modulation would be appeared after some propagation at the $z = z_0$ plane.

4.3 Probing thermal phase fluctuations by free expansion

Consider a monochromatic laser light propagating in free space along the z direction as shown in Fig. 4.7. When the phase ϕ of electric field $E_0 = \sqrt{I(r,z)}e^{\phi(r,z)}$ has random distribution, while its modulus is uniform, we can expect intensity modulation after the light propagation because of the initial phase distribution[4].

[4]With paraxial approximation the beam propagation satisfy a set of coupled equation called transport intensity equation [37].

This phenomena can be observed in the 2D matter wave since the sample has initial random phase fluctuations caused by thermal energy. In analogous to the beam propagation, the phase fluctuations in the trapped gas could be represented as a density modulation in the course time-of-flight. The tight axial confinement is beneficial for observing the phase fluctuations because of the following reason. Expansion dynamics of degenerate Bose gas usually described by hydrodynamic equation [20], which includes the two-body interaction during the trap off. The interaction effect, however, could be ignored in low dimensional sample because the gas rapidly expands in the tight confinement direction and the atomic density is reduced dramatically. Therefore, the expansion dynamics could be approximated to a ballistic expansion of free particles and the initial phase fluctuations could be developed into the density ripples during the expansion.

This method has been exploited in elongated Bose-Einstein condensates [38] and 1D Bose gases [39]. Recently A. Imambekov *et, al.* [40] have developed an analytic theory that relates the spectrum of density modulation with correlation function of initially fluctuating gas in low dimension $D = 1$ or 2. The main point is that because the ballistic expansion is single particle dynamics, one can trace back and obtain the physical property of trapped sample. Here is the brief summery of their result on 2D. The atomic field operator after the free expansion is simply described by

$$\hat{\Psi}(\mathbf{r}, t) = \int d^2\mathbf{r}' G(\mathbf{r} - \mathbf{r}', t)\hat{\Psi}(\mathbf{r}', 0), \tag{4.15}$$

where $G(\mathbf{r}', t)$ is free particle green's function, $\left(\frac{m}{2\pi i\hbar t}\right) \exp\left(i\frac{mr^2}{2\hbar t}\right)$ and t is the free propagating time. Then correlation function $g_1(\mathbf{r}) = \langle\hat{\Psi}^\dagger(\mathbf{r}, 0)\hat{\Psi}(0, 0)\rangle$ of trapped gas is revealed at the Fourier transform of density ripples after t_e expansion time. In two dimensional system, for example, the power spectrum reads

$$P(\mathbf{q}, t) = |\int d^2\mathbf{r}\ e^{i\mathbf{q}\cdot\mathbf{r}} n(\mathbf{r}, t_e)|^2 \tag{4.16}$$

$$= \int d^2\mathbf{r} \cos\mathbf{qr} \times \left\langle \hat{\Psi}^\dagger(\frac{\hbar\mathbf{q}t_e}{m}, 0)\hat{\Psi}^\dagger(\mathbf{r}, 0)\hat{\Psi}(\mathbf{r} + \frac{\hbar\mathbf{q}t_e}{m})\hat{\Psi}(0, 0)\right\rangle. \tag{4.17}$$

Remarkably, due to the power law decay of the first order correlation function in 2D superfluid, the power spectrum would show scaling behavior over the expansion time which is stark contrast to one-dimensional quasi-condensate. Moreover, one can extract superfluid fraction from the shape of power spectrum, which opens up the possibility to observe the universal jump of superfluid density in two dimension.

This section describes experimental results on the power spectrum of the density distribution of a freely expanding 2D degenerate Bose gas, where irregular density modulations gradually develop due to the initial phase fluctuations in the sample. The spectrum has an oscillatory shape, where the peak positions are found to be independent of temperature. The relative intensity of phase fluctuations is estimated from the normalized spectral peak strength and observed to decrease at lower temperatures, confirming the thermal nature of the phase fluctuations in 2D system. Also, the relaxation dynamics of nonequilibrium states is investigated at various temperature.

4.3.1 Power spectrum of density fluctuations

We observe that density fluctuations develop in an expanding 2D Bose [Fig. 4.8], where the characteristic size and visibility of the density lumps increases with the expansion time. Density fluctuations appear discernible only when the sample shows a bimodal density distribution, so that we refer to the center part as the coherent part of the sample [28, 32]. In order to obtain the density correlation information, we measure the power spectrum of the density distribution as the square of the magnitude of its Fourier transform,

$$P(\mathbf{q}) = |\int dxdy e^{\mathbf{q}\cdot\mathbf{r}} n(\mathbf{r})|. \tag{4.18}$$

Although the spatial pattern of the density modulation appears random in each realization, the power spectrum clearly reveals a multiple ring structure that scales down with the expansion time [Fig. 4.8(c) and 4.8(f)]. For quantitative analysis, we obtain a 1D spectrum $P(q)$, by azimuthal averaging the 2D spectrum [Fig 4.9]. The resolution of our imaging system is about 5 μm, so the spectral signal at $q > 1$ μm^{-1} is purely contributed from photon shot noise. We subtract the constant offset value at high q from the spectrum, which is typically a few % of $P(q_1)$. The strong signal around $q = 0$ corresponds to the finite size of the coherent part.

The scaling behavior of the spectrum can be qualitatively understood in terms of the Talbot effect [41, 42]. It is well known in near-field diffraction that when a grating illuminated by monochromatic waves, the identical self-image of the grating is formed at a distance $L_T = 2d^2/\lambda$ away from the grating, where

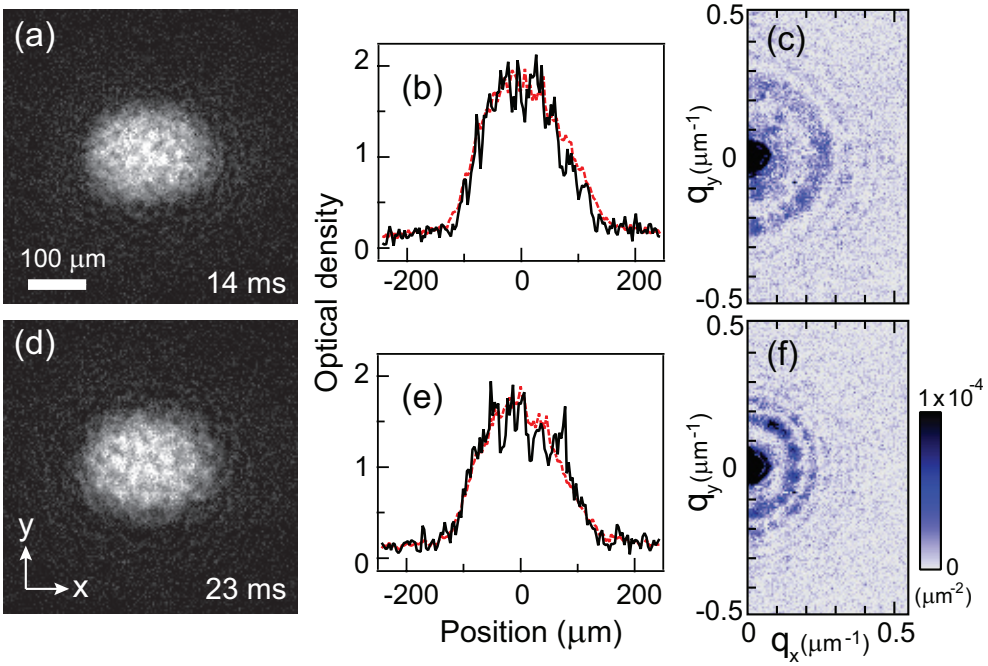

Figure 4.8: Emergence of density fluctuations in a freely expanding 2D Bose gas. Density distributions after a time-of-flight t_e of (a) 14 ms and (d) 23 ms. Density fluctuations gradually develop during expansion, increasing their characteristic length scale and visibility. (b,e) The horizontal density profiles at the center of the samples. The red dashed lines indicate the averaged profiles over 10 individual realizations of the same experiment. The coherent part fraction $\eta \approx 30\%$ for the data (see text for details). The power spectrum of the density distribution is measured with the magnitude square of its Fourier transform. (c,f) The averaged power spectra corresponding to (a,d).

d is the grating period and λ is the wavelength of the incident light. The same effect occurs with phase grating [43].

In matter wave optics, $\lambda = h/mv$, where v is the incident speed of atoms [44]; so the propagation time for self-imaging is defined as $t_T = L_T/v = 2md^2/h$ is independent of v. If we consider a 2D Bose gas as a macroscopic matter wave containing phase fluctuations at all length scales, it is expected that the component of wave number q satisfying the Talbot condition $q^2 = 4\pi m/\hbar t_e$ will emerge predominantly in the density distribution at a given expansion time t_e. The multiple peaks in $P(q)$ can be accounted for by the fractional Talbot effect where self-image with smaller period d/n ($n > 0$ is an integer) are produced at $L_T/2n$ [42].

The theoretical calculation [40] of the spectrum of density modulation show that the n-th peak position q_n closely satisfies the following relation

$$\hbar q_n^2 t_e/2\pi m = (n - 1/2). \tag{4.19}$$

In particular, they predict that for sufficiently long expansion times, the spectrum remains self-similar during expansion, and its shape is determined only by the exponent of the power-law decay of the first order correlation function.

In our experiment, we observe that the spectrum preserves its oscillatory shape during expansion and that the peak positions , q_n's, are independent of temperature [Fig. 4.9(b)], which are in qualitatively agreement with the theoretical prediction. However, we find different scaling behavior of q_n's in the

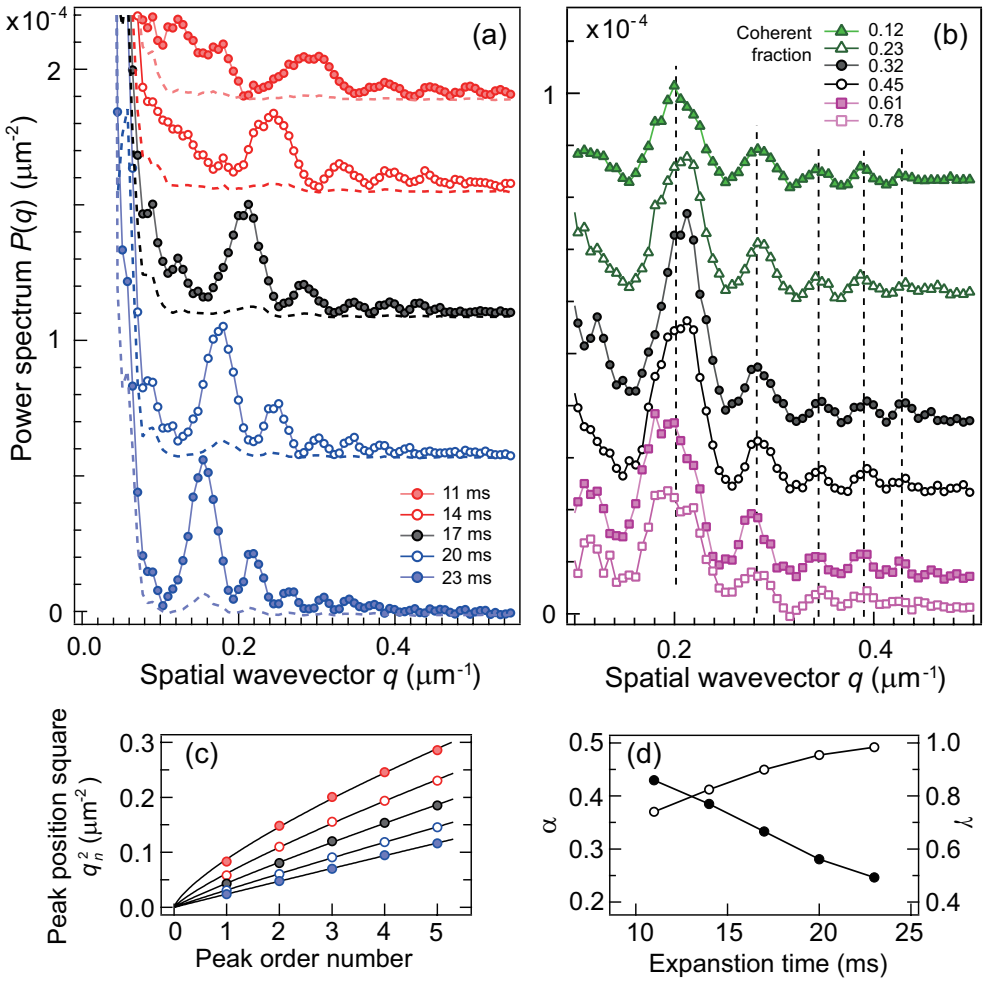

Figure 4.9: Time evolution of the power spectrum of the density fluctuations. (a) 1D power spectra $P(q)$ are obtained by azimuthally averaging the 2D spectra for various expansion times (Fig. 4.7). Each spectrum is displayed with a constant offsets are added for clarity. The strong signal $q < 0.08\ \mu\text{m}^{-1}$ corresponds to the finite size of the sample. (b) The spectral peak positions q_n show scaling behavior during expansion, fit to $\hbar q_n^2 t_e/2\pi m = \alpha n^\gamma$ (dashed lines), where n is the peak order number. (c) The expansion time dependence of α and γ.

measured spectra, which is well described as

$$\hbar q_n^2 t_e / 2\pi m = \alpha n^\gamma, \tag{4.20}$$

with $0.2 < \alpha < 0.45$ and $0.7 < \gamma < 0.1$ for $t_e = 10 \sim 25$ ms [Fig. 4.9(d)].

The gap between the prediction and our experiment could be bridged if we consider the interaction effect during the free expansion and defocusing effect caused by gravity falling. After the experimental result is published in Physical Review Letters, a study by Mazets [45] points out that the peak position q_n of the power spectrum would not satisfy the Eq. (4.19) because our axial trap frequency is not tight enough to fully ignore the atom-atom interaction during the expansion. Moreover, since the quasi-2D sample is free falling [46], images after the expansion involves defocusing effect [47]. Adjusting the CCD position at the imaging plane of sample, we measure the power spectrum and the peak position shows in good agreement with the numerical prediction.

4.3.2 Thermal dependences of the phase fluctuations

The universality of the spectral peak position suggests that the spectral peak strength can be used as a measure of magnitude of phase fluctuations in the sample. In order to quantify the relative intensity of phase fluctuations, we normalize the strength of the first spectral peak with the square of the central density n_c of the coherent part in the sample, $\tilde{P}(q_1) = P(q_1)/n_c^2$, where n_c is determined from a fit of two Gaussian curves to the density distribution. At low temperature, the density profile of the coherent part is close to a parabola

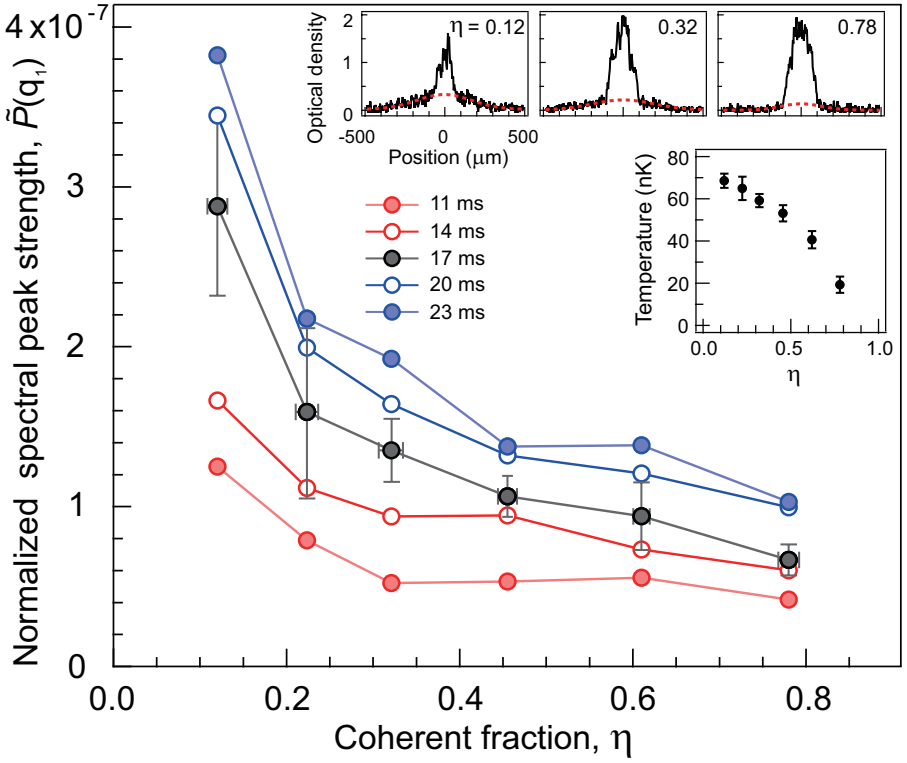

Figure 4.10: Temperature dependence of phase fluctuations at thermal equilibrium. The relative intensity of phase fluctuations is estimated from the strength of the first spectral peak $P(q_1)$ normalized with the square of the central density n_c of the coherent part in a sample. The relative temperature is parameterized with the coherent part fraction. The insets show the density profiles for different temperatures, where the rad dashed lines are gaussian fits to the thermal wings.

shape, but the Gaussian fit still gives a good estimation for n_c within few %

Using $\tilde{P}(q_1)$, we first investigate the temperature dependence of phase fluctuations in thermal equilibrium. To estimate the relative temperature to the critical point in a model-independent way, we use the coherent fraction, η, defined as the ratio of the atom number of coherent part to the total atom num-

ber[5]. Figure 4.10 shows that $\tilde{P}(q_1)$ is suppressed at lower temperature (higher η), confirming the thermal nature of phase fluctuations. The rapid increases of $\tilde{P}(q_1)$ at $\eta < 0.2$ might indicate the behavior in the proximity of the critical point. Since the spatial extent of the coherent part fraction become small, the signal-to-noise ratio is poor when $\eta < 0.05$, and we cannot study the presuperfluid regime where the decay of the coherence function changes from algebraic to exponential, which might be reflected in the spectral shape.

4.3.3 Non-equilibrium relaxation process

The power spectrum can be used to study nonequilibrium dynamics in 2D Bose gas. For this study, we prepare a 2D sample in a nonequilibrium state by transferring a condensate instead of thermal atoms from the plugged magnetic trap into the optical trap. The induced perturbations are sufficiently small so that the density profiles in the optical trap is quite close to that at equilibrium.

In Fig. 4.11(a), we plot the time evolutions of the sample in various initial conditions in the plane of $\tilde{P}(q_1)$ and η [Fig. 4.11(f)], clearly showing that the nonequilibrium states decay to equilibrium. The decay time of the excess phase fluctuations with respect to the equilibrium value is measured to ~ 4 s, corresponding to ~ 10 collision time in our typical condition[6]. Note that the hottest sample first decays, and then moves along the equilibrium line with increasing η because of the evaporation cooling due to the finite trap depth.

[5]The value of η was constant within 5% for our expansion times.

[6]The collision rate is $8\pi a_s^2 n\sqrt{k_B T/m}$. The peak density in the sample was $n \approx 7\times10^{12}/cm^3$ at our lowest temperature ≈ 20 nK.

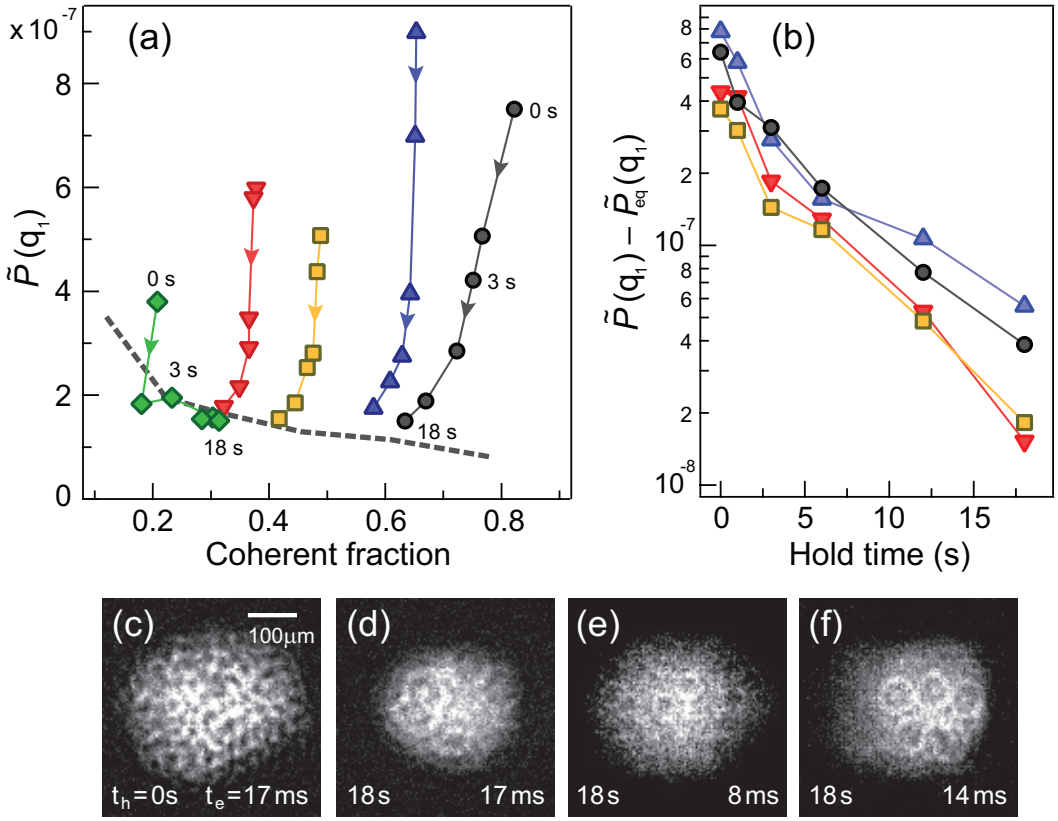

Figure 4.11: Relaxation of a nonequilibrium 2D Bose gas. (a) Time evolutions of various nonequilibrium states in the plane of $\tilde{P}(q_1)$ and η ($t_e = 17$ ms). The dashed line is the interpolation for the thermal equilibrium data points with $t_e = 17$ ms in Fig. 4.10. (b) The decay curves of the excess phase fluctuations $\tilde{P}(q_1) - \tilde{P}_{eq}(q_1)$, where $\tilde{P}_{eq}(q_1)$ is the equilibrium value corresponding to η at $t_h = 18$ s of hold time. Density distributions of the lowest temperature sample at (c) $t_h = 0$ s andd (d) $t_h = 18$ s with $t_e = 17$ ms, and $t_h = 18$ s with (e) $t_e = 8$ ms with $t_e = 23$ ms. The sample in (e) and (f) were strongly perturbed to obtain more ring-shape density ripples.

This confirms that our previous measurements are indeed for phase fluctuations in thermal equilibrium.

The vortex appears more often at lower temperatures with stronger perturbations. In the two lowest temperature cases (circle and triangle in Fig. 4.11), the appearance probability is about 60% at $t_h = 18$ s of hold time, where the spectral strength of the sample with vortices is about 10% higher than without them. in Fig. 4.11(b), the decay rates of the two coldest sample become slightly slower after $t_h > 5$ s, which might be attribute to the long lifetime of vortices. Figure 4.11(c)-(e) show the expansion dynamics of vortex ripples caused by defocusing.

In conclusion, we have demonstrated the power spectrum of density fluctuations in a freely expanding 2D Bose gas as a new quantitative probe for phase fluctuations. Together with more controlled perturbations [48, 49], we expect this method to be extended for studying nonequilibrium phenomena in BKT physics such as critical exponents [50, 51] and dynamic transitions [52, 53].

4.4 Observation of thermal vortex pairs in superfluid

The pairing of vortices below critical temperature is responsible for two dimensional superfluid. Since vortex-antivortex pairs carry no net phase slip, the BKT superfluid can be described as topologically identical to a state with a spatially uniform phase like BEC on the length scale large compared to the vortex

pair size, although it shows long-wavelength phase fluctuations due to thermal phonon excitations. Above the critical temperature, the topological character of the system disappears as free vortices, i.e. point defects, proliferate via unbinding the vortex pairs, which is reflected in the decay behavior of phase coherence changing from algebraic to exponential. However, its direct observation has been elusive until this work.

In this section, the in-plane distribution of thermally activated vortices in a trapped quasi-2D Bose gas would be presented, where the visibility of density depletion core is enhanced by radially compressing the 2D superfluid before releasing the trap. The pairing of vortices is revealed by the two-vortex spatial correlation function obtained from the vortex distribution. The vortex density decreases gradually as temperature is lowered, which indicate thermal property of the vortex pair. Moreover, we observe that vortex-free region is emerged at the center of the sample below a certain temperature, which shows the crossover from BKT phase containing vortex-pair excitations to a vortex free BEC phase in a finite-size 2D system.

4.4.1 Radial compression

The conventional method for detecting quantized vortices is observing density-depleted vortex cores after releasing the trap [54]. Because the vortex core size $\xi \propto n^{-1/2} \propto R^{3/2}$, where n is the atom density and R is the sample size, the vortex core expands faster than the sample in a typical 3D case [55], facilitating its detection. However, this simple method is not adequate for detecting thermally

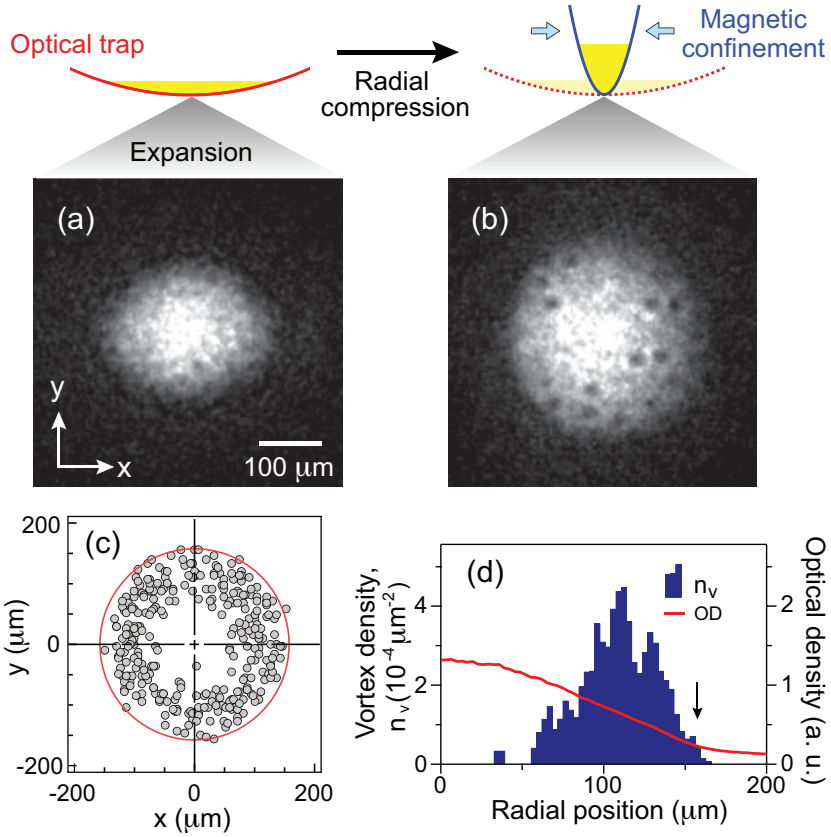

Figure 4.12: Observation of thermally activated vortices. (a) Optical density image of a quasi-2D Bose gas, taken after a 17-ms time-of-flight expansion. Density ripples develop during the expansion due to phase fluctuations in the sample. (b) Image with applying a radial compression before expansion. The radial compression is achieved by superposing a magnetic potential onto the sample in an optical trap. Quantized vortices are observed with density-depleted cores. (c) Positions of vortices with respect to the sample center, recorded for 20 realizations of the same experiment. (d) Radial profile of the vortex density $n_v(r)$. The red solid line displays the atom density profile $n(r)$ of the sample in (b), showing a bimodal distribution. The center part is referred to as the coherent part of the sample and its boundary is indicated by a red solid line in (c) and an arrow in (d). The data are acquired for $N = 1.6(2) \times 10^6$ atoms at $T = 50(6)$ nK. The vortex number in an image is $N_v = 16(4)$.

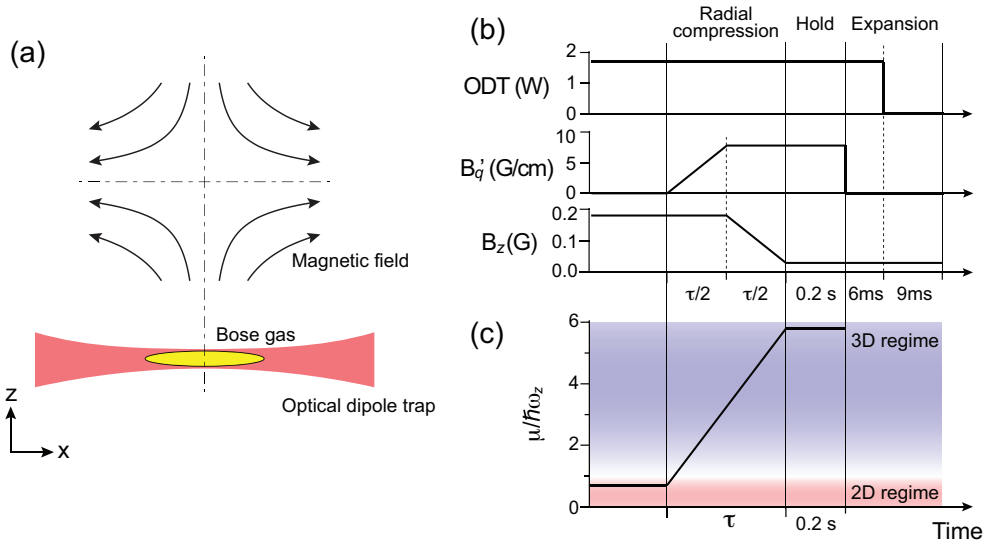

Figure 4.13: (a) Experimental set up for radial compression and (b) timing diagram of radial compression process. (c) Evolution of the scaled chemical potential $\mu/\hbar\omega_z$ in the radial compression sequence.

activated vortices in a 2D Bose gas. The fast expansion of the sample along the tight direction rapidly reduces the atom interaction effects which are necessary to maintain the spatial structure of vortex cores in the expansion dynamics. Furthermore, phase fluctuations due to thermal excitations of vortices as well as phonons evolve into complicated density ripples [Fig. 4.12(a)], and thus it becomes more difficult to distinguish individual vortices in the density image.

In order to enhance the visibility of the vortex cores, we apply a radial compression to the sample before releasing the trap. This compression transforms the 2D sample into an oblate 3D sample with $\mu/\hbar\omega_z > 5$, restoring the favorable condition for the vortex detection [55]. Also, the density of states changes to 3D, inducing thermal relaxation of phonons. Although tightly bound

vortex pairs would annihilate, loosely bound pairs and free vortices could survive the compression process [56].

For the radial compression, the axial axis of the magnetic quadrupole field was aligned with that of the optical dipole trap, Fig. 4.13 (a), so that the atoms were confined in the hybrid potential

$$\begin{aligned} V(x,y,z) &= \frac{1}{2}m(\omega_x^2 x^2 + \omega_y^2 y^2 + \omega_z^2 z^2) \\ &\quad + g_L B'_q \sqrt{\frac{x^2+y^2}{4} + (z - \frac{B_z}{g_L B'_q})^2} + mgz, \end{aligned} \tag{4.21}$$

where $\omega_i, g_L,\ B'_q,\ B_z$ and g are harmonic trapping frequencies of optical trap along i-axis, Landé g factor $\mu_B/2$ (μ_B is Bohr magneton), axial field gradient, bias field in the z-direction and gravitational acceleration respectively.

The field gradient and the position of the zero-field point were controlled to increase the trapping frequencies almost linearly. The axial field gradient strength was increased to 7.8 G/cm in 0.2 s under 0.7 G of the uniform magnetic field. The field gradient strength was set to below gravity force, 8.1 G/cm, so that atoms are confined in the radial direction only. Further increase of radial confinement was done by reducing the bias field to 0.03 G and radial trapping frequency becomes $\omega_r = 2\pi\times 39$ Hz. In the experiments, the radial compression was carried out in 0.4 s, quarter period of the optical trap frequency, to prevent severe perturbation of the sample and let the sample relax for 0.2 s which corresponds to about 10 collision times. The atom number fraction for the coherent part was reduced by about 7% in the compression process.

Finally, we probe the in-plane atom density distribution by absorption

imaging after 15 ms expansion. We first turn off the magnetic potential and switch off the optical trap 6 ms later, which we find helpful to improve the core visibility in our experiments.

4.4.2 Pair correlation

We observe thermally activated vortices with clear density-depleted cores of size $\xi_v \approx 8$ μm [Fig. 4.12(b)]. By locating the vortex positions by hand, we obtain the vortex distribution $\rho_v(\vec{r}) = \Sigma_{i=1}^{N_v} \delta(\vec{r} - \vec{r}_i)$, where N_v is the number of vortices in the image and $\vec{r}_i$ denotes the vortex position with respect to the center of the sample. Vortices mainly appear in the outer region of the coherent part [Fig. 4.12(c)], implying a vortex-driven phase transition. At the boundary of the coherent part, density modulations suggestive of vortex cores are often observed, but not included in the vortex counting. There is no azimuthal dependence of the vortex distribution and we determine the radial profile of the vortex density $n_v(r)$ by azimuthally averaging the vortex distribution $\bar{\rho}_v(\vec{r})$ which is averaged for at least 12 images of the same experiment [Fig. 4.12(d)]. For a slightly thicker sample with $\mu/\hbar\omega_z \approx 1.5$, we observe that the vortex number rapidly decrease, confirming that the vortex excitations result from the 2D nature of the system.

One notable feature in the vortex distribution is frequent appearance of a pair of vortices which are closely located to each other but well separated from the others (see the inset in Fig. 4.14). The average distance to the nearest-neighbor vortex is measured to be $d_m \approx 4\xi_v$. Because direct generation of single vortices is forbidden by the angular momentum conservation, the thermal acti-

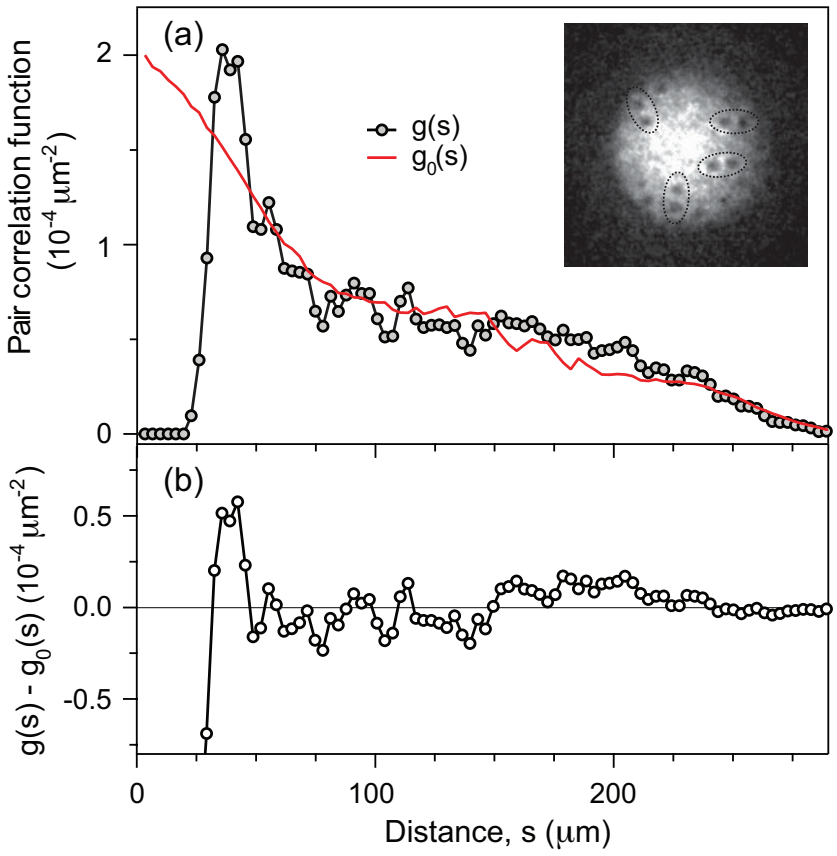

Figure 4.14: Pair correlations of vortices. (a) Two-vortex spatial correlation function $g(s)$ for the experimental condition in Fig. 4.12. The red solid line represents the correlation function $g_0(s)$ for a random distribution with the same vortex density profile $n_v(r)$ in Fig. 4.12(d). (b) The difference $g(s) - g_0(s)$ shows oscillatory behavior with a noticeable enhancement at $s \sim 35$ μm. The inset displays the same image in Fig. 4.12(b) with guide lines for pairs of vortices whose separation is less than 30 μm.

vation of vortices must involve vortex-antivortex-pair excitations.

A more quantitative study of the pair correlations is performed with the two-vortex spatial correlation function:

$$g(s) = \frac{1}{\pi s N_v(N_v-1)} \sum_{i>j} \delta(s - r_{ij}), \tag{4.22}$$

where $r_{ij} = |\vec{r}_i - \vec{r}_j|$. This function displays the probability of finding a vortex at distance s from another vortex. We determine $g(s)$ as the average of the pair correlation functions obtained from individual images for the same experiment [Fig. 4.14(a)]. In order to extract the pairing features, we compare $g(s)$ to the correlation function for a random distribution with the same vortex density profile $n_v(r)$:

$$g_0(s) = \frac{\int dr d\theta \; r n_v(r) n_v(r')}{[\int dr 2\pi r n_v(r)]^2}, \tag{4.23}$$

where $r' = \sqrt{r^2 + 2rs\cos\theta + s^2}$. The difference $g(s) - g_0(s)$ shows a noticeable enhancement around $s \sim d_m$ and small oscillatory behavior for $s > d_m$ [Fig. 4.14(b)], indicating the attraction between closely located vortices. The strong suppression at $s < 3\xi_v$ is attributed to the annihilation of tightly bound vortex pairs during the compression process. These observations clearly demonstrate the pairing of vortices in the superfluid phase in a quasi-2D Bose gas.

4.4.3 BKT-BEC crossover

In a finite-size 2D system, a BEC forms at finite temperature when the phase coherence extends over the whole system. This suggests that there are two microscopically distinct superfluid phases for a trapped 2D Bose gas: a BKT phase

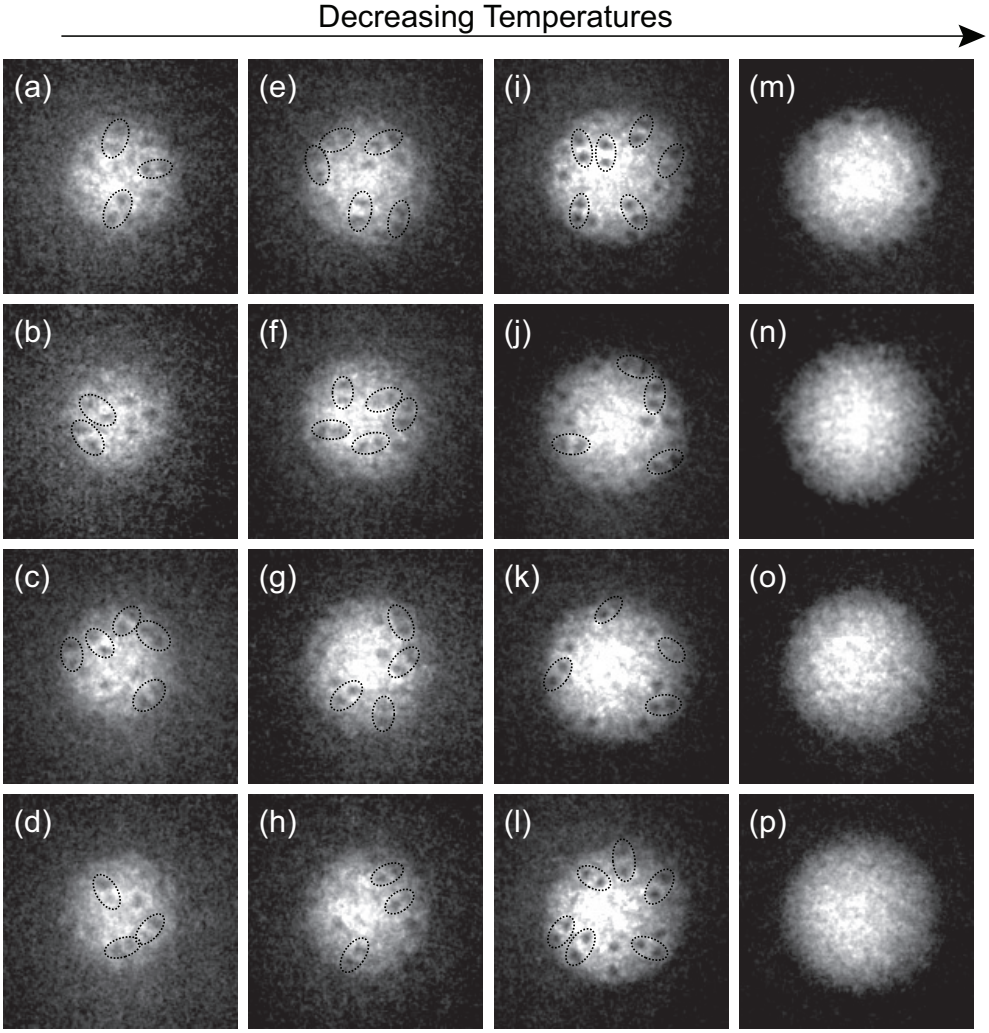

Figure 4.15: Thermal dependence of vortex pairs in a quasi-two dimensional Bose gas. The four images in each column represent vortices in 2D sample with similar experimental condition. Temperature and atom number are 67(12)nK, $1.5(2)\times10^6$ for (a) - (d), 56(6) nK, $1.4(3)\times10^6$ for (e) - (h), 48(8) nK, $1.3(1)\times10^6$ for (i) - (l), and 23(4) nK, $1.0\ (3)\times10^6$ for (m) - (p). The guide lines represent vortex pairs whose separations are 30 μm$\sim$ 40 μm.

with vortex-pair excitations and a BEC phase with no thermal vortices [57, 58]. Since the vortex pairs are also thermal excitations, the two distinct superfluid phase could be investigated by varying the temperature. As shown in Fig 4.15, vortex-free regime gradually develop as we lower the temperature, which could demonstrate the BKT-BEC crossover behavior of the finite 2D system.

To have quantitative analysis, the vortex density profiles $n_v(r)$ for various temperatures are displayed in Fig 4.16. At high temperature below the critical point, vortex excitations prevail over the whole coherent part. As temperature is lowered, the vortex density is suppressed and a vortex-free region emerges in the center of the sample. At the lowest temperature, only a few vortices appear near the boundary of the coherent part. Because a vortex pair of size d carries a linear momentum of h/d, it might be expected that vortex diffusion distorts the vortex distribution during the compression, but we observe that the vortex region ($n_v > 0$) does not change significantly for longer compression times as shown in Fig 4.17. Probably, it is energetically unfavorable for vortices to intrude into the center region of high atom density.

The temperature dependence of the vortex distribution can be understood with the thermal excitation probability p of a vortex-antivortex pair in a uniform superfluid. The excitation energy of a vortex pair is $E \sim \frac{h^2}{2\pi m} n_s \ln(d/\xi)$ where n_s is the superfluid density [57]. The number of distinguishable microstates for the vortex pair in the superfluid of size R is $\sim \frac{R^2}{\xi^2}\frac{\pi d}{\xi}$, giving the entropy $S = k\ln(\pi d R^2/\xi^3)$ (k is the Boltzmann constant). From the associated free energy $F = E - TS$, $p \propto e^{-F/kT} = \frac{\pi R^2}{\xi^2}(d/\xi)^{-(n_s\lambda^2-1)}$, exponentially

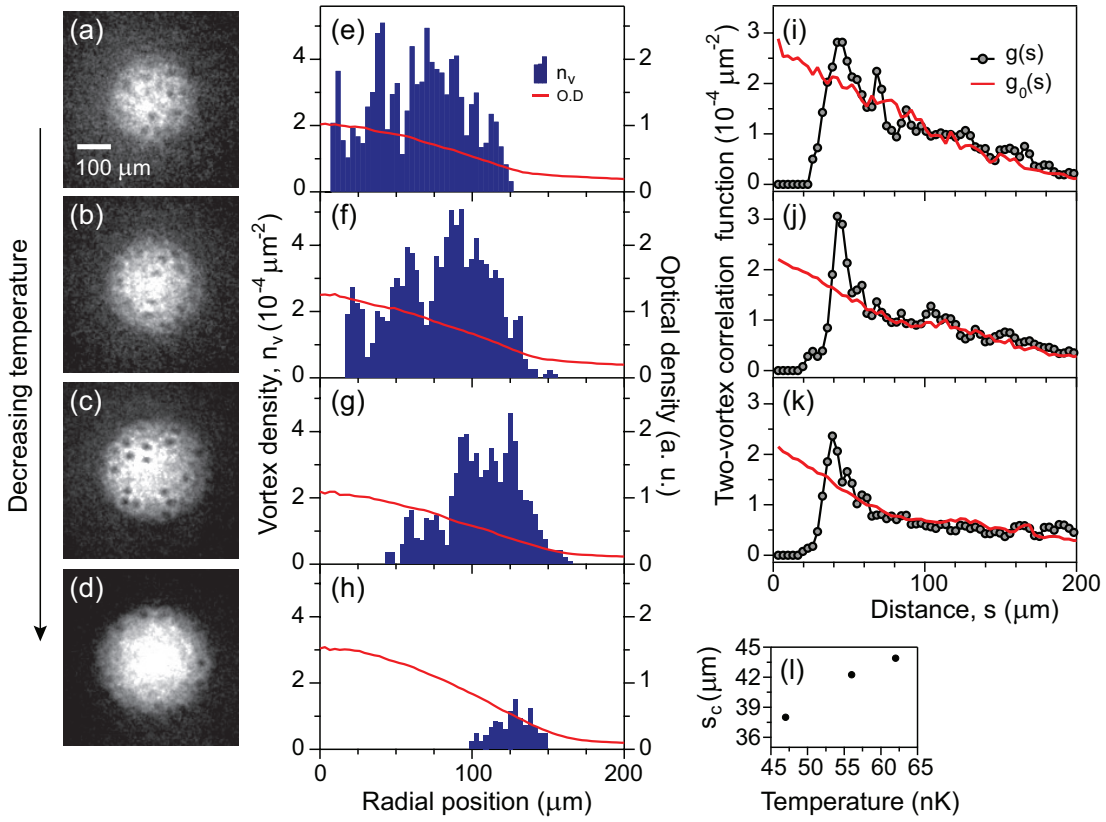

Figure 4.16: Temperature dependence of the vortex distribution in a trapped 2D Bose gas. The left column (a-d) displays representative vortex images for various temperatures as show in Fig. 4.15. The middle column (e-h) and the right column (i-k) show the radial profiles of the vortex density $n_v(r)$ and the pair correlation function $g(s)$, respectively, for the experimental condition in (a-d). The red solid lines in (e-h) and (i-k) represents $n(r)$ and $g_0(s)$, respectively. (l) The maximal vortex correlation distance s_c at various temperature. The data are obtained from at least 12 images for each condition. $g(s)$ for the lowest temperature (d) is not reliably determined due to the small vortex number.

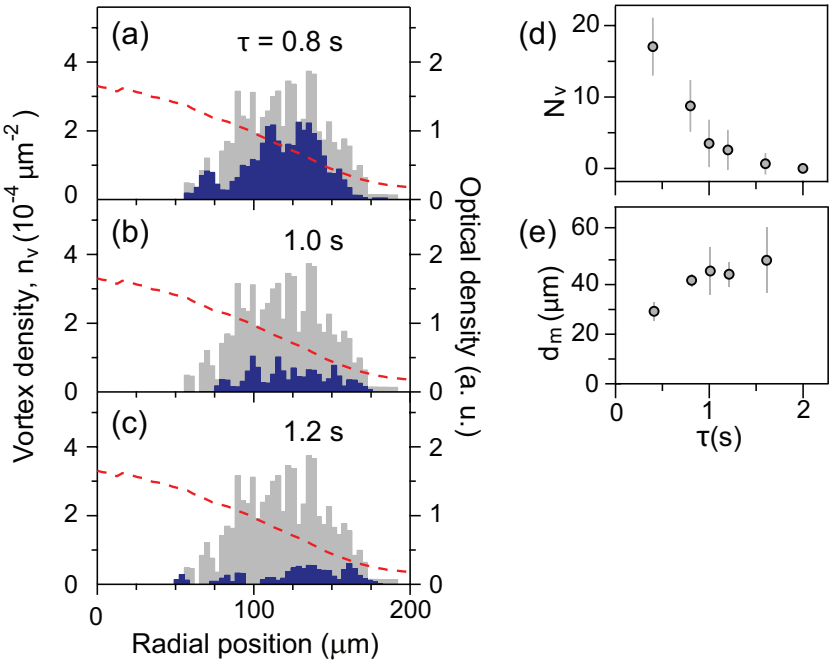

Figure 4.17: The radial profiles of vortex density $n_v(r)$ and optical density (red solid line) are shown in with different compression time (τ). The vortex density $n_v(r)$ in the left column (a) - (c) are obtained with aspect ratio ($\lambda = 108$). The vortex density profile and optical density for $(\lambda, \eta, \tau) = (108, 0.53, 0.4)$ is displayed in the background. These data are acquired for $N = 1.8(2) \times 10^6$ atoms. The data are obtained from at least 10 images for each condition. (d) Vortex number N_v and (e) nearest vortex distance d_m versus compression time τ. Error bars indicate standard deviation.

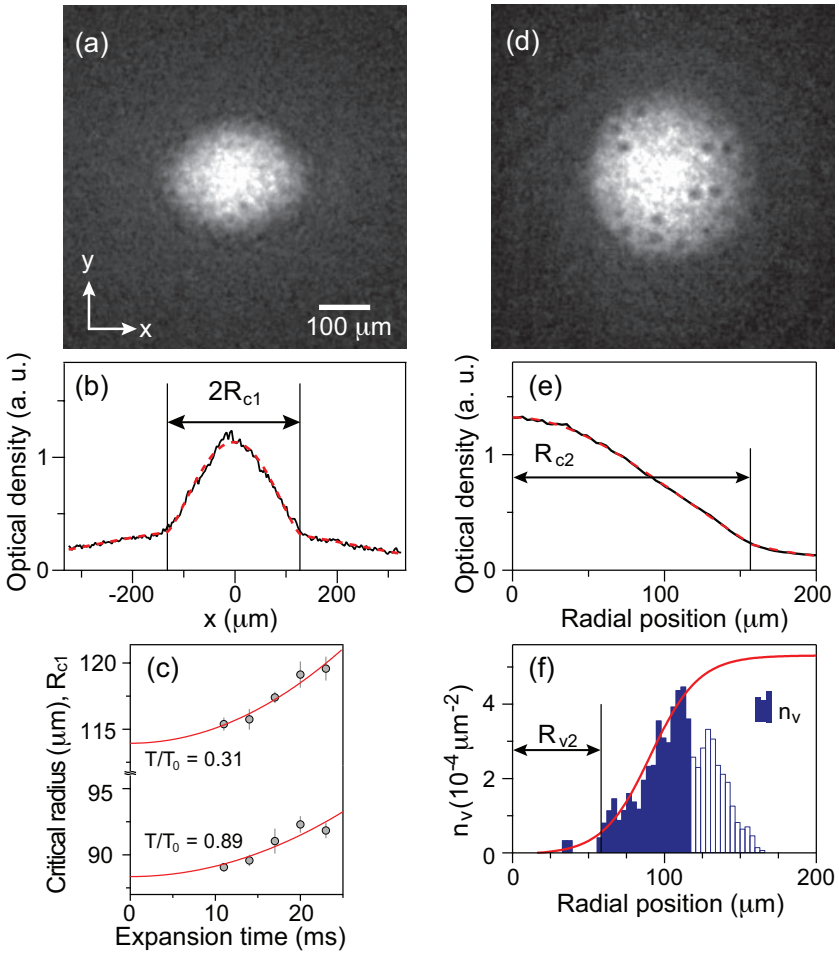

Figure 4.18: (a) Optical density image of a quasi-2D sample after 17ms time-of-flight and (b) its total cross section view. Solid line and dashed line are optical density profile and parabolic fitting curve, respectively. R_{c1} is critical radius of quasi-2D sample. (c) Critical radius, R_{c1}, at various expansion time. The in-situ radius R_{c0} of the coherent part is estimated from a fit (red line) of $R_c(1+\alpha t^2)$. (d) Time-of-flight image after radial compression of the Bose gas and (e) its optical density profile with azimuthal averaging. Dashed line is parabolic fitting profile of the optical density curve (solid line) with gaussian thermal wing. (f) R_{v2} marks the point where tangent-hyperbolic curve fitting of $n_v(r) \simeq 6\times10^{-5}$. Opaque region is excluded from the fitting range. The data are obtained in experimental condition of Fig 4.12

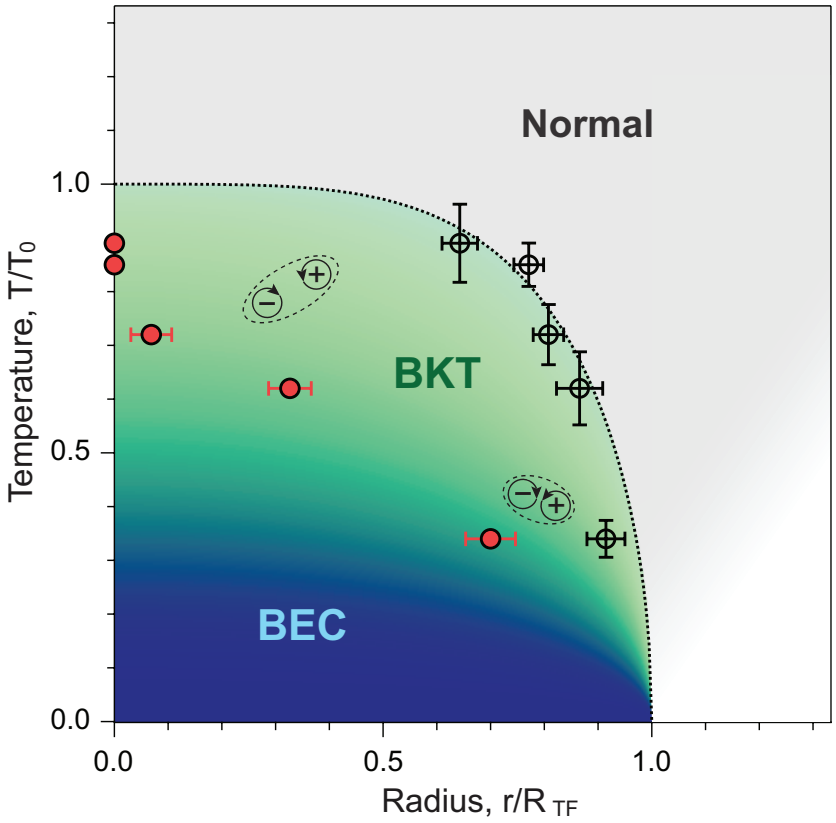

Figure 4.19: BKT-BEC crossover. A schematic phase diagram of a weakly interacting 2D Bose gas trapped in a harmonic potential is depicted in the plane of T/T_0 and $r/R_{\rm TF}$. T_0 is the BEC temperature for a quasi-2D ideal gas (see text), and $R_{\rm TF}$ is the zero-temperature 2D Thomas-Fermi radius. Open circles and solid circles indicate the radii of the coherent part and the inner radii of the vortex region ($n_v > 0$), respectively (see text). The dashed line is a guide for the critical line for the superfluid transition. As thermal excitations of vortex pairs are suppressed at lower temperatures, the BKT superfluid evolves into a BEC in the finite system.

suppressed by $n_s\lambda^2$, where $\lambda = \frac{h}{\sqrt{2\pi mkT}}$ is the thermal wavelength. The vortex density profile $n_v(r)$ reflects the spatial distribution of the superfluid density $n_s(r)$ in the inhomogeneous trapped sample.

This observation suggest that a vortex region emerges below a certain temperature, manifesting the BKT-BEC crossover. We determine the inner boundary R_v of the vortex-free region from a hyperbolic tangent fit to the inner region of $n_v(r)$ with a threshold value of 6×10^{-5} μm^{-2}, see Fig. 4.18 (f), which defines the characteristic radius.

We summarize our results in Fig. 4.19 with a schematic phase diagram for a trapped 2D Bose gas in the plane of temperature and radial position. Here we normalize the temperature to the ideal condensate critical temperature in quasi-2D potential and use the radius of the coherent part as a critical radius for the superfluid phase transition. The *in-situ* critical radius R_{c0} is determined from a bimodal fit to the density profile in the images taken without the compression [Fig. 4.18(b)], including the time-of-flight expanding factor. And the *in-situ* inner vortex radius R_{v0} is obtained as $R_{v0} = R_{c0}(R_{v2}/R_{c2})$ with assuming that the relative position of the vortex region is preserved in the compression and expansion process. Then, the radius is normalized by 2D Tomas-Fermi radius $R_{TF} = (\frac{4\hbar^2 N\tilde{g}\omega_y}{\pi m^2\omega_x^3})^{1/4}$.

In recent theoretical studies [59, 60], the characteristic temperature for the emergence of a BEC phase was calculated by determining the point when the thermal excitation probability of a vortex pair in a sample becomes of order unity. Our results show qualitative agreement with the predictions, but their

direct comparison is limited because the vortex detection efficiency in our experiments is not determined.

4.4.4 Effects of the radial compression

The underlying assume of the vortex pairs is that the vortices are not nucleated through the radial compression. The statement can be justified by the argument that the ring symmetry of magnetic quadrupole filed could not impose angular momentum during the radial compression. Supporting experiment is carried out by preparing a slightly tighter trap composed of the optical trap and a weak magnetic potential ($\mu/\hbar\omega_z \approx 1.5$). Even with similar number of atoms and temperature, we observed that the vortex number rapidly decreases in comparison to the samples prepared in the original optical trap ($\mu/\hbar\omega_z < 1$) [Fig 4.20]. This shows that the observed vortex excitations result from the 2D nature of the system.

In summary, we have observed thermally activated vortex pairs in a 2D Bose gas trapped in a harmonic potential. This provides the clear confirmation of BKT superfluidity of the system. In ultracold atom experiments, the study of 2D superfluidity has been recently extended to systems with Fermi gases [61,62] or including disorder potentials [63,64]. The vortex detection method developed in this work will be an important tool to probe the microscopic properties of these systems. Integrated with an inteferometric technique [32,65], this method can be upgraded to be sensitive to the sign of a vortex.

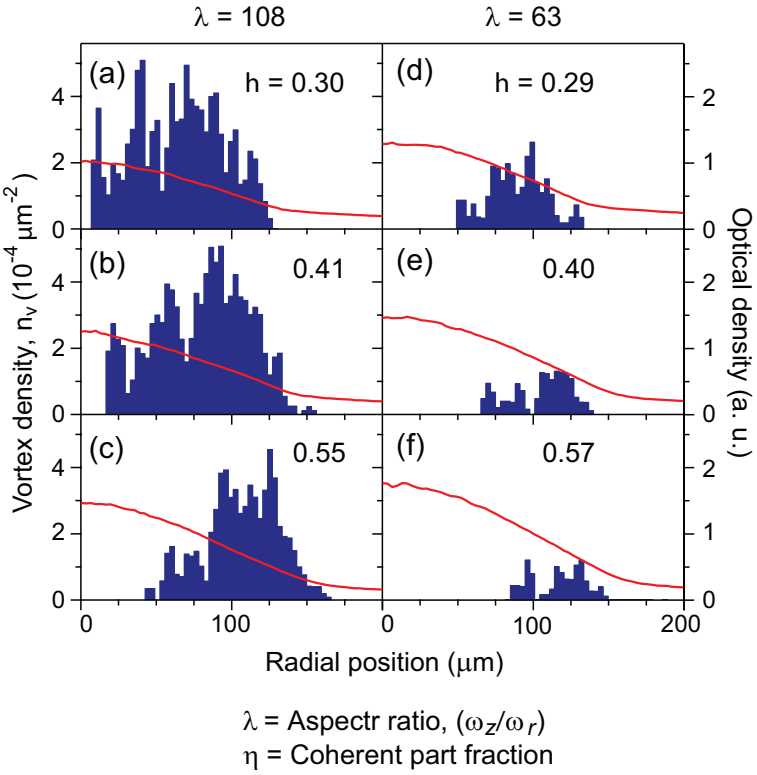

Figure 4.20: The radial profiles of vortex density $n_v(r)$ and optical density (red solid line) are shown in (a) - (f) with different experimental conditions such as aspect ratio, atom number, coherent part fraction and vortex number (λ, N, η, N_v). The vortex density $n_v(r)$ in the left column (a) - (c) are obtained with aspect ratio ($\lambda = 108$) and compression time ($\tau = 0.4$). The atom number, coherent part fraction and the vortex number are $(N, \eta, N_v) = (1.5(2) \times 10^6, 0.30(0.04), 13(4))$ for (a), $(1.4(3) \times 10^6, 0.41(0.02), 16(4))$ for (b) and $(1.3(1) \times 10^6, 0.55(0.04), 15(5))$ for (c). The middle column (d)-(f) represents the vortex density profiles with thicker sample ($\lambda = 63$) and $\tau = 0.4$. The other experimental parameters are $(N, \eta, N_v) = (1.9(2) \times 10^6, 0.29(0.03), 6(3))$ for (d), $(1.8(2) \times 10^6, 0.4(0.02), 4(2))$ for (e) and $(1.7(2) \times 10^6, 0.57(0.02), 3(2))$ for (f).

Bibliography

[1] P. Kapitza, Nature **141**, 74 (1938).

[2] J. F. Allen and A. D. Misener, Nature **141**, 75 (1938).

[3] F. London, Nature **141**, 643 (1938).

[4] L. Tisza, Journal. de Physique et Radium **1**, 164 (1940).

[5] L. D. Landau , J. Phys. U.S.S.R. **5**, 71 (1941).

[6] L. D. Landau , J. Phys. U.S.S.R. **11**, 91 (1941).

[7] N. N. Bogoliubov, J. Phys. U.S.S.R. **11**, 23 (1947).

[8] J. L. Yarnell, G. P. Arnold, P. J. Bendt, and E. C. Kerr, Phys. Rev. **113**, 1379 (1959).

[9] D. G. Henshaw and A. D. B. Woods, Phys. Rev. **121**, 1266 (1961).

[10] A. Griffin, *Bose-Einstein Condensation in Atomic Gases* (IOP Press, Amsterdam, 1999).

[11] S. Balibar, J. Low Tem. Phys. **146**, 441 (2007).

[12] N. D. Mermin and H. Wagner, Phys. Rev. Lett. **17**, 1133 (1966).

[13] P. Hohenberg, Phys. Rev. **158**, 383 (1967).

[14] D. J. Bishop and J. D. Reppy, Phys. Rev. Lett. **40**, 1727 (1978).

[15] V. Berezinskii, Sov. Phys. JETP **34**, 610 (1972).

[16] J. M. Kosterlitz and D. J. Thouless, J. Phys. C **6**, 1181 (1973); J. M. Kosterlitz, ibid. **7**, 1046 (1974).

[17] M. Holzmann, G. Baym, J. .P. Blaizot, and F. Laoë, Proc. Natl. Acad. Sci. U.S.A. **104**, 1476 (2000).

[18] O. Penrose and L. Onsager, Phys. Rev. **104**, 576 (1956).

[19] D. R. Nelson and J. M. Kosterlitz, Phys. Rev. Lett. **39**, 1201 (1977).

[20] C. Pethick and H. Smith. *Bose-Einstein condensation in dilute gases.* (Cambridge University Press, 2002.)

[21] D. S. Petrov, M. Holzmann,and G. V.Shlyapnikov, Phys. Rev. Lett. **84**, 2551 (2000).

[22] D. S. Petrov and G. V. Shlyapnikov, Phys. Rev. A **64**, 012706 (2001).

[23] L. A. Sidorenkov, M. K. Tey, R. Grimm, Y. -H. Hou, L. Pitaevskii, and S. Stringari, Nature **498**, 78 (2013).

[24] C.-L. Hung, X. Zhang, N. Gemelke, and C. Chin, Nature **470**, 236 (2011).

[25] L.-C. Ha, C.-L. Hung, X. Zhang, U. Eismann, S.-K. Tung, and C. Chin, Phys. Rev. Lett. **110**, 145302 (2013).

[26] V. N. Popov and J. Niederle *Functional Integrals in Quantum Field Theory and Statistical Physics.* (D. Reidel Publishing Company, 1983.)

[27] N. Prokof'ev, O. Ruebenacker, and B. Svistunov, Phys. Rev. Lett. **87**, 270402 (2010).

[28] S. Stock, Z. Hadzibabic, B. Battelier, M. Cheneau, and J. Dalibard, Phys. Rev. Lett. **95**, 190403 (2005).

[29] Z. Hadzibabic, P. Krüger, M. Cheneau, B. Battelier and J. Dalibard, Nature **441**, 1118 (2006).

[30] P. Krüger, Z. Hadzibabic, and J. Dalibard, New J. Phys. **10**, 045006 (2008).

[31] T. Yefsah, R. Desbuquois, L. Chomaz, K. J. Günter and J. Dalibard, Phys. Rev. Lett. **107**, 130403 (2011).

[32] P. Cladé, C. Ryu, A. Ramanathan, K. Helmerson, and W. D. Phillips, Phys. Rev. Lett. **102**, 170401 (2009).

[33] S. Tung, G. Lamporesi, D. Lobser, L. Xia and E. A. Cornell, Phys. Rev. Lett. **105**, 230408 (2010).

[34] T. Plisson, B. Allard, M. Holzmann, G. Salomon, A. Aspect, P. Bouyer, and T. Bourdel, Phys. Rev. A **84**, 061606(R) (2011).

[35] R. Desbuquois, L. Chomaz, T. Yefsah, J. Léonard, J. Beugnon, C. Weitenberg, and J. Dalibard, Nat. Phys. **8**, 645 (2012).

[36] H. Holzmann, M. Chevallier, and W. Krauth, Europhys. Lett. **82**, 30001 (2008).

[37] T. E. Gureyev and K. A. Nugent, J. Opt. Soc. Am. A **13**, 1670 (1996).

[38] S. Dettmer *et al.*, Phys. Rev. Lett. **87**, 160406 (2001).

[39] S. Manz *et al.*, Phys. Rev. A **81**, 031601(R) (2010).

[40] A. Imambekev, I. E. Mazets, D. S. Petrov, V. Gritsev, S. Manz, S. Hofferberth, T. Schumm, E. Demler, and J. Schmeidmayer, Phys. Rev. A **80**, 032604 (2009).

[41] H. F. Talbot, Philos. Mag. **9**, 401 (1836); L. Reyleigh *ibid.***11**, 196 (1881).

[42] J. T. Winthrop and C. R. Worhington, J. Opt. Soc. Am. **55**, 373 (1965).

[43] A. W. Lohmann and J. A. Thomas, Appl. Opt **29**, 4337 (1990).

[44] M. S. Chapman, C. R. Ekstrom, T. D. Hammond, J. Schmeidmayer, B. E. Tannian, S. Wehinger, and D. E. Pritchard, Phys. Rev. A **51**, R14 (1995).

[45] I. E. Mazets, Phys. Rev. A **86**, 055603 (2012).

[46] T. Langen (*private communication*).

[47] S. W. Seo, J. Choi, Y. Shin, J. Korean Phys. Soc. **64**, 53 (2014).

[48] L. E. Sadler, J. M. Higbie, S. R. Leslie, M. Vengalattore and, D. M. Stamper-Kurn, Nature **443**, 312 (2006).

[49] S .Hofferberth, I. Lesanovsky, B .Fisher, T. Schumm and, J. Schiedmayer, Nature **449**, 324 (2006).

[50] B. Yurke, A. N. Pargellis, T. Kovas, and D. A. Huse, Phys. Rev. E **47**, 1525 (1993).

[51] A. J. Bray, A. J. Briant and, D. K. Jervis, Phys. Rev. Lett. **84**, 1503 (2000).

[52] L. Mathey, K. J.Günter, J. Dalibard and, A. Polkovnikov, arXiv:1112.1204 (2011).

[53] G. Roumpos *et al.*, Proc. Natl. Acad. Sci. U.S.A. **109**, 6467 (2012).

[54] K. W. Madison, F. Chevy, W. Wohlleben, and J. Dalibard, Phys. Rev. Lett. **84**, 806 (2000).

[55] F. Dalfovo and M. Modugno, Phys. Rev. A **61**, 023605 (2000).

[56] V. Schweikhard, S. Tung, and E. A. Cornell, Phys. Rev. Lett. **99**, 030401 (2007).

[57] T. P. Simula, M. D. Lee, and D. A. W. Hutchinson, Philos. Mag. Lett. **85**, 395 (2005).

[58] T. Esslinger and G. Blatter, Nature **441**, 1053 (2006).

[59] T. P. Simula and P. B. Blakie, Phys. Rev. Lett. **96**, 020404 (2006).

[60] D. Schumayer and D. A. W. Hutchinson, Phys. Rev. A **75**, 015601 (2007).

[61] M. Feld, B. Fröhlich, E. Vogt, M. Koschorreck, and M. Köhl, Nature **480**, 75 (2011).

[62] A. T. Sommer, L. W. Cheuk, M. J. H. Ku, W. S. Bakr, and M. W. Zwierlein, Phys. Rev. Lett. **108**, 045302 (2012).

[63] B. Allard, T. Plisson, M. Holzmann, G. Salomon, A. Aspect, P. Bouyer, and T. Bourdel, Phys. Rev. A **85**, 033602 (2012).

[64] M. C. Beeler, M. E. W. Reed, T. Hong, and S. L. Rolston, New J. Phys. **14**, 073024 (2012).

[65] G. Roumpos, M. D. Fraser, A. Löffler, S. Höfling, Al. Forchel, and Y. Yamamoto, Nat. Phys. **7**, 129 (2011).

Chapter 5

Two-dimensional Skyrmion in a spinor condensate

Topological excitations are geometrically non-trivial structures, which are classified by n-th homotopy group, and play a central role in describing the physics of ordered mediums such as superfluid Heliums, liquid crystals, and atomic Bose-Einstein condensates. Well-developed manipulation techniques for atomic motion and spin states enable us to engineer topological state of interest for investigating their dynamics and stability in a highly controllable manner. Quantized vortices have been created in single or multi-component condensates by external rotation [1] and phase imprinting methods [2–4], leading to the successful study of their many interesting phenomena such as line defect deformation [5], Tachenko's mode in vortex lattices [6], vortex dipole dynamics [7, 8] and dynamical instability of doubly charged vortices [9].

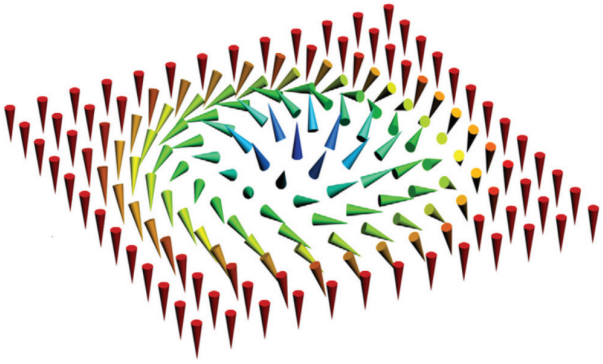

Figure 5.1: Spin configuration of two-dimensional skyrmion. The cone vectors represent spin vectors.

In particular, Bose-Einstein condensates of atoms have internal spin degree of freedom, where the different spin states have the same energy. This property provides unique opportunities for the study of various topological excitations. Recent studies show that because of the rich structure of their order parameters, spinor condensate can host various topological objects such as Half-quantum vortices [10], Skyrmions [11], Alice ring [12], Knots [13], and Dirac-monopole [14]. However, experimental demonstration of those topological excitations remains to be achieved.

Skyrmions are particle-like topological solitons [15] that have been studied in various research fields, ranging from high energy physics to condensed matter physics. While stable 3D Skyrmions remain to be discovered, 2D Skyrmions have been observed in many condensed matter systems such as liquid ^{3}He-A [16], quantum Hall systems [17], liquid crystals [18], helical ferromagnets [19,20], and one-atomic-layer systems [21]. Recently, coreless vortex state and skyrmion spin texture were created in the spinor condensate by using spatilly tailored magnetic

field rotation [22] or optical Raman transition [23].

However, the condensate were not trapped [22,23] so that the stability of the spin texture cannot be investigated. It is important to not that the ferromagnetic phase with SO(3) symmetry studied in the previous experiment [22, 23] have the trivial second homotopy group, implying that the spin texture are not topologically protected. The coreless vortex state with 2D skyrmion spin textures, referred to as Mermin-Ho vortices [24] or Anderson-Touluse [25], have infinite energy in a 2D plane and therefore are fundamentally different from the Skyrmion, which are localized topological soliton with finite energy [26].

In this chapter, we present magnetic field rotation method for imprinting Skyrmion spin textures in a spinor Bose-Einstein condensate. By rapidly moving the zero-field point of a 3D magnetic quadrupole field through a trapped spin-1 condensate, we could create 2D Skrymions and coreless spin vortices in a polar phase and the Anderson-Toulouse and Mermin-Ho vortex states in a ferromagnetic phase. We analyze the spatial structure of the created spin textures and find that the tilt angle of spins is quantitatively well described by the local field rotation, showing that the effects due to atom-atom interactions are not involved in our spin texture imprinting process. This observation allows us to propose a scheme with multiple applications of the imprinting process and we demonstrate the creation of a highly charged Skyrmion in a trapped condensate.

Finally, 2D Skyrmions dynamics in a harmonic potential is studied, where the spin texture dynamically deforms and decays to an uniform spin texture. The examination of the spin textures in the deformation process suggests that

half-quantum vortices might be generated around non-polar defects in the condensates. Related results are published in the following articles.

- Jae-yoon Choi, Woo Jin Kwon, and Yong-il Shin. *"Observation of topologically stable 2D Skyrmions in an antiferromagnetic spinor Bose-Einstein condensate"* Physical Review Letters **108**, 035301 (2012).

- Jae-yoon Choi, Woo-Jin Kwon, Moonjoo. Lee, Hyunseok Jeong, Kyungwon An, and Yong-il Shin. *"Imprinting Skyrmion spin textures in spinor Bose-Einstein condensates "* New Journal of Physics **14**, 053013 (2012).

5.1 Classification of topological excitations

In our universe, there are various kinds of geometric structures which is similar in shape but in different scale: Stars are spherical shape just like basket balls and Galaxies have singular point similar to donuts. We intuitively know that basket balls and donuts would be geometrically different but hard to characterize the properties of different geometry. The homotopy group is very useful in classifying geometrical structures and I would introduce the concept briefly in this section.

Let's consider the two different geometry shown in Fig. 5.2. One disk (a) has a hole inside of it, while the other (b) does not. If we consider a loop winding the hold of the disk [Fig. 5.2(a)], we find that the loop cannot be shrunk to a point without tearing the loop because of the hole. In contrast, all loops in the disk without a hole [Fig. 5.2(b)] can be easily shrunk to a point continuously.

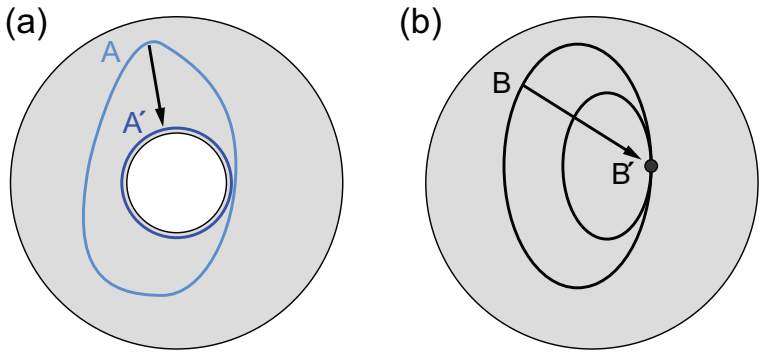

Figure 5.2: Geometric structure can be classified by a set of loop. (a) All loops winding the hole of the disk (marked by A) cannot be shrunk to a point continuously. (b) Any kinds of loops can be shrunk into a point B' without distortion.

In other words, loops in Fig. 5.2(b) are in the same class in that they can be deformed into a point smoothly. Thus, if we characterize the disk by a set of loops, its group structure would be trivial. For the annular disk, however, loops with different winding number[1] cannot be the same class because of the singular point and it is equivalent to an integer group $\mathbb{Z}$.

Mathematically [27], the homotopy group consider a continuous deformation of some mapping function. Let X and Y be topological spaces and $\mathfrak{S}$ be a set of continuous maps from X to Y. For two maps $f, g \in \mathfrak{S}$, if the image $f(X)$ is continuously deformed to $g(X)$ in Y, we can call the two maps are homotopic equivalent. Usually X is chosen to be some standard topological spaces whose structures are well defined. The n-sphere[2] or S^n is the standard space and we can classify any geometric structure by studying all the maps from S^n to Y and see its homotopic equivalence.

[1] It means how many times does a loop wrap around the hole.
[2] The n-sphere is the generalized $n+1$-dimensional surface satisfying $x_1^2 + x_2^2 \cdots x_n^2 = 1$.

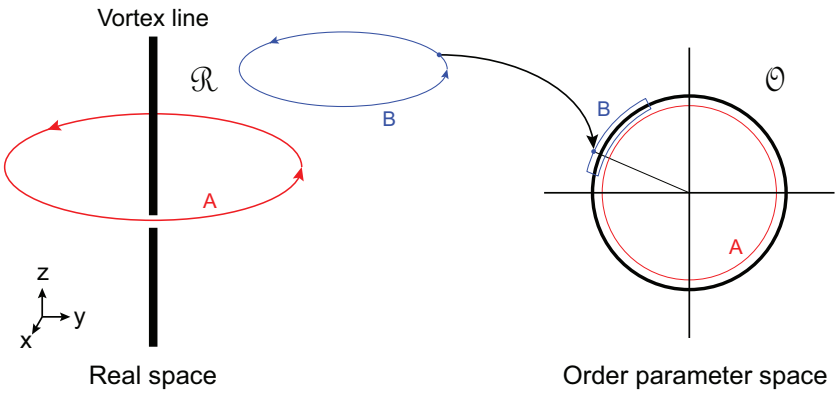

Figure 5.3: Mapping a loop in real space to its order parameter manifold S^1 by the function: $\mathbf{r} \rightarrow$Arg $\psi(\mathbf{r})$. The mapping function defines the first homotopy group of vortex line $\pi_1(S^1)$. The red circle (A) can wind up the order parameter space $\mathcal{O}$, while the blue circle (B) covers only one segment of S^1.

Applying this concept, we can predict possible types of topological excitations at a given order parameter manifold [28, 29]. Consider a $U(1)$ manifold, for example, where the first homopoty group of $U(1)$ is integer, $\pi_1(U(1)) = \mathbb{Z}$. It means that topological excitation of the $U(1)$ manifold can be characterized by a circle with different winding number. The vortex excitation (line defect) in a scalar condensate could be a physical example, where its wave function is $\psi(\mathbf{r}) = |\psi(\mathbf{r})|e^{\phi(\mathbf{r})}$. Consider a mapping function, defined in Eq (5.1), that projects a point in the real space to a value in the $U(1)$ manifold.

$$\mathbf{r} \rightarrow \text{Arg } \psi(\mathbf{r}) = \phi(\mathbf{r}). \tag{5.1}$$

If a loop encloses no line defect like a blue circle in Fig 5.3, its image under the mapping function covers only some part of the 1-sphere. Only when a loop encircles the singular point, can its image entirely map the $U(1)$ manifold.

If it covers the 1-sphere in n_w times, we can say the winding number of the line defect is n_w. Remark that the loops with different winding number cannot continuously deformed into each other as long as it does not cross the vortex line. This topological feature makes the line defect to be characterized by the winding number n_w.

	M	π_1	π_2	π_3
Scalar BEC	U(1)	$\mathbb{Z}$	0	0
Ferromagnetic spin-1 BEC	SO(3)	$\mathbb{Z}_2$	0	$\mathbb{Z}$
Polar spin-1 BEC	$\frac{S^2 \times U(1)}{\mathbb{Z}_2}$	$\mathbb{Z}$	$\mathbb{Z}$	$\mathbb{Z}$

Table 5.1: The order parameter manifold of spinor condensates and their homotopy group.

Extending the idea into higher dimension, a geometric structure can be classified by n-sphere. For example, three dimensional point defect such as monopole can be characterizes 2-sphere. We list a possible type of order parameter space of Bose-Einstein condensates and their topological property.

π_n	Defetcs	Solitons
π_1	Vortices	Nonsingular domain walls
π_2	Monopoles	2D Skyrmions
π_3		Skyrmions, Knots

Table 5.2: Topological excitation in spinor condensates.

From the list we can consider possible type of topological excitations for each order parameter manifold and Table 5.2 summarizes the results. The defect is a topological excitation with singularity in real space while soliton is referred to an excitation without singularity. Detail structures and properties of the possible topological excitations are well described in the review paper

in Ref. [28, 29] and this chapter would only describe 2D Skyrmion and half-quantum vortices, which are topological objects in the polar phase of spinor condensate.

5.2 Polar phase vs ferromagnetic phase of spin-1 condensates

We consider a Bose-Einstein condensate of spin-1 atoms, whose order parameter can be written as $\Psi = (\psi_1, \psi_0, \psi_{-1})^{\mathrm{T}} = \sqrt{n}e^{i\vartheta}\zeta$, where $\psi_{0,\pm1}$ is the $|m_z = 0, \pm1\rangle$ component of the order parameter [30], n is the atomic number density, ϑ is the superfluid phase and ζ is a three-component spinor. The atomic interactions are dominated by two body s-wave collision and the total spin $\mathbf{F}_{\mathrm{tot}} = \mathbf{F}_1 + \mathbf{F}_2$ can have values of $2F, 2F-1, \cdots, 0$. Since the s-wave collision cannot change the spatial wave function of the two atoms, the symmetric(anti-symmetric) requirement of identical Boson(Fermion) give $\mathbf{F}_{\mathrm{tot}}$ =even(odd) value. Therefore, spinor condensate of $F = 1$ have two possible channel of $\mathbf{F}_{\mathrm{tot}} = 2, 0$. The interacting Hamiltonian of the spin collision process in the total spin basis, $\sum_{m_F} |F_{\mathrm{tot}} = 2, m_F\rangle \otimes |F_{\mathrm{tot}} = 0, m_F\rangle$, is given by

$$H_{\mathrm{int}}(\mathbf{r}_1, \mathbf{r}_2) = \delta(\mathbf{r}_1 - \mathbf{r}_2) \sum_{F=0,2} g_F \mathbf{P}_F, \tag{5.2}$$

where $g_F = \frac{4\pi\hbar^2 a_F}{m}$ with scattering length a_F corresponding for the total spin 2, 0 and $\mathbf{P}_F$ is projection operator $\sum_{m_F} |F_{\mathrm{tot}}, m_F\rangle\langle F_{\mathrm{tot}}, m_F|$.

The two body interacting Hamiltonian could be also represented by pauli 3-by-3 matrix $\mathbf{F}_i$ of each particle, where the matrix elements are

$$\hat{F}_x = \frac{1}{\sqrt{2}} \begin{bmatrix} 0 & 1 & 0 \\ 1 & 0 & 1 \\ 0 & 1 & 0 \end{bmatrix}, \; \hat{F}_y = \frac{i}{\sqrt{2}} \begin{bmatrix} 0 & -1 & 0 \\ 1 & 0 & -1 \\ 0 & 1 & 0 \end{bmatrix}, \; \hat{F}_z = \begin{bmatrix} 1 & 0 & 0 \\ 0 & 0 & 0 \\ 0 & 0 & -1 \end{bmatrix}. \tag{5.3}$$

Since the operator satisfy the below relation,

$$\begin{aligned} \mathbf{F}_1 \cdot \mathbf{F}_2 &= (\mathbf{F}_1 \cdot \mathbf{F}_2)\mathbf{1} \\ &= \sum_F (\mathbf{F}_1 \cdot \mathbf{F}_2)\mathbf{P}_F = P_2 - 2P_0, \end{aligned} \tag{5.4}$$

we can represent the Hamiltonian of the Eq. (5.2) by

$$H_{\text{int}}(\mathbf{r}_1, \mathbf{r}_2) = \delta(\mathbf{r}_1 - \mathbf{r}_2) \sum_{F=0,2} g_F P_F \tag{5.5}$$

$$= \delta(\mathbf{r}_1 - \mathbf{r}_2)(g_0 P_0 + g_2 P_2) \tag{5.6}$$

$$\begin{aligned} &= \delta(\mathbf{r}_1 - \mathbf{r}_2)(c_0(P_0 + P_2) + c_2(P_0 - 2P_2)) \\ &= \delta(\mathbf{r}_1 - \mathbf{r}_2)(c_0 + c_2 \mathbf{F}_1 \cdot \mathbf{F}_2), \end{aligned}$$

where $c_0 = \frac{g_0 + 2g_2}{3}$ and $c_2 = \frac{g_2 - g_0}{3}$.

In a second quantization representation the interacting Hamiltonian becomes

$$H_{\text{int}} = \frac{1}{2} \int d^3r \{c_0(\Psi_i^\dagger \Psi_j^\dagger \Psi_j \Psi_i) + c_2(\Psi_i^\dagger \Psi_j^\dagger (\mathbf{F}_i \cdot \mathbf{F}_j) \Psi_j \Psi_i)\}. \tag{5.7}$$

We can express the interaction in terms of three spin components, displaying

various spin collision channel

$$
\begin{aligned}
H_{\text{int}} =& \frac{1}{2}\int d^3r\{(c_0+c_2)\Psi_1^\dagger\Psi_1^\dagger\Psi_1\Psi_1 + c_2\Psi_0^\dagger\Psi_0^\dagger\Psi_0\Psi_0 + (c_0+c_2)\Psi_{-1}^\dagger\Psi_{-1}^\dagger\Psi_{-1}\Psi_{-1} \\
&+ 2(c_0+c_2)\Psi_1^\dagger\Psi_0^\dagger\Psi_0\Psi_1 + 2(c_0-c_2)\Psi_1^\dagger\Psi_{-1}^\dagger\Psi_{-1}\Psi_1 + 2(c_0+c_2)\Psi_0^\dagger\Psi_{-1}^\dagger\Psi_{-1}\Psi_0 \\
&+ 2c_2\Psi_{-1}^\dagger\Psi_1^\dagger\Psi_0\Psi_0 + 2c_2\Psi_0^\dagger\Psi_0^\dagger\Psi_{-1}\Psi_1\}. \qquad (5.8)
\end{aligned}
$$

The first three terms represent self scattering and the following three terms mean collisions between different spin state. The final two terms is spin mixing term, which allows coherent spin dynamics and relaxation through dissipation when the initial spinor state is not prepared in their ground state.

The ground state of the spinor condensate at zero magnetic field is determined by the spin-dependent interactions whose energy density is given as $E = \frac{c_2}{2}n^2|\langle\mathbf{f}\rangle|^2$. The ground state is polar, i.e. $|\langle\mathbf{F}\rangle| = 0$, for $c > 0$ (e.g. ^{23}Na [31]) or ferromagnetic, i.e. $|\langle\mathbf{F}\rangle| = 1$, for $c < 0$ (e.g. ^{87}Rb [32]). The general expression of ground state for each spinor condensate can be obtained by applying rotation matrix $U(\alpha,\beta,\gamma) = e^{-iF_z\alpha}e^{-iF_y\beta}e^{-iF_z\gamma}$ to the $\zeta = (0,0,1)^{\text{T}}$ ferromagnetic condensate and to the $\zeta = (0,1,0)^{\text{T}}$ for polar condensate, which is represented as follows

$$
\zeta_{ferro}(r,\phi) = U(\alpha,\beta,\gamma)\begin{pmatrix}0\\0\\1\end{pmatrix} = e^{i\gamma}\begin{pmatrix}e^{-i\alpha}\sin^2\frac{\beta}{2}\\ \frac{1}{\sqrt{2}}\sin\beta \\ e^{i\alpha}\cos^2\frac{\beta}{2}\end{pmatrix}, \qquad (5.9)
$$

and

$$\zeta_{polar}(r,\phi) = U(\alpha,\beta,\gamma)\begin{pmatrix} 0 \\ 1 \\ 0 \end{pmatrix} = \begin{pmatrix} -\frac{1}{\sqrt{2}}e^{-i\alpha}\sin\beta \\ \cos\beta \\ \frac{1}{\sqrt{2}}e^{i\alpha}\sin\beta \end{pmatrix}. \tag{5.10}$$

From the above expression, we can see the ferromagnetic spinor condensate has SO(3) symmetry while the polar condensate does not depend on the γ and has different symmetry. Therefore, even with the same spin texture, topological structure can be different because of the distinct order parameter space. Especially order parameter manifold of polar condensate is $U(1)\times S^2/\mathbb{Z}_2$, where the $U(1)$ is the gauge symmetry of the superfluid phase, S^2 is for the rotational symmetry of the spinor and $\mathbb{Z}_2$ comes from the invariant symmetry under $\vec{n} \to -\vec{n}$ and $\vartheta \to \vartheta + \pi$ [33]. Because of the $\mathbb{Z}_2$ symmetry polar condensate can posses intriguing form of topological excitation such as half-quantum vortex and 2D skyrmion.

In the following sections, creation method for skyrmion spin texture both in ferromagnetic and polar phase would be introduced. First, we present a brief theoretical description of the imprinting method and introduce various excitations with the spin texture in spin-1 condensate. Then we compare our experimental results and the quantitative analysis of the spatial distribution of the spin tilt angle in the spin texture. Finally, experimental study of dynamics about topological skyrmion in the polar condensate would be discussed.

5.3 Spin texture imprinting by spin rotation

5.3.1 Spin tilting by B-field rotation

The motion of a spin in a time-dependent, external magnetic field $\vec{B}(t)$ is governed by

$$\frac{d\vec{s}}{dt} = \frac{g\mu_B}{\hbar}\vec{s} \times \vec{B}(t), \tag{5.11}$$

, where $\vec{s}$ is a unit vector for the spin direction, g is the g-factor of the spin, μ_B is the Bohr magneton, and $\hbar$ is the Planck constant h divided by 2π. The spin precesses around the axis of the magnetic field with the Larmor frequency $\omega_L = g\mu_B|\vec{B}|/\hbar$ and the precession axis of the spin is dragged to the field direction when the direction of the magnetic field changes. If the changing rate of the field direction $\omega_B = \frac{\vec{B}}{|\vec{B}|^2} \times \frac{d\vec{B}}{dt}$ is much slower than the Larmor frequency, the spin adiabatically follows the magnetic field, i.e. preserving its angle from the field direction. On the other hand, if the field direction changes relatively fast, the angle evolves dynamically, i.e. inducing the diabatic population transfer between the magnetic sublevels of the spin.

Let's consider the situation depicted in Fig. 5.4(a), where the spin, initially aligned to the $+\hat{z}$-direction, is placed in an external magnetic field, which rotates from $+\hat{z}$ to $-\hat{z}$ as $\vec{B}(t) = B_0\hat{x} + B_z(t)\hat{z}$ with linearly sweeping $B_z(t)$ from $+\infty$ to $-\infty$. With $B_0 = 0$, the magnetic field suddenly changes its direction to the opposite so the spin is not affected and keeps pointing to the $+z$-direction. On the other hand, when $B_0 \gg 1$, the spin adaptively follows the rotating field and ends up with pointing to the $-z$-direction. We numerically calculate the

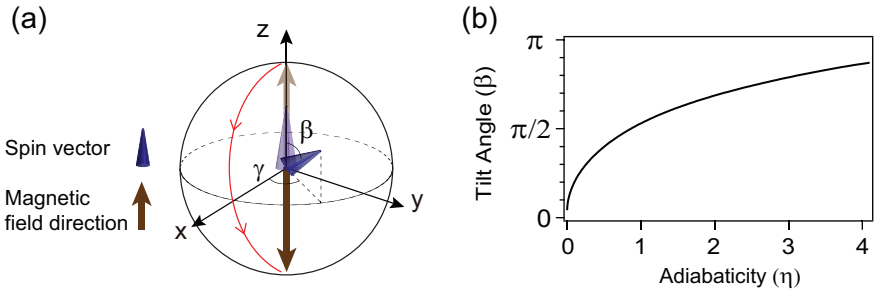

Figure 5.4: Spin vector dynamics under time-varying magnetic field. (a) When the local Larmor frequency is fast enough to follow the vector field changes, spin vector adiabatically follows the field direction. (b) When those time scale is comparable, the spin vector precess around the changed field axis with the tilting angle, β.

final tilt angle β of the spin from the z-axis after the field rotation and show the result in Fig. 1(b) as a function of $\eta = \min(\omega_L/\omega_B) = g\mu_B B_0^2/\hbar|\dot{B}_z|$. Here η is a dimensionless measure of the adiabaticity of the field sweep process. We emphasize that β shows a monotonic behavior on η. This means that the tilt angle can be deterministically controlled by the transverse field B_0 or the field sweep rate $\dot{B}_z$, and furthermore, a target spin texture $\beta(x, y)$ in a 2D system can be generated by tailoring the spatial distribution of $\vec{B}_0(x, y)$ for a given field sweep process.

5.3.2 Skyrmion spin texture with a magnetic quadrupole field

Fig. 5.5 illustrates how to imprint a Skyrmion spin texture on a 2D atomic condensate by using a 3D magnetic quadrupole field. The magnetic quadrupole field is given as $\vec{B}(r, z) = \frac{1}{2}B_q r\hat{r} + (B_z - B_q)\hat{z}$ and the zero-field center is

located at $z_0 = B_z/B_q$. By linearly sweeping the uniform bias field B_z, we move the zero-field point through the sample placed on the $z = 0$ plane so that a local spin in the sample experiences a field rotation by π as in the previous example. The local adiabaticity of the field sweep process varies over the sample as $\eta(r) = \mu B_q^2 r^2/4\hbar|\dot{B}_z|$. Ignoring the effects due to the translational motion of atoms and atom-atom interactions, the resultant spatial distribution of the spin direction of the condensate would be

$$\vec{s}(r,\phi) = \cos\beta(r)\hat{z} + \sin\beta(r)(\cos\gamma(r)\hat{r} + \sin\gamma(r)\hat{\phi}), \tag{5.12}$$

where $\beta(r)$ monotonically increases from $\beta(0) = 0$ to $\beta(\infty) = \pi$. $\gamma(r)$ is the azimuthal angle due to the precession accumulated during the field sweep process.

The local spin continuously rotates to the opposite direction from the far-field uniform spin and this is a Skyrmion spin texture. This structure is topologically protected in the $O(3)$ spin space and its topological charge is defined as

$$Q = \frac{1}{4\pi}\int dxdy\ \vec{s}\cdot(\partial_x\vec{s}\times\partial_y\vec{s}) = 1, \tag{5.13}$$

representing the number of times the spin texture encloses the whole spin space. Note that Eq. (13) gives the topological charge is independent of γ.

5.3.3 Experimental results

We have performed the spin texture imprinting experiments with $F = 1$ ^{23}Na condensates. A pancake-shaped, quasi-pure condensate was prepared in a 1064-nm optical dipole trap with trapping frequencies of $\omega_{x,y,z} = 2\pi\times(3.5,\ 4.6,$

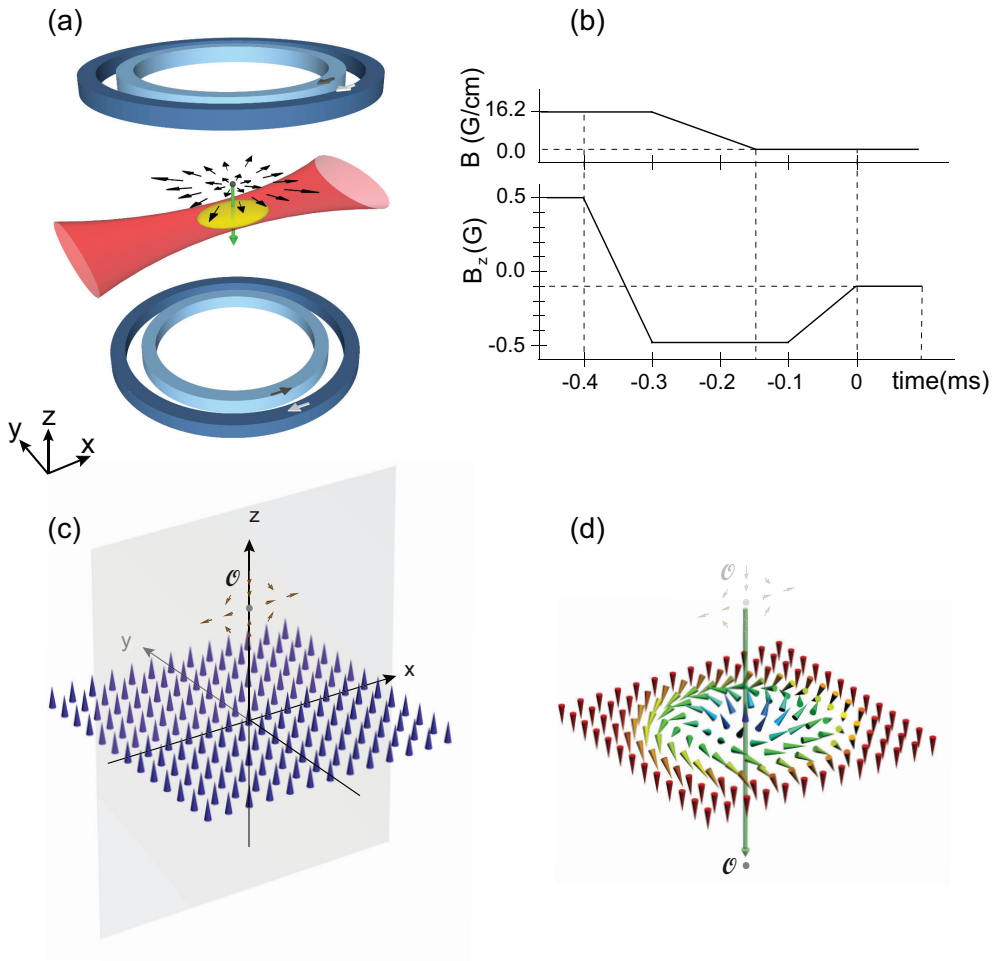

Figure 5.5: Illustration of the creation process of a 2D Skyrmion in a spinor Bose-Einstein condensate. (a) A quasi-2D condensate is prepared in an optical trap and a 3D magnetic quadrupole field is generated from a pair of coils with opposite currents. An additional pair of coils provides a uniform bias field to control the z-position of the zero-field center of the quadrupole filed. (b) Active control of bias field B_z and quadrupole field gradient B_q imprints skyrmion spin texture. (c) As the zero-field point, $\mathcal{O}$, penetrates through the condensate, the atomic spin vector evolves in according to the local magnetic field strength. (d) Skyrmion spin texture configuration without considering precession effect.

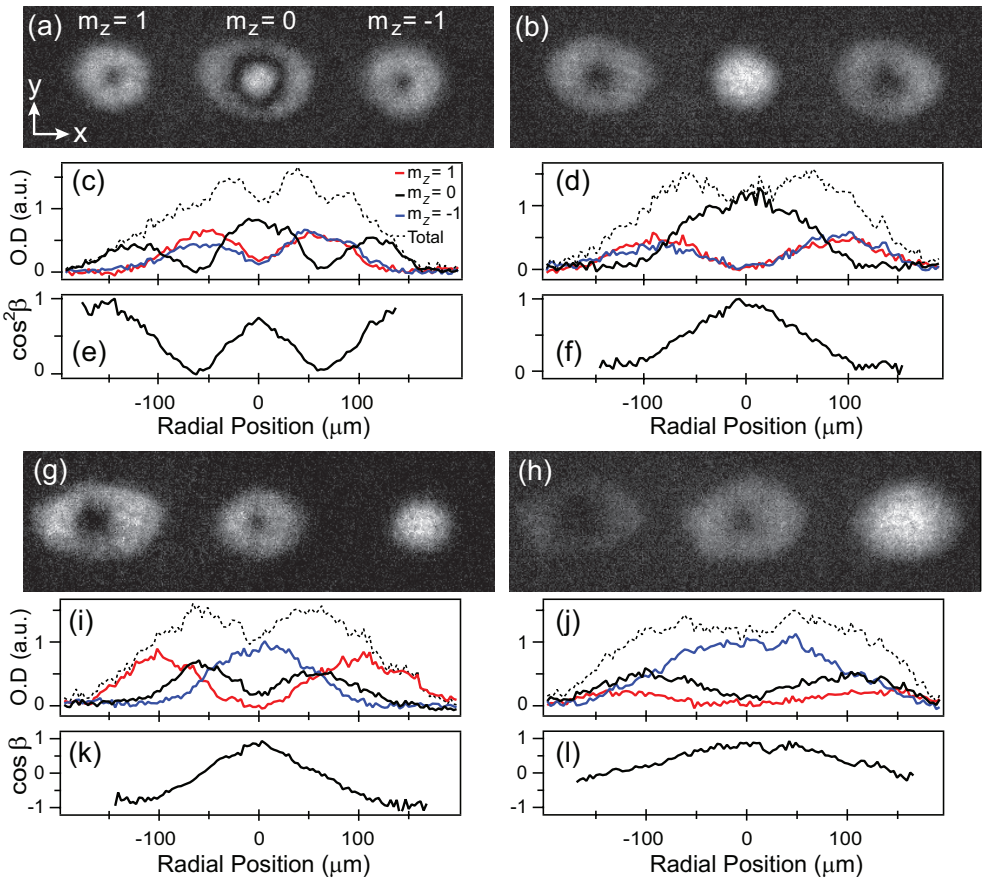

Figure 5.6: Skyrmion spin textures in spin-1 Bose-Einstein condensates. Skyrmion spin textures were imprinted with the field rotation method in trapped condensates that were initially prepared in (a,g) the $|m_z = 0\rangle$ (polar) or (d,j) $|m_z = -1\rangle$ (ferromagnetic) state. Density distributions of the three spin components, measured after a Stern-Gerlach spin separation, represent (a) a 2D Skyrmion, (g) a coreless spin vortex, (d) the Anderson-Toulouse vortex, and (j) the Mermin-Ho vortex. The quadrupole field gradient was $B_q = 14$ G/cm and the field ramp rate was (a) $|\dot{B}_z|$ =10, (d) 46, (g) 10, and (j) 35 G/ms. (b,h,e,k) display the central cuts of the optical densities of the spin components along the x-direction and (c,i,f,l) show the corresponding tilt angle distributions $\beta(x)$ (see text). The field of view in the images is 1.3 mm$\times$ 390 μm.

430) Hz. With a typical atom number of 1.2×10^6, the transverse Thomas-Fermi radii of the trapped condensate are (R_x, R_y)≈(150, 120) μm and the atomic peak density $n = 1.2\times10^{13}$ cm^{-3}. The spin healing length $\xi_s = 2\pi\hbar/\sqrt{2mcn} \approx 40$ μm ($a_2 - a_0 \simeq 5.7a_B$ and a_B is the Bohr radius [34]) is much larger than the thickness of the condensate ≈ 1 μm, so our sample is an effective 2D spin system. The condensate was initially generated in the $|m_F = -1\rangle$ state [35, 36]. For the study of the spin textures of the polar phase, a full population transfer to the $|m_F = 0\rangle$ state was made before applying a spin texture imprinting process, using an adiabatic Landau-Zener RF sweep at a uniform bias field of $B_z = 20$ G, where the quadratic Zeeman shift is about 0.1 MHz.

The magnetic field for the spin texture imprinting is provided by three pairs of coaxial coils: one is for the quadrupole field and the others are for the uniform bias field to the $\pm z$-directions, respectively. The quadrupole field was adiabatically turned on to $B_q = 14$ G/cm in 3.5 ms with $B_z = 2$ G and the the axial bias field was rapidly ramped to $B_z < -1$ G at a variable ramp rate $\dot{B}_z$. Then the quadrupole field was switched off within 150 μs and the bias field was stabilized to $B_z = -500$ mG within 100 μs. The quadrupole field provides an additional, transverse (anti-)trapping potential to atoms in the $|m_z = -1(1)\rangle$ state so it can induce breathing-mode excitations for the field sweep process. To reduce this deleterious effect, we shortened the turn-on time of the quadrupole field as much as possible without losing the adiabaticity of the field change. During the imprinting process, the radial size of the condensate initially prepared in the $|m_z = -1\rangle$ state was observed to change by less than

3% so the mechanical perturbation was negligible.

The density distributions $n_{0,\pm1}$ of the $|m_z = 0, \pm1\rangle$ components were measured by taking an absorption image after the Stern-Gerlach separation. After the field sweep, the optical trap was switched off and a magnetic field gradient was adiabatically applied for 6 ms to spatially separate the spin components in the x-direction. An absorption image was taken using the $|F = 2\rangle \rightarrow |F' = 3\rangle$ cycling transition after pumping the atoms into the $|F = 2\rangle$ state. For a 15-ms time-of-flight the condensate expanded by about 10% in the transverse direction.

In order to characterize the spin textures, we reconstructed the distribution of the tilt angle $\beta(x, y)$ from the measured density distributions using the relations $\cos^2\beta = n_0/(n_1 + n_0 + n_{-1})$ and $\cos\beta = (n_1 - n_{-1})/(n_1 + n_0 + n_{-1})$ for the polar and ferromagnetic phases, respectively [see Eq. (5.9) and (5.10)]. Figure 5.6 displays the typical spin textures observed in the condensates. The tilt angle clearly shows radial symmetry and monotonically increases from the center to the boundary of the condensate as expected. The tilt angle at the sample boundary could be controlled with the field sweep rate and we observed 2D Skyrmions and the coreless spin vortex states with the polar phase, and the Anderson-Toulouse and Mermin-Ho vortex states with the ferromagnetic phase.

5.3.4 Characterization of the imprinting method

The magnetic field sweep was performed very rapidly within a few 100 μs. Since this time scale is too short for the dynamics due to atom-atom interactions to be involved, we expect that the spin tilt angle $\beta(x, y)$ might be fully determined

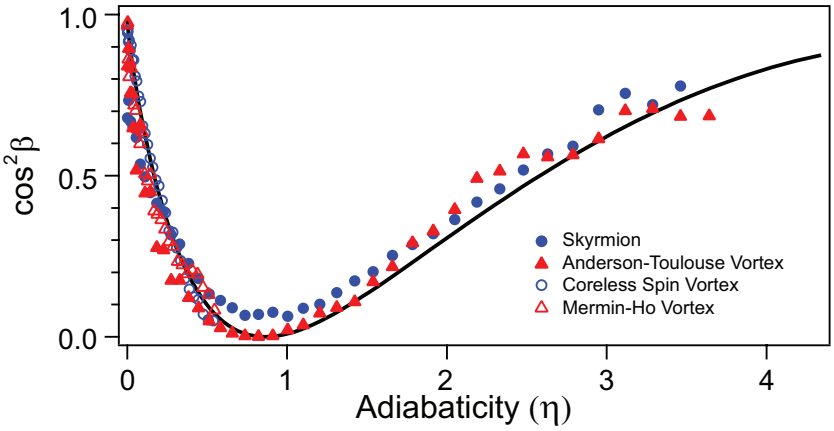

Figure 5.7: Spin tilt angle versus adiabaticity of the field rotation. The data points are obtained from the four different spin textures: 2D Skyrmion (blue solid circle), Anderson-Toulouse vortex (red solid triangle), coreless spin vortex (red open circle) and Mermin-Ho vortex (red open triangle). The solid line is the numerical calculation.

by the local adiabaticity $\eta(x, y)$ of the field rotation, which we found is the case. Figure 5.7 shows $\cos^2\beta(\eta)$ obtained by azimuthally averaging $\cos^2\beta(x, y)$ and $\cos\beta(x, y)$ of the polar and ferromagnetic spin textures, respectively. We estimate the local adiabaticity as $\eta(r) = \mu_B/2B_q^2(\kappa r)^2/4\hbar|\dot{B}_z|$ with $\kappa = 0.9$ to account for the transverse expansion due to the time-of-flight, which is an over-simplification of the expansion dynamics. Remarkably, the data from the four different spin textures, regardless of the phase of the sample, nicely overlap and furthermore, show good quantitative agreement with the numerical calculation for an single spin. This observation clearly demonstrates that with this field rotation method the spin textures are generated in a controllable and deterministic manner. We infer that the expansion dynamics during the time-of-flight does not significantly modify the spin textures in our experimental conditions,

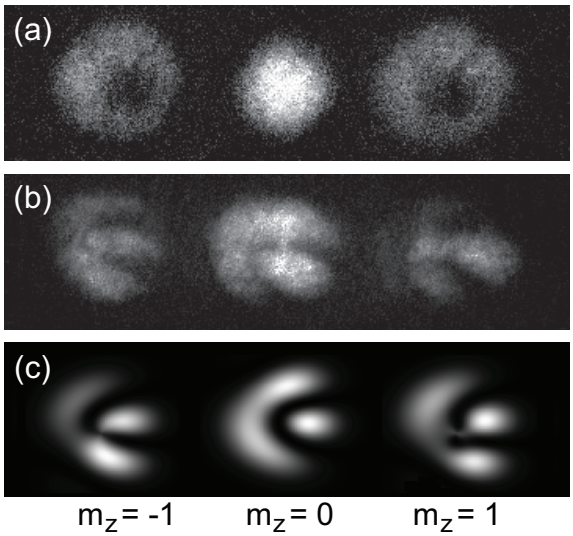

Figure 5.8: Interference of the coreless spin vortex state. (a) Initial density distribution of the three spin components. (b) A RF pulse was applied before a Stern-Gerlach separation and fork-shaped interference fringes appear in the $|m_z = 0\rangle$ atom cloud. (c) Numerical simulation of our experimental condition with the phase winding numbers $(-1, 0, 1)$ for the $|m_z = +1\rangle$, $|0\rangle$, and $|-1\rangle$ components.

assuring that the measured density distributions adequately reveal the in-situ distributions.

The spin winding structure of the spin texture was confirmed from the matter wave interference between the spin components. A 14-μs RF pulse of 430 kHz was applied at B_z=620 mG before turning off the optical trap. The power and duration of the RF pulse were set with a $|m_z = 0\rangle$ condensate to transfer all atoms equally into the $|m_z = \pm 1\rangle$ states. Three-to-one, fork-shaped interference fringe patterns were observed [Fig. 5.8], clearly demonstrating that the relative phase winding between the $|m_z = \pm 1\rangle$ components around the core $|m_z = 0\rangle$ component is 4π [37, 38]. The fork-shaped patterns well coincide

with the numerical simulation which considers residual field gradient in our lab (order of 10 mG/cm) and rf-detuning[3]. Since the total angular momentum of the condensate should be conserved to be zero in the imprinting process [39], the phase winding numbers of the spin components are $(-1, 0, 1)$. The phase winding nature of the other skyrmion spin textures have been confirmed in the previous experiments by measuring the quadrupole oscillation frequencies [4], observing the splitting of a doubly charged vortex core [9].

5.4 Topological Skyrmions

5.4.1 Skyrmions in polar phase

As described in the introduction, even with the same spin texture its topological property can be different. Figure 5.9(a) display a 2D skyrmion spin texture with its boundary condition $\beta(r \to \infty) = \pi$. If the order parameter manifold of the spin vector is S^2, the spin texture can completely warp up the two sphere one time [Fig. 5.9(b)]. The same spin texture, however, cannot cover the SO(3) space which is order parameter manifold of ferromagnetic spinor condensate. In this respect, topologically stable excitation among the four spin textures in Fig. 5.6 is (a), which is imprinted within polar condensate manifold.

[3]See appendix B for the numeric code.

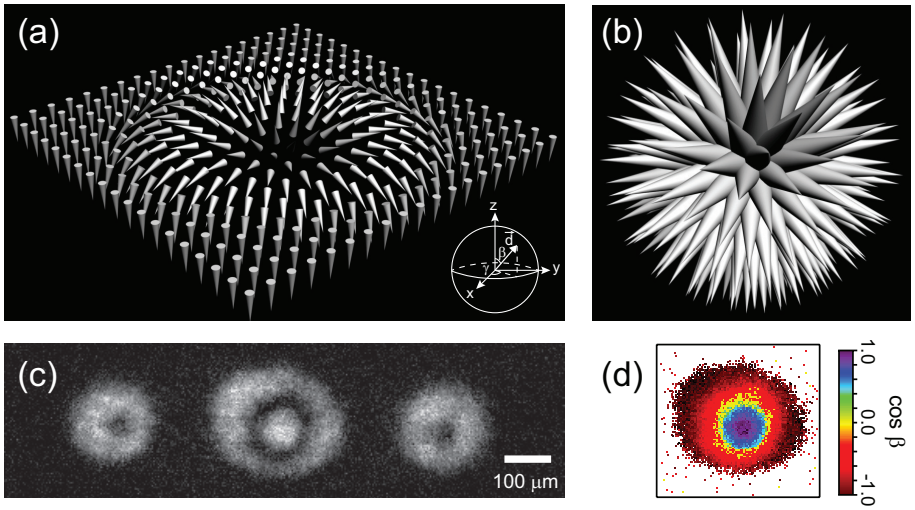

Figure 5.9: (a) Two dimensional skyrmion structure. The cone vector represents nematic vector of the polar condensate and in the inset figure at the bottom is two-sphere. (b) When the spin texture maps into its order parameter manifold S^2, the vectors can completely wrap up the two-sphere. (c) Density distribution of the $|m_z = 0, \pm 1\rangle$ spin components were measured by taking absorption images after a Stern-Gerlach separation. The field ramp rate was $|\dot{B}_z|$ =12 with a quadrupole field gradient B_q =16.2 G/cm. (d) The contour plot shows the distribution of the tilt angle $\beta(x, y)$ in (c).

The three spin components the 2D skyrmion with z-axis symmetry is

$$\zeta_S(r,\phi) = \begin{pmatrix} -\frac{1}{\sqrt{2}} e^{-i(\phi+\gamma)} \sin\beta(r) \\ \cos\beta(r) \\ \frac{1}{\sqrt{2}} e^{i(\phi+\gamma)} \sin\beta(r) \end{pmatrix}, \tag{5.14}$$

with the boundary conditions, $\beta(0) = 0$ and $\beta(\infty) = \pi$, where the spin winding structure is expressed with the opposite phase windings of the $|m_z = 1\rangle$ and $|m_z = -1\rangle$ components. The spinor can be expressed by a unit spin vector $\vec{d}$ parallel to the spin quantization axis, $\zeta = (\frac{-d_x+id_y}{\sqrt{2}}, d_z, \frac{d_x+id_y}{\sqrt{2}})^{\mathrm{T}}$. And this relation gives

$$\vec{d}(r,\phi) = \cos\beta(r)\hat{z} + \sin\beta(r)[\cos\gamma\hat{r} + \sin\gamma\hat{\phi}], \tag{5.15}$$

and the topological index

$$Q = \frac{1}{4\pi} \int dxdy\ \vec{d} \cdot (\partial_x \vec{d} \times \partial_y \vec{d}) = 1, \tag{5.16}$$

representing the number of times the spin texture encloses the whole spin space.

5.4.2 Creation of highly charged Skyrmions

One can envisage the creation of highly charged, i.e. $Q > 1$ Skyrmion spin textures by applying multiple times of the imprinting process to a trapped sample. We explored this possibility with an experimental sequence with two consecutive field sweeps as described in Fig. 5.10. It is important to note that the additional tilt angle β_2 from the second field sweep depends on not only the adiabaticity of the field sweep but also both of the initial tilt angle β_1 and the

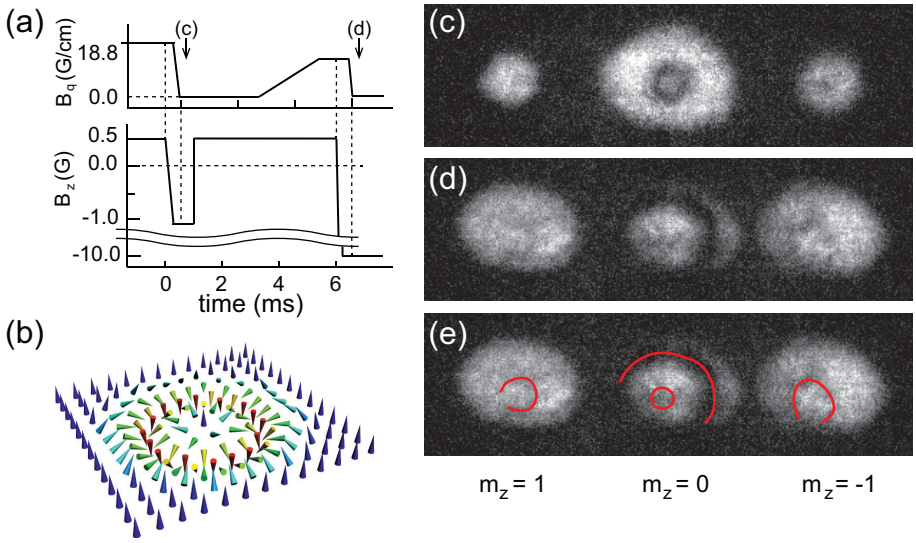

Figure 5.10: Creation of highly charged Skrymions in a spinor condensate. A Skyrmion spin texture with $Q > 1$ is generated by consecutively applying two times of the imprinting process. (a) The control sequence of the magnetic field. (b) 3D illustration of a $Q = 2$ Skyrmion spin texture. (c,d) Absorption images of the spin texture after the first and second field sweep, respectively. A small Skyrmion is generated by the first field sweep and an additional spin bending structure is imprinted at the outer region by the second field sweep.

azimuthal angle γ after the first field sweep. Moreover, γ keeps evolving in the interim between the two field sweeps. Although we know that it is possible to trace the evolution of the spin texture for a short time scale, precise control of the trajectory of the magnetic field would be technically demanding.

Reasoning that the dependence of β_2 on γ decreases when β_1 is close to zero or π, we adopted a more reliable scheme where the ratio of the local adiabaticities of the two field sweeps $\eta_2/\eta_1 \ll 1$ so that the first Skyrmion spin texture would be almost intact for the second field sweep process. In other words, the second field sweep creates an additional spin bending structure in the outer region of the first Skyrmion. Fig. 5.10(a) illustrates the control sequence of the magnetic field. First, we imprinted a Skyrmion spin texture with $B_q =$ 18.8 G/cm and $|\dot{B}_z| = 12$ G/ms $[\eta(R_x) = 7.3]$ in a polar condensate, resulting in a small, but distinguishable density-depletion ring in the $|m_z = 0\rangle$ component [Fig. 5.10(c)]. Within 5 ms, we abruptly changed the field direction and applied the second field sweep with $B_q = 14.0$ G/cm and $|\dot{B}_z| = 40$ G/ms $[\eta(R_x) =$ 1.2]. Fig. 5.10(d) shows the final spin texture where a double ring structure is observed, albeit having low visibility, in all the spin components, indicating $Q > 1$.

5.4.3 Dynamical evolution of the Skyrmion

Stability and dynamics of spin texture is one of the key issues in the study of Skyrmions [11, 26, 40, 41]. In order to study the stability of the 2D Skyrmion, we measured the time evolution of the 2D Skyrmion with a variable dwell time

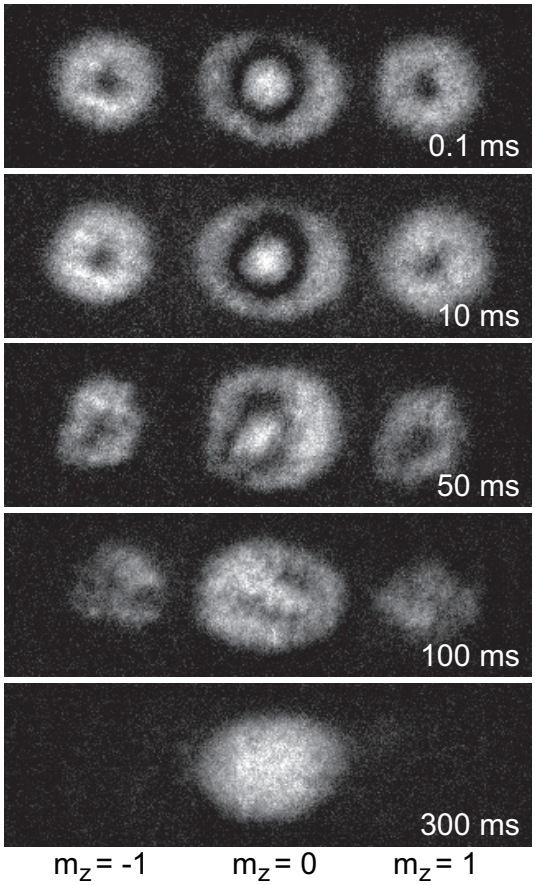

Figure 5.11: Deformation and decaying of the 2D Skyrmion in a harmonic potential. The time evolution of the spin texture was measured with a variable dwell time in an optical trap. For this data, $|\dot{B}_z|$ =20 G/ms and B_q =16.2 G/cm. The field of view is 1.0 mm$\times$ 330 μm.

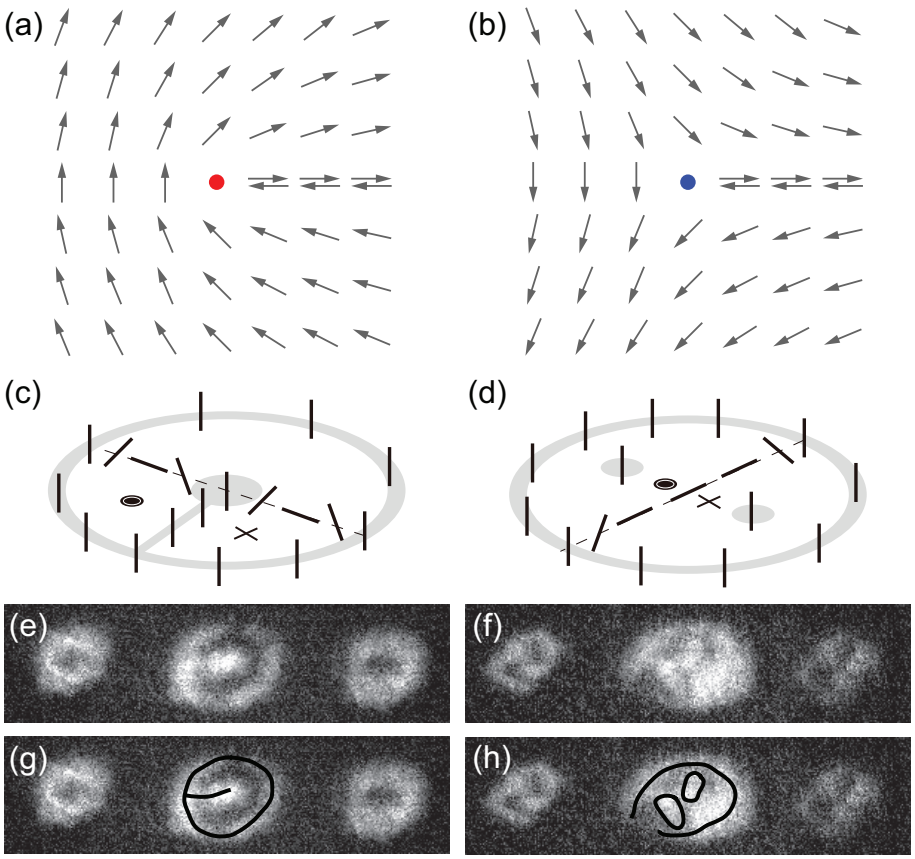

Figure 5.12: Spin vector configuration of half-quantum vortices lying in the x-y plane with (a) positive charge and (b) negative charge. Dynamic formation of a pair of half-quantum vortices. (c,d) The line segments represent the axis of the spin vector $\vec{d}$ and the grey area indicates the region where the $|m_z = 0\rangle$ component mainly occupies. The non-polar cores of the half-quantum vortices are marked by $\odot$ and $\times$, implying opposite windings of the superfluid phase. (e,f) Examples of the dynamic evolution of the 2D Skyrmion spin texture, displaying density profiles similar to those in (c) and (d). (g,h) Same as (e,f) with guidelines for the peak density regions in the $|m_z = 0\rangle$ atom cloud.

t in the optical trap and found that the Skyrmion spin texture dynamically deforms and decays to an uniform spin texture [Fig. 5.11]. Modulation of the ring structure gradually developed and scrambled the whole spin texture over 100 ms. Eventually, the spin texture became uniform $|m_z = 0\rangle$ state at $t > 300$ ms. The upper bound of the condensate temperature < 65 nK and we estimate that the thermal dissipation is negligible in our experiments. Indeed, the spin relaxation time of a $|m_z = \pm 1\rangle$ equal mixture was measured to be over 5 s at $B_z = 100$ mG, indicating that the decaying of the Skyrmion to an uniform spin texture is dynamically driven. We expect that the ellipticity of the transverse trapping potential ($\omega_y \sim 1.2\,\omega_x$) might enhance the dynamical instability of the Skyrmion.

In the deformation process, the $|m_z = \pm 1\rangle$ components seemed to keep occupying the $|m_z = 0\rangle$ density-depleted region without developing noticeable local spin polarization $n_1 - n_{-1}$, suggesting that the polar phase might be maintained in the condensate. However, it is topologically impossible for the Skyrmion to decay to a uniform spin texture with preserving the polar phase unless the Skrymion expands in a finite-sized sample [41], which is not the case in our experiments. Therefore, non-polar defects must have developed in the condensates during the time evolution, expected from the quadratic Zeeman effects as well as the induced spin currents [13].

Interesting observation is that the core $|m_z = 0\rangle$ component could be connected to the outer component or divided into two parts in the time evolution as described in Fig. 5.12. Because of the symmetry of the order parameter of

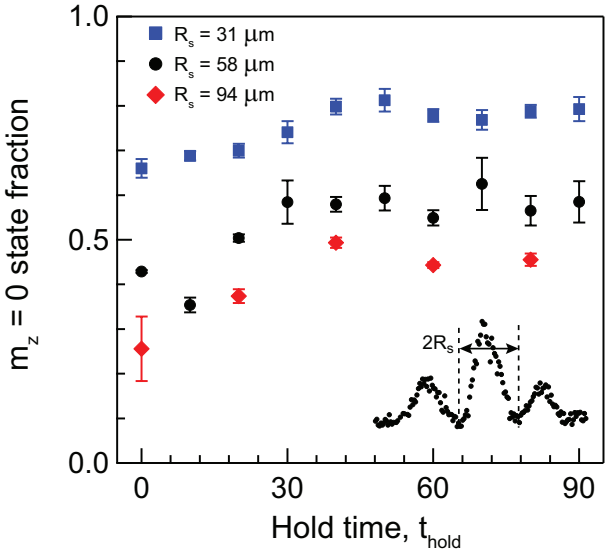

Figure 5.13: Temporal evolution of a number fraction in $m_z = 0$ state under a 500 mG of constant magnetic field at various skyrmion core size. Inset figure at the bottom represents optical density distributions of the $m_z = 0$ state measured by taking absorption imaging after Stern-Gerlach separation.

the polar BEC under $(\vec{d}, \vartheta) \rightarrow (-\vec{d}, \vartheta + \pi)$, the two regions with a π disclination in $\vec{d}$ can be continuously connected via a π change of the superfluid phase. This observation suggests possible formation of half-quantum vortices around non-polar local defects in the decaying process [Fig. 5.12]. A similar situation has been studied with a point defect in a polar 3D BEC, where the 't Hooft-Polyakov monopole continuously deforms to a half-quantum vortex ring (Alice ring) [12].

5.5 Discussion

Despite the interesting observation of decay dynamics, physical mechanism for the decay process is not well understood. In this section, we present several experiments for studying the spin texture decay dynamics and introduce our opinions that might explain the results. Since the Skyrmion excitation has a spin bending energy, one can expect that the observations are relaxation dynamics and the decay time would depend on the core size of the Skyrmion[4]. Figure 5.13 represents temporal evolution of n_0 ($m_z = 0$ state population) with various core size. The results show similar increasing rate of the n_0 for all different spin textures, which suggests that the spin bending energy could not fully explain our observation.

Studying dynamical evolution of simple spin texture could be helpful to understand the Skyrmion decay. When a uniform spin texture (nematic vector point along the x-direction) was prepared under a constant magnetic field, we observed sudden increase of n_0 at 30 ms of hold time and cocentric ring structures were developed in all three spin components as the time evolved [Fig. 5.14]. Such spontaneous pattern formations in spinor Bose gases are already studied in $F = 2$ ^{87}Rb condensates [42, 43], where the modulation instability from quadratic Zeeman energy leads to the spin domains. However, the time scale at which n_0 starts to increase was 10 times faster than theoretical predictions.

The rapidly emerged spin domains might be attributed from thermal

[4]We defined the Skyrmion core size R_s that satisfies $\cos\beta(R_s) = 0$.

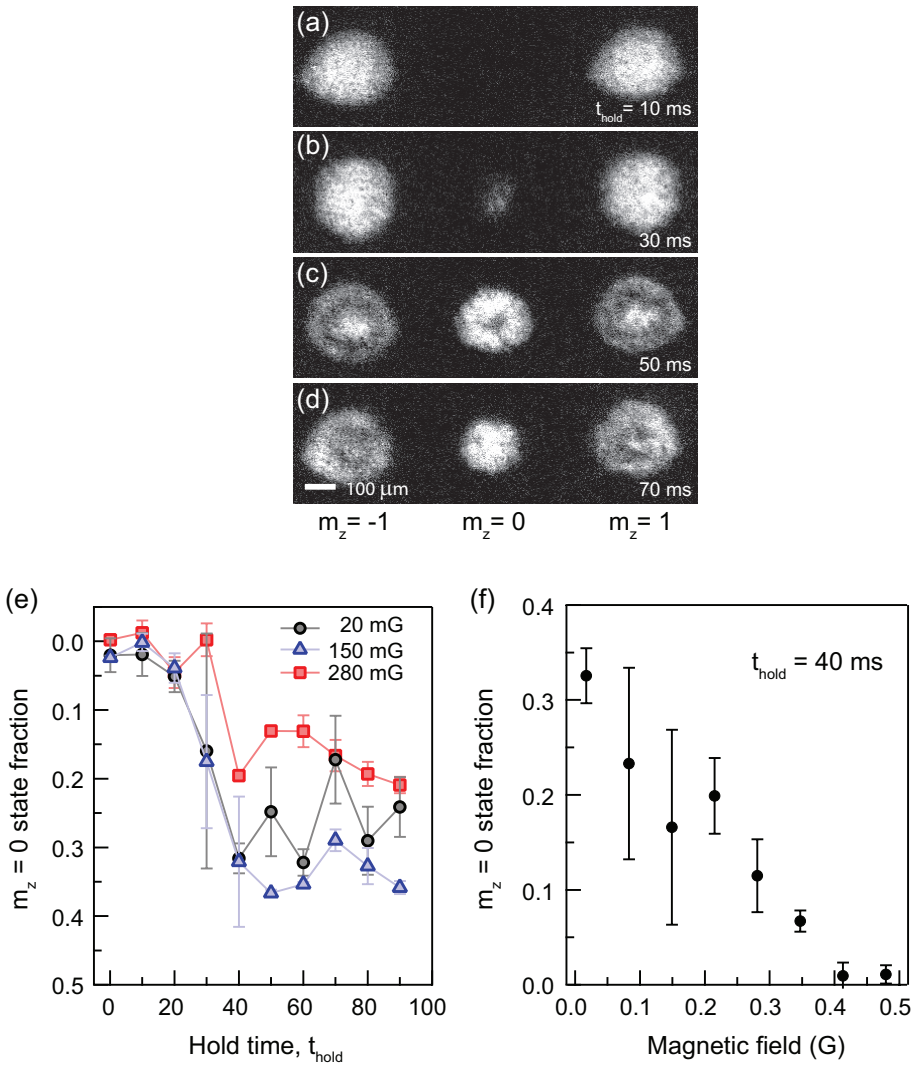

Figure 5.14: Spin texture dynamics in the antiferromangetic spinor condensates (a)-(d) The uniform spin texture are deformed under a 150 mG of constant magnetic field. (e) $m_z = 0$ state population is investigated under various hold time at different magnetic field. (f) At constant hold time, $t_{\rm hold}$= 40 ms, number population in $m_z = 0$ state is displayed at different magnetic field.

phase fluctuations in the quasi-2D sample which could enhance unstable modes and accelerate the formation of spin domain. Another scenario that might explain our result is a counterflow instability [44] caused by the residual field gradient in our lab. A recent study points out that unstable mode can arises when a relative counterflow V_R between the $m_z = 1$ and $m_z = -1$ state is comparable to a sound velocity. Notable prediction is that the instability in the $m_z = \pm 1$ state is triggered by isotropic density modulations in the $m_z = 0$ state for anti-ferromagnetic spinor condensates, which is similar to our observation. We expect that under a well-controlled field gradient and non-destructive measurement of magnetization [45] of spinor gas could study the mysterious spin texture dynamics more clearly.

Bibliography

[1] K. W. Madison, F. Chevy, F. Wohlleben, and J. Dalibard, Phys. Rev.Lett. **84**, 2498 (2000).

[2] M. R. Mattews, B. P. Anderson, P. C. Haljan, D. S. Hall, C. E. Wieman, and E. A. Cornell, Phys. Rev. Lett. **83**, 2498 (1999).

[3] M. F. Andersen, C, Ryu, P. Cladè, V. Natarajan, A. Vaziri, K. Helmerson, and W. D. Phillips, Phys. Rev. Lett. **97**, 170406 (2006).

[4] A. E. Leanhardt, A. Görlitz, A. P. Chikkatur, D. Kielpinski, Y. Shin. D. E. Pritchard, and W. Ketterle, Phys. Rev. Lett. **89**, 190403 (2002).

[5] V. Bretin, P. Rosenbusch, F. Chevy, G. V. Shlyapnikov, and J. Dalibard, Phys. Rev. Lett. **90**, 100403 (2003).

[6] I. Coddington, P. Engels, V. Schweikhard, and E. A. Cornell, Phys. Rev. Lett. **91**, 100402 (2003).

[7] T. W. Neely, E. C. Samson, A. S. Bradley, M. J. Davis, and B. P. Anderson, Phys. Rev. Lett. **104**, 160401 (2010).

[8] D. V. Freilich, D. M. Bianchi, A. M. Kaufman, T. K. Langin, and D. S. Hall, Science **329**, 1182 (2010).

[9] Y. Shin, M. Saba, M. Vengalattore, T. A. Pasquini, C. Sanner, A. E. Leanhardt, M. Prentiss, D. E. Pritchard, and W. Ketterle, Phys. Rev. Lett. **93**, 160406 (2004).

[10] U. Leonhardt and G. E. Volovik, JETP Letters **72**, 46 (2000).

[11] U. A. Khawaja, and H. Stoof, Nature **411**, 918 (2001).

[12] J. Ruostekoski and J. R. Anglin, Phys. Rev. Lett. **91**, 190402 (2003).

[13] Y. Kawaguchi, M. Nitta, and M. Ueda, Phys. Rev. Lett. **100**, 180403 (2008).

[14] V. Pietilä, and M. Möttönen, Phys. Rev. Lett. **103**, 030401(2009).

[15] T. A. Skyrme, Nucl. Phys. **31**, 556 (1962).

[16] P. W. Anderson and G. Toulouse, Phys. Rev. Lett. **38**, 508 (1977).

[17] A. Schmeller, J. P. Eisenstein, L. N. Pfeiffer, and K. W. West, Phys. Rev. Lett. **75**, 4290 (1995)

[18] D C. Wright and N. D. Mermin, Rev. Mod. Phys. **61**, 385 (1989).

[19] A. Neubauer, C. Pfleiderer, B. Binz, A. Rosch, R. Ritz, P. G. Niklowitz, and P. Böni, Phys. Rev. Lett. **102**, 186602 (2009).

[20] X. Z. Yu, Y. Onose, N. Kanazawa, J. H. Park, J. H. Han,Y. Matsui, N. Nagaosa, and Y. Tokura, Nature **465**, 901 (2010).

[21] S. Heinz, K. Bergmann, M. Menzel, J. Brede, A. Kubetzka, R. Wiesendanger, G. Bihlmayer, and S. Blügel, Nat. Phys. **7**, 713 (2011).

[22] A. E. Leanhardt, Y. Shin, D. Kielpinski, D. E. Pritchard, and W. Ketterle, Phys. Rev. Lett. **90**, 140403 (2003).

[23] L. S. Leslie, A. Hansen, K. C. Wright, B. M. Deutsch, and N. P. Bigelow, Phys. Rev. Lett. **103**, 250401 (2009).

[24] N. D. Mermin, and T. L. Ho, Phys. Rev. Lett. **36**, 594 (1976).

[25] P. W. Anderson, and G. Toulouse, Phys. Rev. Lett. **38**, 508(1977).

[26] C. M. Savage and J. Ruostekoski, Phys. Rev. Lett. **91**, 010403 (2002).

[27] M. Nakahara, *Geometry, Topology and Physics* (Institude of Physics publishing, Bristol and Philadelphia, 2003).

[28] M. Ueda and Y. Kawaguchi, Phys. Rep. **520**, 253 (2012).

[29] D. M. Stamper-Kurn, M. Ueda, Rev. Mod. phys. **85**, 1191 (2013).

[30] T. -L. Ho, Phys. Rev. Lett. **81**, 742 (1998).

[31] J. Stenger, S. Inouye, D. M. Stamper-Kurn, H. -J. Miesner, A. P. Chikkatur, and W. Ketterle, Nature **396**, 345 (1998).

[32] M. S. Chang C. D. Hamley, M. D. Barrett, J. A. Sauer, K. M. Fortier, W. Zhang, L. You, and M. S. Chapman, Phys. Rev. Lett. **92**, 140403 (2004).

[33] S. Mukerjee, C. Xu, and J. E. Moore, Phys. Rev. Lett. **97**, 120406 (2006).

[34] J. P. Burke, C. H. Greene, and J. L. Bohn, Phys. Rev. Lett. **81**, 3355 (1998).

[35] M. S. Heo, J. Choi, and Y. Shin, Phys. Rev. A **83**, 013622 (2011).

[36] J. Choi, M. S. Heo, and Y. Shin, J. Korean Phys. Soc. **59**, 211 (2011).

[37] F. Chevy, K. W. Madison, V. Bretin, and J. Dalibard, Phys. Rev. A **64**, 031601(R) (2001).

[38] S. Inouye S. Gupta, T. Rosenband, A. P. Chikkatur, A. Görlitz, T. L. Gustavson, A. E. Leanhardt, D. E. Pritchard, and W. Ketterle, Phys. Rev. Lett. **87**, 080402 (2001).

[39] M. V. Berry, Proc. R. Soc. Lond. A **392**, 1802 (1984).

[40] R. A. Battye, N. R. Cooper and P M. Sutcliffe, Phys. Rev. Lett. **88**, 080401 (2002).

[41] H. Zhai, W. Q. Chen, Z. Xu, and L. Chang, Phys. Rev. A **68**, 043602 (2003).

[42] M. Scherer, B. Lucke, G. Gebreyesus, O. Topic, F. Deuretzbacher, W. Ertmer, L. Santos, J. J. Arlt, and C. Klempt, Phys. Rev. Lett. **105**, 135302 (2010).

[43] J. Kronjäger, C. Becker, P. Soltan-Panahi, K. Bongs, and K. Sengstock, Phys. Rev. Lett. **105**, 135302 (2010).

[44] K. Fujimoto and M. Tsubota, Phys. Rev. A **85**, 033642 (2012).

[45] J. M. Higbie, L. E. Sadler, S. Inouye, A. P. Chikkatur, S. R. Leslie, K. L. Moore, V. Savalli, and D. M. Stamper-Kurn, Phys. Rev. Lett. **95**, 050401 (2005).

Chapter 6

Geometric Hall effect with a Skyrmion spin texture

When a particle carrying a spin slowly moves in a spatially varying magnetic field, and its spin adiabatically follows the field direction, the particle acquires a quantum-mechanical phase known as the Berry phase [1]. This phase originates from the geometrical properties of the parameter space of the system and in the Hamiltonian description, it can be represented as a gauge potential [2]. Just like the vector potential for a charged particle, the gauge potential generates forces from its spatial and temporal variations [3], and the geometric forces act like magnetic and electric forces on the spin-carrying particle.

The emergent electromagnetism of this spin origin have lead to novel spin transport phenomena. In magnetic materials, because of the coupling of a spin current to magnetization, a non-coplanar spin texture of magnetization gives

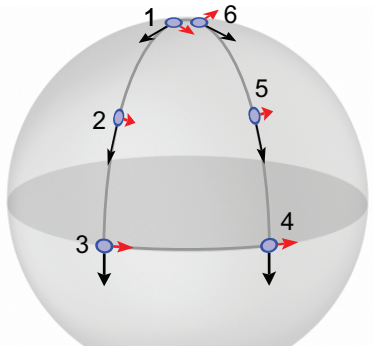

Figure 6.1: Intuitive picture of geometric phase during the parallel transport of a vector [9]. The vectors on each point of surface stay tangential to the curved sphere and keep its direction as parallel as possible to its pointing vector at each infinitesimal step. After the vectors coming back to their initial position (north pole), the final state requires additional rotation compare to the initial state. The additional rotation is purely geometrical property that proportional to the solid angle of curved surface (90° for this example).

rise to an effective internal magnetic field, leading to the intrinsic anomalous Hall effect [4, 5]. Recently, the topological Hall effects were observed in chiral magnets with skyrmion lattice spin textures [6–8]. Since the Berry phase is proportional to the spin value, effective electromagnetic forces are intrinsically spin-dependent and thus, they have been actively investigated for spintronics applications [10–12].

One of the frontiers in the current quantum gas research is experimental realization of artificial gauge fields for neutral atoms. In recent experiments with ultracold neutral atoms, artificial magnetic and electric fields were synthesized using atom-light interaction [13, 14], presenting a new opportunity for exploring quantum many-body phenomena in gauge fields. This experimental technique is based on the gauge field from a pseudo-spin texture of light-dressed atoms [15].

Despite the versatile application of light-induced gauge potential, the technique suffers from atom loss or heating associated with spontaneous scattering of light and thus new direction would be using atomic species that has extremely low scattering rate or synthesizing gauge field without the laser light [16]. This chapter describes gauge field from real spin texture generated by a magnetic quadrupole field and experimental observation of a geometric Hall effect in a spin-polarized atomic Bose-Einstein condensate, where a rigid spin texture of skyrmion configuration is imposed by a spatially varying external magnetic field. We investigate the condensate dynamics under translational oscillations of the spin texture and observe that a circular motion of the condensate is resonantly induced from the translational drive. This directly manifests the existence of the effective Lorentz force acting on the condensate. Furthermore, we observe that quantized vortices are dynamically nucleated in the circulating condensate, which we attribute to the inhomogeneity of the effective magnetic field.

- Yong-il Shin and Jae-yoon Choi. *"Gauge potential for neutral atoms in a magnetic quadrupole field"* Journal of the Korean Physical Society **63**, 951 (2013).

- Jae-yoon Choi, Sang Won Seo, and Yong-il Shin. *"Observation of a Geometric Hall effect in a Spinor Bose-Einstein Condensate with a Skyrmion Spin Texture"* Physical Review Letters **111**, 245301 (2013).

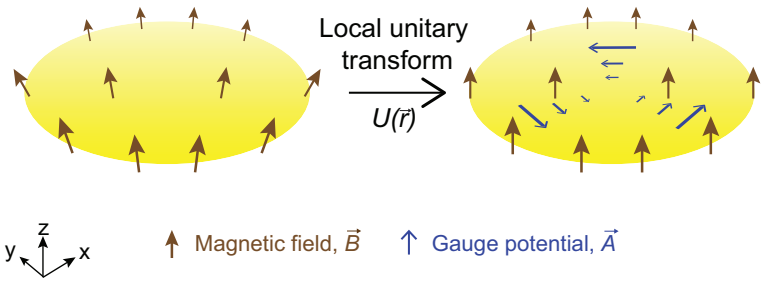

Figure 6.2: Under a local unitary transformation $U(\mathbf{r})$, the system in a spatially varying magnetic field is mapped to an effective system where the magnetic field direction is uniform, introducing a gauge potential $\mathbf{A} = -iU\nabla U^{\dagger}$

6.1 Gauge potential in a magnetic quadrupole field

Consider a neutral atom of mass m with hyperfine spin F is moving in real magnetic field $\mathbf{B}(\mathbf{r}, t)$, which is non-uniform and time dependent. The Hamiltonian of the system is given by

$$H = \frac{\mathbf{p}^2}{2m} + g_L \mu_B \mathbf{F} \cdot \mathbf{B}, \tag{6.1}$$

where g_L is Landé g-factor, μ_B is Bohr magneton and $\mathbf{F} = (F_x, F_y, F_z)$ hyperfine spin operator with its quantization axis to be $+z$ direction,

$$\frac{F_x}{\hbar} = \frac{1}{\sqrt{2}} \begin{pmatrix} 0 & 1 & 0 \\ 1 & 0 & 1 \\ 0 & 1 & 0 \end{pmatrix}, \frac{F_y}{\hbar} = \frac{i}{\sqrt{2}} \begin{pmatrix} 0 & -1 & 0 \\ 1 & 0 & -1 \\ 0 & 1 & 0 \end{pmatrix}, \frac{F_z}{\hbar} = \begin{pmatrix} 1 & 0 & 0 \\ 0 & 0 & 0 \\ 0 & 0 & -1 \end{pmatrix}. \tag{6.2}$$

The gauge potential can be derived by taking a local unitary transform of the Hamiltonian [17] by unitary matrix U that rotates the local magnetization

direction $\hat{b} = \mathbf{B}/|\mathbf{B}|$ to the reference z-axis (Fig 6.2). The local transformation satisfies $U(\hat{b}\cdot\mathbf{F})U^\dagger = F_z$ with $U = \exp(-i\beta\hat{n}\cdot\mathbf{F})$, where β is tilting angle from $\hat{b}$ to z-axis and $\hat{n} = (\hat{b}\times\hat{z}/|\hat{b}\times\hat{z}|)$.

From the unitary transformation, we can express the Hamiltonian in the $|\phi_m\rangle = U|\Psi\rangle$ basis

$$\begin{aligned} i\hbar\frac{\partial}{\partial t}|\Psi\rangle &= H|\Psi\rangle \\ i\hbar\frac{\partial}{\partial t}|\phi_m\rangle &= (UHU^\dagger - i\hbar U\partial_t U^\dagger)|\phi_m\rangle \\ &= H'|\phi_m\rangle \\ &= \left(\frac{1}{2m}(\mathbf{p}+\hbar\mathbf{A})^2 - \hbar V + g_L\mu_B F_z|\mathbf{B}|\right)|\phi_m\rangle, \end{aligned} \tag{6.3}$$

where $\mathbf{A}(\mathbf{r},t) = -iU\nabla U^\dagger$ and $V(\mathbf{r},t) = iU\partial_t U^\dagger$. The effective vector potential $\mathbf{A}(\mathbf{r},t)$ arises due to the non-coplanar spin structure and additional scalar potential $V(\mathbf{r},t)$ comes from time-varying spin texture. In analogous electro-magnetic potential, we can define the gauge potentials $\mathfrak{A}_\mu = -iU\partial_\mu U^\dagger$[1] or $\mathfrak{A} = (V, A_x, A_y, A_z)$.

When the rotation axis $\hat{n} = \sin\alpha\hat{x} - \cos\alpha\hat{y}$, the local transform matrix is represented as

$$\begin{aligned} U &= \exp(-i\beta\hat{n}\cdot\mathbf{F}) \\ &= \begin{pmatrix} \cos^2\frac{\beta}{2} & -\frac{\sin\beta}{\sqrt{2}}e^{-i\alpha} & \cos^2\frac{\beta}{2}e^{-i2\alpha} \\ -\frac{\sin\beta}{\sqrt{2}}e^{i\alpha} & \cos\beta & -\frac{\sin\beta}{\sqrt{2}}e^{-i\alpha} \\ \sin^2\frac{\beta}{2}e^{i2\alpha} & -\frac{\sin\beta}{\sqrt{2}}e^{i\alpha} & \cos^2\frac{\beta}{2} \end{pmatrix}. \end{aligned} \tag{6.4}$$

[1]The covariant derivative is defined by $\partial_\mu = (-\frac{\partial}{\partial t}, \nabla)$.

After some algebra, we can explicitly write the effective gauge potential as $\mathbf{A} = \mathbf{A_x}F_x + \mathbf{A_y}F_y + \mathbf{A_z}F_z$, where

$$\begin{aligned} \mathbf{A_x} &= \cos\alpha \sin\beta \ \partial_\mu\alpha + \sin\alpha \ \partial_\mu\beta, \\ \mathbf{A_y} &= \sin\alpha \sin\beta \ \partial_\mu\alpha - \cos\alpha \ \partial_\mu\beta, \\ \mathbf{A_z} &= (1-\cos\beta) \ \partial_\mu\alpha. \end{aligned} \tag{6.5}$$

Note that the component of the gauge potential $\mathbf{A}$ does not commute each other and represents an example of a non-Abelian gauge potential. In the adiabatic condition, no spin flip transition, the off-diagonal components of the transformed Hamiltonian can be ignored so the gauge potential is $\mathbf{A}_{\rm ad} = m_F(1-\cos\beta)\nabla\alpha$ and $V_{\rm ad} = -m_F(1-\cos\beta)\partial_t\alpha$.

The effective gauge field is also defined by electromagnetic field tensor $\mathfrak{F}_{lm} = \partial_l\mathfrak{A}_m - \partial_m\mathfrak{A}_l$ and can be represented by the local field direction $\hat{b}$,

$$\mathbf{E}_i^e = -\hbar\partial_i V - \hbar\partial_t A_i = -m_F\hbar\hat{b}\cdot(\partial_t\hat{b}\times\partial_t\hat{b}), \tag{6.6}$$

$$\mathbf{B}_i^e = -\hbar\epsilon^{ijk}(\partial_j A_k - \partial_k A_j) = -m_F\frac{\hbar}{2}\epsilon^{ijk}\hat{b}\cdot(\partial_j\hat{b}\times\partial_i\hat{b}). \tag{6.7}$$

Remark that the geometric force, $\mathbf{F}^e = \mathbf{E}^e + \mathbf{v}\times\mathbf{B}^e$, can simulate the Lorentz force to a neutral particle with velocity $\mathbf{v}$, so Hall effects could be studied in atomic superfluid system.

The additional term $\hbar$ in the gauge field can be understood by considering the Hamiltonian H_B for a charged particle in real magnetic field $\mathbf{B}^r$. It reads $H_B = \frac{1}{2m}(\mathbf{p} - q\mathbf{A}_B)^2$, where q is the electric charge, $\mathbf{A}_B$ is vector potential with $\mathbf{B}^r = \nabla\times\mathbf{A}_B$. Comparing the gauge potential of neutral atom, $\mathbf{A}_B = -\frac{\hbar}{q}\mathbf{A}_{\rm ad}$

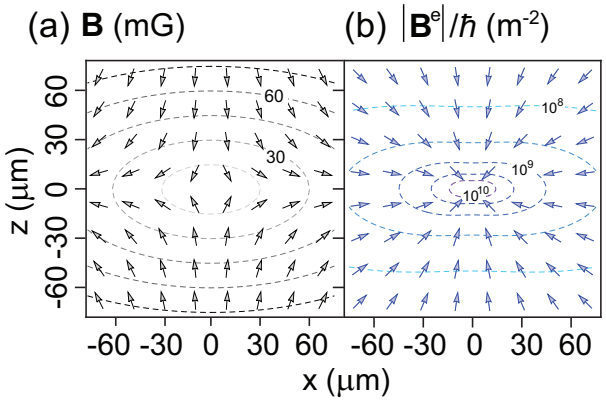

Figure 6.3: (a) magnetic field distribution in the x-z plane with the quadrupole field strength is 10 G/cm. Dashed lines arrow symbol represent contour line of the magnetic field and field direction respectively. (b) Effective magnetic field $\mathbf{B}^e$ for the atom in the m_F=1 state.

so the moving atoms would experience force by the effective magnetic field $\mathbf{B}^e = -\hbar\nabla \times \mathbf{A}_{\rm ad}$.

A magnetic quadrupole field has a zero-field center and since the Zeeman energy is degenerated at the point, the field distribution can generate finite Berry curvature. Interestingly, the gauge field shows magnetic monopole structure and we describe the result as follows. When we have a quadrupole field with axial field gradient B_q,

$$\mathbf{B}(x, y, z) = \frac{B_q}{2}(x\hat{x} + y\hat{y} - 2z\hat{z}), \tag{6.8}$$

the two angles describing the magnetic field direction $\hat{b}$ at $\mathbf{r} = (x, y, z)$ are

$$\alpha = \tan^{-1}(\frac{y}{x}) = \phi, \tag{6.9}$$

$$\beta = \tan^{-1}(\frac{\sqrt{x^2 + y^2}}{2z}), \tag{6.10}$$

where ϕ is polar direction in the x-y plane. From Eqs. (6.7), the gauge potential

and effective magnetic field for an atom are

$$\mathbf{A}_{\mathrm{ad}} = m_F \frac{1+\cos\beta}{r\sin\beta}\hat{\phi}, \tag{6.11}$$

$$\mathbf{B}^e = -m_F \frac{2\hbar}{R^{3/2}}\mathbf{r}, \tag{6.12}$$

where $R = \sqrt{x^2+y^2+4z^2}$. We can associate the effective magnetic field with a fictitious monopole with a flux of $\Phi_B = \oint \mathbf{B}^e \cdot d\sigma = -2m_F h$. Figure 6.3(b) displays the gauge field generated by magnetic quadrupole field in the x-z plane.

Now we can give the physical explanation of the phase engineered vortex state [18, 19] both in polar and ferromagnetic phase of spinor condensate by the magnetic monopole. As the singular point penetrates the condensate, the wave function have to obtain phase winding proportional to the monopole flux if spin adiabaticity is preserved. Recent proposal [20] about vortex pumping with quadrupole and hexapole magnetic field also shares the same underlying principle.

The mass flows in a cordless vortex state in oblate condensate Ψ_c can be also understood as a response of superfluid velocity to the monopole field. Let us consider a situation where, for example, a condensate is initially prepared in the $|m_z = -1\rangle$ state with $B_q = 0$ and $B_z > 0$. The initial order parameter is described by $\Psi = \sqrt{n(r)}e^{i\phi}(0,0,1)^T$, where $n(r)$ is the superfluid density. As the zero-field point moves from $z = +\infty$ to z_0, the local atomic spin adaptively follows the rotating magnetic field. Then, the final order parameter Ψ_c is given

by

$$\Psi_c = \sqrt{n(r)}e^{i\phi}\begin{pmatrix} \sin^2\frac{\beta}{2}e^{-i2\theta} \\ -\frac{\sin\beta}{\sqrt{2}}e^{-i\theta} \\ \cos^2\frac{\beta}{2} \end{pmatrix}. \tag{6.13}$$

This description shows that the by applying the quadrupole field, the atom initially populated in the $|m_z = -1\rangle$ state are transferred to the $|m_z = 0, 1\rangle$ states which have orbital angular momentum $-\hbar$ and $-2\hbar$, respectively. Then the total angular momentum of the state is

$$\begin{aligned} L_z &= \int [-\hbar n_0(r) - 2\hbar n_1(r)] 2\pi r dr \\ &= -2\hbar \int n(r) \sin^2\frac{\beta}{2} 2\pi r dr, \end{aligned} \tag{6.14}$$

where $n_0, 1$ are the densities of the $m_z = 1, 0$ components.

This expression is identical to the angular momentum estimated from the superfluid velocity for the $|m_F = -1\rangle$ state

$$L_z = \int n(r)\hat{z} \cdot [\mathbf{r} \times m\mathbf{v}_s(r)] 2\pi r dr. \tag{6.15}$$

Here, the superfluid velocity $\mathbf{v}_s$ under the gauge field could be obtained from the kinetic momentum of the atom, $\mathbf{\Pi} = \mathbf{p} + \hbar\mathbf{A}$,

$$\mathbf{v}_s = \frac{\hbar}{m}(\nabla\phi + \mathbf{A}_{\rm ad}) = \frac{\hbar}{m}(1 + \cos\beta)\hat{\theta}. \tag{6.16}$$

Note that because of the gauge potential the quantization condition for the superfluid circulation is expressed as

$$\oint (\mathbf{v}_s - \frac{\hbar}{m}\mathbf{A}_{\rm ad}) \cdot d\mathbf{l} = \frac{\hbar}{m} q_v. \tag{6.17}$$

6.2 Vortex ground state under the monopole gauge field

Quantized vortices are the characteristic response of a superfluid system to a rotation, which are typically observed with their density depletion cores [21, 22]. The Hamiltonian for a particle in a reference frame rotating with angular velocity $\omega = \omega\hat{z}$ is given by

$$\begin{aligned} H_R &= \frac{\mathbf{p}^2}{2m} - \omega \cdot \mathbf{L} \\ &= \frac{1}{2m}(\mathbf{p} - m\omega \times \mathbf{r})^2 - \frac{1}{2}m\omega^2 r^2, \end{aligned} \tag{6.18}$$

which shows that a gauge field can be considered as an effective rotation of $\omega = \frac{\hbar}{2m}\mathbf{B}^e$. Since the strength of gauge field at the trap center, $B_0^e = 1/4z_m^2$, dramatically increases as the $z_m \to 0$, vortex state can be a ground state of the spinor condensate because of the external rotation by the gauge field.

For a condensate trapped in a three dimensional harmonic condensate, the critical frequency ω_c for nucleating a single vortex is estimated to be [23]

$$\omega_c = \frac{5\hbar}{2mR^2} \ln \frac{0.67R}{\xi}, \tag{6.19}$$

where R is the Tomas-Fermi radius and ξ is the healing length of the condensate or the vortex core radius. When $\omega > \omega_c$, the energy of the vortex state in the rotating frame is lower than that of the non-vortex state. One can simply expect that a vortex state would be preferred when $B_0^e/2m > \omega_c$, which is studied in Ref. [24]. However, since the monopole field has spatial inhomogeneity, the

energetic argument based on the rotating frame does not work and critical condition has to be modified by considering the inhomogeneous effective field.

The critical condition under the monopole gauge field can be estimated by considering kinetic energy of the coreless vortex state Ψ_c and vortex state Ψ_v which is written as $\Psi_v = \Psi_c \times \sqrt{s(r)}e^{i\theta}$, where $s(r)$ represents density profile of depletion core in an infinite system. The superfluid velocity for each state is given by

$$\mathbf{v}_{s,c}(r) = \frac{\hbar}{m}\mathbf{A}_{\rm ad} = \frac{\hbar}{mr}(1+\cos\beta(r))\hat{\theta}, \tag{6.20}$$

$$\mathbf{v}_{s,v}(r) = \frac{\hbar}{m}(\mathbf{A}_{\rm ad} + \frac{\hat{\theta}}{r}) = \frac{\hbar}{mr}\cos\beta(r)\hat{\theta}. \tag{6.21}$$

In the hydrodynamic regime, $\xi \ll R$, the energy difference of the vortex states is

$$\Delta E = \pi n(0)\frac{\hbar^2}{m}\ln\frac{1.46b}{\xi} + \int_b^R \frac{mn(r)}{2}[\mathbf{v}_{s,v}^2 - \mathbf{v}_{s,c}^2]2\pi r dr \ , \tag{6.22}$$

where the first term comes from density variation in the center region $r < b$ ($\xi \ll b \ll R$) [25] caused by the singly quantized vortex and second term is kinetic energy difference in the outer region $r > b$. In a Tomas-Fermi approximation, the atomic density is given by the trapping potential, $n(r) = n(0)[1 - r^2/R^2]$ and the integral becomes

$$\frac{m\Delta E}{\pi\hbar^2 n(0)} \approx \ln\frac{1.46b}{\xi} + \int_b^R (1-\frac{r^2}{R^2})\frac{4z_m - \sqrt{r^2+4z_m^2}}{r\sqrt{r^2+4z_m^2}}dr \tag{6.23}$$

$$\approx \ln\frac{2.41R}{\xi} - \frac{2}{t^2}(\sqrt{1+t^2}-1) + 2\ln\frac{2}{1+\sqrt{1+t^2}} \ , \tag{6.24}$$

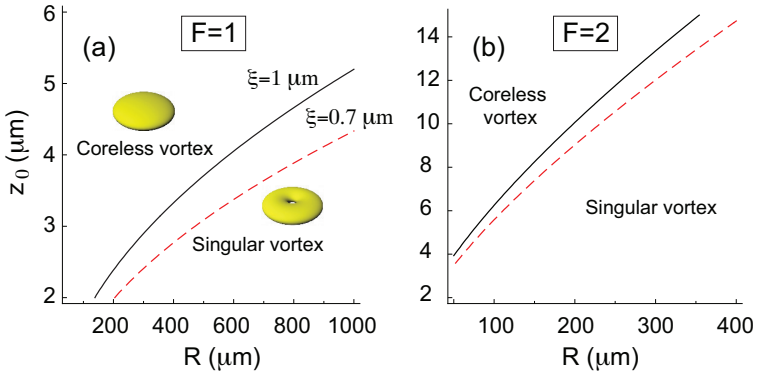

Figure 6.4: Phase boundary of the quantized-vortex ground state of a quasi-2D spinor condensate of (a) hyperfine spin $F = 1$ and (b) $F = 2$ in a magnetic quadrupole field. R is the radius of the condensate and ξ is the healing length, representing the characteristic size of the vortex core.

where t is tilting angle at the condensate boundary $\tan\beta(R) = R/2z_m$ and high orders in b/R are neglected.

In Figure 6.4, we display the critical curve of $\Delta E = 0$ in the $z_m - R$ plane, showing the existence of a large-t region where the quantized vortex state becomes energetically favored over the coreless vortex state. However, it seems to be experimentally demanding to fulfill the condition. For example, for $R = 100$ μm, the zero-field point of the quadrupole field needs to be placed less than a few μm away from the condensate. This requires tight confinement of the condensate along the z-direction as well as extremely stable control of the magnetic field.

6.3 Geometric Hall effect in a spinor BEC

The Hall effect is one example of novel transport phenomena of electron system under a magnetic field. This section describes our experimental approaches to observe a Hall effect of the gauge field origin. Our experiment does not involve laser light to generate gauge field and thus enable to study superfluid dynamics in a gauge field in a more dissipation free condition [26, 27].

The Hall effect is the emergent motion caused by the Lorentz force in perpendicular direction to an external magnetic field and electric current. Usually quantum gases are confined in a harmonic potential and the effect of artificial magnetic field could be studied by a dipole motion of condensates. When the sample undergoes harmonic oscillation with velocity $\mathbf{v}_d$ in x-direction under a uniform gauge field in z-direction, the oscillation axis of dipole motion would rotate because the geometric Lorentz force $\mathbf{F}_L = q\mathbf{v}_d \times \mathbf{B}^e$ induces y-directional motion[2]. Since the additional y-motion of the condensate has the same physical origin of the Hall effect, we call the motion a *geometric Hall effect*.

In our experimental condition, however, the cyclotron frequency $\omega_c = \frac{|\mathbf{B}^e|}{m} \leq \frac{\hbar}{4mz_m^2}$ is three orders of magnitude smaller than the trap frequency ω_r, implying that it would be experimentally challenging to directly detect the Lorentz force by examining an atom's motion. However, the effective Lorentz force can be amplified through resonant behavior of the system because the trapping frequencies for x and y directions are same.

[2]This is analogues to the Puco's pendulum, where the earth's rotation precesses the axis of harmonic motion.

A schematic diagram of the experimental setup is shown in Fig. 6.5. The quasi-two dimensional optical is formed by focusing a 1064 nm laser beam which is described in the Chapter 4. The optical trap is coaxially aligned with the zero-field center of magnetic quadrupole field and trapping potential for sodium atom in the polarized state $|F = 1, m_F = -1\rangle$ state can be expressed as

$$\begin{aligned} V_t(x,y,z) &= \frac{m}{2}(\omega_x^2 x^2 + \omega_y^2 y^2 + \omega_z^2 z^2) \\ &\quad + g_L \mu_B B_q \sqrt{\frac{(x-x_m)^2 + y^2}{4} + (z-z_m)^2} + mgz \ , \end{aligned} \tag{6.25}$$

where m, $g_L = 1/2$, μ_B, m, B_q and g are atomic mass of sodium, Landé-g factor, Bohr magneton, axial field gradient and gravitational acceleration, respectively. The harmonic trap frequencies of the hybrid potential in radial direction are approximated to be $\omega_{r_x,r_y} = \sqrt{\omega_{(x,y)}^2 + \frac{g_L \mu_B B_q}{4 m z_m}}$ near the trap center. Since radial force from the magnetic field is much stronger than the optical force, $\omega_{r_x} \simeq \omega_{r_y}$ within 0.4% and we can approximation $\omega_{r_x,r_y} \simeq \sqrt{\frac{g_L \mu_B B_q}{4 m z_m}}$.

When an atom slowly moves in the magnetic quadrupole field, it feels an effective Loretnz force $\mathbf{F}_B = \mathbf{v} \times \mathbf{B}^e$ and an effective electric force $\mathbf{F}_E = -\mathbf{v}_m \times \mathbf{B}^e$, where $\mathbf{v} = \frac{d\mathbf{r}}{dt}$ is the atom's velocity and $\mathbf{v}_m = \frac{d\mathbf{r}_m}{dt}$ is the velocity of the zero-field center of the magnetic quadrupole field. The temporal variation of the spin texture generates an effective electric field $\mathbf{E}^e = -\dot{\mathbf{r}}_m \times \mathbf{B}^e$ [Eq. (6.6)], perpendicular to the driving direction $\hat{x}$. This field can be understood as an induced electric field from the moving magnetic monopole with velocity $\mathbf{v}_m = \dot{\mathbf{r}}_m$ [Fig. 6.5(c)]. Including the restoring force from the hybrid trap, the equation of

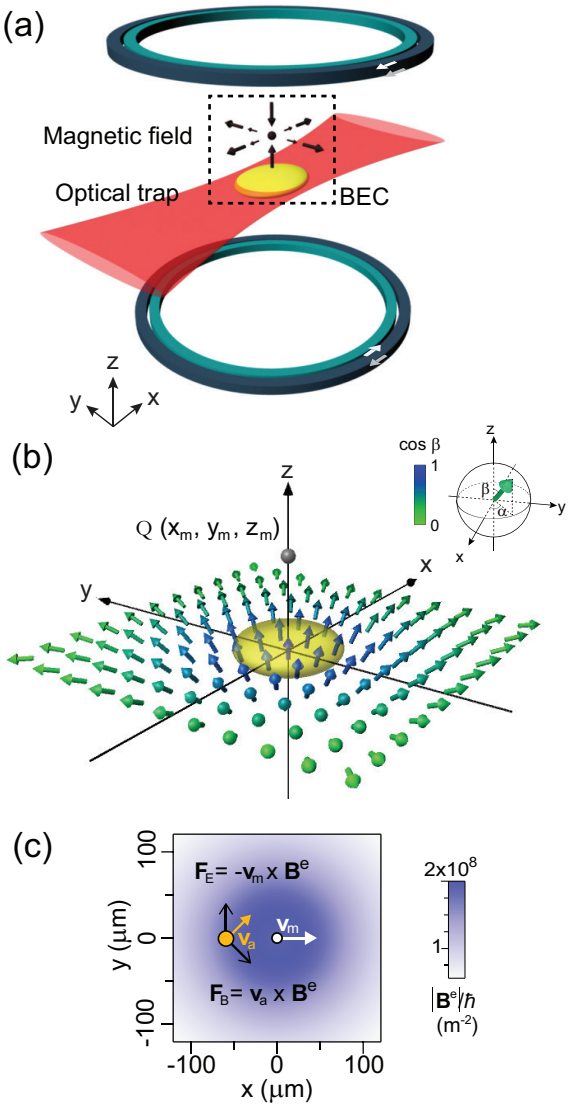

Figure 6.5: Schematic diagram of experimental setup for observing geometric Hall effect. (a) A pancake shape condensate (yellow ellipsoid) is prepared in an optical dipole trap and a 3D magnetic quadrupole field is generated from a pair of coils with opposite currents. An additional pairs of coils provide uniform bias field to control the x and z position of zero-field center of the magnetic field. (b) Magnetic field configuration of the condensate in x-y plane. The zero-field center is indicated by a point $\mathcal{Q}$ and tilting angle is represented by color scale. (c) When the atom and the zero-field center move with velocities $\mathbf{v}_a$ and $\mathbf{v}_m$, respectively, an effectively Lorentz force $\mathbf{F}_B = \mathbf{v}_a \times \mathbf{B}^e$ and an effective electric force $\mathbf{F}_E = -\mathbf{v}_m \times \mathbf{B}^e$ occur on the atom.

motion for the atom in the $z = 0$ plane is given as

$$\begin{aligned} m\frac{d^2\mathbf{r}_\perp}{dt^2} &= -m\omega_r^2(\mathbf{r}-\mathbf{r}_m)_\perp + (\mathbf{F}_B+\mathbf{F}_E)_\perp \qquad (6.26)\\ &= -m\omega_r^2(\mathbf{r}-\mathbf{r}_m)_\perp + (\frac{d\mathbf{r}}{dt}-\frac{d\mathbf{r}_m}{dt})_\perp \times \mathbf{B}_z^e\hat{z}\ , \end{aligned}$$

where $\mathbf{r}_\perp = (x, y)$, the subscript $\perp$ denotes vectors in $x - y$ plane and B_z^e is effective magnetic field[3] in z direction.

We assume no z-directional motion of the atom and the zero-field center. In the reference frame fixed to the spin texture, i.e with the coordinate transformation of $\mathbf{r}' = \mathbf{r} - \mathbf{r}_m$,

$$\begin{aligned} m\frac{d^2\mathbf{r}'_\perp}{dt^2} &= m\frac{d^2}{dt^2}(\mathbf{r}-\mathbf{r}_m)_\perp \qquad (6.27)\\ &= -m\omega_r^2(\mathbf{r}-\mathbf{r}_m)_\perp + (\frac{d\mathbf{r}}{dt}-\frac{d\mathbf{r}_m}{dt})_\perp \times \mathbf{B}_z^e\hat{z} - m\frac{d^2\mathbf{r}_m}{dt^2}|_\perp\ . \qquad (6.28) \end{aligned}$$

Finally, for the spin-texture oscillation with $\mathbf{r}_m = (X_m \sin\omega_m t, 0, z_m)$, we have

$$m\frac{d^2\mathbf{r}'_\perp}{dt^2} = -m\omega_r^2\mathbf{r}'_\perp + \frac{d\mathbf{r}'_\perp}{dt}\times\mathbf{B}^e\hat{z} + m\omega_m^2 X_m \sin(\omega_m t)\hat{x}. \qquad (6.29)$$

In Fig 6.6, single-particle trajectories from Eq. (6.28) are displayed for $z_m = 36\ \mu$m, $\omega_r = 2\pi \times 40.3$ Hz, $X_m = 1.9\ \mu$m, and various driving frequencies ω_m. Fig 6.6(f)-(j) show the numerical results where we refine the restoring force term in Eq. 28 with that from the magnetic trapping potential $2m\omega_r z_m^2\sqrt{1+\frac{r^2}{2z_m^2}}$. The anharmonicity of the magnetic trapping potential lowers the effective trapping frequency as the oscillation amplitude increases. When $\omega_m = \omega_r$ in Eq. (6.28), the x-directional amplitude linearly increases

[3] $B_z^e(r'_\perp) = \frac{2\hbar z_m}{(r'^2_\perp + 4z_m^2)^{3/2}}$.

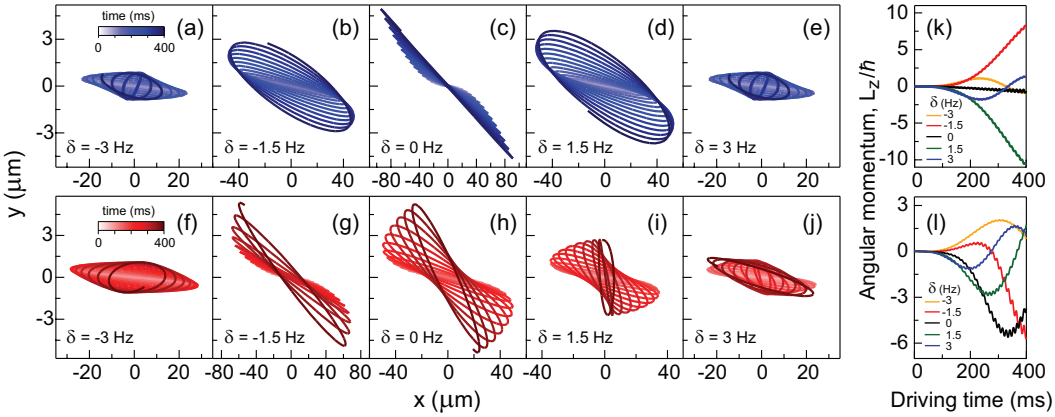

Figure 6.6: Single-particle trajectory under the spin-texture oscillation. (a)-(e) Numerical results obtained from Eq. (6.28) for $z_m = 36$ μm, $\omega_r = 2\pi \times 40.3$ Hz, $X_m = 1.9$ μm, and various detunings of the driving frequency $\delta = (\omega_m - \omega_r)/2\pi$. (f)-(j) Numerical result taking into account the anharmonicity of the magnetic trapping potential. (k) and (l) show the temporal evolution of the angular momentum of the particle with respect to the trap center for (a)-(e) and (f)-(j) respectively.

as $\frac{\omega_r X_m}{2} t$, leading to a quadratic amplification of the y-directional motion as $\frac{\omega_c \omega_r X_m}{8m} t^2$. For $\omega_c/\omega_r \sim 10^{-3}$, the y-directional amplitude is expected to become comparable to the modulation amplitude X_m within 0.5 s [Fig. 6.6].

6.3.1 Sample preparation

Sample preparation is started by evaporation cooling of thermal gas by rf-induced spin flip transition in plugged quadrupole trap and we obtain 1.5×10^7 of $T \sim 1$ μK thermal gases. To avoid perturbation from optical plug laser, we transfer the thermal gases into a potential consist of the magnetic quadrupole field and quasi-two dimensional optical potential. Atoms are confined in the plane of optical sheet potential because the strength axial field gradient 7.6 G/cm below

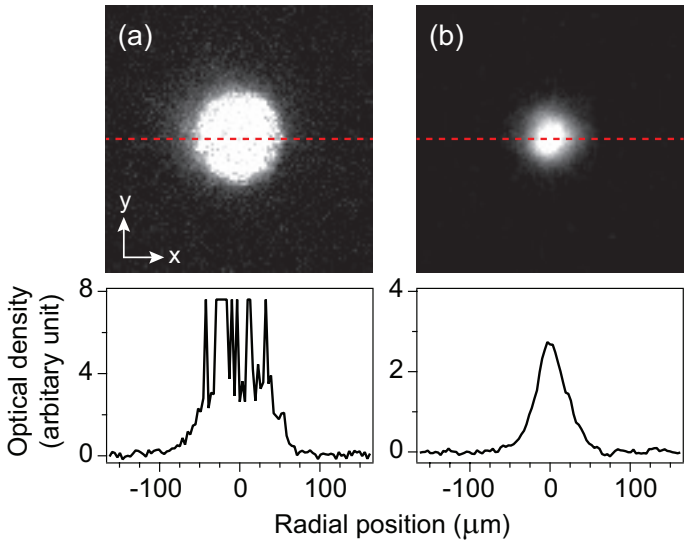

Figure 6.7: In trap absorption images (a) without the $F = 1$ resonant pulse beam and (b) after the 100 μs pulse beam. The density distributions along the red dashed lines are displayed at the bottom. The resonant pulse beam reduces the peak optical density of the sample less than 5, and we determine the center position of the condensate through a 2D Gaussian fit to the image (b).

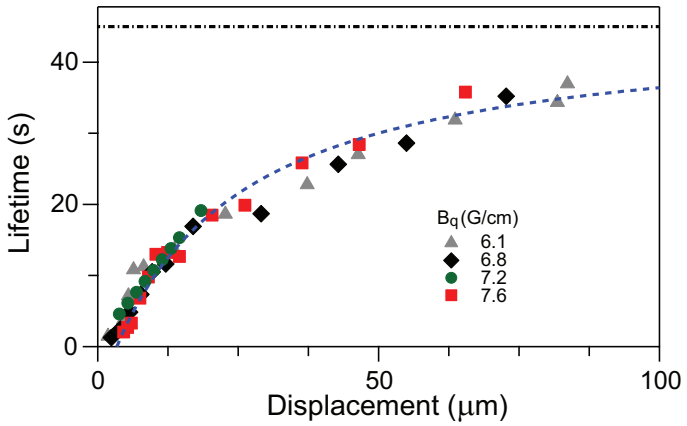

Figure 6.8: Lifetime of the atom number trapped in the hybrid potential as a function of the displacement z_m at various axial field gradient. Dashed-dot line is the lifetime of the condensate (τ_0=45.4 s) confined in the optical trap only. Dashed line is the curve fit $(\tau_0 + \frac{a}{b-z_m})$ to the data of $B_q = 7.6$ G/cm (red square).

gravitational force 8.1 G/cm. The magnetic levitation effect is weaker than the gravitational force, allowing evaporation cooling of the sample by reducing the trap depth of the optical dipole trap. The experiments are carried out with pure condensates of $2 \sim 3 \times 10^6$ atoms.

Time evolution of condensate center is studied from in-trap absorption imaging using the $|F = 1, m_F = -1\rangle \rightarrow |F' = 2, m_{F'} = -2\rangle$ transition (Fig. 6.7). By applying 100 μs of the resonant pulse beam, the optical density at the trap center does not exceeds 5 and we can measure the center position within 1 μm by 2D gaussian fit to the image.

The field stability is about 1 mG, which is estimated by loss rate of the condensate in the hybrid potential. It shows $1/z_m$ dependence due to the flicker noise ($1/f$ noise) of magnetic field [Fig. 6.8] and atoms can be lost by absorbing

rf-photon from the technical noise [28]. The $z_m = 0$ position is inferred from the maximal loss rate with 2 μm error. Under the experimental accuracy, the measured center positions from in-trap images are highly reproducible within our imaging resolution 5 μm.

6.3.2 Emergence of Hall motion

We study a Hall response of the system under translational oscillations of the spin texture, $\mathbf{r}_m(t) = X_m \sin \omega_m t \, \hat{x}$, which is driven by sinusoidal modulation of the external bias field B_x. When we start with an atom at rest, the atom will undergo forced oscillations along the x direction and its transverse motion will be induced by the effective Lorentz force [Fig. 6.6].

We investigate the center-of-mass motion of the condensate by taking its in-situ absorption images for various driving times t_m and $X_m \approx 2$ μm. The condensate position was determined from a 2D Gaussian fit to the images. Figure 6.9 (a)-(d) display the temporal evolutions of the displacement of the condensate from its initial position for various driving frequencies ω_m near the resonance. The initial increasing rate of the x-directional amplitude is measured to be about 2.3×10^{-4} m/s, which is close to the estimated value of $\frac{\omega_r X_m}{2} = 2.5\times 10^{-4}$ m/s, and discernible y-directional motion appears after a few 100 ms. In the peak response at $\omega_m = 2\pi \times 39.2$ Hz, we observe that a circular motion with almost zero ellipticity develops for $t_m > 600$ ms [Fig. 6.9(e)]. The radius of the trajectory is about 30 μm, corresponding to external angular momentum $L_z \approx -80\hbar$ per atom. Figure 6.10 is the condensate trajectory at $\omega_m = 2\pi \times 39.2$ Hz

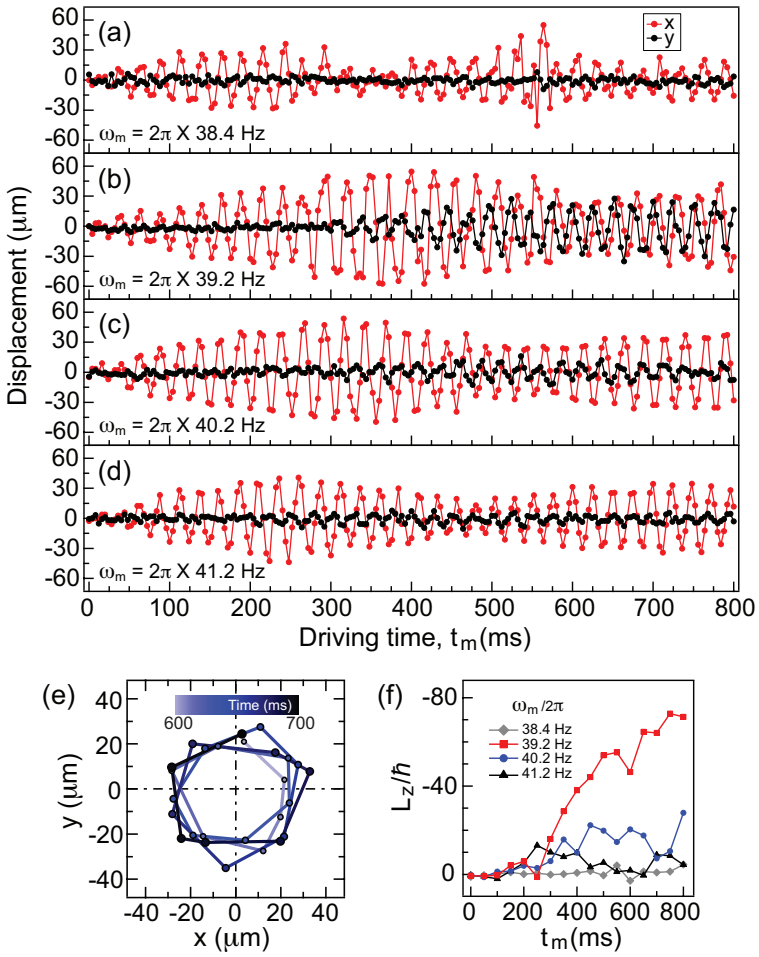

Figure 6.9: (a)-(d) Temporal evolution of the condensate position under translational oscillations of the skyrmion spin texture for various driving frequencies ω_m. The condensate position was measured for every 4 ms and each data point was obtained from a single measurement. (e) Trajectory of the condensate position in the x-y plane for $\omega_m/2\pi = 39.2$ Hz. (f) Temporal evolution of the external angular momentum L_z of the condensate. The condensate velocity was determined from the position data and L_z is displayed with 50-ms binning.

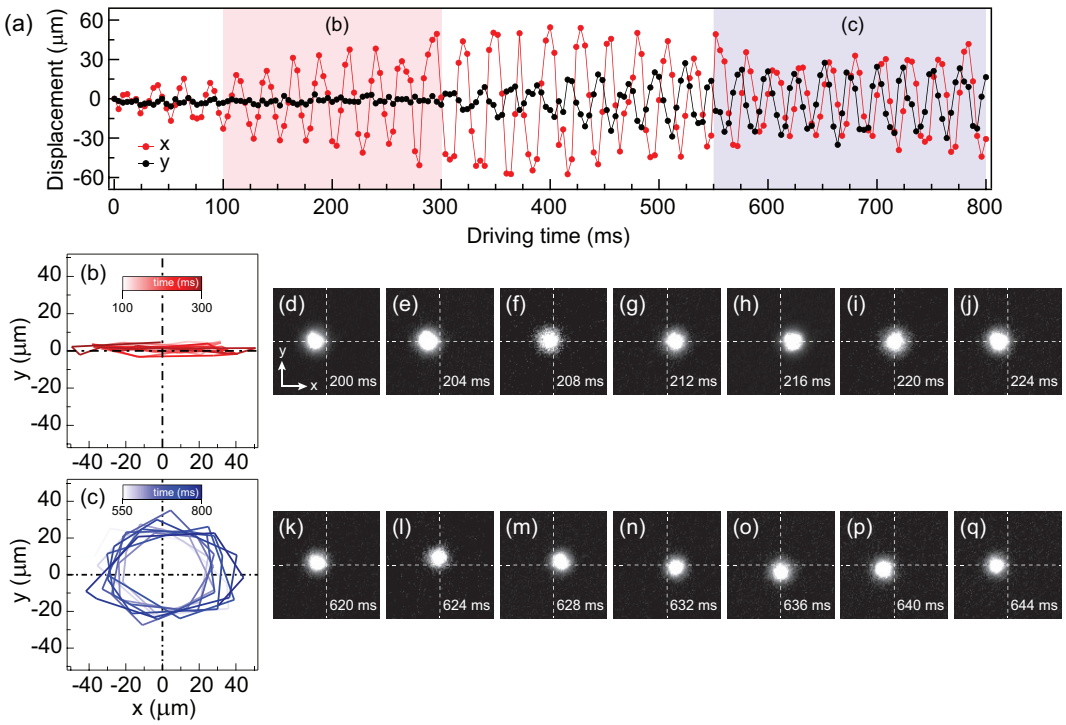

Figure 6.10: Temporal evolution of the condensate position under the spin-texture oscillation. (a) the same data in Fig. 6.9(b) with $\omega_m = 2\pi \times 39.2$ Hz. Trajectory of the condensate in the $x-y$ plane for (b) dirving time $t_m = 100 \sim 300$ ms [red zone in (a)] and (c) $t_m = 500 \sim 800$ ms [blue zone in (a)]. The initial linear motion evolves into a circular motion. (d)-(j) and (k)-(q) show in-trap images of the condensate for one oscillation period in (b) and (c), respectively. The field of view in the images is 300 μm×300 μm.

and it clearly demonstrate two different phases of condensate motion. In the first phase, its dipole motions were amplified because of the external driving and circular motion were appeared due to the presence of gauge force.

The circulation direction of the condensate is observed to be always clockwise, giving negative L_z [Fig. 6.9(f)]. Numerical simulation of the single-particle dynamics predicts circulation in the opposite direction for large negative detuning of the driving frequency, $(\omega_m - \omega_r)/2\pi < -1$ Hz [Fig. 6.6]. However, in our experiment for $\omega_m < 2\pi \times 38.5$ Hz, there is no detectable y-directional motion and even the development of x-directional oscillation seems to be strongly suppressed [Fig. 6.9(a)].

Full accounting for the condensate dynamics requires a superfluid hydrodynamics description including the interplay between the spin texture and the internal mass current [29, 30]. The superfluid velocity $\mathbf{v}_s$ is required to satisfy the Mermin-Ho relation $\nabla \times \mathbf{v}_s = -\mathbf{B}^e/m$ in the gauge field [24], and therefore the condensate has always an internal rotational motion. Note that the initial state of the condensate is a coreless vortex state with $\mathbf{v}_s = \frac{\hbar}{m}\mathbf{A}$ due to the skyrmion spin texture [31–33]. We speculate that the external circulation of the condensate might be rectified by its internal rotational motion.

Recently, the dynamics of a spinor condensate with a skyrmion spin texture was theoretically investigated [34–36]. In the study of a rigid spin texture case [36], it was shown that the spin texture can precesses around the center of the condensate and its precession direction is determined by the chirality of the spin texture. In terms of the relative motion between the rigid spin texture and

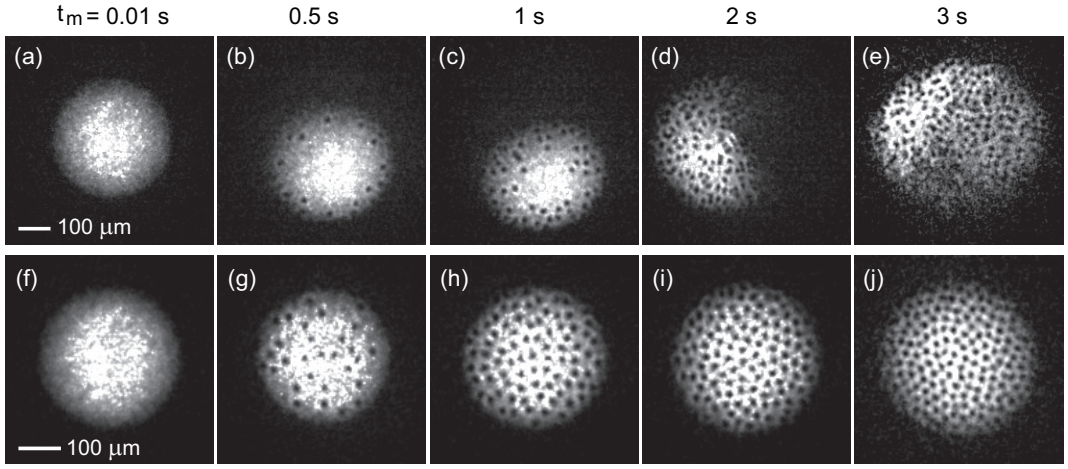

Figure 6.11: Vortex nucleation in the spinor condensate circulating around the skyrmion spin texture. (a)-(e) Absorption images after 15-ms time-of-flight for various driving times t_m. The condensate is deformed into an elliptical shape and quantized vortices are nucleated in its boundary. (f)-(j) Images after 2-s relaxation in a stationary trap without the spin texture modulations.

the condensate center, the circulation direction observed in our experiment is consistent with the theoretical prediction, but their direct comparison is limited because our system is an externally driven system.

6.3.3 Quantized vortices in the circulating condensates

Another remarkable observation is the nucleation of quantized vortices during the condensate circular motion. Figure 6.11 shows time-of-flight images of the condensate for various driving times t_m, where quantized vortices are detected with density-depleted cores. The condensate first deforms into an elliptical shape and after a few 100 ms, quantized vortices start to appear in its boundary region. Eventually, the condensate becomes packed with many vortices. In order to

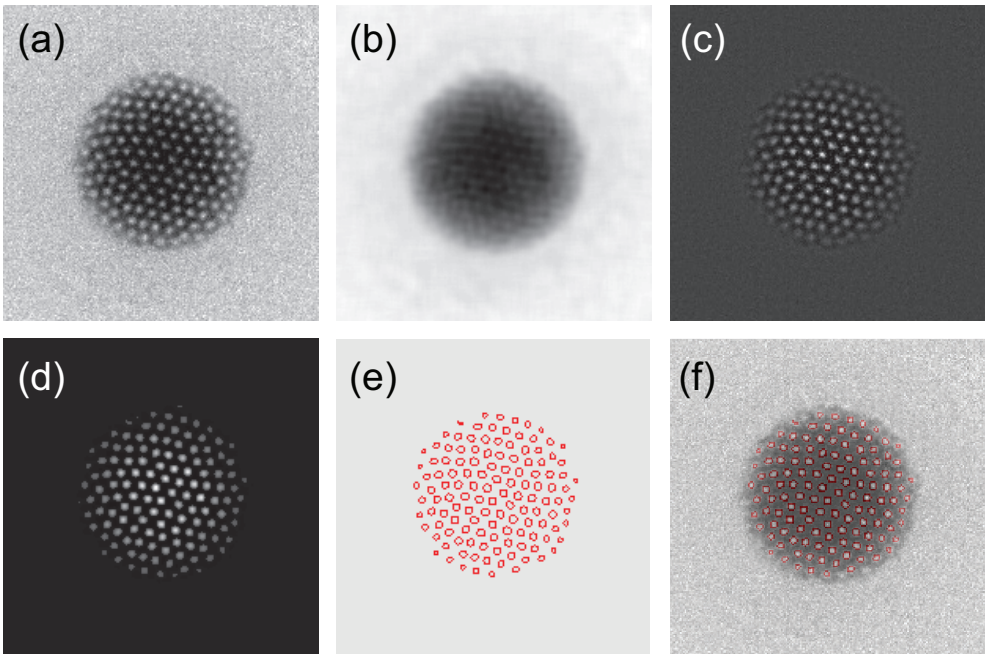

Figure 6.12: Vortex counting algorithm. (b) The raw image in (a) is blurred about 4 pixel to smoothing density depletion core. (c) we divided the raw image by the blurred data. (d) After enhancing the visibility of bright spot, (e) we count the number of cores with particle analysis package in IGOR program. (f) Overlapping the boundary of vortex core with the raw image, we can see the reliability of the algorithm. The Hand count number of vortices in the raw image is 131, while the program give 128.

count the vortex number, we stop the external driving and relax the sample for 2-s in a stationary trap. The vortices form a triangular lattice [Fig. 6.11(f)-(j)], indicating that they are of the same sign [37].

Characterizing vortex nucleation, we count the vortex number by computer program which is well described by J. R. Abo-sheer [38]. The counting algorithm is summarized in Fig. 6.12. The core information is extracted after we divide the raw image by the blurred image of itself. After enhancing the core

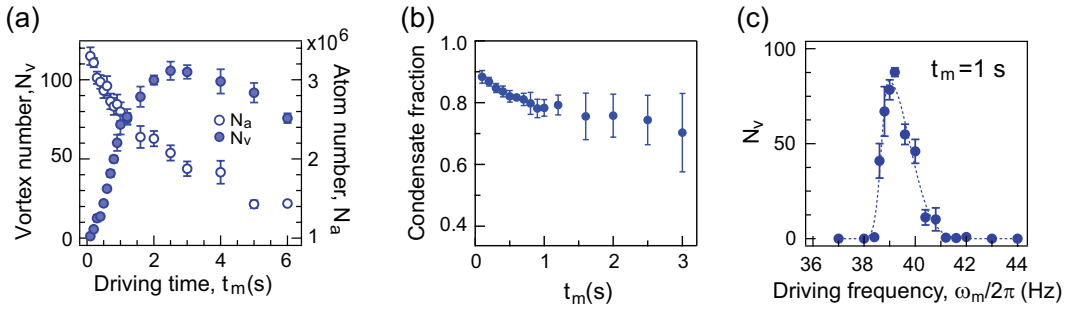

Figure 6.13: (a) Temporal evolution of the vortex number N_v (solid) and the atom number N_a (open) for $\omega_m/2\pi = 39.2$ Hz. (b) The condensate fraction as a function of t_m, which is determined from a bimodal fit to images after relaxation. (c) Vortex number N_v for $t_m = 1$ s versus driving frequency ω_m. The dashed line is an asymmetric Gaussian curve fit to the data, which has the center frequency at 39.0 Hz, and the left and right $1/e^2$ linewidth of 0.4 Hz and 1.2 Hz, respectively. Each data point was obtained by averaging at least 9 measurements and the error bars indicate the standard deviation of the measurements.

visibility, the *ImageAnalyzeParticles* algorithm in the IGOR program counts the number of particles in Fig. 6.12(e). The result shows quite good agreement with hand-counting result[4].

For $\omega_m = 2\pi \times 39.2$ Hz, the vortex number N_v almost linearly increases for $t_m < 1$ s and becomes saturated to $N_v > 100$ within 3 s, Fig. 6.13(a). There is no significant heating during the process and the condensate fraction decreases by less than 20%. Since the vortex number has resonance feature under external driving, which is represented in Fig. 6.13(c), we can examine the behavior by varying radial trap frequency ω_r.

Figure 6.14 shows the vortex number under various driving frequencies and driving time at a given distance $z_m = 64$ μm and 15 μm, where the radial

[4]For Images with small number of vortices, the vortex counting algorithm does not work so we count the core by hand.

trap frequencies at the center are $\omega_r = 2\pi$ Hz and 30.2 Hz respectively. The vortex number N_v is measured under the same condition that after moving the zero-field center to $z_m = 102$ μm in 1 s and a subsequent 1-s holding. Similar to the experiments at $z_m = 15$ μm the vortex number shows resonance behavior and the peak frequency is shown to very close to the radial trap frequency. The negative shift of the driving frequency ω_m from ω_r for the maximum Hall response could comes from anharmonic effect of linear trap which is described in Fig. 6.6. Moreover, by varying the amplitude of external motion [Fig. 6.15] we can measure the initial vortex nucleation rate as a function of driving motion X_m. We observe saturation at $X_m > 4$ μm and 2 μm of driving amplitude is in linear driving regime.

This Hall effect could present a new method for rapidly rotating atomic superfluid with much simple geometry than optical laser beam. The internal rotating frequency Ω is estimated to be $\frac{\hbar N_v}{mR_{TF}^2} \approx 0.7\omega_r$. Though this value is far below to observe quantum Hall effect, still condensate fraction is decreased less than 20% and no significant heating observed. We consider the anharmonicity of the magnetic trapping potential restricts the amplification of the oscillation amplitude, which prevents a further increases of the vortex number. Indeed, the observed maximum amplitude for the x-directional motion was closed to z_m.

We attribute the vortex nucleation in the circulating condensate to the inhomogeneity of the effective magnetic field $\mathbf{B}^e(\mathbf{r})$. The induced electric force $\mathbf{F}_E = -\mathbf{v}_m \times \mathbf{B}^e$ has $\nabla \times \mathbf{F}_E = (\mathbf{v}_m \cdot \nabla)\mathbf{B}^e \neq 0$ and thus, it can play as a shearing force to deform the condensate and consequently lead to the dynami-

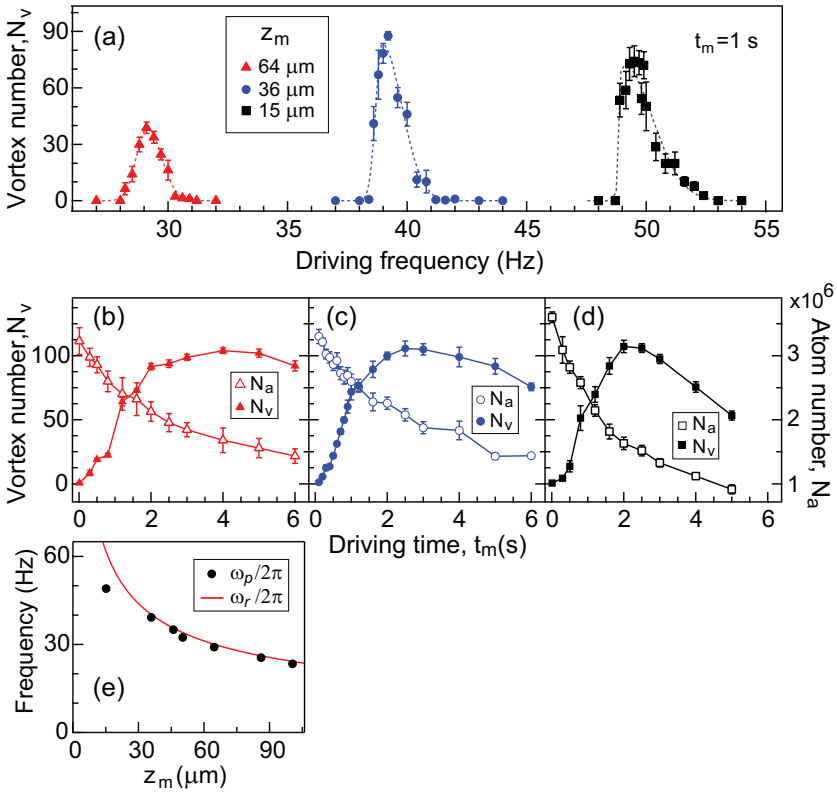

Figure 6.14: (a) Number of nucleated vortices for $t_m = 1$ s as a function of the driving frequency $\omega_m/2\pi$. The distance z_m of the zero-field center to the condensate was changed with B_z for $B_q = 7.6$ G/cm. Dashed lines are asymmetric Gaussian fits to the vortex number. The peak-response driving frequency, and the left and right $1/e^2$ linewidths are $(\omega_p, \gamma_L, \gamma_R)/2\pi$ = (29.1, 0.6, 0.8) Hz for $z_m = 64$ μm, (39.2, 0.4, 1.2) Hz for $z_m = 36$ μm, and (49.0, 0.2, 1.8) Hz for $z_m = 15$ μm. Temporal evolution of the vortex number N_v (solid) and the atom number N_a (open) for (b) $(z_m, \omega_m/2\pi)$=(64 μm, 29.1 Hz), (c) (36 μm, 39.2 Hz), and (d) (15 μm, 49 Hz). The peak-response driving frequency $\omega_p/2\pi$ (solid circle) and the estimated trapping frequency ω_r (red line) as a function of z_m. Each data point was obtained from at least 8 measurements and the error bar represent the standard deviation of the measurements.

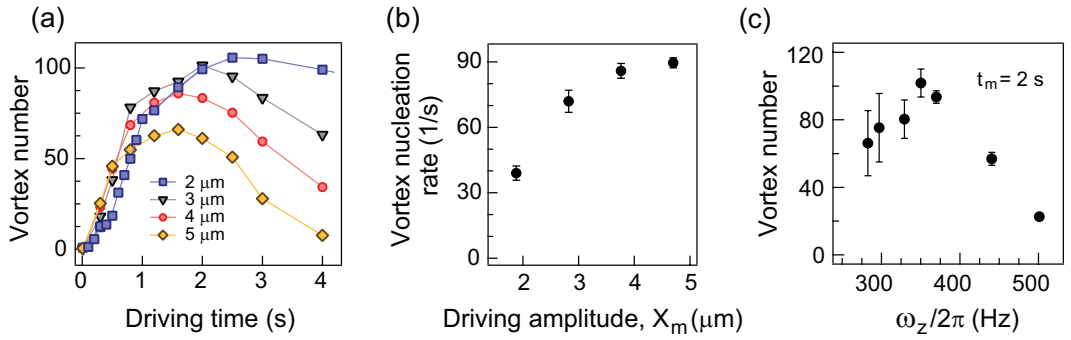

Figure 6.15: (a) Number of vortices in the condensate during the external driving with various driving amplitude X_m. (b) The nucleation rate of the defect is measured from the linear curve fit to the data with time interval $t_m < 0.5$ s.(c) Vortex number N_v as a function of the axial trapping frequency ω_z (B_q = 7.6 G/cm, $z_m = 36$ μm, $X_m = 1.9$ μm, $\omega_m = 2\pi \times 39.2$ Hz, and $t_m = 2$ s). Each data point is obtained at leat 6 measurements.

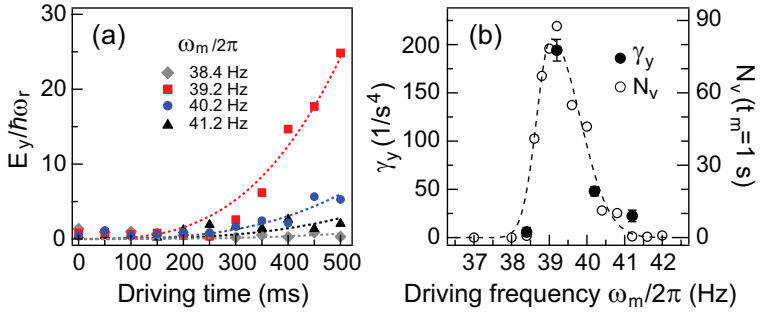

Figure 6.16: Temporal evolution of the y-directional mechanical energy $E_y = m\omega_r^2\langle y^2\rangle$ for the data in Fig. 6.9(a)-(d). $\langle y^2\rangle$ was obtained by averaging over a 50-ms time bin. In the single particle dynamics of the Eq $\langle y^2\rangle \propto t^4$ on resonance with $\omega_m = \omega_r$. The dashed lines are curve fits of $E_y/\hbar\omega_r = \gamma_r t_m^4$ to the data points of each ω_m. (b) γ_y versus $\omega_m/2\pi$, displayed together with the vortex number data from Fig. 6.13(c).

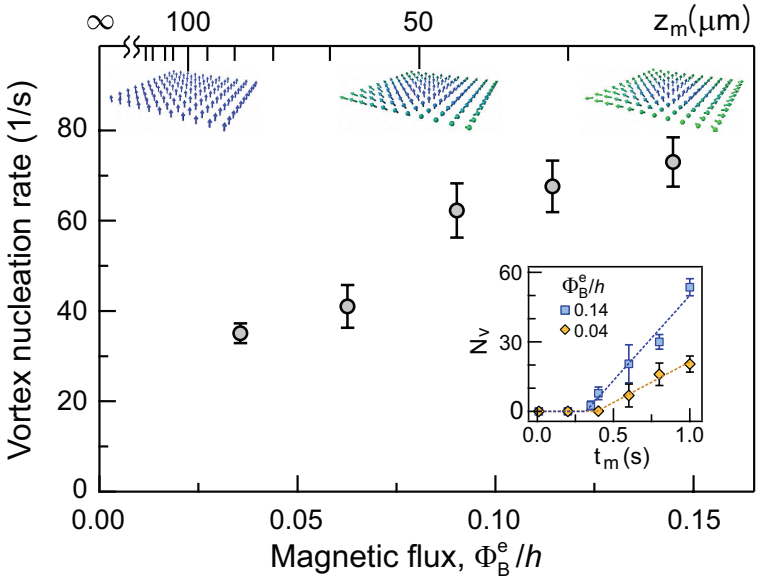

Figure 6.17: (a) Vortex nucleation rate Γ_v versus effective magnetic flux Φ_{B^e} passing through the condensate. The inset displays the vortex number N_v as a function of a driving time t_m and Γ_v is determined from a linear fit (solid line) to the data. Trajectories of the condensate position for (b) $\Phi_{B^e}/h = 0.14$ and (c) 0.04. The data were acquired with condensates containing about 2.3×10^6 atoms, where the estimated radial trapping frequency $\omega_r/2\pi = 35.2$ Hz, $\omega_m/2\pi = 35.0$ Hz, and $X_s = 2.8$ μm.

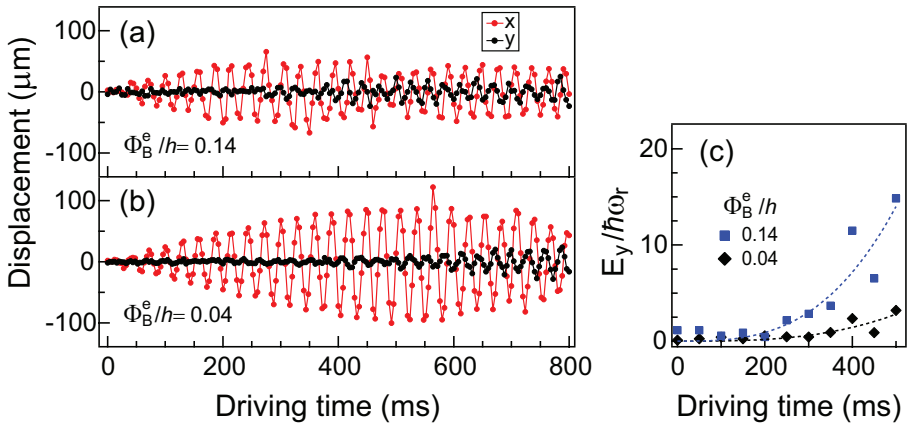

Figure 6.18: Temporal evolution of the condensate position for (a) $\Phi_B^e/h = 0.14$ and (b) 0.04 in Fig. 6.17, and (c) the corresponding evolution of the y-directional mechanical energy $E_y(t_m)$. The dashed lines are the curve fits of $E_y/\hbar\omega_r = \gamma_y t_m^4$

cal nucleation of quantized vortices in the boundary region. We observed that the vortex nucleation is affected by the axial trapping frequency ω_z, implying that a three-dimensional description might be necessary to explain the vortex nucleation dynamics, including the coupling between the axial and transverse motions [Fig. 6.15 (c)].

In our experiment, the nucleated vortex number shows the same asymmetric dependence on the driving frequency ω_m as observed in the amplification rate of the y-directional motion as shown in Fig. 6.16. This suggests that the vortex nucleation rate Γ_v can be used as a quantitative measure for the geometric Hall effect in our superfluid system. We measure Γ_v for various values of the effective magnetic flux Φ_B^e by changing the distance z_m of the zero-field center from the condensate [Fig. 6.17]. Here, we set $\omega_m = 2\pi \times 35$ Hz and adjust the radial trapping frequency $\omega_r \propto \sqrt{\frac{B_q^2}{B_z}}$ with B_q and B_z to obtain a

maximum Hall response for a given $z_m = B_z/B_q$. The vortex nucleation rate Γ_v was determined from a linear fit of $\Gamma_v(t_m - t_0) \times \theta(t_m - t_0)$ to $N_v(t_m)$ for $t_m \leq 1$ s [Fig. 6.17], where $\theta(t)$ is the Heaviside step function. We find that Γ_v monotonically increases with Φ_B^e. The onset time $t_0 = 390 \pm 50$ ms, showing no clear dependence on Φ_B^e. The condensate trajectory data for high and low flux are provided in Fig. 6.18 (a) and (b), respectively. The coupling between x and y motion become strong at higher field.

In conclusion, we have observed the geometric Hall effect in a spinor Bose-Einstein condensate with a skyrmion spin texture and presented the first study of superfluid dynamics in an inhomogeneous gauge field. We expect the spin-texture oscillation method to be extended to spin mixture systems for studying spin-dependent transport phenomena such as spin drag [39] and spin Hall effects [27, 40]. A strong effective magnetic field might be possibly achieved by employing nano-fabricated ferromagnetic structures [41].

Bibliography

[1] M. V. Berry, Proc. R. Soc. London Ser. A **392**, 45 (1984).

[2] A. Shapere and F. Wilczek, *Geometric Phase in Physics* (World Scientific, Singapore, 1989).

[3] A. Stern, Phys. Rev. Lett. **68**, 1022 (1992).

[4] Y. Taguchi, Y. Oohara, H. Yoshizawa, N. Nagaosa, and Y. Tokura, Science **291**, 2573 (2001).

[5] N. Nagaosa, J. Sinova, S. Onoda, A. H. MacDonald, and N. P. Ong, Rev. Mod. Phys. **82**, 1539 (2010).

[6] M. Lee, W. Kang, Y. Onose, Y. Tokura, and N. P. Ong, Phys. Rev. Lett. **102**, 186601 (2009).

[7] A. Neubauer, C. Pfleiderer, B. Binz, A. Rosch, R. Ritz, P. G. Niklowitz, and P. Böni, Phys. Rev. Lett. **102**, 186602 (2009).

[8] Y. Li, N. Kanazawa, X. Z. Yu, A. Tsukazaki, M. Kawasaki, M. Ichikawa, X. F. Jin, F. Kagawa, and Y. Tokura, Phys. Rev. Lett. **110**, 117202 (2013).

[9] B. Goss Levi, Phys. Today **46**, 17 (1993).

[10] S. E. Barnes and S. Maekawa, Phys. Rev. Lett. **98**, 246601 (2007).

[11] P. N. Hai, S. Ohya, M. Tanaka, S. E. Barnes, and S. Maekawa, Nature **458**, 489 (2009).

[12] S. A. Yang, G. S. D. Beach, C. Knutson, D. Xiao, Q. Niu, M. Tsoi, and J. L. Erskine, Phys. Rev. Lett. **102**, 067201 (2009).

[13] Y. J. Lin, R. L. Compton, K. Jiménez-García, J. V. Porto, and I. B. Spielman, Nature **462**, 628 (2009).

[14] Y. J. Lin, R. L. Compton, K. Jiménez-García, W. D. Phillips, J. V. Porto, and I. B. Spielman, Nat. Phys. **7**, 531 (2011).

[15] J. Dalibard, F. Gerbier, G. Juzeliūnas, and P. Öhberg, Rev. Mod. Phys. **83**, 1523 (2011).

[16] V. Galitski and I. B. Spielman, Nature **494**, 49 (2013).

[17] T. Fujita, M. B. A. Jalil, S. G. Tan, and S. Murakami, J. Applied Phys. **110**, 121301 (2011).

[18] J. Choi, W. J. Kwon, and Y. Shin, Phys. Rev. Lett. **108**, 035301 (2012).

[19] V. Pietilä and M. Möttönen, Phys. Rev. Lett. **103**, 030401 (2009).

[20] M. Möttönen, V. Pietilä, and Sami M. M. Virtanen, Phys. Rev. Lett. **99**, 250406 (2007).

[21] M. R. Mtthews, B. P. Anderson. P. J. Haljan, D. S. Hall, C. E. Wieman, E. C. Cornell, Phys. Rev. Lett. **83**, 2498 (1999).

[22] K. W. Madison, F. Chevy, W. Wohlleben, and J. Dalibard, Phys. Rev. Lett. **84**, 806 (2000).

[23] E. Lundh, C. J. Pethick, and H. Smith, Phys. Rev. A **55**, 2126 (1997).

[24] T.-L. Ho and V. B. Shenoy, Phys. Rev. Lett. **77**, 2595 (1996).

[25] V. L. Ginzburg and L. P. Piatevskii, Sov. Phys. JETP **7**, 858 (1958).

[26] L. J. LeBlanc, K. Jiménez-García, R. A. Williams, M. C. Beeler, A. R. Perry, W. D. Phillips, and I. B. Spielman, Proc. Natl. Acad. Sci. U.S.A. **109**, 10811 (2012).

[27] M. C. Beeler, R. A. Williams, K. Jiménez-García, L. J. LeBlanc, A. R. Perry, and I. B. Spielman, Nature **498**, 201 (2013).

[28] A. E. Leanhardt, Y. Shin, A. P. Chikkatur, D. Kielpinski, W. Ketterle, and D. E. Pritchard, Phys. Rev. Lett. **90**, 100404 (2003).

[29] A. Lamacraft, Phys. Rev. A **77**, 063622 (2008).

[30] Y. Kawaguchi and M. Ueda, Phys. Rep. **520**, 253 (2012).

[31] A. E. Leanhardt, Y. Shin, D. Kielpinski, D. E. Prtichard, and W. Ketterle, Phys. Rev. Lett. **90**, 140403 (2003).

[32] P. Zhang, H. H. Jen, C. P. Sun, and L. You, Phys. Rev. Lett. **98**, 030403 (2007).

[33] J. Choi, W. J. Kwon, M. Lee, H. Jeong, K. An, and Y. Shin, New J. Phys. **14**, 053013 (2012).

[34] X.-Q. Xu and J. H. Han, Phys. Rev. A **86**, 063619 (2012).

[35] C.-C. Huang and S.-K. Yip, Phys. Rev. A **88**, 013628 (2013).

[36] J. Armaitis, H. T. C. Stoof, and R. A. Duine, Phys. Rev. Lett. **110**, 260404 (2013).

[37] A. L. Fetter, Rev. Mod. Phys. **81**, 647 (2009).

[38] Jamil R. Abo-sheer, *Novel ground state of Bose-condensed gases*. PhD thesis, Massachusetts Institute of Technology, 2004.

[39] R. A. Duine and H. T. C. Stoof, Phys. Rev. Lett. **103**, 170401 (2009).

[40] M. Taillefumier, E. K. Dahl, A. Brataas, and W. Hofstetter, Phys. Rev. B **80** 020407(R) (2009).

[41] P. Bruno, V. K. Dugaev, and M. Taillefumier, Phys. Rev. Lett. **93**, 096806 (2004).

Chapter 7

Conclusions

Ever since the first discovery of Bose-Einstein condensation in atomic gases, now more than ten atomic species can be Bose condensed and scientists still look forward to making noble quantum fluid, for example, having strong dipole-dipole interactions and narrow natural linewidth. Moreover, because of the unprecedented experimental environment, there is a growing body of research which has revealed lots of interesting quantum phenomena more directly.

My colleagues and I have put a little experimental achievements along this line and this dissertation describes the details of our the research. The superfluid state in a two-dimensional system is intriguing because the formation of long-range order is prohibited by large thermal fluctuations and consequently the picture of Bose-Einstein condensation is not applicable to the superfluid phase transition. For studying the 2D superfluid of atomic system, we built a robust and stable experimental apparatus for generating ultra-cold gases. The

machine can generate a pure condensates of ^{23}Na atoms in the two different hyperfine spin states, $|F = 1\rangle$ state and $|F = 2\rangle$ state. In the near future, the apparatus could be upgraded to produce degenerated Fermi gases of ^{6}Li atoms.

Studying the 2D superfluid phase of atomic gas, we prepare a degenerate qausi-2D Bose gas in a single pancake-shaped optical dipole trap. The phase fluctuations were demonstrated by the density modulations in the course of free expansion, which could be understood by matter wave version of the optical Talbot effect. We characterized the strength of the phase fluctuations by studying the power spectrum of the density modulations. This method was employed to study the thermal nature of the phase fluctuations in two-dimensional superfluid. We also observed relaxation dynamics of a nonequilibrium states of the quasi-2D system using the power spectrum. Furthermore, by enhancing the vortex core visibility, we measured the spatial distribution of vortices in the two-dimensional superfluid and pairing features were revealed by two vortices correlation function of the vortex profiles. Studying the vortex profiles at various temperatures, we studied BKT-BEC crossover phenomena in a finite-size 2D system.

Many research groups around the world are still investigating different aspects of the two-dimensional quantum gases. Measuring the superfluid fraction in the two-dimensional atomic sample, one could observe the universal jump of superfluid density across the critical temperature. Using the hyperfine spin degree of freedom, one can explore new types of BKT phase transition mediated by another type of topological defects such as half quantum vortices and

Skyrmions. Including disorder potential, which is inevitable in the real solid state material, produces a rich phase diagram of the two dimensional Bose system. *In-situ* measurement of the vortex pairs would be interesting since the criterion of vortex pairs is vague in a finite size sample near the critical temperature and thus could provide remarkable benchmarks for the BKT theory.

Appendix

Appendix A

Optical System for Laser cooling

Thus appendix includes the schematic diagrams of optical configurations at the laser table.

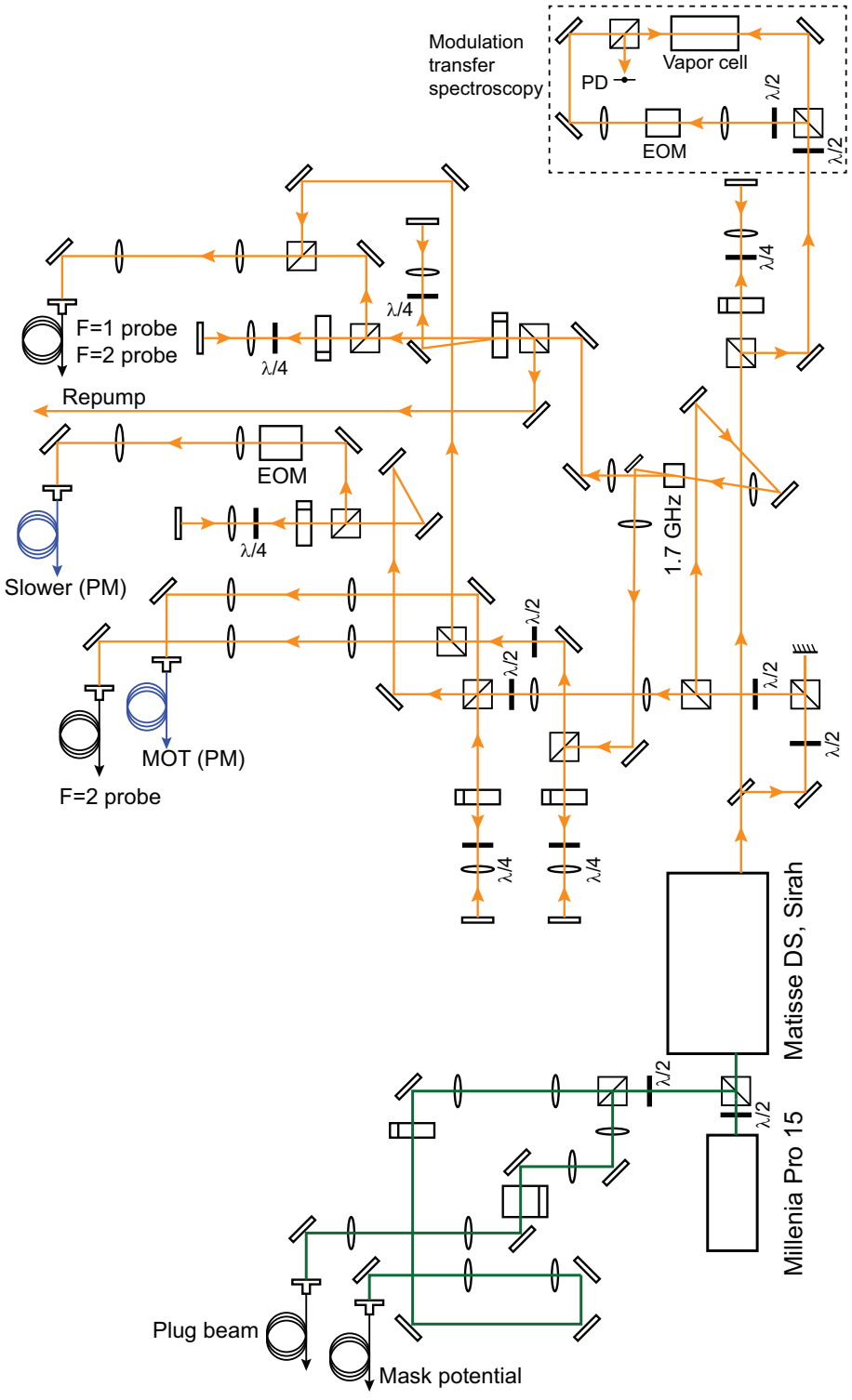
Modulation
transfer
spectroscopy
PD
Vapor cell
EOM
λ/2
λ/2
λ/4
λ/4
F=1 probe
F=2 probe
λ/4
Repump
EOM
λ/4
1.7 GHz
Slower (PM)
λ/2
λ/2
λ/2
λ/2
MOT (PM)
F=2 probe
λ/4
λ/4
Matisse DS, Sirah
λ/2
λ/2
Millenia Pro 15
Plug beam
Mask potential

Appendix B

Numeric code for vortex interference

Thus appendix describes the numeric code for simulating interference patters with *Wolfram Mathematica* program with version 7.0.0

Define the three level Rabi oscillation

c = 0.7; (∗ coupling constant∗)

b = -1; (∗ detuning ∗)

a = $\begin{pmatrix} -1-b & c & 0 \\ c & 0 & c \\ 0 & c & 1+b \end{pmatrix}$ (∗ Hamiltonian in the rotating frame∗)

values = Eigenvalues[a]

vectors = Eigenvectors[a]

Clear[initial];

p[t_] := initial.vectors[[1]]*vectors[[1]]*Exp[-I*values[[1]]*t] +

initial.vectors[[2]]*vectors[[2]]*Exp[-I*values[[2]]*t] +

initial.vectors[[3]]*vectors[[3]]*Exp[-I*values[[3]]*t]

Density plot of the vortex interference fringes

DensityPlot[

Abs[p[1.75][[1]]]^2 /.

initial → { $1.2e^{-0.3(x^2+y^2)}\sqrt{\frac{x^2+y^2}{9+x^2+y^2}}$∗Sign[$x$]∗Exp[I∗ArcTan[$\frac{y}{x}$]-1∗$x$], $e^{-0.2(x^2+y^2)}$

,$1.2e^{-0.3(x^2+y^2)}\sqrt{\frac{x^2+y^2}{9+x^2+y^2}}$∗Sign[$x$]∗Exp[-I∗ArcTan[$\frac{y}{x}$]-1∗$x$] }, {x, -4, 4}, {y, -4, 4},

PlotRange → All, ColorFunction → GrayLevel, PlotPoints → 50, Frame → False]

Appendix C

Experimental appartus for producing large ^{23}Na Bose-Einstein condensates

This appendix includes a reprint of Ref. : Jae-yoon Choi, Myoung-sun Heo, and Yong-il Shin. *"Experimental appartus for producing large ^{23}Na Bose-Einstein condensates "* Journal of the Korean Physical Society **59**, 211 (2011).

Journal of the Korean Physical Society, Vol. 59, No. 2, August 2011, pp. 211∼216

Experimental Apparatus for Producing Large ^{23}Na Bose-Einstein Condensates

Jae-yoon Choi, Myoung-Sun Heo and Yong-il Shin*
Department of Physics and Astronomy, Seoul National University, Seoul 151-747, Korea

(Received 10 June 2011)

We describe our experimental apparatus for quickly producing large Bose-Einstein condensates of ^{23}Na atoms. We collect atoms in a dark magneto-optical trap from a zero-crossing Zeeman slower and then capture the atoms in an optically plugged magnetic quadrupole trap and apply rf evaporation to cool the atoms into the quantum degenerate regime. We slightly displace a circular plug beam from the magnetic trap center to break the ring symmetry and form a single global minimum in the combined trapping potential. Our system reliably generates a quasipure condensate with over 10^7 atoms every 17 s. We load the condensate into an elongated optical dipole trap.

PACS numbers: 03.75.Hh, 37.10.De
Keywords: Bose-Einstein condensation, Magnetic quadrupole trap, Optical plug, Optical trap
DOI: 10.3938/jkps.59.211

I. INTRODUCTION

Quantum degenerate atomic gases are highly controllable and clean samples with wide quantum applications, for example, simulation of quantum many-body physics [1] and precision measurements [2]. Persistent efforts have been made to develop more reliable and simpler methods to produce quantum degenerate gases and extend to new atomic species [3–5]. In this report, we describe the design and the performance of our experimental apparatus to rapidly produce a large Bose-Einstein condensate (BEC) of alkali ^{23}Na atoms. Sodium atoms have interesting spin interactions to form a polar spinor condensate in the $|F = 1\rangle$ hyperfine ground state, providing a unique opportunity to explore fundamental spinor dynamics with antiferromagnetic interactions [6]. In particular, exotic topological objects, such as half quantum vortices and t'Hooft-Polyakov monopoles, are expected [7,8] to exist in the ground-state manifold of an antiferromagnetic spinor condensate.

Our system makes use of a magnetic quadrupole trap combined with an off-center optical plug. A magnetic quadrupole trap is a simple and robust trap, but has a critical drawback, the Majorana nonadiabatic spin-flip losses near the zero-field point. One easy method to suppress the losses is to use a repulsive optical potential to push the atoms away from the zero-field point, which is formed by focusing a blue-detuned laser beam at the magnetic trap center. This optical plug marginally affects the linearity of the trapping potential, thus being advantageous for fast evaporation cooling. The first sodium BEC experiment was performed with this approach [9]. However, it has not been widely used because it requires high beam pointing stability for reliable BEC production.

We improve the pointing stability of the plug beam by using a fiber that enables us to adjust the plug position in a fine manner and eventually to search for an optimal plug position. We find that a slight displacement of the plug of less than a beam waist from the magnetic trap center is much more favorable for BEC production, which we attribute to a breaking of the ring symmetry and the forming of a single global minimum in the combined magnetic and optical potential. Our system reliably generates a quasipure ^{23}Na BEC with over 10^7 atoms in 17 s, comparable to the best recorded in terms of condensate size and production time. Finally, we transfer the condensates into an optical dipole trap.

II. BEC MACHINE

1. Vacuum System

The vacuum system of our apparatus consists of an atom oven, a Zeeman slower and a ultra-high-vacuum (UHV) main chamber (Fig. 1). In order to obtain the UHV, we first pre-bake the stainless-steel vacuum chamber at 250 °C with blank metal flanges and then mildly rebake the whole system at 150 °C for a week with all the components assembled, including viewports and coils for the slower. Finally, a pressure below 10^{-11} Torr is achieved at the main chamber, by pumping with a 75-L/s ion pump and a Ti-sublimation pump.

*E-mail: yishin@snu.ac.kr

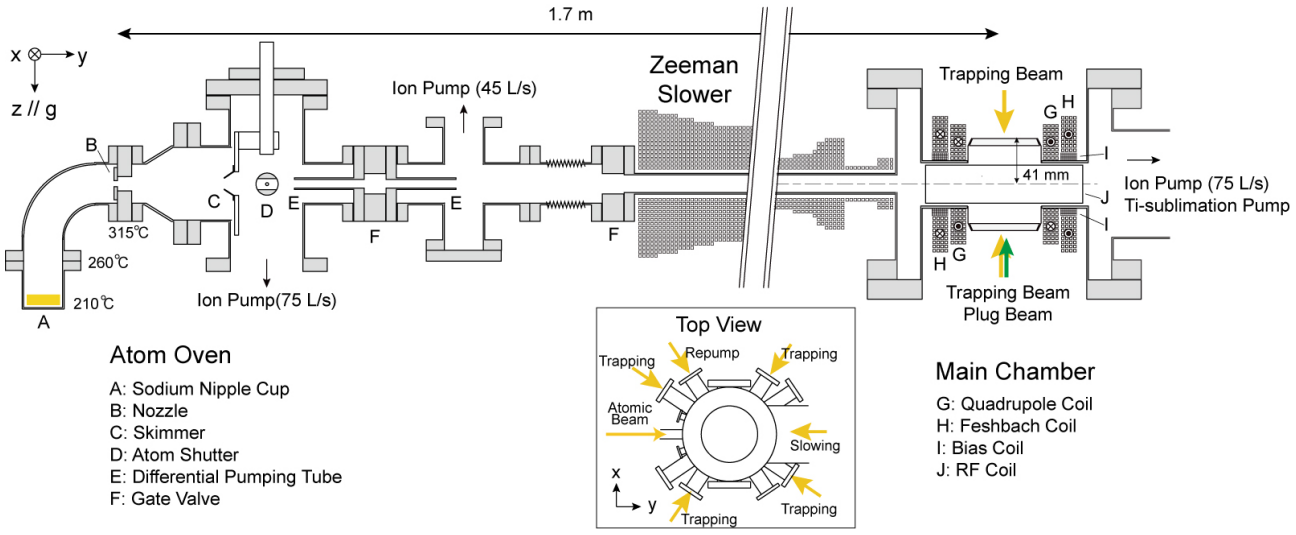

Fig. 1. (Color online) Cross-sectional diagram of the vacuum system. A sodium atomic beam is generated from the oven and propagates into the main chamber through the zero-crossing Zeeman slower. The magnetic coil sets are secured inside the recessed bucket flanges of the main chamber. The inset shows a top view of the main chamber with the MOT beam setup.

The UHV condition is critical for efficient evaporation cooling. The vacuum system was designed to keep the UHV in the main chamber against an oven pressure up to 10^{-8} Torr, placing two differential pumping tubes in series between the oven and the slower by using a long tube for the slower(inner diameters of $5-6$ mm) [10]. At a typical running condition, the pressures in the oven and the slower are low 10^{-9} and high 10^{-11} Torr, respectively. Pressure readings are taken from the ion pumps.

2. Atom Oven and Zeeman Slower

A sodium atomic beam is generated from the oven and propagates into the main chamber. Sodium is loaded in a half nipple cup and heated to 210 °C for a vapor pressure of 2.7×10^{-4} Torr. Sodium atoms effuse out of a 4-mm diameter nozzle, which is maintained at 315 °C, resulting in a mean velocity of 740 m/s. The atomic beam passes through a skimmer, an atom shutter and the differential pumping tubes. The atom shutter is a ball-valve-type shutter installed on a rotational feedthrough, and the shutter's motion is precisely controlled by using a stepping motor. The range of the rotational motion is set to be less than 50 degrees to prolong the feedthrough lifetime. The shutter is closed within 200 ms. The distance from the nozzle to the center of the main chamber is $\simeq$1.7 m, and the atom flux into the main chamber is estimated to be about 3.0×10^{11} atoms/s.

The atomic beam is decelerated by using a zero-crossing Zeeman slower. The slower was designed for a capture velocity of 950 m/s with a 700-MHz red-detuned, slowing laser beam, so its magnetic field changes from 650 to -480 G over 1 m, even at half of the maximum deceleration. The magnetic field is generated by using three tapered solenoids: one for the decreasing part (16 A) and two for the increasing part (15 A and 79 A). The solenoids are wound on 1″-diameter brass pipes with 1/8″ square hollow copper tubes (copper alloy 102, Daglas insulated) and are cemented with non-magnetic epoxy (Duralco NM25, Contronics Corp., USA). Cooling water flows through 1/16″ square inner holes, and the wire resistivity is $\leq$2.6 mΩ/m. A compensation coil is placed on the other side of the main chamber to cancel the slower field at the center of the main chamber. The residual field gradient is estimated to be < 1 G/cm along the y-direction. All the slower currents, including the compensation coil current, are simultaneously switched by using one insulated-gate bipolar transistor (IGBT) module.

In order to precisely align the atomic beam line to the center of the main chamber, the decreasing part of the slower and the oven assembly are secured on independent adjustable supports and are connected with flexible bellows. Direct visual inspection of the beam line alignment was performed before installing the sodium cup. Note that the running temperature of our oven is relatively lower than typical temperatures, which are higher than 250 °C [11], which we attribute to the proper alignment of the atomic beam. With 15 g of sodium, we could run the oven for over 1000 hr.

3. Main Chamber

Sample preparation and measurement are performed in the main chamber. This chamber is constructed of polished 304 stainless steel and are electropolished for UHV service (Sharon Vacuum Co. Inc., USA). The center experiment zone with twelve viewports is connected to a

pumping body through a $6'' \times 4''$ rectangular tube. The pumping body is equipped with a 75-L/s ion pump (75S-DI-6S-SC, Gamma Vacuum) and a Ti-sublimation pump (P/N9160050, Varian Inc.). The recessed bucket flanges on the top and the bottom of the main chamber feature non-magnetic window pipes with 50-mm-diameter clearance (UKAEA Fusion Special Technique Group, UK), providing a large numerical aperture of ≈0.5, which is beneficial to high-resolution imaging. All the viewport windows are AR coated on both sides for 532, 589, 670, and 1064 nm.

A pair of magnetic coil sets are secured around the window pipes (Fig. 1). Each quadrupole and Feshbach coil are wound by 36 turns with square copper tubing. The quadrupole and the Feshbach coil pairs generate a field gradient of 1.5 G/(cm A) and a uniform field of 4.5 G/A along the z-axis, respectively. Since a strong magnetic field would be generated along the vertical z-axis, we mount the whole vacuum system on a non-magnetic optical table (Kinetic Systems Inc., USA) to suppress field reflection. The flow rate of cooling water through a 12-m-long quadrupole coil tube was 250 ml/s at a 22-bar water pressure, so a current of 580 A would increase the temperature of the cooling water by less than 10 °C. Two pairs of rectangular coils of UHV-compatible kapton wires are mounted inside the chamber for rf evaporation and are connected via electric feedthroughs. The stray magnetic field, including the earth's field, is compensated for by using three pairs of magnetic coils surrounding the chamber.

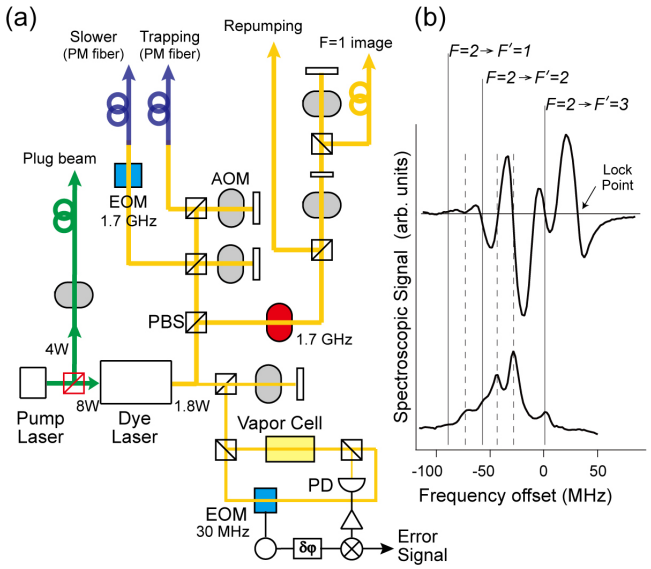

Fig. 2. (Color online) (a) Schematic diagram of the sodium laser system. A 589-nm yellow light is generated from a dye laser system: AOM - acousto-optic modulator; PBS - polarization beam splitter; EOM - elecro-optic modulator; PD - photo diode; PM fiber - polarization maintaining fiber. Most AOMs are set up in double pass configuration. (b) Modulation transfer spectroscopy (top) and saturation absorption spectroscopy (bottom) of sodium. Solid and dash vertical lines indicate optical transitions and their crossovers, respectively. The laser frequency is locked using the zero-crossing point on the blue side of the $|F = 2\rangle \rightarrow |F' = 3\rangle$ transition in modulation transfer spectroscopy.

4. Laser System

Figure 2 shows a schematic layout of our laser system. A 1.8-W laser beam at the frequency of the sodium D_2 line (589 nm) is generated from a dye laser system (Matisse DS, Sirah, Germany) by pumping with a 8-W, 532-nm laser light (Millennia Pro 15, Spectra-Physics). The laser frequency is stabilized to an external reference cavity, whose long-term drift is locked using modulation transfer spectroscopy of a sodium vapor cell, where we use a homemade 30-MHz elecro-optic modulator (EOM) [12]. The lock point is chosen at the zero-crossing point on the blue side of the $|F = 2\rangle \rightarrow |F' = 3\rangle$ cooling transition, where F and F' are the total angular momenta of the ground and the excited hyperfine states, respectively. The laser linewidth is estimated to be less than 200 kHz, much smaller than the natural linewidth $\Gamma = 9.8$ MHz of the D_2 line.

The repumping and imaging lights for the $|F = 1\rangle \rightarrow |F' = 2\rangle$ transition are derived using a single 1.7-GHz, high-frequency acousto-optic modulator (AOM) (TEF-1700-100-589, Brimrose Corp., USA) with a diffraction efficiency of ≈25%. The slowing light is phase-modulated at 1.7 GHz with an EOM (4421-M, New Focus), transferring 10% of the total power into the first-order sidebands. In the low-field region of the slower, the high-frequency sideband component pumps atoms into the proper spin state to keep them decelerating. Most AOMs are set up in a double-pass configuration to facilitate frequency tuning and shuttering of light. All the light except the repumping light is delivered to the experiment table via single-mode optical fibers to clean beam modes and to enhance the beam pointing stability. The typical fiber coupling efficiency is above 60%.

A part of the output of the 532-nm pump laser is allocated for an optical plug (see Sec. III-B), and a 5-W Ytterbium fiber laser at 1070 nm (YLR-5-LP, IPG Photonics) is used to form an optical dipole trap.

III. EXPERIMENT

1. Dark Magneto-Optical Trap

We adopt the dark magneto-optical trap (MOT) scheme to increase the atom density in a MOT [13]. By simply blocking the center part of the repumping beam, one can reduce the re-radiation pressure at the core of a MOT, enabling more atoms to be collected in the $|F = 1\rangle$ hyperfine state at higher density.

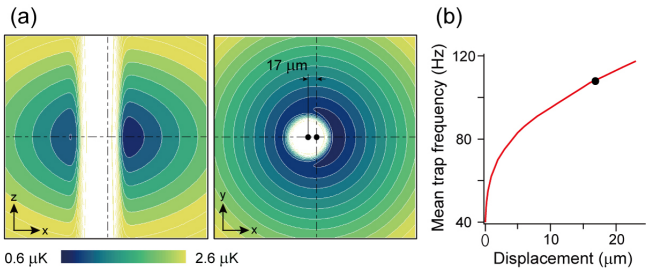

Fig. 3. (Color online) Optically plugged magnetic quadrupole trap. (a) Contour plots of the combined trapping potential in the x-z plane (left) and the x-y plane (right) with an optical plug displaced from the magnetic field center by $d = 17$ μm. The field of view of each plot is 200 μm $\times$ 200 μm. (b) Geometric mean of the trapping frequencies at the minimum of the combined trapping potential versus the displacement. The circle indicates the experimental condition for sample preparation.

Our trapping, slowing, and repumping beams have $1/e^2$ beam diameters of $\approx$2.5 cm. The frequencies of the trapping and the slowing beams are 15 MHz and 700 MHz red-detuned to the $|F = 2\rangle \rightarrow |F' = 3\rangle$ transition, respectively, and that of the repumping beam is 10 MHz red-detuned to the $|F = 1\rangle \rightarrow |F' = 2\rangle$ transition. The trapping beam powers for the vertical and the horizontal directions were 17 mW and 23 mW, respectively, and the total power of the repumping beam was 18 mW, where the 1-cm-diameter center part was blocked to implement a dark MOT. A 50-mW slowing beam was aligned to the atomic beam line and focused to the oven nozzle. We observed that the MOT performance for BEC production was deteriorated with a higher slowing beam power, which might be attributed to the induced AC stark shift ($\approx$1 MHz). The quadrupole field gradient along the z-direction B' was 7.5 G/cm. The loading time and the lifetime of our dark MOT were 0.94 s and 4.2 s, respectively. In a typical experimental run, more than 10^{10} atoms were collected within a 3-s loading. In a bright MOT, *i.e.*, one with an unblocked, bare repumping beam, the number of trapped atoms was reduced by a factor of 50.

2. Evaporation Cooling in a Plugged Linear Trap

The laser-cooled atoms are transferred into a magnetic quadrupole trap for further cooling by rf evaporation. The magnetic quadrupole trap is beneficial for fast and efficient evaporation due to its large trap volume and tight linear geometry, as well as its requiring no additional magnetic coils. Once the MOT light was swtiched off, we captured atoms in the $|F = 1, m_F = -1\rangle$ low-field seeking state (m_F is the magnetic quantum number) by quickly ramping up B' to 180 G/cm at a rate of 10 G/(cm·ms) (ESS25-400, TDK Lambda Corp., Japan). Typically, 3.0×10^9 atoms were loaded at 250 μK. The lifetime of the atoms in the magnetic trap was over 70 s.

Majorana spin-flip atom losses were suppressed by applying a repulsive optical potential near the zero-field point of the magnetic trap center. This optical plug was formed by focusing a blue-detuned 532-nm, circular Gaussian laser beam. The effective potential of this hybrid magneto-optical trap is

$$U(\mathbf{r}) = \mu B' \sqrt{\frac{(x^2 + y^2)}{4} + z^2} + U_p e^{-\frac{(x+d)^2+y^2}{2w^2}} - mgz, \quad (1)$$

where $\mu = \mu_B/2$ (μ_B is the Bohr magneton) is the magnetic moment of the atom, U_p and w are the potential height and the beam waist of the optical plug, respectively, d is the offset of the plug beam from the magnetic field's center, m is the mass of the atom, and g is acceleration of gravity [14]. In our experiments, we focused a 1.7-W laser beam to have $w \simeq 45$ μm, resulting in $U_p = k_B \times 90$ μK, where k_B is the Boltzmann constant. The position stability of the optical plug was $\approx$5 μm.

Evaporative cooling was performed by linearly sweeping the applied radio frequency from 30 MHz for 14 s. In the last 2 s, the trapped sample was decompressed by ramping down the quadrupole field gradient B' from 180 G/cm to 30 G/cm to avoid inelastic losses, such as three-body recombinations [15], associated with high atom densities. The details of the evaporation process in the optically plugged magnetic quadrupole trap, including the Majorana loss effects, have been presented in Ref. 15.

3. Absorption Imaging

The atom number and the temperature of atom clouds were determined from absorption images of the samples after a time of flight. A 100-μs pulse of imaging light, resonant on the $|F = 1, m_F = -1\rangle \rightarrow |F' = 2, m_F = -2\rangle$ transition, was applied in the z-direction, and the spatial distribution of the imaging light was captured with a CCD camera (pixelfly qe, Cooke Corp.). The probe light was σ-polarized, and a small magnetic bias field was applied along the direction of light propagation. The density distribution, $\tilde{n}(x, y)$, integrated along the line of sight (z-axis) was obtained from three consecutive images: the first with atoms, $I_1(x, y)$, the second without atoms, $I_2(x, y)$, and the last dark image without light, $I_3(x, y)$:

$$\tilde{n}(x, y) = \int n(x, y, z)dz = -\sigma_0^{-1} \ln(\frac{I_1 - I_3}{I_2 - I_3}), \quad (2)$$

where $\sigma_0 = 3\lambda^2/4\pi$ ($\lambda = 589$ nm) is the resonant cross section. The total atom number is given by integrating $\tilde{n}(x, y)$ over the whole area, and the temperature is determined from the Gaussian width of the spatial distribution of the atoms. In-trap absorption images were

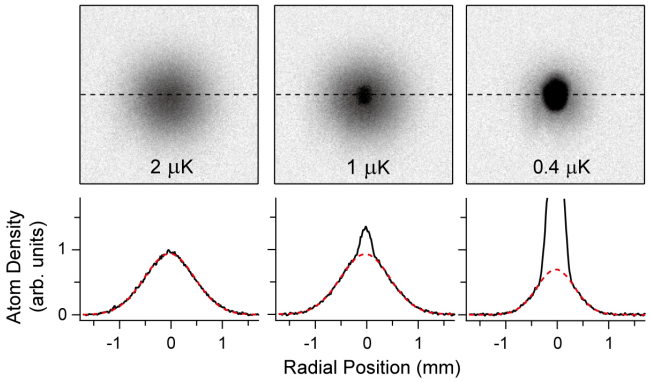

Fig. 4. (Color online) Bose-Einstein condensation. Absorption images taken after a time-of-flight of 24 ms (top) and the atom density distributions along the center dashed lines (bottom). The red dash lines are Gaussian curves fit to the outer thermal wings. Below a critical temperature, the condensate fraction increases with clear bimodality of the momentum distribution of atoms.

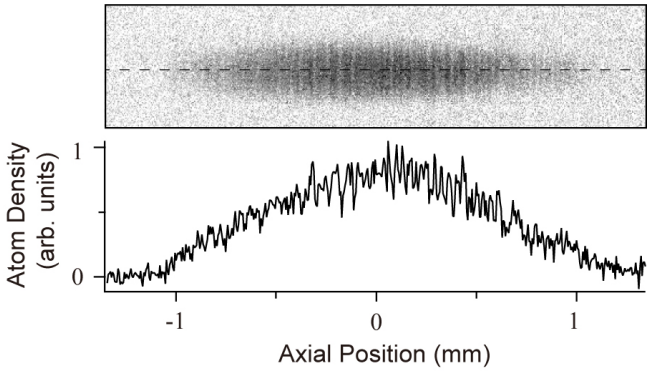

Fig. 5. Absorption image of a condensate released from an elongated optical dipole trap after a 25-ms ballistic expansion (top) shows the axial modulation of the atom density. The atom density profile along the dashed line (bottom).

used for aligning the plug beam and for magnetic field compensation.

IV. BOSE-EINSTEIN CONDENSATION

Bose-Einstein condensation of sodium atoms has been observed with the onset of a bimodal momentum distribution (Fig. 4). For large sample size, we optimized the displacement of the optical plug at $d \simeq 17$ μm, less than half of its beam waist. At the phase transition, the atom number and the critical temperature were $N_c = 2.5 \times 10^7$ and $T_c = 1.4$ μK, respectively. The critical temperature of an ideal gas in a 3D harmonic trap is given as $k_B T_c'$ $= 0.94$ $\hbar \bar{f} N_c^{1/3}$ [9], where $\bar{f}$ is the geometric mean of the trap frequencies. From the local curvatures of our trapping potential, we estimate $\bar{f}$=108 Hz [Fig. 3(b)], leading to $T_c' = 1.4$ μK, which is in agreement with our observation. After a full evaporation of 14 s, a quasipure condensate of 1.0×10^7 atoms was generated. The condensate lifetime in a plugged magnetic trap was over 10 s with an additional decompression to $B' = 15$ G/cm. Note that we could produce fragmented small condensates containing $< 10^6$ atoms with a centered optical plug, *i.e.*, $d \approx 0$ μm, due to an imperfection in the plug beam profile.

Finally, we transferred condensates into an optical dipole trap. The optical trap was created to have an elongated geometry by loosely focusing a 1070-nm IR laser beam. A density fluctuation along the axial direction was observed to develop in a condensate released from the optical trap, indicating the existence of a phase fluctuation in the initial trapped condensate (Fig. 5). The phase fluctuation in a quasi-1D condensate has been investigated in previous works using this technique [17].

V. CONCLUSION

We have described the design and the performance of a ^{23}Na atom-cooling apparatus where we rapidly produce large Bose-Einstein condensates. The off-centered plugging has clear advantages over the conventional method using an elliptical plug beam. We will study antiferromagnetic spinor physics with sodium condensates in an optical dipole trap and upgrade this apparatus to produce ultracold Fermi gases of ^{6}Li atoms via sympathetic cooling with sodium condensates [18].

ACKNOWLEDGMENTS

The authors thank M. S. Lee and W. J. Kwon for experimental help and A. Keshet for the experiment control program. This work was supported by National Research Foundation of Korea (NRF) grants funded by the Korea government (MEST, No. 2011-0004539, 2011-0017527, 2011-0001053, and WCU-R32-10045) and Research Settlement Fund for the new faculty of SNU. J. C. acknowledges the financial support from Global PhD Fellowship.

REFERENCES

[1] I. Bloch, J. Dalibard, and W. Zwerger, Rev. Mod. Phys. **80**, 885 (2008).
[2] A. D. Cronin, J. Schmiedmayer, and D. E. Pritchard, Rev. Mod. Phys. **81**, 1051 (2009).
[3] Y. Takasu, K. Maki, K. Komori, T. Takano, K. Honda, M. Kumakura, T. Yabuzaki, and Y. Takahashi, Phys. Rev. Lett. **91**, 040404 (2003).
[4] A. Griesmaier, J. Werner, S. Hensler, J. Stuhler, and T. Pfau, Phys. Rev. Lett. **94**, 160401 (2005).
[5] S. Kraft, F. Vogt, O. Appel, F. Riehle, and U. Sterr, Phys. Rev. Lett. **103**, 130401 (2009).

[6] J. Stenger, S. Inouye, D. M. S. Kurn, H. J. Miesner, A. P. Chikkatur and W. Ketterle, Nature **396**, 345 (1998).
[7] U. Leonhardt and G. E. Volovik, JETP Lett. **72**, 46 (2000).
[8] H. T. C. Stoof, E. Vliegen, and U. A. Khawaja, Phys. Rev. Lett. **87**, 120407 (2001).
[9] K. B. Davis, M. O. Mewes, M. R. Andrews, N. J. van Druten, D. S. Durfee, D. M. Kurn, and W. Ketterle, Phys. Rev. Lett. **75**, 3969 (1995).
[10] J. F. O'Hanlon, A User's Guide to Vacuum Technology (Wiley, NewYork, 1989), p. 34. The gas conductance C of a long, round tube at room temperature is given by $C = 121$ m/s $\times \frac{d^3}{l}$, where d and l are the diameter and the length of the tube respectively.
[11] E. W. Streed, A. P. Chikkatur, T. L. Gustavson, M. Boyd, Y. Torii, D. Schneble, G. K. Campbell, D. E. Pritchard, and W. Ketterle, Rev. Sci. Inst. **77**, 023106 (2006).
[12] D. J. McCarron, S. A. King and S. L. Cornish, Meas. Sci. Technol. **19**, 105601 (2008).
[13] W. Ketterle, K. B. Davis, M. Joffe, A. Martin, and D. E. Pritchard, Phys. Rev. Lett. **70**, 2253 (1993).
[14] We have ignored the beam focusing because the Rayleigh length $\pi w^2/\lambda_p \approx 12$ mm ($\lambda_p = 532$ nm) is larger than the sample size.
[15] D. M. Stamper-Kurn, M. R. Andrews, A. P. Chikkatur, S. Inouye, H. J. Miesner, J. Stenger, and W. Ketterle, Phys. Rev. Lett. **80**, 2027 (1998).
[16] M. S. Heo, J. Choi and Y. Shin, Phys. Rev. A **83**, 013622(2011).
[17] S. Dettmer, D. Hellweg, P. Ryytty, J. J. Arlt, W. Ertmer, and K. Sengstock, Phys. Rev. Lett. **87**, 160406 (2001).
[18] Z. Hadzibabic, C. A. Stan, K. Dieckmann, S. Gupta, M. W. Zwierlein, A. Gorlitz, and W. Ketterle, Phys. Rev. Lett. **88**, 160401 (2002).

Appendix D

Fast production of large ^{23}Na Bose-Einstein condensates in an optically plugged magnetic quadrupole trap

This appendix includes a reprint of Ref. : Myoung-sun Heo, Jae-yoon Choi, and Yong-il Shin. *"Fast production of large ^{23}Na Bose-Einstein condensates in an optically plugged magnetic quadrupole trap"* Physical Review A **83**, 013622 (2011).

Fast production of large ^{23}Na Bose-Einstein condensates in an optically plugged magnetic quadrupole trap

Myoung-Sun Heo, Jae-yoon Choi, and Yong-il Shin*
Department of Physics and Astronomy, Seoul National University, Seoul 151-747, Korea
(Received 19 August 2010; published 26 January 2011)

We demonstrate a fast production of large ^{23}Na Bose-Einstein condensates in an optically plugged magnetic quadrupole trap. A single global minimum of the trapping potential is generated by slightly displacing the plug beam from the center of the quadrupole field. With a dark magneto-optical trap and a simple rf evaporation, our system produces a condensate with $N \approx 10^7$ atoms every 17 s. The Majorana loss rates and the resultant heating rates for various temperatures are measured with and without plugging. The average energy of a spin-flipped atom is almost linearly proportional to temperature and determined to be about 60% of the average energy of a trapped atom. We present a numerical study of the evaporation dynamics in a plugged linear trap.

DOI: 10.1103/PhysRevA.83.013622 PACS number(s): 03.75.Hh, 37.10.De

I. INTRODUCTION

Ultracold quantum gases have presented a new class of systems to investigate many-particle quantum phenomena [1–3]. Since ultracold gas samples are very dilute at particle densities around 10^{13} or $10^{14}/\text{cm}^3$, we need extremely low nanokelvin temperatures to reach the quantum degenerate regime. Evaporative cooling has been the powerful and exclusive method for producing quantum gas samples, such as Bose-Einstein condensates (BECs) [4–6]. Rapid and efficient evaporation requires fast rethermalization and a conservative environment to minimize undesired atom loss and heating due to, e.g., inelastic collisions and background collisions [7]. In this paper, we describe a fast evaporation to produce a large condensate in an optically plugged magnetic quadrupole trap.

A quadrupole trap provides a large trap volume and tight confinement due to the linearity of the potential, which makes it beneficial to efficient evaporation. Also, the quadruple field can be generated from a simple pair of coaxial coils with opposite currents, providing large optical access to a sample. However, Majorana spin-flip loss is a significant drawback in the quadrupole trap. Near the zero-field point at the trap center, nonadiabatic spin transitions to an untrappable state cause atom loss and resultant heating, eventually limiting the maximum gain in phase-space density [8]. Several techniques have been implemented to avoid this detrimental effect, including applying a time-orbiting bias field [4] or a repulsive optical plug potential [5,9] or transferring to an optical dipole trap [10].

The optical plugging scheme preserves the linearity of the trapping potential, so it is advantageous for fast evaporation. The first ^{23}Na BEC of $\approx 5 \times 10^5$ atoms was produced after 7 s of evaporation [5]. Recently, high efficiency of evaporation cooling in a plugged trap has been demonstrated by producing a large condensate of $\approx 3.0 \times 10^7$ atoms after 40 s of evaporation [9]. Here we report a rapid production of a large condensate with $N \approx 1.0 \times 10^7$ atoms after 14 s of evaporation. The distinct feature of our system is that the plug beam is offset from the magnetic zero-field point. This seems to be contradictory to the role of the plug, but we find that a slight misalignment less than a beam waist is favorable for BEC production because it forms a single global minimum in the combined magnetic and optical potential. The pointing stability of the plug beam was improved by using a fiber, which makes fine adjustment of the plug position possible.

Furthermore, we have investigated the effects of the Majorana loss and the plug by measuring the loss rates and the resultant heating rates for various conditions. The average loss energy of a spin-flipped atom shows an almost linear dependence on temperature and is determined to be about 60% of the average energy of a trapped atom. For a plugged trap, the reduction factor in the loss rate is found to be exponentially proportional to a Boltzmann factor. This confirms that the plugging effect results from density suppression due to the repulsive optical potential in the loss region. Finally, we present numerical simulation for quantitative description of the evaporation dynamics in a plugged quadrupole trap.

II. EXPERIMENT

Our BEC apparatus employs a zero-crossing Zeeman slower, designed to generate a flux of about 10^{11} atoms/s [11]. Slowed atoms were collected for 3 s in a dark magneto-optical trap (MOT) [12], and atoms in the hyperfine state $|F = 1, m_F = -1\rangle$ were transferred in a magnetic quadrupole trap, where F is the total angular momentum and m_F is the magnetic quantum number. The magnetic field was generated from a pair of 36-turn coils, secured around the recessed bucket windows of our main experimental vacuum chamber (Fig. 1). The coils are made from 1/8-in. hollow square copper tubes and cooled with water flowing through the tubes. The average coil diameter is 90 mm, and their spacing is about 63 mm. We measured a gradient of 1.5 G/(cm A) along the symmetry z axis. For the MOT and the magnetic trap, we applied a field gradient $B' = 7.5$ and 180 G/cm with 5 and 120 A in the trap coils, respectively. Atom transferring was simply done by ramping B' at a rate of about 10 G/(cm ms) and simultaneously turning off the MOT laser beams. The initial number and temperature of the atoms in the magnetic trap were $N_i \simeq 3.0 \times 10^9$ atoms and $T_i \simeq 250\ \mu$K, respectively.

Optical plugging was performed by focusing a blue-detuned 532-nm laser beam near the zero of the magnetic field. The plug beam propagated along the z direction with a beam waist of $w \simeq 45\ \mu$m, providing a repulsive potential barrier of

*yishin@snu.ac.kr

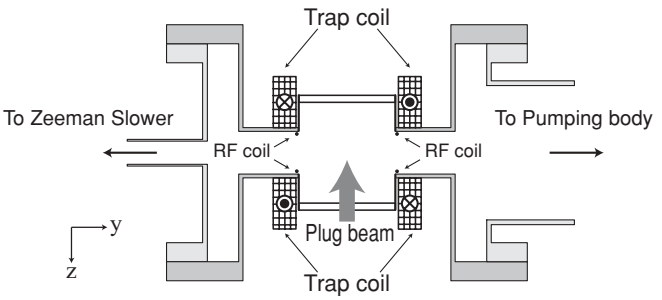

FIG. 1. Experimental apparatus. Recessed bucket windows with 60-mm-diameter clearance are mounted above and below the main vacuum chamber. A pair of 36-turn water-cooled coils are secured around the windows, generating a magnetic quadrupole field at the chamber's center. Radio-frequency (rf) evaporation coils are placed inside the vacuum chamber. A plug beam is aligned with the axial direction of the magnetic field.

$U_p \simeq k_B \times 90\ \mu$K with 1.7 W, where k_B is the Boltzmann constant. In order to improve its pointing stability, we used a fiber to deliver the plug laser beam close to the main chamber, which was critically important for our BEC production [13]. For several weeks of operation, the plug position needed little or no adjustment. Finally, rf evaporative cooling was applied for 14 s to the atoms in the plugged quadrupole trap.

A. Quadrupole trap with an off-center plug beam

When a circular plug beam is placed at the center of the quadrupole field, the combined potential has azimuthal symmetry, forming a ring trap [Fig. 2(a)]. This ring geometry is interesting in terms of persistent current and vortex generation [14]. However, it is desirable to break this symmetry and generate a single point minimum in the trapping potential for controlled production of condensates. Furthermore, the critical temperature in a ring trap for a given atom number is typically low because there is no confinement along the azimuthal direction. In previous experiments, this ring symmetry was broken by applying a plug beam in the transverse direction [5] or using an elliptical beam [9]. In our experiment, we simply displaced the plug beam from the zero of the magnetic field by $\simeq 17\ \mu$m [Fig. 2(b)]. It has been emphasized that misalignment of a plug is detrimental to BEC production [9]. We found that a slight misalignment smaller than a beam waist is effectively helpful without significantly losing the plugging effect. The position stability of our plug beam was estimated to be less than 5 μm.

The effective potential for atoms in the plugged trap is

$$U(\mathbf{r}) = \mu B' \sqrt{\frac{x^2}{4} + \frac{y^2}{4} + z^2} + U_p \exp\left(-\frac{(x+d)^2}{2w^2}\right) - mgz, \quad (1)$$

where $\mu = \mu_B/2$ (μ_B is the Bohr magneton) and m are the magnetic moment and mass of the atom, respectively, d is the plug beam offset from the field center, and g is the gravity acceleration. We have ignored the beam focusing because the Rayleigh length $\pi w^2/\lambda \approx 12$ mm is larger than the sample size. For our typical final condition with $B' = 30$ G/cm and $d = 17\ \mu$m, we estimate the trap minimum to be located at $(x_0, y_0, z_0) = (60, 0, 15)\ \mu$m, with a magnetic field of about 100 mG. From the potential local curvature, the trapping

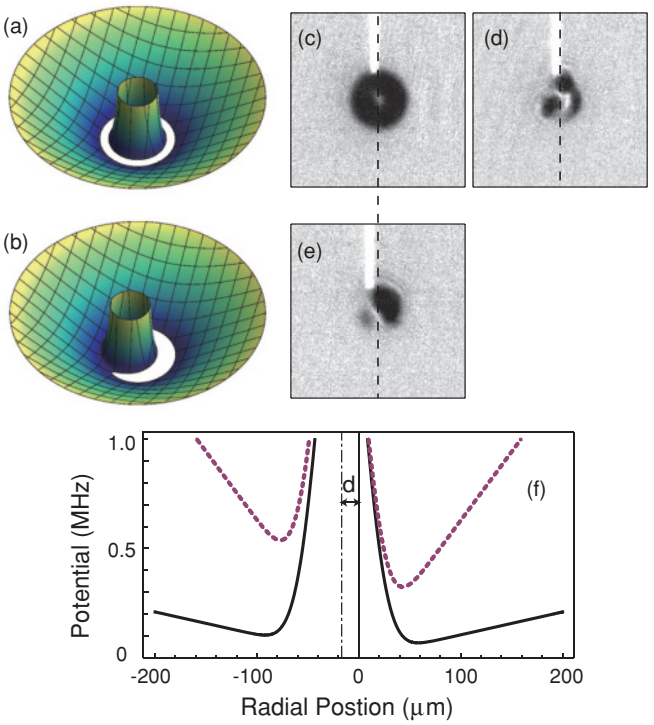

FIG. 2. (Color online) Off-center plugged trap. Schematic diagrams of the combined trapping potential with a plug beam (a) passing the field center and (b) slightly displaced from the center. The ring symmetry is broken by the displacement, and a single minimum is generated in the trap. *In situ* absorption images of atoms in a ring trap after evaporation with a final rf of (c) 150 kHz and (d) 110 kHz, where multiple small condensates containing $<10^6$ atoms are produced due to the imperfection of the plug beam profile. (e) *In situ* image where the plug beam is displaced by $d \approx 17\ \mu$m and the final rf is 105 kHz. A condensate of $\approx 10^7$ atoms is produced in a single potential minimum. The white trace lines in the images are from the leakage of the plug beam out of filters, which are used for determining the relative beam position. The field of view is $750 \times 750\ \mu$m^2. (f) Radial potential along the trap minimum at $B' = 30$ G/cm (solid lines) and 180 G/cm (dashed lines).

frequencies are estimated to be $(f_x, f_y, f_z) \approx (210, 55, 110)$ Hz. With $d = 0.4w$, the plugging potential at the zero-field point is reduced by about 25% to $k_B \times 68\ \mu$K. At low temperatures, we observed multiple atom clouds due to small imperfections in the profile of our plug beam [Fig. 2(d)]. The potential variation leading to this fragmentation was determined to be about $h \times 10$ kHz from the density distributions for various final rf values, where h is the Planck constant. In the off-center plugged trap, a single potential minimum was formed at $h \times 30$ kHz lower than next potential minimum [Fig. 2(e)].

B. Evaporation process

Evaporative cooling was performed by linearly sweeping the applied radio frequency $\nu_{\rm rf}$ from 30 to 2 MHz in 12 s and then to 0.1 MHz in another 2 s [Fig. 3(a)]. The quadrupole field gradient B' was ramped down from 180 to 30 G/cm in the last 2 s. This trap decompression was necessary to achieve a large condensate, reducing inelastic losses associated with high atom density, such as three-body recombinations.

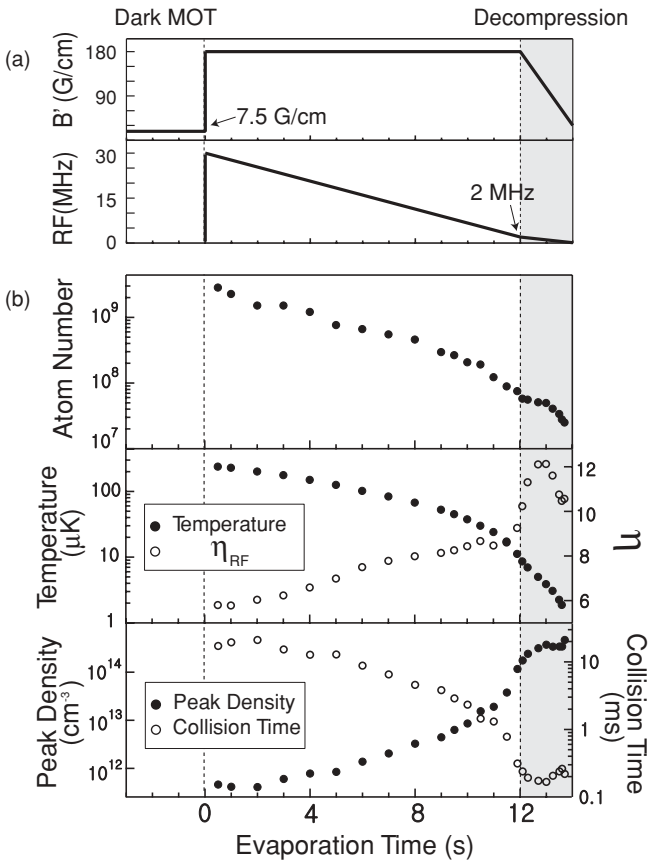

FIG. 3. Experimental sequence for BEC production, which consists of dark MOT, rf evaporation, and trap decompression. (a) Field gradient and radio frequency. (b) Time evolution of atom number, temperature, truncation parameter η, peak density, and collision time. The decompression phase is indicated with a grey zone.

Furthermore, decompression results in adiabatic cooling of the atom cloud, thus relatively enhancing the plugging effect. During the adiabatic process in a linear trap, atom density and temperature scale as B' and $B'^{2/3}$, respectively.

The time evolution of atom number and temperature during the evaporation was determined from absorption images taken after an 18-ms time of flight [Fig. 3]. Peak density n and collision time τ are estimated as $n = N/[32\pi(k_BT/\mu B')^3]$ and $\tau^{-1} = \sqrt{2}n\sigma\bar{v}$, respectively, ignoring gravity and the plug potential. $\sigma = 8\pi a^2$ is the elastic collision cross section, where scattering length $a = 52a_0$ (a_0 is the Bohr radius) [15] and $\bar{v} = (8k_BT/\pi m)^{1/2}$ is the average thermal velocity. The truncation parameter η is defined as $\eta = (h\nu_{\rm rf} - U_0)/k_BT$, where U_0 is the potential at the trap bottom and $U_0/h \approx$ 320 kHz at 180 G/cm and ≈70 kHz at 30 G/cm [Fig. 2(f)]. Runaway evaporation was achieved with increasing collision rate τ^{-1}. When the decompression started, the peak density was estimated to be $\sim 10^{14}/\text{cm}^3$. η smoothly increased from 6 to 9 before the decompression.

Bose-Einstein condensation was observed after 13.7 s of evaporation from the onset of bimodal distribution in the absorption image [Fig. 4(b)]. At this transition point, the atom number and the temperature were $N_c = 2.5 \times 10^7$ and $T_c = 1.4$ μK, respectively. The overall evaporation efficiency is $\gamma = -\ln(D_c/D_i)/\ln(N_c/N_i) = 2.7$, where D is peak phase-space density, given as $D = n\lambda_{dB}^3$ ($\lambda_{dB} = h/\sqrt{2\pi mk_BT}$ is the thermal de Broglie wavelength), and the critical phase-space density is $D_c = 2.61$. With 14 s of full evaporation, an almost-pure condensate with $N = 1.0 \times 10^7$ was obtained. After an additional decompression to $B' =$ 15 G/cm, the lifetime of the condensate was 10 s, which is long enough for further manipulation, such as transferring into an optical dipole trap.

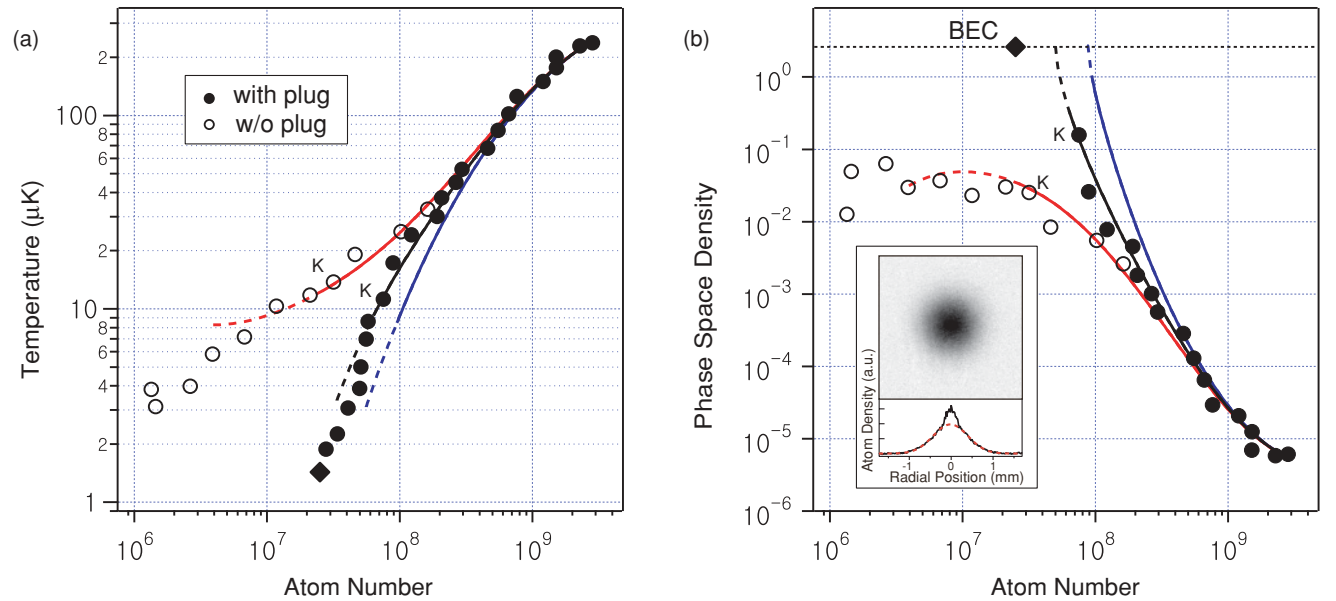

FIG. 4. (Color online) Evaporation trajectory. (a) Temperature versus atom number. (b) Peak phase-space density versus atom number. Data points at 11.9 s (before decompression) are marked with K's. The onset of condensation is observed at 13.7 s in a plugged trap from the bimodal momentum distribution (see inset). The black diamond indicates the transition point. The solid lines are from numerical simulation with a plug (black), no plug (light grey, red online), and no loss (dark grey, blue online). The dashed lines are the evolution after 12 s (see Sec. III).

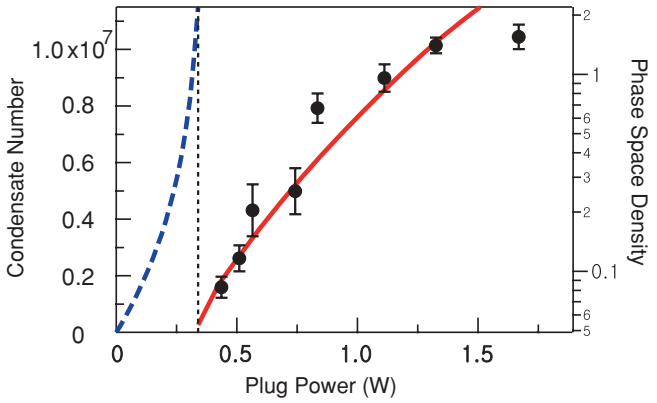

FIG. 5. (Color online) Condensate number versus plug power. Each point is averaged over three separate runs of the experiment. Maximum phase-space density (dashed line) and condensate number (solid line) from numerical simulation (see Sec. III).

The evaporation in a bare quadrupole trap was also investigated without the plug beam. Figure 4 shows the evaporation trajectories in the N-T and N-D planes. At $T < 20$ μK, the plugging effect becomes noticeable from the deviation between the evaporation curves with and without plugging. The maximum phase-space density was about 5×10^{-2} in an unplugged quadrupole trap. The minimum plug beam power for making a condensate of $>10^6$ atoms was $\sim$0.4 W for the 14 s of evaporation (Fig. 5). In our experiment setup, we could minimize the evaporation time to 8 s to observe a condensate.

C. Effects of Majorana loss

The Majorana spin flips cause heating as well as atom number reduction. To quantitatively understand the loss effects, we have measured the loss and heating rate of a thermal gas for various temperatures with and without the plug at $B' = 180$ G/cm (Fig. 6). The initial sample temperature was controlled with the final value of radio frequency. The time evolution of the atom number and temperature were determined with various holding times. The rf field was turned off after the sample preparation in order to exclude the evaporation effects [16]. We observed that the temperature almost linearly increases with a small acceleration and the number decay rate decreases slowly. The initial loss and heating rate were determined from an exponential fit and a linear fit, respectively, to the data points with temperatures lower than 120% of the initial temperature.

A simple argument in Ref. [17] suggests that the Majorana loss rate Γ_m in a quadrupole trap scales as $\Gamma_m \propto \hbar/m(\mu B'/k_B T)^2$. A fit to our data in Fig. 6(a) with $CT^{-2} + \Gamma_b$ yields $C = 139(3)$ μK^2/s and $\Gamma_b = 0.013(7)$ s^{-1}, where Γ_b is the background loss rate (corresponding to a lifetime of 75 s). This result suggests $\Gamma_m = 0.14\hbar/m(\mu B'/k_B T)^2$. The proportionality constant is found to be much smaller than the values of 0.58 [17,18] and 0.87 [10] in previous experiments with ^{87}Rb atoms, which is beyond the simple model. Note that the lifetime of ^{23}Na atoms in a quadrupole trap is comparable to that of ^{87}Rb atoms, even with their mass difference.

A spin flip happens when the spin of a moving atom cannot adiabatically follow the field orientation, so the flipping

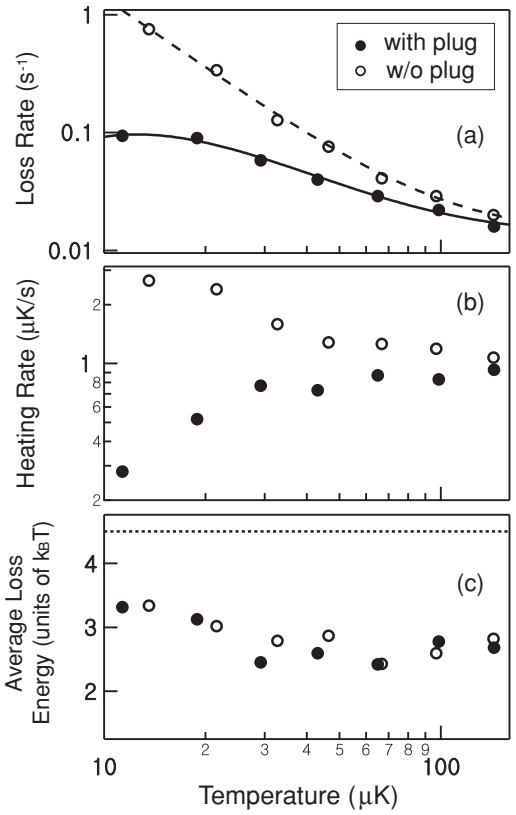

FIG. 6. Majorana loss in a magnetic quadrupole trap. (a) Loss rates and (b) heating rates for various temperature at the field gradient $B' = 180$ G/cm. Solid curves are fits to the data with a loss model, Eq. (2) (see text for detail). (c) Average energy of a lost atom due to the Majorana spin flip. The dot line indicates the average energy of an atom in a linear trap.

probability of an atom at a given position is fully determined by the local field strength, its gradient, and the velocity distribution of the atom, i.e., temperature. Therefore, the plugging effect is a consequence of the density suppression due to the optical repulsive potential in the low-field, spin-flipping region. Including a Boltzmann density suppression factor, the reduced loss rate would be given as

$$\Gamma_m^{\text{plug}} = \Gamma_m f \exp(-U^*/k_B T), \tag{2}$$

where U^* is the characteristic potential of the plug and f is a factor depending on the details of the plug beam, such as shape, position, and power. We find this model nicely fits to our data with $C'T^{-2}\exp(-U^*/k_B T) + \Gamma_b$, where $U^* = k_B \times 25(1)$ μK and $C' = 97(6)$ μK^2/s ($f \approx 0.7$). This exponential behavior clearly supports our picture of the plugging effect. Note that U^* is consistent with the deviation point in the N-T evaporation trajectories and close to the potential at the trap bottom $U_0 \approx k_b \times 15$ μK. In our experiment, the collision rate was approximately 10^3 times faster than the loss rate, validating the thermal equilibrium assumption.

We characterized the heating effect of the Majorana loss with determination of the average loss energy of a spin-flipped atom $\varepsilon_m k_B T$. From the energy conservation relation $\dot{E} = -\varepsilon_m k_B T \dot{N}$, where $E = N\varepsilon k_B T$ is the total energy of the system with the average energy of a trapped atom $\varepsilon k_B T$, we derive a simple relation between the temperature and the

atom number, $\dot{T}/T = (\varepsilon_m/\varepsilon - 1)\dot{N}/N$. When $\varepsilon_m < \varepsilon$, the system is heated up and vice versa. In a power-law trap $U \propto r^{3/\delta}$, $\varepsilon = (3/2 + \delta)$. Our measurements show that ε_m has a very weak temperature dependence, slightly increasing at low temperatures, with an average value of 2.8, which is less than $\varepsilon = 4.5$ for a linear trap ($\delta = 3$) [Fig. 6(b)]. Remarkably, we observe that ε_m is not affected by the optical plug in the temperature range of 10–100 μK. This is somewhat surprising because the average energy of a lost atom should increase in the presence of the plug due to the repulsive optical potential. We estimate that the effective increment in the average loss energy would be $U^* - U_0 \approx k_B \times 10\ \mu$K with respect to the trap bottom, and it might be observable at lower temperatures.

III. NUMERICAL SIMULATION

In this section, we numerically study the dynamics of the evaporation process in an optically plugged quadrupole trap. Including only three loss processes (background collision, rf evaporation, and the Majorana spin flip), the rate equations for the atom number N and temperature T are given as

$$\frac{\dot{N}}{N} = -\Gamma_b - \Gamma_e - \Gamma_m, \tag{3a}$$

$$\frac{\dot{T}}{T} = -\left(\frac{\varepsilon_e}{\varepsilon} - 1\right)\Gamma_e - \left(\frac{\varepsilon_m}{\varepsilon} - 1\right)\Gamma_m, \tag{3b}$$

where Γ_e is the evaporation loss rate and $\varepsilon_e = \eta + \kappa$ is the average energy of an evaporated atom in $k_B T$. The first term in Eq. (3b) corresponds to the cooling from evaporation. We assume that the background collision loss occurs equally to all trapped atoms, thus not affecting the temperature.

The simulation for our experiment was performed under the following conditions: $N(0) = N_i$ and $T(0) = T_i$ at $t = 0$ s, $\nu_{\rm rf}(t) = (30 - 7t/3)$ MHz, $\eta = h\nu_{\rm rf}/k_B T$, $\Gamma_b = 0.013$/s, and $\varepsilon_m = 0.28$. The Majorana loss rate is parameterized with the plug beam power P as $\Gamma_m = C(1 - aP)T^{-2}\exp(-bP/T)$, where $C = 139\ \mu\text{K}^2/\text{s}$, $a = 0.176$/W, and $b = 1.48\ \mu$K/W. For three-dimensional (3D) evaporation in a linear trap ($\delta = 3$), standard evaporation theory [19] gives $\Gamma_e^{\rm theory} = n\sigma\bar{v}e^{-\eta}[\eta P(\frac{9}{2},\eta) - \frac{11}{2}P(\frac{11}{2},\eta)]/P(\frac{9}{2},\eta)^2$ and $\kappa = 1 - P(\frac{13}{2},\eta)/[\eta P(\frac{9}{2},\eta) - \frac{11}{2}P(\frac{11}{2},\eta)]$, respectively, where $P(a,\eta)$ is the incomplete gamma function [20]. However, the observed evaporation speed was almost 2 times faster than the theoretical value. This result is quite surprising because the theoretical estimation accounts for the maximum 3D evaporation, and it is worthy of further investigation. We empirically set $\Gamma_e = 1.95\Gamma_e^{\rm theory}$ in our simulation.

The simulated evaporation trajectories are presented with the experiment data in Fig. 4. The trap decompression is not included in our simulation, so the trajectories deviate from the data points after 12 s. The maximum phase-space density and the critical atom number N_c at the phase transition were numerically estimated as a function of the plug beam power (Fig. 5) and show a good agreement with the experiment results. We approximate the condensate number at 25% of the critical atom number. The simulation with a perfect plug, i.e., $\Gamma_m = 0$ [dark grey lines (blue online) in Fig. 4], suggests that the maximum condensate would have $N \approx 2 \times 10^7$ atoms for the given 14 s of evaporation.

IV. CONCLUSIONS

We have described a rapid production of ^{23}Na Bose-Einstein condensates in an optically plugged magnetic quadrupole trap. The off-axis optical plug generates a single global minimum in the combined trapping potential and consequently enhances the BEC production. The Majorana loss, which is critical in a quadrupole trap, has been quantitatively investigated, determining the average loss energy of a spin-flipped atom and the loss rate suppression of the optical plug. We have presented a simple model to explain the evaporation dynamics in the plugged quadrupole trap. This model will be helpful for developing and optimizing evaporation processes using a magnetic quadrupole trap.

ACKNOWLEDGMENTS

The authors thank A. Keshet for the experimental control software and M. Lee for experimental help. This work was supported by WCU program Grant No. R32-2008-000-10045-0 and NRF Grant No. 2010-0010172. J.C. acknowledges financial supports from MOE through BK21 fellowships.

[1] I. Bloch, J. Dalibard, and W. Zwerger, Rev. Mod. Phys. **80**, 885 (2008).
[2] M. Lewenstein, A. Sanpera, V. Ahufinger, B. Damski, A. Sen, and U. Sen, Adv. Phys. **56**, 243 (2007).
[3] D. Jaksch and P. Zoller, Ann. Phys. **315**, 52 (2005).
[4] M. H. Anderson, J. R. Ensher, M. R. Matthews, C. E. Wieman, and E. A. Cornell, Science **269**, 198 (1995).
[5] K. B. Davis, M. O. Mewes, M. R. Andrews, N. J. van Druten, D. S. Durfee, D. M. Kurn, and W. Ketterle, Phys. Rev. Lett. **75**, 3969 (1995).
[6] M. D. Barrett, J. A. Sauer, and M. S. Chapman, Phys. Rev. Lett. **87**, 010404 (2001).
[7] W. Ketterle and N. J. van Druten, Adv. At. Mol. Opt. Phys. **37**, 181 (1996).
[8] K. B. Davis, M.-O. Mewes, M. A. Joffe, M. R. Andrews, and W. Ketterle, Phys. Rev. Lett. **74**, 5202 (1995).
[9] D. S. Naik and C. Raman, Phys. Rev. A **71**, 033617 (2005).
[10] Y. J. Lin, A. R. Perry, R. L. Compton, I. B. Spielman, and J. V. Porto, Phys. Rev. A **79**, 063631 (2009).
[11] E. W. Streed, A. P. Chikkatur, T. L. Gustavson, M. Boyd, Y. Torii, D. Schneble, G. K. Campbell, D. E. Pritchard, and W. Ketterle, Rev. Sci. Instrum. **77**, 023106 (2006).
[12] W. Ketterle, K. B. Davis, M. A. Joffe, A. Martin, and D. E. Pritchard, Phys. Rev. Lett. **70**, 2253 (1993).
[13] We could not achieve a condensate even with a 6-W plug beam when the beam was sent from a laser in free space. The laser was placed on a different optical table 4 m away from the machine.

[14] C. Ryu, M. F. Andersen, P. Cladé, V. Natarajan, K. Helmerson, and W. D. Phillips, Phys. Rev. Lett. **99**, 260401 (2007).

[15] E. Tiesinga, C. J. Williams, P. S. Julienne, K. M. Jones, P. D. Lett, and W. D. Phillips, J. Res. Natl. Inst. Stand. Technol. **101**, 505 (1996).

[16] In Ref. [10], a rf field was applied to maintain a constant temperature. We observed nonmonotonic behavior of the temperature with this method, i.e., initially cooling and then heating.

[17] W. Petrich, M. H. Anderson, J. R. Ensher, and E. A. Cornell, Phys. Rev. Lett. **74**, 3352 (1995).

[18] The radial half width at half maximum cloud size l is approximately $2.5(k_B T/\mu B')$ in an in-trap column density distribution and $2\ln 2(k_B T/\mu B')$ in a 3D distribution.

[19] O. J. Luiten, M. W. Reynolds, and J. T. M. Walraven, Phys. Rev. A **53**, 381 (1996).

[20] $P(a,\eta) \equiv \frac{1}{\Gamma(a)} \int_0^\eta dt t^{a-1} e^t$. The peak density n is related to the reference density n_0 in Ref. [19] as $n = n_0 P(\frac{9}{2},\eta)$.

Appendix E

Probing phase fluctuations in a 2D degenerate Bose gas by free expansion

This appendix includes a reprint of Ref. : Jae-yoon Choi, Sang Won Seo, Woo Jin Kwon, and Yong-il Shin. *"Probing phase fluctuations in a 2D degenerate Bose gas by free expansion"* Physical Review Letters **109**, 125301 (2012).

Probing Phase Fluctuations in a 2D Degenerate Bose Gas by Free Expansion

Jae-yoon Choi, Sang Won Seo, Woo Jin Kwon, and Yong-il Shin*

Center for Subwavelength Optics and Department of Physics and Astronomy, Seoul National University, Seoul 151-747, Korea

(Received 11 June 2012; published 19 September 2012)

We measure the power spectrum of the density distribution of a freely expanding two-dimensional (2D) degenerate Bose gas, where irregular density modulations gradually develop due to initial phase fluctuations in the sample. The spectrum has an oscillatory shape, where the peak positions are found to be independent of temperature and show scaling behavior in the course of expansion. The relative intensity of phase fluctuations is estimated from the normalized spectral peak strength and observed to decrease at lower temperatures, confirming the thermal nature of the phase fluctuations. We investigate the relaxation dynamics of nonequilibrium states using the power spectrum. Free vortices are observed with ring-shaped density ripples in a perturbed sample after a long relaxation time.

DOI: 10.1103/PhysRevLett.109.125301 PACS numbers: 67.85.−d, 03.75.Hh, 03.75.Lm

Phase coherence is one of the main characteristics of superfluidity and critically affected by the dimensions of the system. In low-dimensional systems, large thermal and quantum phase fluctuations prohibit the establishment of long-range phase coherence, which is a typical order parameter for three-dimensional (3D) superfluid [1,2]. Nevertheless, a two-dimensional (2D) interacting system can undergo a superfluid phase transition at a finite critical temperature with an algebraically decaying coherence. This transition is successfully described in the Berezinskii-Kosterlitz-Thouless (BKT) theory [3,4] as a topological phase transition, where the critical point is associated with the spontaneous pairing of free vortices with opposite circulations.

Recent experiments with 2D atomic Bose gases have demonstrated that this BKT physics can be studied in a finite-size trapped sample [5–11]. Phase coherence and thermodynamic properties have been investigated using matter-wave interference, and by detailed analysis of the *in situ* density and momentum distributions of trapped samples, where the algebraic decay of coherence [5], a presuperfluid regime [7–10], and the scale invariance of the equation of state [9,11] have been observed. It is now highly desirable to have quantitative probes directly sensitive to phase fluctuations in order to study the topological nature of phase transition. In particular, nonequilibrium phase dynamics near the critical point would provide valuable insights into the BKT transition. Relaxation dynamics in the 2D XY model have been under intense theoretical investigation [12,13], and recently an experimental scheme to study the dynamic BKT transition in 2D Bose gases has been proposed [14].

In this Letter, we demonstrate a new quantitative probe for phase fluctuations in a 2D degenerate Bose gas using the density correlations in a freely expanding sample. Irregular density modulations gradually develop in the coherent part of samples during expansion. We observe that the power spectrum of the density distribution has an oscillatory shape, and find that the peak positions are independent of temperature and show scaling behavior in the course of expansion. The relative intensity of phase fluctuations is estimated from the spectral peak strength normalized with the central density of the coherent part, and we show that it decreases at lower temperatures in thermal equilibrium. This confirms the thermal nature of phase fluctuations in the 2D system. In addition, we investigate the relaxation dynamics of nonequilibrium states by measuring the time evolution of the relative intensity of phase fluctuations. Interestingly, ring-shaped density ripples stochastically appear in a perturbed sample after a long relaxation time, which we identify with free vortices having a long lifetime in a 2D sample.

We prepare a 2D degenerate Bose gas of ^{23}Na atoms in a single pancake-shape optical dipole trap [15,16]. Thermal atoms in the $|F = 1, m_F = -1\rangle$ state are loaded from a plugged magnetic trap [17] into the optical trap, and evaporative cooling is applied by reducing the trap depth. The sample temperature is controlled by the final trap depth in evaporation, resulting in 0.6 to 1.3×10^6 atoms in a sample. Finally, the optical trap depth ramps up, and the trapping frequencies $(\omega_x, \omega_y, \omega_z)$ become $2\pi \times (3.0, 3.9, 370)$ Hz. The cooling procedure is intentionally set to be slow over 15 s, ensuring thermal equilibrium. The lifetime in the optical trap is over 50 s. In the Thomas-Fermi approximation, the chemical potential is about $h \times 260$ Hz less than the confining energy $\hbar\omega_z$, and so we expect 2D physics in the phase coherence of the sample at low temperatures. The dimensionless interaction strength $\tilde{g} = a\sqrt{8\pi m\omega_z/\hbar} \simeq 0.013$, where a is the 3D scattering length and m the atomic mass. The in-plane density distribution $n(x, y)$ is measured by taking an absorption image after an expansion time t_e, which is initiated by suddenly turning off the trapping potential.

Expansion has been a conventional and powerful method in quantum gas experiments to study coherence properties of a sample [7,10]. In our experiment, we are

interested in the short expansion regime where $t_e \ll 1/\omega_{x,y}$ and the phase coherence information would be revealed as density correlations. Since the sample initially expands fast along the tight direction, the atom interaction effects are rapidly reduced, and the subsequent evolution in other directions can be described as free expansion. When the sample contains phase fluctuations, self interference would result in density modulations in the expanding sample. This method has been exploited in previous studies of phase fluctuations in elongated Bose-Einstein condensates [18] and 1D Bose gases [19].

We observe that density fluctuations develop in an expanding 2D Bose gas (Fig. 1), where the characteristic size and visibility of the density lumps increases with the expansion time. Density fluctuations appear discernible only when the sample shows a bimodal density distribution, so that we refer to the center part as the coherent part of the sample [6,7]. In order to obtain the density correlation information, we measure the power spectrum of the density distribution as the square of the magnitude of its Fourier transform, $P(\vec{q}) = |\int dxdy e^{i\vec{q}\cdot\vec{r}} n(\vec{r})|^2$. Although the spatial pattern of the density modulations appears random in each realization, the power spectrum clearly reveals a multiple ring structure that scales down with the expansion time [Figs. 1(c) and 1(f)]. For quantitative analysis, we obtain a 1D spectrum, $P(q)$, by azimuthally averaging the 2D spectrum (Fig. 2) [20]. The strong signal around $q = 0$ corresponds to the finite size of the coherent part.

The scaling behavior of the spectrum can be qualitatively understood in terms of the Talbot effect [21,22]. It is well known in near-field diffraction that when a grating is illuminated by monochromatic waves, the identical self-image of the grating is formed at a distance $L_T = 2d^2/\lambda$ away from the grating, where d is the grating period and λ is the wavelength of the incident radiation. The same effect occurs with phase grating [23]. In matter wave optics, $\lambda = h/mv$, where v is the incident speed of atoms [24]; so the propagation time for self-imaging is defined as $t_T = L_T/v = 2md^2/h$ independent of v. If we consider a 2D Bose gas as a macroscopic matter wave containing phase fluctuations at all length scales, it is expected that the component of wave number q satisfying the Talbot condition $q^2 = 4\pi m/\hbar t_e$ will emerge predominantly in the density distribution at a given expansion time t_e. The multiple peaks in $P(q)$ can be accounted for by the fractional Talbot effect where self-images with smaller periods d/n ($n > 0$ is an integer) are produced at $L_T/2n$ [22].

Recently, theoretical calculations on the spectrum of density modulations have been performed for a homogeneous 2D Bose gas at low temperatures [25], showing that the nth peak position q_n closely satisfies $\hbar q_n^2 t_e/2\pi m \approx (n - 1/2)$. In particular, they predict that

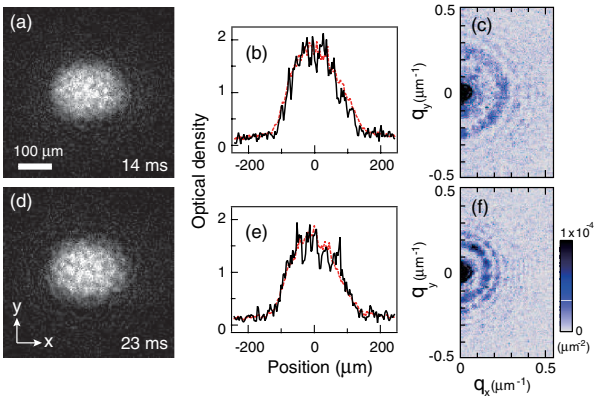

FIG. 1 (color online). Emergence of density fluctuations in a freely expanding 2D Bose gas. Density distributions after (a) $t_e = 14$ ms and (d) 23 ms of time of flight. Density fluctuations gradually develop during expansion, increasing their length scale and visibility. (b), (e) The horizontal density profiles in the center of the samples. The red dashed lines indicate the averaged profiles over 10 individual realizations of the same experiment. The coherent fraction $\eta \approx 30\%$ (see text for details). The power spectrum of density distribution is measured with the magnitude square of its Fourier transform. (c), (f) The averaged power spectra corresponding to (a), (d).

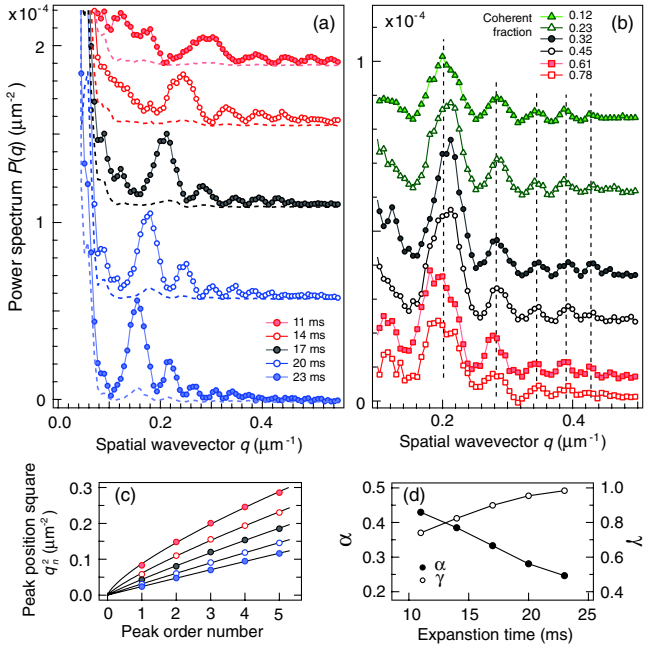

FIG. 2 (color online). The power spectrum of density fluctuations. (a) 1D power spectra $P(q)$ are obtained by azimuthally averaging the averaged 2D spectra for various expansion times t_e. Each spectrum is displayed with an offset for clarity. The dashed lines are the corresponding spectra for the averaged density distributions over 10 individual realizations. (b) $P(q)$ at $t_e = 17$ ms for various temperatures. The spectral peak positions, q_n's, are determined from a fit of multiple Gaussian curves to each spectrum (n is the peak order number). The vertical dashed lines indicate the average peak positions. (c) The empirical function $\hbar q_n^2 t_e/2\pi m = \alpha n^\gamma$ are fit to the peak positions in (a) for each t_e. (d) The expansion time dependence of the two free parameters α and γ.

for sufficiently long expansion times, the spectrum remains self-similar during expansion, and its shape is determined only by the exponent of the power-law decay of the first-order coherence function.

In our experiment, we observe that the spectrum preserves its oscillatory shape during expansion and that the peak positions, q_n's, are independent of temperature (Fig. 2), which are in qualitative agreement with the theoretical prediction. However, we find different scaling behavior of q_n's in the measured spectra, which is well described as $\hbar q_n^2 t_e/2\pi m = \alpha n^\gamma$ with $0.2 < \alpha < 0.45$ and $0.7 < \gamma < 1$ for $t_e = 10 \sim 25$ ms [Fig. 2(d)]. Furthermore, the phase of the spectral oscillation is opposite to the theoretical prediction, suggesting that an additional peak is present at $q_0 = 0$, which is also hinted by the shoulder-like hump in $q < q_1/\sqrt{2}$. We rule out the finite-size effects by seeing no dependence of q_n's on the sample size as well as temperature, implying that the observed scaling behavior might be intrinsic to the expansion dynamics. We note that the long expansion time condition $\sqrt{\hbar t_e/m} \gg \xi_{2D}$ for the validity of the theoretical prediction is marginally fulfilled in our experiment, where $\xi_{2D} = \hbar/\sqrt{m\mu}$ is the 2D healing length, μ being the chemical potential [26].

The universality of the spectral peak positions suggests that the spectral peak strength can be used as a measure of the magnitude of phase fluctuations in the sample. In order to quantify the relative intensity of phase fluctuations, we normalize the strength of the first spectral peak with the square of the central density n_c of the coherent part in the sample, $\tilde{P}(q_1) = P(q_1)/n_c^2$, where n_c is determined from a fit of two Gaussian curves to the density distribution [6,7,27–29].

Using $\tilde{P}(q_1)$, we first investigate the temperature dependence of phase fluctuations in thermal equilibrium. To estimate the relative temperature to the critical point in a model-independent way [8,11], we use the coherent fraction η, defined as the ratio of the atom number of the coherent part to the total atom number. The value of η was constant within 5% for our expansion times. Figure 3 shows that $\tilde{P}(q_1)$ is suppressed at lower temperatures (higher η), confirming the thermal nature of phase fluctuations.

For a weakly interacting 2D Bose gas, especially for our small $\tilde{g} = 0.013$, the BKT critical temperature T_c is close to the Bose-Einstein condensation critical temperature for a trapped ideal Bose gas $T_{\mathrm{BEC}} = 0.94\hbar(\omega_x\omega_y\omega_z N)^{1/3}/k_B$ [7,27,28]. We estimate $T_c \approx 80$ nK for $N \approx 1.3 \times 10^6$. Since $k_B T_c \approx 4\hbar\omega_z$, thermal populations in the tight direction is not negligible, accounting for the Gaussian-like profile of the saturated thermal cloud [27,28]. The rapid increase of $\tilde{P}(q_1)$ at $\eta < 0.2$ might indicate the behavior in the proximity of the critical point. In Ref. [7], the critical point was identified at $\eta \approx 0.1$, with an abrupt change in the width of the coherent part. Since the spatial extent of the coherent part becomes small, the signal-to-noise ratio is poor when $\eta \leq 0.05$, and we cannot study the presuperfluid regime where the decay of the coherence function changes from algebraic to exponential, which might be reflected in the spectral shape.

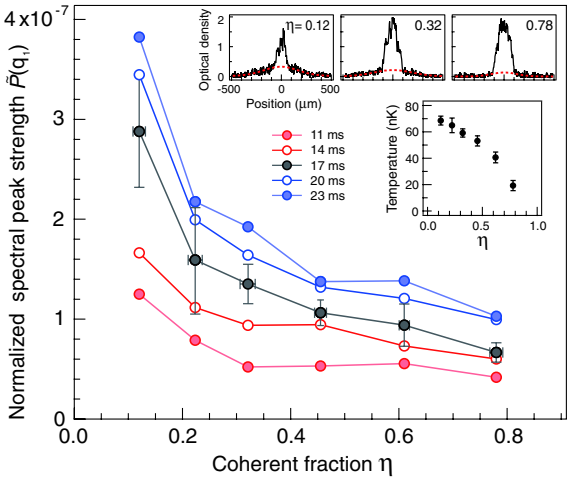

FIG. 3 (color online). Temperature dependence of phase fluctuations at thermal equilibrium. The relative intensity of phase fluctuations is estimated from the normalized strength of the first spectral peak $\tilde{P}(q_1)$, and the relative temperature is parameterized with the coherent fraction. The upper insets show the density profiles for different temperatures. The red dashed lines are Gaussian fits to the thermal wings, from which temperatures are estimated (lower inset). Each data point consists of 10 independent measurements, and error bars indicate standard deviation.

The power spectrum can be used to study nonequilibrium dynamics in a 2D Bose gas. For this study, we prepare a 2D sample in a nonequilibrium state by transferring a condensate instead of thermal atoms from the plugged magnetic trap into the optical trap. The induced perturbations are sufficiently small so that the density profile in the optical trap is quite close to that at equilibrium. In Fig. 4(a), we plot the time evolutions of the samples in various initial conditions in the plane of $\tilde{P}(q_1)$ and η [Fig. 4(f)], clearly showing that the nonequilibrium states decay to equilibrium. The decay time of the excess phase fluctuations with respect to the equilibrium value is measured to ~4 s, corresponding to ~10 collision times in our typical condition. Note that the hottest sample first decays, and then moves along the equilibrium line with increasing η because of the evaporation cooling due to the finite trap depth. This confirms that our previous measurements are indeed for phase fluctuations in thermal equilibrium.

Remarkably, ring-shaped density ripples are observed in the perturbed samples after long relaxation times (Fig. 4). We believe that this corresponds to vortex excitations generated in the sample transferring procedure. Since a vortex in two-dimensions can decay only via pairing with another vortex with opposite circulation

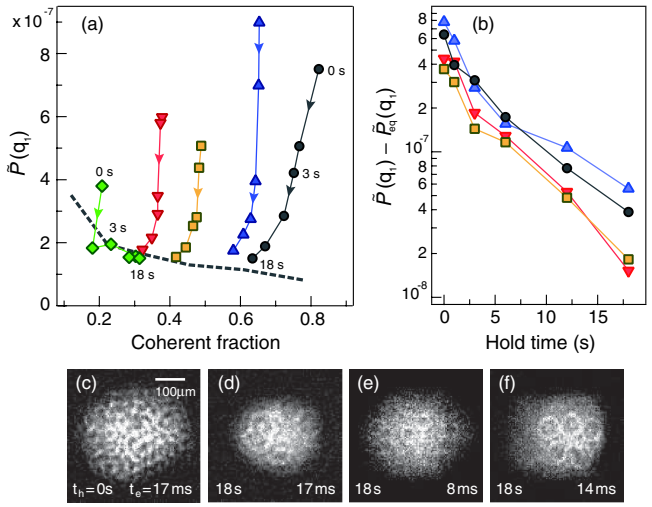

FIG. 4 (color online). Relaxation of a nonequilibrium 2D Bose gas. (a) Time evolutions of various nonequilibrium states in the plane of $\tilde{P}(q_1)$ and η ($t_e = 17$ ms). The dashed line is the interpolation for the thermal equilibrium data with $t_e = 17$ ms in Fig. 3. (b) The decay curves of the excess phase fluctuations $\tilde{P}(q_1) - \tilde{P}_{\rm eq}(q_1)$, where $\tilde{P}_{\rm eq}(q_1)$ is the equilibrium value corresponding to η at $t_h = 18$ s of hold time. Density distributions of the lowest temperature sample at (c) $t_h = 0$ s and (d) 18 s with $t_e = 17$ ms, and at $t_h = 18$ s with (e) $t_e = 8$ ms and (f) 23 ms. The samples in (e) and (f) were strongly perturbed to obtain more ring-shaped density ripples.

or by drifting out of the finite sample, we may expect a metastable state, with vortices having a long lifetime. Recently, it has been reported that vortex excitations survive longer in an oblate condensate because Kelvin mode excitations on a vortex line are suppressed [30,31]. The ring pattern appears more often at lower temperatures with stronger perturbations. In the two lowest temperature cases (circle and triangle in Fig. 4), the appearance probability is about 60% at $t_h = 18$ s of hold time, where the spectral strength of the samples with vortices is about 10% higher than without them. In Fig. 4(b), the decay rates of the two coldest samples become slightly slower after $t_h > 5$ s, which might be attributed to the long lifetime of vortices. Figures 4(d)–4(f) show the expansion dynamics of the ring-shape density ripples. In the thermal equilibrium case, the ring pattern was never clearly seen for $\eta > 0.2$.

In conclusion, we have demonstrated the power spectrum of density fluctuations in a freely expanding 2D Bose gas as a new quantitative probe for phase fluctuations. Together with more controlled perturbations [32,33], we expect this method to be extended for studying nonequilibrium phenomena in BKT physics such as critical exponents [12,13] and dynamic transitions [14,34].

This work was supported by the NRF grants funded by the Korea government (MEST) (Grants No. 2010-0010172, No. 2011-0017527, No. 2008-0062257, and No. WCU-R32-10045). J. C, S. S. W, and Y. S. acknowledge support from the Global PhD Fellowship, the Kwanjeong Scholarship, and the T. J. Park Science Fellowship, respectively.

*yishin@snu.ac.kr

[1] N. D. Mermin and H. Wagner, Phys. Rev. Lett. **17**, 1133 (1966).
[2] P. Hohenberg, Phys. Rev. **158**, 383 (1967).
[3] V. L. Berezinskii, Sov. Phys. JETP **34**, 610 (1972).
[4] J. M. Kosterlitz and D. J. Thouless, J. Phys. C **6**, 1181 (1973); J. M. Kosterlitz *ibid.* **7**, 1046 (1974).
[5] Z. Hadzibabic, P. Krüger, M. Cheneau, B. Battelier, and J. Dalibard, Nature (London) **441**, 1118 (2006).
[6] P. Krüger, Z. Hadzibabic, and J. Dalibard, Phys. Rev. Lett. **99**, 040402 (2007).
[7] P. Cladé, C. Ryu, A. Ramanathan, K. Helmerson, and W. D. Phillips, Phys. Rev. Lett. **102**, 170401 (2009).
[8] S. Tung, G. Lamporesi, D. Lobser, L. Xia, and E. A. Cornell, Phys. Rev. Lett. **105**, 230408 (2010).
[9] C.-L. Hung, X. Zhang, N. Gemelke, and C. Chin, Nature (London) **470**, 236 (2011).
[10] T. Plisson, B. Allard, M. Holzmann, G. Salomon, A. Aspect, P. Bouyer, and T. Bourdel, Phys. Rev. A **84**, 061606(R) (2011).
[11] T. Yefsah, R. Desbuquois, L. Chomaz, K. J. Günter, and J. Dalibard, Phys. Rev. Lett. **107**, 130401 (2011).
[12] B. Yurke, A. N. Pargellis, T. Kovacs, and D. A. Huse, Phys. Rev. E **47**, 1525 (1993).
[13] A. J. Bray, A. J. Briant, and D. K. Jervis, Phys. Rev. Lett. **84**, 1503 (2000).
[14] L. Mathey, K. J. Günter, J. Dalibard, and A. Polkovnikov, arXiv:1112.1204.
[15] J. Choi, W. J. Kwon, and Y. Shin, Phys. Rev. Lett. **108**, 035301 (2012).
[16] J. Choi, W. J. Kwon, M. Lee, H. Jeong, K. An, and Y. Shin, New J. Phys. **14**, 053013 (2012).
[17] M. S. Heo, J. Choi, and Y. Shin, Phys. Rev. A **83**, 013622 (2011).
[18] S. Dettmer *et al.*, Phys. Rev. Lett. **87**, 160406 (2001).
[19] S. Manz *et al.*, Phys. Rev. A **81**, 031610(R) (2010).
[20] The resolution of our imaging system is about 5 μm, so the spectral signal at $q > 1$ μm^{-1} is purely contributed from photon shot noises. We subtract the constant offset value at high q from the spectrum, which is typically a few % of $P(q_1)$.
[21] H. F. Talbot, Philos. Mag. **9**, 401 (1836); L. Rayleigh *ibid.* **11**, 196 (1881).
[22] J. T. Winthrop and C. R. Worthington, J. Opt. Soc. Am. **55**, 373 (1965).
[23] A. W. Lohmann and J. A. Thomas, Appl. Opt. **29**, 4337 (1990).
[24] M. S. Chapman, C. R. Ekstrom, T. D. Hammond, J. Schmiedmayer, B. E. Tannian, S. Wehinger, and D. E. Pritchard, Phys. Rev. A **51**, R14 (1995).
[25] A. Imambekov, I. E. Mazets, D. S. Petrov, V. Gritsev, S. Manz, S. Hofferberth, T. Schumm, E. Demler, and J. Schmiedmayer, Phys. Rev. A **80**, 033604 (2009).

[26] In our experiment, $\sqrt{\frac{\hbar t_e}{m}}/\xi_{2D} = \sqrt{t_e \mu/\hbar} < 6$. The focal depth of our imaging system is ~ 100 μm, limiting the expansion time $t_e < 40$ ms.

[27] Z. Hadzibabic, P. Krüger, M. Cheneau, S. P. Rath, and J. Dalibard, New J. Phys. **10**, 045006 (2008).

[28] H. Holzmann, M. Chevallier, and W. Krauth, Europhys. Lett. **82**, 30001 (2008).

[29] At low temperatures, the density profile of the coherent part is close to a parabola shape, but the Gaussian fit still gives a good estimation for n_c within a few %.

[30] T. W. Neely, E. C. Samson, A. S. Bradley, M. J. Davis, and B. P. Anderson, Phys. Rev. Lett. **104**, 160401 (2010).

[31] S. J. Rooney, P. B. Blakie, B. P. Anderson, and A. S. Bradley, Phys. Rev. A **84**, 023637 (2011).

[32] L. E. Sadler, J. M. Higbie, S. R. Leslie, M. Vengalattore, and D. M. Stamper-Kurn, Nature (London) **443**, 312 (2006).

[33] S .Hofferberth, I. Lesanovsky, B. Fisher, T. Schumm, and J. Schiedmayer, Nature (London) **449**, 324 (2007).

[34] G. Roumpos *et al.*, Proc. Natl. Acad. Sci. U.S.A. **109**, 6467 (2012).

Appendix F

Observation of thermally activated vortex pairs in a Quasi-2D Bose gas

This appendix includes a reprint of Ref. : Jae-yoon Choi, Sang Won Seo, and Yong-il Shin. *"Observation of thermally activated vortex pairs in a Quasi-2D Bose gas"* Physical Review Letters **110**, 175302 (2013).

Observation of Thermally Activated Vortex Pairs in a Quasi-2D Bose Gas

Jae-yoon Choi, Sang Won Seo, and Yong-il Shin*

Center for Subwavelength Optics and Department of Physics and Astronomy, Seoul National University, Seoul 151-747, Korea

(Received 4 February 2013; published 25 April 2013)

We measure the in-plane distribution of thermally activated vortices in a trapped quasi-2D Bose gas, where we enhance the visibility of density-depleted vortex cores by radially compressing the sample before releasing the trap. The pairing of vortices is revealed by the two-vortex spatial correlation function obtained from the vortex distribution. The vortex density decreases gradually as temperature is lowered, and below a certain temperature, a vortex-free region emerges in the center of the sample. This shows the crossover from a Berezinskii-Kosterlitz-Thouless phase containing vortex-pair excitations to a vortex-free Bose-Einstein condensate in a finite-size 2D system.

DOI: 10.1103/PhysRevLett.110.175302 PACS numbers: 67.85.−d, 03.75.Lm, 64.60.an

Understanding the emerging mechanisms of superfluidity has been a central theme in many-body physics. In particular, the superfluid state in a two-dimensional (2D) system is intriguing because the formation of long-range order is prohibited by large thermal fluctuations [1,2] and consequently the picture of Bose-Einstein condensation is not applicable to the phase transition. The Berezinskii-Kosterlitz-Thouless (BKT) theory provides a microscopic mechanism for the 2D phase transition [3,4], where vortices with opposite circulation are paired below a critical temperature. Because vortex-antivortex pairs carry a zero net phase slip on the large length scale compared to the vortex pair size, the decay of the phase coherence changes from exponential to algebraic. The BKT mechanism has been experimentally tested in many 2D systems [5–9].

Ultracold atomic gases in 2D geometry present a clean and well-controlled system for studying BKT physics. Previous experimental studies of phase coherence [8,10] and thermodynamic properties [11–13] showed that a BKT-type transition occurs in a quasi-2D Bose gas trapped in a harmonic potential. Recently, superfluid behavior was demonstrated by measuring a critical velocity for frictionless motion of an obstacle [14]. One of the appealing features of the ultracold atomic gas system is that individual vortices can be detected, which would provide unique opportunities to investigate the details of the microscopic nature of the BKT transition. The pairing of vortices is the essential part for establishing quasi-long-range order in the 2D superfluid. However, its direct observation has been elusive so far.

In this Letter, we report the observation of thermally activated vortex pairs in a trapped quasi-2D Bose gas. We measure the in-plane vortex distribution of the sample by detecting density-depleted vortex cores and observe that the two-vortex spatial correlation function obtained from the vortex distribution shows the pairing of vortices. We investigate the temperature evolution of the vortex distribution. As the temperature is lowered, the vortex density decreases, preferentially in the center of the sample, and eventually, a vortex-free region emerges below a certain temperature. This manifests the crossover of the superfluid from a BKT phase containing thermally activated vortices to a Bose-Einstein condensate (BEC). In a finite-size 2D system, forming a BEC is expected at finite temperature when the coherence length becomes comparable to the spatial extent of the system [15,16]. Our results clarify the nature of the superfluid state in an interacting 2D Bose gas trapped in a harmonic potential.

Our experiments are carried out with a quasi-2D Bose gas of ^{23}Na atoms in a pancake-shaped optical dipole trap [17]. The trapping frequencies of the harmonic potential are $(\omega_x, \omega_y, \omega_z) = 2\pi \times (3.0, 3.9, 370)$ Hz, where the z axis is along the gravity direction. The dimensionless interaction strength is $\tilde{g} = \sqrt{8\pi}a/l_z \simeq 0.013$, where a is the three-dimensional (3D) scattering length and $l_z = \sqrt{\hbar/m\omega_z}$ is the axial harmonic oscillator length (m is the atomic mass). For a typical sample of $N = 1.3 \times 10^6$ atoms, the zero-temperature chemical potential is estimated to be $\mu \simeq 0.7\hbar\omega_z$, where $\hbar$ is the Planck constant h divided by 2π. For our small $\tilde{g}$, the BKT critical temperature is estimated to be $T_c \approx 0.99T_0 = 75$ nK in the mean-field theory [18], where T_0 is the Bose-Einstein condensation temperature for a quasi-2D, noninteracting ideal gas of N atoms in the harmonic trap [19]. Below the critical temperature, the sample shows a bimodal density distribution after time-of-flight expansion [20]. We refer to the center part as the coherent part of the sample and determine the sample temperature T from a Gaussian fit to the outer thermal wings.

The conventional method for detecting quantized vortices is observing density-depleted vortex cores after releasing the trap [21]. Because the vortex core size $\xi \propto n^{-1/2} \propto R^{3/2}$, where n is the atom density and R is the sample radius, the vortex core expands faster than the sample in a typical 3D case [22], facilitating its detection. However, this simple method is not adequate for detecting thermally activated vortices in a 2D Bose gas. The fast

expansion of the sample along the tight direction rapidly reduces the atom interaction effects so that phase fluctuations due to thermal excitations of vortices as well as phonons evolve into complicated density ripples as a result of self-interference [Fig. 1(a)] [17]. Thus, it is impossible to unambiguously distinguish individual vortices in the image of the simply expanding 2D Bose gas.

In order to enhance the visibility of the vortex cores, we apply a radial compression to the sample before releasing the trap. This compression transforms the 2D sample into an oblate 3D sample with $\mu/\hbar\omega_z > 5$, restoring the favorable condition for the vortex detection [22]. Also, the density of states changes to 3D, inducing thermal relaxation of phonons. Although tightly bound vortex pairs might annihilate, loosely bound pairs and free vortices would survive the compression process [9].

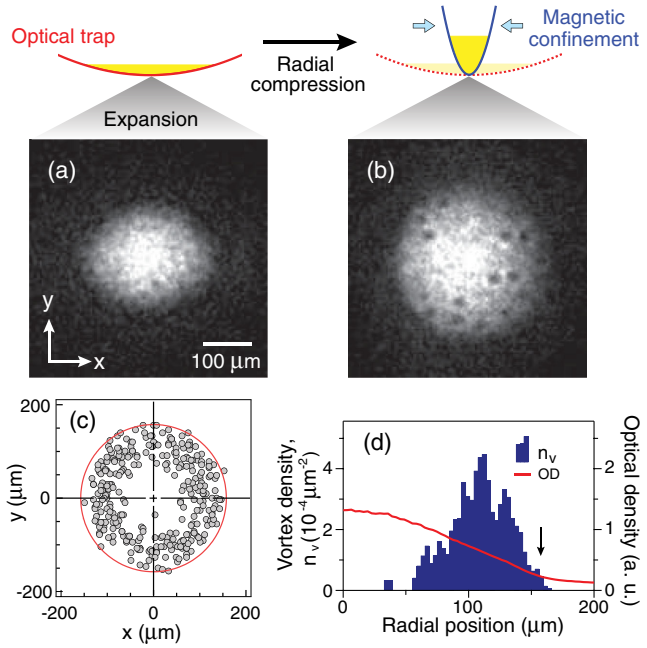

FIG. 1 (color online). Observation of thermally activated vortices. (a) Optical density image of a quasi-2D Bose gas, taken after a 17-ms time-of-flight expansion. Density ripples develop during the expansion due to phase fluctuations in the sample. (b) Image with applying a radial compression before expansion. The radial compression is achieved by superposing a magnetic potential onto the sample in an optical trap, and the expansion includes a 6-ms expansion in the optical trap and a subsequent 9-ms time of flight. Quantized vortices are observed with density-depleted cores. (c) Positions of vortices with respect to the sample center, recorded for 20 realizations of the same experiment. (d) Radial profile of the vortex density $n_v(r)$. The solid red line displays the atom density profile $n(r)$ of the sample in (b), showing a bimodal distribution. The center part is referred to as the coherent part of the sample and its boundary R_c is indicated by a solid red line in (c) and an arrow in (d). The data are acquired for $N = 1.6(2) \times 10^6$ atoms at $T = 50(6)$ nK. The vortex number in an image is $N_v = 16(4)$.

In our experiments, the radial compression is achieved by superposing a magnetic potential onto the sample [23]. We increase the radial trapping frequencies at the center of the hybrid trap to $2\pi \times 39$ Hz for 0.4 s without any significant collective oscillation of the sample, and let the sample relax for 0.2 s which corresponds to about 10 collision times (see the Supplemental Material [24]). Finally, we probe the in-plane atom density distribution by absorption imaging after 15 ms expansion. We first turn off the magnetic potential and switch off the optical trap 6 ms later, which we find helpful to improve the core visibility in our experiments.

We observe thermally activated vortices with clear density-depleted cores [Fig. 1(b)], where the visibility of the cores is about 50% and the full width at half maximum depletion is $\xi_v \approx 8$ μm. By locating the vortex positions by hand, we obtain the vortex distribution $\rho_v(\vec{r}) = \Sigma_{i=1}^{N_v} \delta(\vec{r} - \vec{r}_i)$, where N_v is the number of vortices in the image and $\vec{r}_i$ denotes the vortex position with respect to the center of the sample. The averaged vortex distribution $\bar{\rho}_v(\vec{r})$ shows no azimuthal dependence [Fig. 1(c)], and we obtain the radial profile of the vortex density $n_v(r)$ by azimuthally averaging $\bar{\rho}_v(\vec{r})$ [Fig. 1(d)]. Vortices mainly appear in the outer region of the coherent part, implying a vortex-driven phase transition. At the boundary of the coherent part, density modulations suggestive of vortex cores are often observed but not included in the vortex counting if they have no local density-minimum points.

When samples were prepared in a slightly tighter trap composed of the optical trap and a weak magnetic potential ($\mu/\hbar\omega_z \approx 1.5$), we observed that the vortex number rapidly decreases in comparison to the samples prepared in the original optical trap at similar atom-number and temperature conditions ($\mu/\hbar\omega_z < 1$) (see the Supplemental Material [24]). This shows that the observed vortex excitations result from the 2D nature of the system.

One notable feature in the vortex distribution is frequent appearance of a pair of vortices that are closely located to each other but well separated from the others (see inset in Fig. 2). The average distance to the nearest-neighbor vortex is measured to be $d_m \approx 4\xi_v$. Since direct generation of single vortices is forbidden by the angular momentum conservation, the thermal activation of vortices should involve vortex-antivortex-pair excitations. Therefore, we infer that the observed vortex pairs consist of vortices with opposite circulation, attracting each other.

A more quantitative study of the pair correlations is performed with the two-vortex spatial correlation function

$$g(s) = \frac{1}{\pi s N_v (N_v - 1)} \sum_{i>j} \delta(s - r_{ij}), \qquad (1)$$

where $r_{ij} = |\vec{r}_i - \vec{r}_j|$. This function displays the probability of finding a vortex at distance s from another vortex, reflecting the vortex-vortex interaction effects [25]. We determine $g(s)$ as the average of the pair correlation

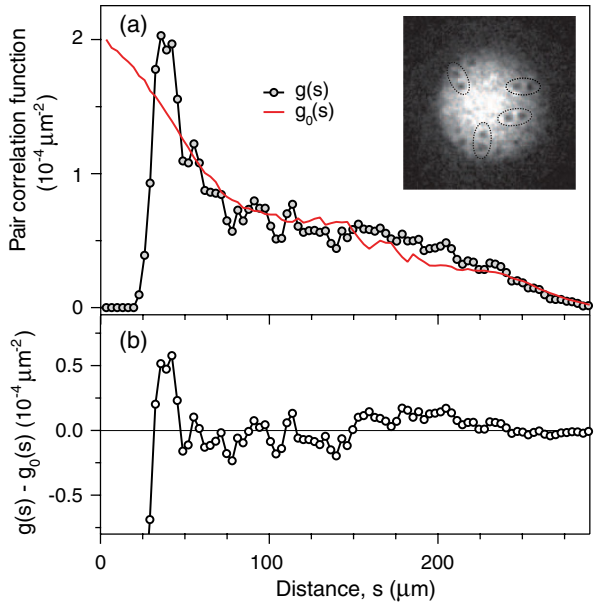

FIG. 2 (color online). Pair correlations of vortices. (a) Two-vortex spatial correlation function $g(s)$ for the experimental condition in Fig. 1. The solid red line represents the correlation function $g_0(s)$ for a random distribution with the same vortex density profile $n_v(r)$ in Fig. 1(d). (b) The difference $g(s) - g_0(s)$ shows oscillatory behavior with a noticeable enhancement at $s \sim 35$ μm. The inset displays the same image in Fig. 1(b) with guidelines for pairs of vortices whose separation is less than 30 μm.

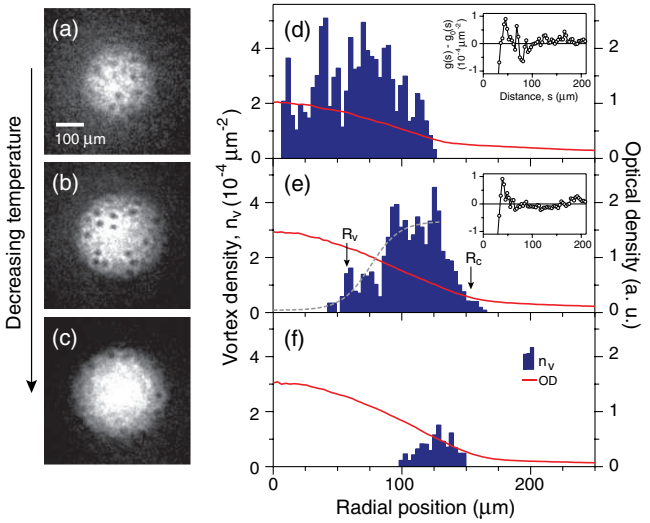

FIG. 3 (color online). Temperature dependence of the vortex distribution in a trapped 2D Bose gas. (a)–(c) Images of samples for various temperatures and (d)–(f) the corresponding vortex density profiles $n_v(r)$. The insets show the difference of the pair correlations functions, $g(s) - g_0(s)$. For the lowest temperature, $g(s)$ is not reliably determined due to the small vortex number. The inner boundary R_v of the vortex region is determined from a hyperbolic-tangent fit (dashed line) to the inner increasing part of $n_v(r)$. The sample conditions and the vortex numbers are $(N, T, N_v) = [1.5(2) \times 10^6, 67(12)$ nK, $13(4)]$ for (a) and (d), $[1.3(1) \times 10^6, 48(8)$ nK, $15(5)]$ for (b) and (e), and $[1.0(3) \times 10^6, 23(4)$ nK, $2(4)]$ for (c) and (f). The data are obtained from at least 12 images for each condition.

functions obtained from individual images for the same experiment [Fig. 2(a)]. In order to extract the pairing features, we compare $g(s)$ to the correlation function $g_0(s)$ for a random distribution with the same vortex density profile $n_v(r)$, which is calculated as $g_0(s) = \int dr d\theta r n_v(r) n_v(r') / [\int dr 2\pi r n_v(r)]^2$, where $r' = \sqrt{r^2 + 2rs\cos\theta + s^2}$. The difference $g(s) - g_0(s)$ shows a noticeable enhancement around $s \sim d_m$ and small oscillatory behavior for $s > d_m$ [Fig. 2(b)], indicating the attraction between closely located vortices. The strong suppression at $s < 3\xi_v$ is attributed to the annihilation of tightly bound vortex pairs during the compression process. These observations clearly demonstrate the pairing of vortices in the superfluid phase in a quasi-2D Bose gas.

We study the temperature evolution of the vortex distribution. Figure 3 displays the vortex density profiles $n_v(r)$ for various temperatures. At high temperature below the critical point, vortex excitations prevail over the whole coherent part. As the temperature is lowered, the vortex excitations are suppressed preferentially in the center of the sample, and at the lowest temperature, only a few vortices appear near the boundary of the coherent part. The pairing features in the two-vortex spatial correlation function is preserved over all temperatures (see insets in Fig. 3).

The evolution of $n_v(r)$ can be qualitatively understood with estimating the thermal excitation probability p of a vortex-antivortex pair in a uniform superfluid. The excitation energy of a vortex pair is $E \sim \frac{h^2}{2\pi m} n_s \ln(d/\xi)$, where n_s is the superfluid density and d is the separation of the vortices [15]. In the superfluid of radius R, the number of distinguishable microstates for the vortex pair is $\sim \frac{R^2}{\xi^2} \frac{\pi d}{\xi}$, and the entropy $S = k \ln(\pi d R^2 / \xi^3)$ (k is the Boltzmann constant). The associated free energy $F = E - TS$ gives $p \propto e^{-F/kT} = \frac{\pi R^2}{\xi^2} (d/\xi)^{-(n_s \lambda^2 - 1)}$, which is exponentially suppressed by $n_s \lambda^2$, where $\lambda = \frac{h}{\sqrt{2\pi m k T}}$ is the thermal wavelength. Thus, the vortex density profile $n_v(r)$ reflects the spatial distribution of the superfluid density $n_s(r)$ in the inhomogeneous trapped sample. Distortion of the vortex distribution might be anticipated due to vortex diffusion during the compression time. Indeed, a vortex pair carries a linear momentum of h/d. However, we observe that the vortex region ($n_v > 0$) does not change significantly for longer compression times, while the vortex density decreases, which is attributed to the vortex-pair annihilation (see the Supplemental Material [24]).

In a trapped 2D system, the density of states is modified by the trapping potential so that a BEC can form even at finite temperature [26]. This suggests that the superfluid in the trapped 2D Bose gas would evolve into a BEC at low temperatures, where the phase coherence becomes

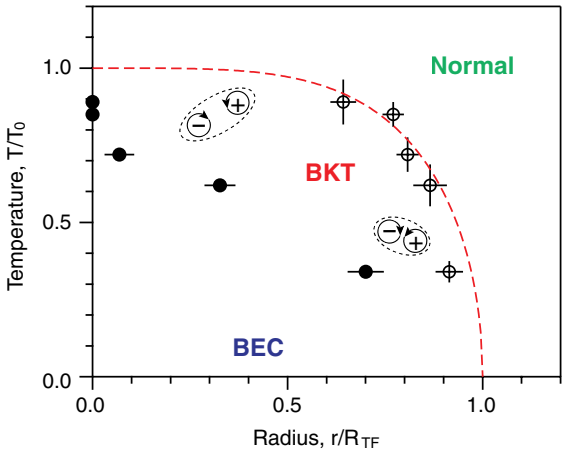

FIG. 4 (color online). BKT-BEC crossover. A schematic phase diagram of a weakly interacting 2D Bose gas trapped in a harmonic potential is depicted in the plane of T/T_0 and r/R_{TF}. T_0 is the BEC temperature for a quasi-2D ideal gas [19], and R_{TF} is the zero-temperature 2D Thomas-Fermi radius. Open and solid circles indicate the radii of the coherent part and the inner radii of the vortex region ($n_v > 0$), respectively (see the Supplemental Material [24]). The dashed line is a guide for the critical line for the superfluid transition. As thermal excitations of vortex pairs are suppressed at lower temperatures, the BKT superfluid evolves into a BEC in the finite system.

extended over the whole superfluid via suppressing thermal excitations of vortices [15,16]. We observe that a vortex-free region emerges below a certain temperature, and this is a manifestation of the BKT-BEC crossover behavior of the system. We determine the inner boundary R_v of the vortex region from a hyperbolic-tangent fit to the inner increasing part of $n_v(r)$ with a threshold value of $6 \times 10^{-5}/\mu\mathrm{m}^2$ [Fig. 3(e)], which defines the characteristic radius for the BKT-BEC crossover.

We summarize our results in Fig. 4 with a schematic phase diagram for a trapped 2D Bose gas in the plane of temperature and radial position. Here we use the coherent part as a marker for the superfluid phase transition [20]. The *in situ* radius R_c is determined from a bimodal fit to the density profile in the images taken without the compression [Fig. 1(a)], including the time-of-flight expansion factor, and R_v/R_c is measured from the images taken with the compression [Fig. 1(b)] (see the Supplemental Material [24]). In recent theoretical studies [27,28], the characteristic temperature for the BKT-BEC crossover was calculated by determining when the thermal excitation probability of a vortex pair in a sample becomes of order unity. Our results show qualitative agreement with the predictions, but their direct comparison is limited because the vortex detection efficiency in our experiments is not determined.

In conclusion, we have observed thermally activated vortex pairs in a 2D Bose gas trapped in a harmonic potential. This provides the clear confirmation of BKT superfluidity of the system. Ultracold atom experiments have been recently extended to 2D systems with Fermi gases [29,30] or including disorder potentials [31,32]. The vortex detection method developed in this work will be an important tool to probe the microscopic properties of these systems. Integrated with an inteferometric technique [10,33], this method can be upgraded to be sensitive to the sign of a vortex.

We thank W. J. Kwon for experimental assistance. This work was supported by the NRF of Korea funded by MEST (Grants No. 2011-0017527, No. 2008-0062257, and No. WCU-R32-10045).

*yishin@snu.ac.kr

[1] N. D. Mermin and H. Wagner, Phys. Rev. Lett. **17**, 1133 (1966).
[2] P. C. Hohenberg, Phys. Rev. **158**, 383 (1967).
[3] V. L. Berezinskii, Sov. Phys. JETP **34**, 610 (1972).
[4] J. M. Kosterlitz and D. J. Thouless, J. Phys. C **6**, 1181 (1973).
[5] D. J. Bishop and J. D. Reppy, Phys. Rev. Lett. **40**, 1727 (1978).
[6] D. J. Resnick, J. C. Garland, J. T. Boyd, S. Shoemaker, and R. S. Newrock, Phys. Rev. Lett. **47**, 1542 (1981).
[7] A. I. Safonov, S. A. Vasilyev, I. S. Yasnikov, I. I. Lukashevich, and S. Jaakkola, Phys. Rev. Lett. **81**, 4545 (1998).
[8] Z. Hadzibabic, P. Krüger, M. Cheneau, B. Battelier, and J. Dalibard, Nature (London) **441**, 1118 (2006).
[9] V. Schweikhard, S. Tung, and E. A. Cornell, Phys. Rev. Lett. **99**, 030401 (2007).
[10] P. Cladé, C. Ryu, A. Ramanathan, K. Helmerson, and W. D. Phillips, Phys. Rev. Lett. **102**, 170401 (2009).
[11] S. Tung, G. Lamporesi, D. Lobser, L. Xia, and E. A. Cornell, Phys. Rev. Lett. **105**, 230408 (2010).
[12] C. L. Hung, X. Zhang, N. Gemelke, and C. Chin, Nature (London) **470**, 236 (2011).
[13] T. Yefsah, R. Desbuquois, L. Chomaz, K. J. Günter, and J. Dalibard, Phys. Rev. Lett. **107**, 130401 (2011).
[14] R. Desbuquois, L. Chomaz, T. Yefsah, J. Léonard, J. Beugnon, C. Weitenberg, and J. Dalibard, Nat. Phys. **8**, 645 (2012).
[15] T. P. Simula, M. D. Lee, and D. A. W. Hutchinson, Philos. Mag. Lett. **85**, 395 (2005).
[16] T. Esslinger and G. Blatter, Nature (London) **441**, 1053 (2006).
[17] J. Choi, S. W. Seo, W. J. Kwon, and Y. Shin, Phys. Rev. Lett. **109**, 125301 (2012).
[18] H. Holzmann, M. Chevallier, and W. Krauth, Europhys. Lett. **82**, 30001 (2008).
[19] The BEC temperature T_0 is calculated from the relation $N = \frac{k^2 T_0^2}{\hbar^2 \omega_x \omega_y} \sum_{\nu=0}^{\infty} \mathrm{Li}_2(e^{-\nu(\hbar\omega_z/kT_0)})$ [18], considering thermal population in the tight direction, where $\mathrm{Li}_2(z)$ is the polylogarithm of order 2.
[20] P. Krüger, Z. Hadzibabic, and J. Dalibard, Phys. Rev. Lett. **99**, 040402 (2007).
[21] K. W. Madison, F. Chevy, W. Wohlleben, and J. Dalibard, Phys. Rev. Lett. **84**, 806 (2000).

[22] F. Dalfovo and M. Modugno, Phys. Rev. A **61**, 023605 (2000).
[23] J. Choi, W. J. Kwon, and Y. Shin, Phys. Rev. Lett. **108**, 035301 (2012).
[24] See Supplemental Material at http://link.aps.org/supplemental/10.1103/PhysRevLett.110.175302 for details on the experimental sequence of the radial compression and the phase diagram construction.
[25] C.-H. Sow, K. Harada, A. Tonomura, G. Crabtree, and D. G. Grier, Phys. Rev. Lett. **80**, 2693 (1998).
[26] V. Bagnato and D. Kleppner, Phys. Rev. A **44**, 7439 (1991).
[27] T. P. Simula and P. B. Blakie, Phys. Rev. Lett. **96**, 020404 (2006).
[28] D. Schumayer and D. A. W. Hutchinson, Phys. Rev. A **75**, 015601 (2007).
[29] M. Feld, B. Fröhlich, E. Vogt, M. Koschorreck, and M. Köhl, Nature (London) **480**, 75 (2011).
[30] A. T. Sommer, L. W. Cheuk, M. J. H. Ku, W. S. Bakr, and M. W. Zwierlein, Phys. Rev. Lett. **108**, 045302 (2012).
[31] B. Allard, T. Plisson, M. Holzmann, G. Salomon, A. Aspect, P. Bouyer, and T. Bourdel, Phys. Rev. A **85**, 033602 (2012).
[32] M. C. Beeler, M. E. W. Reed, T. Hong, and S. L. Rolston, New J. Phys. **14**, 073024 (2012).
[33] G. Roumpos, M. D. Fraser, A. Löffler, S. Höfling, Al. Forchel, and Y. Yamamoto, Nat. Phys. **7**, 129 (2011).

Appendix G

Observation of topologically stable 2D Skyrmions in an antiferromagnetic spinor Bose-Einstein condensate

This appendix includes a reprint of Ref. : Jae-yoon Choi, Woo Jin Kwon, and Yong-il Shin. *"Observation of topologically stable 2D Skyrmions in an antiferromagnetic spinor Bose-Einstein condensate"* Physical Review Letters **108**, 035301 (2012).

Observation of Topologically Stable 2D Skyrmions in an Antiferromagnetic Spinor Bose-Einstein Condensate

Jae-yoon Choi, Woo Jin Kwon, and Yong-il Shin*

Center for Subwavelength Optics and Department of Physics and Astronomy, Seoul National University, Seoul 151-747, Korea

(Received 16 October 2011; published 19 January 2012)

We present the creation and time evolution of two-dimensional Skyrmion excitations in an antiferromagnetic spinor Bose-Einstein condensate. Using a spin rotation method, the Skyrmion spin textures were imprinted on a sodium condensate in a polar phase, where the two-dimensional Skyrmion is topologically protected. The Skyrmion was observed to be stable on a short time scale of a few tens of ms but to dynamically deform its shape and eventually decay to a uniform spin texture. The deformed spin textures reveal that the decay dynamics involves breaking the polar phase inside the condensate without having topological charge density flow through the boundary of the finite-sized sample. We discuss the possible formation of half-quantum vortices in the deformation process.

DOI: 10.1103/PhysRevLett.108.035301 PACS numbers: 67.85.−d, 03.75.Lm, 03.75.Mn, 12.39.Dc

Skyrmions are particlelike topological solitons, first proposed to account for the existence of protons and neutrons in high energy physics [1] and recognized to have an important role in many condensed matter systems such as liquid ^{3}He-A [2], quantum Hall systems [3], liquid crystals [4], and helical ferromagnets [5,6]. Atomic Bose-Einstein condensates (BECs) with internal spin degrees of freedom are attractive for the study of topological objects. The rich structure of their order parameters can accommodate various topological excitations [7–12]. Furthermore, precise spin manipulation techniques have been developed to prepare topological spin structures of interest, providing unique opportunities to study their stability and dynamics [13–19].

Stability is one of the key issues in the study of Skyrmions [8,20–22]. Three-dimensional Skyrmions, which have not been experimentally discovered yet, are anticipated to be energetically unstable against shrinking to zero size without additional stabilizing mechanisms. In the search for stable Skyrmions, spinor BECs are particularly appealing because of the possibility of engineering experimental conditions such as interaction properties and external potentials including rotation [21]. Earlier experimental efforts were focused on creating 2D Skyrmion spin textures in spinor BECs by using phase imprinting methods [15,19], where, however, the BECs were not trapped so that the stability of the spin textures could not be investigated. It is important to note that the ferromagnetic phases with SO(3) symmetry studied in the previous experiments [15,19] have the trivial second homotopy group, meaning that the spin textures are not topologically protected [23]. The coreless vortex states with 2D Skyrmion spin textures, referred to as Anderson-Toulouse [24] or Mermin-Ho vortices [25], have infinite energy in a 2D plane and therefore are fundamentally different from the Skyrmions, which are localized topological solitons with finite energy [21].

In this Letter, we demonstrate the creation of 2D Skyrmions in an antiferromagnetic $F = 1$ spinor BEC in a polar phase and study their time evolution in a harmonic potential. The order parameter manifold of the polar phase is $M = [U(1) \times S^2]/\mathbb{Z}_2$, having the nontrivial second homotopy group $\pi_2(M) = \mathbb{Z}$ [23,26]. Thus, the spin textures realized in this work represent the first example of topologically stable 2D Skyrmions in a spinor BEC. Their nature is confirmed by the observation that the spin textures are stable on a short time scale. They, however, dynamically deform and eventually decay to a uniform texture. The spatial patterns of the deformed spin textures reveal that the decay dynamics involves breaking the polar phase inside the Skyrmion without having topological charge density flow via the boundary of the condensate. We suggest that half-quantum vortices may be nucleated with the nonpolar defects in the deformation process.

In terms of a unit spin vector $\vec{d}$, the 2D Skyrmion spin texture with z-axis symmetry is given as

$$\vec{d}(r, \phi) = \cos\beta(r)\hat{z} + \sin\beta(r)\hat{r} \tag{1}$$

with the boundary conditions, $\beta(0) = 0$ and $\beta(\infty) = \pi$. This spin texture has the topological charge

$$Q = \frac{1}{4\pi}\int dx\, dy\ \vec{d}\cdot(\partial_x\vec{d}\times\partial_y\vec{d}) = 1 \tag{2}$$

which represents the number of times the spin texture encloses the whole spin space. The order parameter of a $F = 1$ BEC can be written as $\Psi = (\psi_1, \psi_0, \psi_{-1})^{\mathrm{T}} = \sqrt{n}e^{i\vartheta}\zeta$, where ψ_m is the $|m_z = m\rangle$ component of the order parameter ($m = 0, \pm 1$), n is the atomic number density, ϑ is the superfluid phase, and ζ is a three-component spinor. The ground state of an antiferromagnetic BEC is polar, i.e., $|m_F = 0\rangle$ [27]. Setting $\vec{d}$ as the spin quantization axis, $\zeta = (\frac{-d_x+id_y}{\sqrt{2}}, d_z, \frac{d_x+id_y}{\sqrt{2}})^{\mathrm{T}}$ and the 2D Skyrmion spin texture in a polar BEC is

$$\zeta_S(r,\phi) = \begin{pmatrix} -\frac{1}{\sqrt{2}} e^{-i\phi} \sin\beta(r) \\ \cos\beta(r) \\ \frac{1}{\sqrt{2}} e^{i\phi} \sin\beta(r) \end{pmatrix}. \quad (3)$$

The spin winding structure around the z axis is expressed with the opposite phase windings of the $|m_z = 1\rangle$ and $|m_z = -1\rangle$ components. Note that the total angular momentum of this spin texture is zero.

To create a 2D Skyrmion spin texture, we employed a spin rotation method [15,16,28] as illustrated in Fig. 1. A quasi-2D, polar BEC confined in an optical dipole trap is placed on the $z = 0$ plane and a 3D quadrupole magnetic field is generated as

$$\vec{B}(r,z) = B'(r\hat{r} - 2z\hat{z}) + B_z\hat{z}, \quad (4)$$

where B' is the radial magnetic field gradient. The z position of the zero-field center of the quadrupole field is controlled by the axial bias field B_z. Initially, the spin vector of the polar BEC is $\vec{d} = +\hat{z}$ with $B_z \gg B'R > 0$, where R is the radial extent of the condensate. By increasing B_z to $B_z \ll -|B'R| < 0$, the zero-field point penetrates through the condensate and the magnetic field on the condensate rotates by π. In the outer region $R > r \gg r_c \sim [\hbar|\dot{B}_z|/\mu_B B'^2]^{1/2}$, where μ_B is the Bohr magneton, and $\hbar$ is the Planck constant divided by 2π, the local field direction changes slowly with respect to the local Lamor frequency and $\vec{d}(r)$ adiabatically follows the local field direction to $-\hat{z}$. On the other hand, in the center region $r \ll r_c$, the local field rotates so abruptly that $\vec{d}(r)$ cannot follow the field direction. It is obvious that $\vec{d}(0)$ keeps its direction in $+\hat{z}$. Consequently, the tilt angle $\beta(r)$ of $\vec{d}(r)$ continuously changes from $\beta(0) = 0$ to $\beta(R) = \pi$, satisfying the boundary conditions of the Skyrmion spin texture.

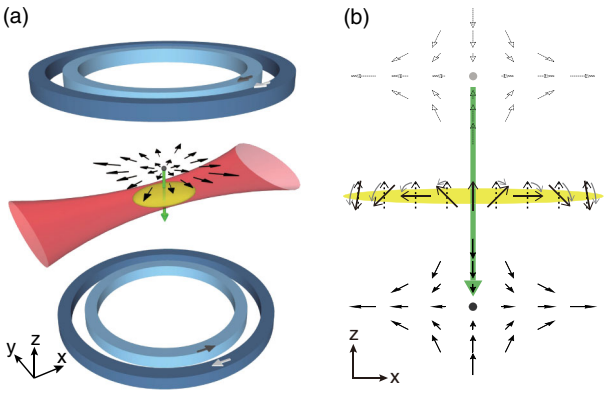

FIG. 1 (color online). Illustration of the creation process of a 2D Skyrmion in a spinor Bose-Einstein condensate. (a) A quasi-2D condensate is prepared in an optical trap and a 3D quadrupole magnetic field is generated from a pair of coils with opposite currents. An additional pair of coils provides a uniform bias field to control the z position of the zero-field center of the quadrupole field. (b) The zero-field point penetrates through the condensate and the atomic spin is driven to rotate by the change of the local magnetic field direction. The tilt angle of the atomic spin depends on its radial position, resulting in a 2D Skyrmion spin texture.

Bose-Einstein condensates of ^{23}Na atoms were generated in the $|F = 1, m_F = -1\rangle$ state in an optically plugged magnetic quadrupole trap [29] and transferred into an optical dipole trap formed by focusing a 1064-nm laser beam with a $1/e^2$ beam waist of 1.9 mm (17 μm) in the $y(z)$ direction. Further evaporation cooling was applied by lowering the trap depth and a quasipure condensate of 1.2×10^6 atoms was obtained. The condensate was prepared in the $|m_z = 0\rangle$ state by using an adiabatic Landau-Zener radio frequency (rf) sweep at a uniform bias field $B_z = 21$ G. The trapping frequencies of the final optical trap were $(\omega_x, \omega_y, \omega_z) = 2\pi \times (3.5, 4.6, 430)$ Hz and the transverse Thomas-Fermi radii of the trapped condensate were $(R_x, R_y) \approx (150, 120)$ μm. For a typical atom density $n = 1.2 \times 10^{13}$ cm^{-3}, the spin healing length $\xi_s \approx 40$ μm [30] which is much larger than the thickness of the condensate, so the spin dynamics in the condensate is of 2D character.

For the spin texture imprinting, the quadrupole field was adiabatically turned on to $B' = 8.1$ G/cm in 40 ms with $B_z = 500$ mG and the axial bias field was rapidly ramped to $B_z < -500$ mG at a variable ramp rate $\dot{B}_z$. Then the quadrupole field was switched off within 150 μs and the axial bias field was stabilized to $B_z = -500$ mG within 100 μs. The structure of the spin texture was determined by measuring the density distributions $n_{0,\pm1}(x,y)$ of the $|m_z = 0, \pm1\rangle$ components after a Stern-Gerlach spin separation. After switching off the optical trap, the magnetic field was adiabatically rotated and a field gradient was applied for 5 ms in the x direction to spatially separate the three spin components. Then atoms were pumped into the $|F = 2\rangle$ state and an absorption image was taken using the $|F = 2\rangle \rightarrow |F' = 3\rangle$ cycling transition. During the total 15-ms time of flight the condensate expanded transversely by less than 10% and we assume that the measured density distributions adequately reveal the *in situ* spin texture.

Ring-shaped spin textures were observed in the condensate after the imprinting process (Fig. 2). The $|0\rangle$ component shows a clear density-depleted ring and the $|\pm1\rangle$ components occupy the ring region with equal densities. The radius $R_{\pi/2}$ of the ring, characterizing the size of the spin texture, could be controlled with the field ramp rate $\dot{B}_z$ and the quadrupole field gradient B', as $R_{\pi/2} \propto |\dot{B}_z|^{1/2}/B'$, having the same dependence of the critical radius r_c of the adiabatic spin rotation. This validates the aforementioned qualitative description of the imprinting process. The tilt angle $\beta(x,y)$ was reconstructed from $n_{0,\pm1}(x,y)$ with the relation $\cos^2\beta = n_0/(n_1 + n_0 + n_{-1})$. When $R_{\pi/2} < 0.3R_x$, $|\cos\beta(R_x)| > 0.95$, satisfying the boundary condition of the 2D Skyrmion within our imaging resolution. When $R_{\pi/2} \approx R_x$, the outer ring part of the $|0\rangle$ component disappears and a coreless spin vortex state is formed, where

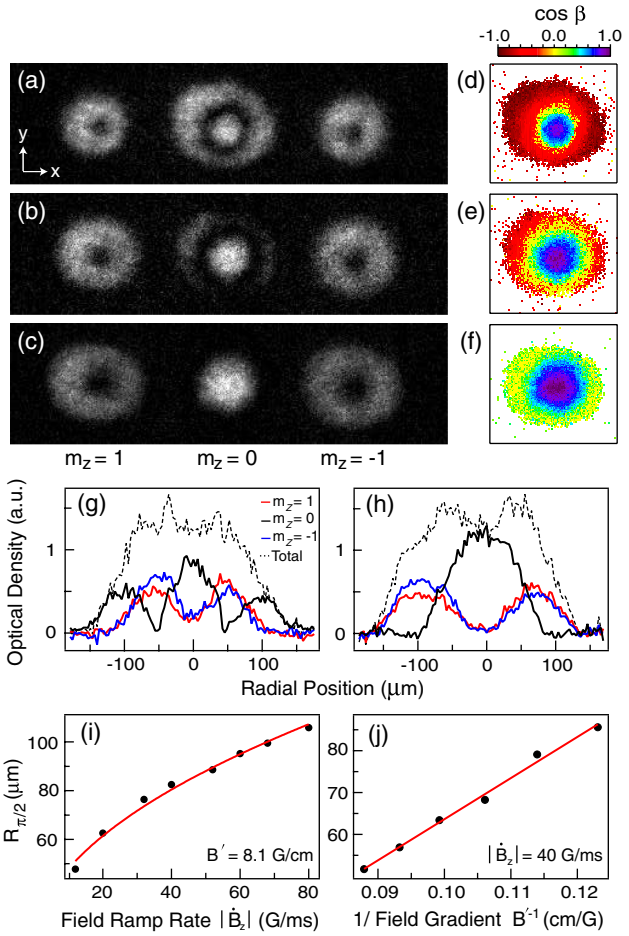

FIG. 2 (color online). Creation of 2D Skyrmions in spin-1 polar Bose-Einstein condensates. (a)–(c) Density distributions of the $|m_z = 0, \pm 1\rangle$ spin components were measured by taking absorption images after a Stern-Gerlach separation. The field ramp rate was (a) $|\dot{B}_z| = 12$, (b) 32, and (c) 80 G/ms with a quadrupole field gradient $B' = 8.1$ G/cm. The contour plots (d)–(f) show the distribution of the tilt angle $\beta(x, y)$ in (a)–(d), respectively. (g),(h) The density profiles of the spin components are the horizontal center cuts in (a),(c). The Skyrmion size $R_{\pi/2}$ versus (i) $|\dot{B}_z|$ and (j) B'^{-1}. The solid lines are square-root and linear fits to the data points, respectively. The field of view in (a)–(c) is 1.2 mm × 330 μm.

the stationary $|0\rangle$ atoms fill the core of the $|\pm 1\rangle$ vortices with opposite circulations [32]

The spin winding structure of the spin texture was confirmed from the matter wave interference between the spin components. A 14-μs rf pulse of 430 kHz was applied at $B_z = 620$ mG before turning off the optical trap. The power and duration of the rf pulse were set with a $|m_z = 0\rangle$ condensate to transfer all atoms equally into the $|m_z = \pm 1\rangle$ states. Three-to-one, fork-shaped interference fringe patterns were observed (Fig. 3), clearly demonstrating that the relative phase winding between the $|\pm 1\rangle$ components around the core $|0\rangle$ component is 4π [33,34]. Since the total angular momentum of the condensate should be conserved to be zero in the imprinting process

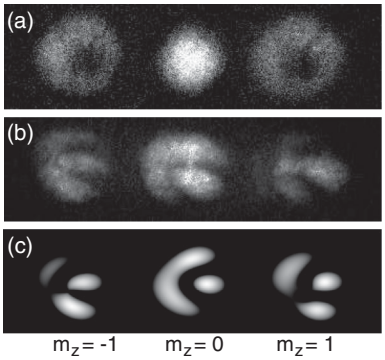

FIG. 3. Interference of the coreless spin vortex state. (a) Initial density distribution of the three spin components. (b) A rf pulse was applied before a Stern-Gerlach separation and fork-shaped interference fringes appear in the $|m_z = 0\rangle$ atom cloud. (c) Numerical simulation of our experimental condition with the phase winding numbers $(-1, 0, 1)$ for the $|m_z = +1\rangle$, $|0\rangle$, and $|-1\rangle$ components.

[35], the phase winding numbers of the spin components are $(-1, 0, 1)$. Together with the radial distribution of β, this clearly shows that a 2D Skyrmion is indeed created in the polar condensate.

In order to study the stability of the 2D Skyrmion, we measured the time evolution of the spin texture with a variable dwell time t in the optical trap and observed that it dynamically deforms and decays to a uniform spin texture (Fig. 4). Modulation of the ring structure gradually developed and distorted the whole spin texture over 100 ms. Eventually, the spin texture became uniform in the $|m_z = 0\rangle$ state at $t > 300$ ms. Recent theoretical calculations have shown that 2D Skyrmion excitations are energetically unstable and decay to a uniform spin texture by expanding or shrinking in a harmonic potential [22] but we estimate that the thermal dissipation is negligible in our experiments for the upper bound of the condensate temperature <65 nK. The decay of the Skyrmion is a dynamically driven process.

It is remarkable that the outer $|0\rangle$ component kept surrounding the $|\pm 1\rangle$ components in the decay dynamics, implying that there was no topological charge density flow via the boundary of the finite-sized condensate. Since it is topologically impossible for the isolated Skyrmion to unwind to a uniform spin texture when the global polar phase is preserved, nonpolar defects must have developed inside the condensates during the decay dynamics. Breaking the polar phase might be attributed to the quadratic Zeeman effects and the induced spin currents [10]. The spin relaxation time of a $|m_z = \pm 1\rangle$ equal mixture was measured to be over 1 s at $B_z = 500$ mG, clearly indicating that the rapid development of nonpolar defects is due to the presence of the Skyrmion spin texture.

One interesting observation in the deformed spin textures is that the core $|0\rangle$ component could be connected to

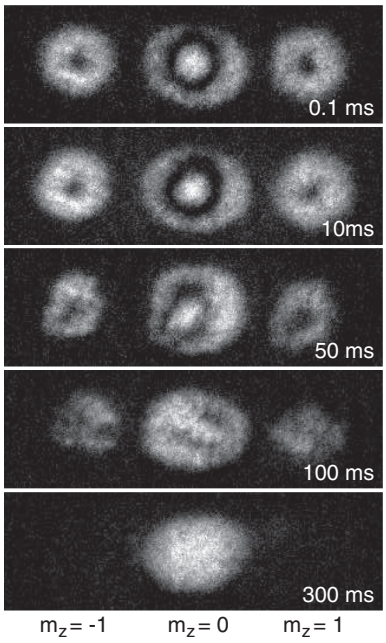

FIG. 4. Deformation and decaying of the 2D Skyrmion in a harmonic potential. The time evolution of the spin texture was measured with a variable dwell time in an optical trap. For this data, $|\dot{B}_z| = 20$ G/ms and $B' = 8.1$ G/cm. The field of view is 1.0 mm $\times$ 330 μm.

the outer component or divided into two parts (Fig. 5). Because of the symmetry of the order parameter of the polar BEC under $(\vec{d}, \vartheta) \rightarrow (-\vec{d}, \vartheta + \pi)$, the two regions with a π disclination in $\vec{d}$ can be continuously connected via a π change of the superfluid phase. This observation suggests possible formation of half-quantum vortices around nonpolar local defects in the deformation process

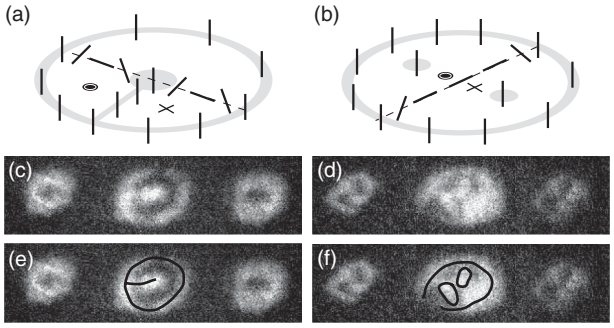

FIG. 5. Dynamic formation of a pair of half-quantum vortices. The line segments represent the axis of the spin vector $\vec{d}$ and the grey area indicates the region where the $|m_z = 0\rangle$ component mainly occupies. The nonpolar cores of the half-quantum vortices are marked by $\odot$ and $\times$, implying opposite windings of the superfluid phase. Examples of the dynamic evolution of the 2D Skyrmion spin texture at (c) $t = 30$ and (d) 50 ms, displaying density profiles similar to those in (a) and (b). (e),(f) Same as (c), (d) with guidelines for the peak density regions in the $|m_z = 0\rangle$ atom cloud.

as described in Fig. 5. The $|\pm 1\rangle$ components seemed to keep occupying the density-depleted region of the $|0\rangle$ component without developing noticeable local spin polarization $n_1 - n_{-1}$, supporting the possibility. A similar situation has been studied with a point defect in a polar 3D BEC, where the 't Hooft-Polyakov monopole continuously deforms to a half-quantum vortex ring (Alice ring) [36].

In conclusion, we have demonstrated the creation of topologically stable 2D Skyrmions in a polar BEC and presented the first measurement of the dynamics of the Skyrmion in a harmonic potential. This work opens a new perspective for the study of Skyrmion dynamics in spinor BECs. The experimental technique can be extended to create multiple Skyrmions in a condensate or other exotic spin textures such as knots [10] and monopoles [36] in 3D condensates.

The authors thank W. Ketterle and J. H. Han for discussions. This work was supported by National Research Foundation of Korea Grants (No. 2011-0004539, No. 2011-0017527, No. 2011-0001053, and No. WCU-R32-10045) and Research Settlement Fund for the new faculty of SNU. J. C. and W. J. K. acknowledge support from Global PhD Fellowship and BK21 Fellowship, respectively.

*yishin@snu.ac.kr

[1] T. A. Skyrme, Nucl. Phys. **31**, 556 (1962).
[2] P. W. Anderson and G. Toulouse, Phys. Rev. Lett. **38**, 508 (1977).
[3] A. Schmeller, J. P. Eisenstein, L. N. Pfeiffer, and K. W. West, Phys. Rev. Lett. **75**, 4290 (1995).
[4] D. C. Wright and N. D. Mermin. Rev. Mod. Phys. **61**, 385 (1989).
[5] A. Neubauer *et al.*, Phys. Rev. Lett. **102**, 186602 (2009).
[6] X. Z. Yu *et al.*, Nature (London) **465**, 901 (2010).
[7] U. Leonhardt and G. E. Volovik, JETP Lett. **72**, 46 (2000).
[8] U. A. Khawaja and H. Stoof, Nature (London) **411**, 918 (2001).
[9] T. Mizushima, K. Machida, and T. Kita, Phys. Rev. Lett. **89**, 030401 (2002).
[10] Y. Kawaguchi, M. Nitta, and M. Ueda, Phys. Rev. Lett. **100**, 180403 (2008).
[11] V. Pietilä and M. Möttönen, Phys. Rev. Lett. **103**, 030401 (2009).
[12] Y. Kawaguchi *et al.*, Prog. Theor. Phys. Suppl. **186**, 455 (2010).
[13] M. R. Matthews *et al.*, Phys. Rev. Lett. **83**, 2498 (1999).
[14] V. Bretin, P. Rosenbusch, F. Chevy, G. V. Shlyapnikov, and J. Dalibard, Phys. Rev. Lett. **90**, 100403 (2003).
[15] A. E. Leanhardt, Y. Shin, D. Kielpinski, D. E. Pritchard, and W. Ketterle, Phys. Rev. Lett. **90**, 140403 (2003).
[16] Y. Shin *et al.*, Phys. Rev. Lett. **93**, 160406 (2004).
[17] V. Schweikhard, I. Coddington, P. Engels, S. Tung, and E. A. Cornell, Phys. Rev. Lett. **93**, 210403 (2004).
[18] L. E. Sadler *et al.*, Nature (London) **443**, 312 (2006).

[19] L. S. Leslie, A. Hansen, K. C. Wright, B. M. Deutsch, and N. P. Bigelow, Phys. Rev. Lett. **103**, 250401 (2009).
[20] R. A. Battye, N. R. Cooper, and P. M. Sutcliffe, Phys. Rev. Lett. **88**, 080401 (2002).
[21] C. M. Savage and J. Ruostekoski, Phys. Rev. Lett. **91**, 010403 (2003).
[22] H. Zhai, W. Q. Chen, Z. Xu, and L. Chang, Phys. Rev. A **68**, 043602 (2003).
[23] M. Ueda and Y. Kawaguchi, arXiv:1001.2072.
[24] P. W. Anderson and G. Toulouse, Phys. Rev. Lett. **38**, 508 (1977).
[25] N. D. Mermin and T. L. Ho, Phys. Rev. Lett. **36**, 594 (1976).
[26] S. Mukerjee, C. Xu, and J. E. Moore, Phys. Rev. Lett. **97**, 120406 (2006).
[27] J. Stenger *et al.*, Nature (London) **396**, 345 (1998).
[28] T. Isoshima, M. Nakahara, T. Ohmi, and K. Machida, Phys. Rev. A **61**, 063610 (2000).
[29] M. S. Heo, J. Y. Choi, and Y. I. Shin, Phys. Rev. A **83**, 013622 (2011); J. Choi, M. S. Heo, and Y. Shin, J. Korean Phys. Soc. **59**, 211 (2011).
[30] $\xi_s = 2\pi\hbar/\sqrt{2mc_2n}$, where m is the atomic mass and $c_2 = 4\pi\hbar^2(a_2 - a_0)/3m$. $a_{0,2}$ are the s-wave scattering lengths for total spin 0, 2 and $a_2 - a_0 \simeq 5.7a_B$ (a_B is the Bohr radius) [31].
[31] J. P. Burke, C. H. Greene, and J. L. Bohn, Phys. Rev. Lett. **81**, 3355 (1998).
[32] The vortex state is often referred to as a ''half'' Skyrmion because $\beta(R_{\mathrm{TF}}) = \pi/2$, which is not a topologically stable object.
[33] F. Chevy, K. W. Madison, V. Bretin, and J. Dalibard, Phys. Rev. A **64**, 031601(R) (2001).
[34] S. Inouye *et al.*, Phys. Rev. Lett. **87**, 080402 (2001).
[35] M. V. Berry, Proc. R. Soc. A **392**, 45 (1984).
[36] J. Ruostekoski and J. R. Anglin, Phys. Rev. Lett. **91**, 190402 (2003).

Appendix H

Imprinting Skyrmion spin textures in spinor Bose-Einstein condensates

This appendix includes a reprint of Ref. : Jae-yoon Choi, Woo-Jin Kwon, Moon-joo. Lee, Hyunseok Jeong, Kyungwon An, and Yong-il Shin. *"Imprinting Skyrmion spin textures in spinor Bose-Einstein condensates "* New Journal of Physics **14**, 053013 (2012).

Imprinting Skyrmion spin textures in spinor Bose–Einstein condensates

2012 New J. Phys. 14 053013

(http://iopscience.iop.org/1367-2630/14/5/053013)

New Journal of Physics
The open-access journal for physics

Imprinting Skyrmion spin textures in spinor Bose–Einstein condensates

Jae-yoon Choi[1,2], Woo Jin Kwon[1,2], Moonjoo Lee[1,2], Hyunseok Jeong[1], Kyungwon An[1] and Yong-il Shin[1,2,3]

[1] Department of Physics and Astronomy, Seoul National University, Seoul 151-747, Korea

[2] Center for Subwavelength Optics, Seoul National University, Seoul 151-747, Korea

E-mail: yishin@snu.ac.kr

New Journal of Physics **14** (2012) 053013 (11pp)
Received 23 December 2011
Published 9 May 2012
Online at http://www.njp.org/
doi:10.1088/1367-2630/14/5/053013

Abstract. We investigate an experimental method for imprinting Skyrmion spin textures in a spinor Bose–Einstein condensate by rapidly moving the zero-field center of a three-dimensional (3D) quadrupole magnetic field through the condensate. Various excitations such as 2D Skyrmions and coreless vortices were created in spin-1 sodium condensates, initially prepared in a uniform polar or ferromagnetic phase. The spin textures were characterized with the spatial distribution of the spin tilt angle, which is found to be in good quantitative agreement with the local description of single spins under the field rotation. We demonstrate the creation of a highly charged Skyrmion in a trapped condensate by applying the imprinting process multiple times.

[3] Author to whom any correspondence should be addressed.

Contents

1. Introduction

Topological excitations play a central role in describing the physics of ordered mediums such as superfluid helium, liquid crystals and atomic Bose–Einstein condensates. In particular, Bose–Einstein condensates of atoms with internal spin degrees of freedom provide unique opportunities for the study of topological excitations. The rich structure of their order parameters can host various topological objects [1–5], and well-developed manipulation techniques for atomic motion and spin states enable us to engineer topological states of interest for investigating their dynamics and stability in a highly controllable manner. Quantized vortices have been created in single- or multi-component condensates by external rotation [6] and phase imprinting methods [7–9], leading to the successful study of their many interesting phenomena such as line defect deformation [10], Tachenko's modes in vortex lattices [11], vortex dipole dynamics [12, 13] and dynamical instability of doubly charged vortices [14]. Recently, coreless vortex states with Skyrmion spin textures were created in spinor condensates by using spatially tailored magnetic field rotation [15] or optical Raman transitions [16].

In this paper, we investigate the magnetic field rotation method for imprinting Skyrmion spin textures in a spinor Bose–Einstein condensate. The Skyrmion spin texture is characterized by a local spin that is continuously inverted to the opposite direction from a uniform spin texture. In our experiments, this spin texture is imprinted by rapidly moving the zero-field point of a three-dimensional (3D) quadrupole magnetic field through a trapped spin-1 condensate, creating 2D Skyrmions and coreless spin vortices in a polar phase and the Anderson–Toulouse and Mermin–Ho vortex states in a ferromagnetic phase. We analyze the spatial structure of the created spin textures and find that the tilt angle of spins is quantitatively well described by the local field rotation, showing that the effects due to atom–atom interactions are not involved in our spin texture imprinting process. This observation allows us to propose a scheme with multiple applications of the imprinting process and we demonstrate the creation of a highly charged Skyrmion in a trapped condensate.

In section 2, we present a brief theoretical description of the imprinting method and introduce various excitations with the Skyrmion spin texture in spin-1 condensates. Section 3 shows the experimental results and the quantitative analysis of the spatial distribution of the

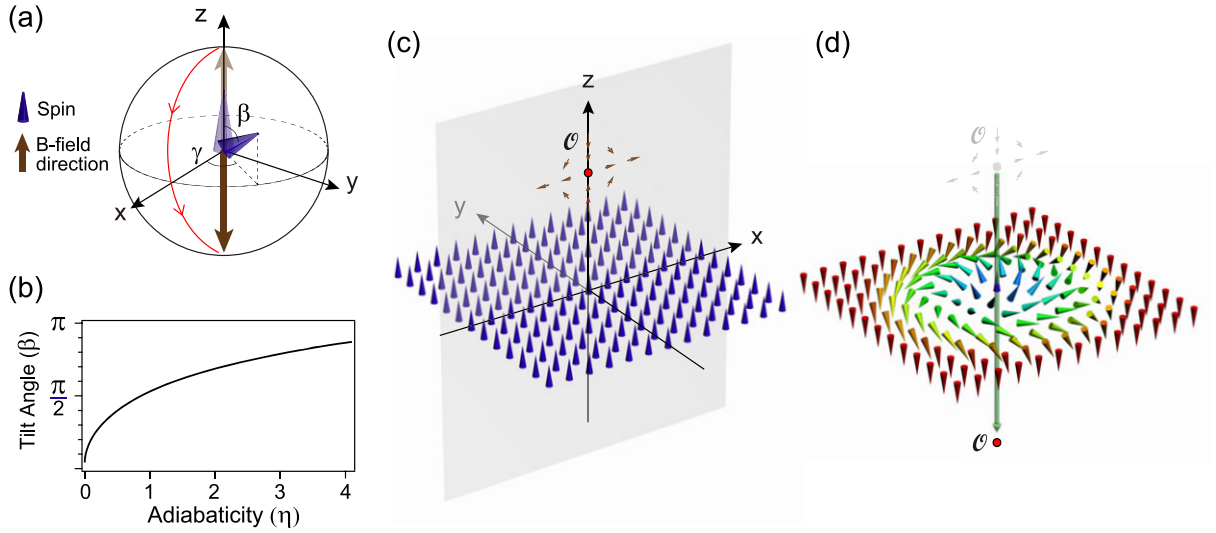

Figure 1. Spin texture imprinting by magnetic field rotation. (a) A spin, initially aligned to the $+z$-direction, tilts under magnetic field rotation (arrowed red line). (b) Numerical results for the final tilt angle β as functions of the adiabaticity η of the field rotation process (see the text for details). (c,d) Imprinting a Skyrmion spin texture with a 3D quadrupole magnetic field. As the zero-field point $\mathcal{O}$ penetrates through a 2D spinor condensate, each atomic spin experiences local magnetic field rotation, resulting in a Skyrmion spin texture. The direction of a local spin is indicated by an arrowhead, colored as its tilt angle to the z-axis.

spin tilt angle in the spin textures. Finally, in section 4 we demonstrate an experimental scheme for creating highly charged Skyrmion spin textures with two consecutive applications of the imprinting process to a trapped condensate.

2. Spin texture imprinting by spin rotation

2.1. Spin tilting by B-field rotation

The motion of a spin in a time-dependent, external magnetic field $\vec{B}(t)$ is governed by

$$\frac{\mathrm{d}\vec{s}}{\mathrm{d}t} = \frac{g\mu_\mathrm{B}}{\hbar}\vec{s} \times \vec{B}(t), \tag{1}$$

where $\vec{s}$ is a unit vector for the spin direction, g is the g-factor of the spin, μ_B is the Bohr magneton and $\hbar$ is the Planck constant h divided by 2π. The spin precesses around the axis of the magnetic field with the Larmor frequency $\omega_\mathrm{L} = g\mu_\mathrm{B}|\vec{B}|/\hbar$ and the precession axis of the spin is dragged to the field direction when the direction of the magnetic field changes. If the changing rate of the field direction $\omega_\mathrm{B} = \frac{\vec{B}}{|\vec{B}|^2} \times \frac{\mathrm{d}\vec{B}}{\mathrm{d}t}$ is much lower than the Larmor frequency, the spin adiabatically follows the magnetic field, i.e. preserving its angle from the field direction. On the other hand, if the field direction changes relatively rapidly, the angle evolves dynamically, i.e. inducing diabatic population transfer between the magnetic sublevels of the spin.

Let us consider the situation depicted in figure 1(a) where the spin is initially aligned to the $+z$-direction and the external magnetic field rotates from $+\hat{z}$ to $-\hat{z}$ as $\vec{B}(t) = B_0\hat{x} + B_z(t)\hat{z}$ with

linearly sweeping $B_z(t)$ from $+\infty$ to $-\infty$. With $B_0 = 0$, the magnetic field suddenly changes its direction to the opposite one, so the spin is not affected and keeps pointing to the $+z$-direction. On the other hand, when $B_0 \gg 1$, the spin adaptively follows the rotating field and ends up pointing in the $-z$-direction. We numerically calculate the final tilt angle β of the spin from the z-axis after the field rotation and show the result in figure 1(b) as a function of $\eta = \min(\omega_L/\omega_B) = g\mu_B B_0^2/\hbar|\dot{B}_z|$. Here η is a dimensionless measure of the adiabaticity of the field sweep process. We emphasize that β shows monotonic behavior on η. This means that the tilt angle can be deterministically controlled by the transverse field B_0 and the field sweep rate $\dot{B}_z$. In a 2D spin system, a target spin texture $\beta(x, y)$ can be generated by tailoring the spatial distribution of $\vec{B}_0(x, y)$ for a given field sweep process.

2.2. Skyrmion spin texture with a quadrupole magnetic field

Figure 1(c) illustrates how to imprint a Skyrmion spin texture on a 2D atomic condensate by using a 3D quadrupole magnetic field. The quadrupole magnetic field is given as $\vec{B}(r, z) = B'r\hat{r} + (B_z - 2B'z)\hat{z}$ and the zero-field center is located at $z_0 = B_z/2B'$. By linearly sweeping the uniform bias field B_z, we move the zero-field point through the sample placed on the $z = 0$ plane so that a local spin in the sample experiences a field rotation by π as in the previous example. The local adiabaticity of the field sweep process varies over the sample as $\eta(r) = \mu B'^2 r^2/\hbar|\dot{B}_z|$. Ignoring the effects due to the translational motion of atoms and atom–atom interactions, the resultant spatial distribution of the spin direction of the condensate would be

$$\vec{s}(r, \phi) = \cos\beta(r)\hat{z} + \sin\beta(r)(\cos\gamma(r)\hat{r} + \sin\gamma(r)\hat{\phi}), \tag{2}$$

where $\beta(r)$ monotonically increases from $\beta(0) = 0$ to $\beta(\infty) = \pi$. Here $\gamma(r)$ is the azimuthal angle due to the precession accumulated during the field sweep process.

The local spin continuously rotates to the opposite direction from the far-field uniform spin and this is a Skyrmion spin texture. This structure is topologically protected in the $O(3)$ spin space and its topological charge is defined as

$$Q = \frac{1}{4\pi}\int \mathrm{d}x\,\mathrm{d}y\ \vec{s}\cdot(\partial_x\vec{s}\times\partial_y\vec{s}) = 1, \tag{3}$$

representing the number of times the spin texture encloses the whole spin space. Note that the topological charge is independent of γ.

2.3. The polar phase versus the ferromagnetic phase of spin-1 condensates

We consider a Bose–Einstein condensate of spin-1 atoms, whose order parameter can be written as $\Psi = (\psi_1, \psi_0, \psi_{-1})^{\mathrm{T}} = \sqrt{n}\,\mathrm{e}^{\mathrm{i}\vartheta}\zeta$, where $\psi_{0,\pm1}$ is the $|m_z = 0, \pm1\rangle$ component of the order parameter, n is the atomic number density, ϑ is the superfluid phase and ζ is a three-component spinor. The ground state of the spinor condensate at zero magnetic field is determined by the spin-dependent interactions whose energy density is given as $E = \frac{c}{2}n^2|\langle\mathbf{F}\rangle|^2$, where $c = 4\pi\hbar^2(a_2 - a_0)/3m$ (a_F is the two-body s-wave scattering length in the total spin F channel and m is the atomic mass) and $\mathbf{F}$ is the 3×3 Pauli spin matrices. The ground state is polar, i.e. $|\langle\mathbf{F}\rangle| = 0$, for $c > 0$ (e.g. ^{23}Na [17]), or ferromagnetic, i.e. $|\langle\mathbf{F}\rangle| = 1$, for $c < 0$ (e.g. ^{87}Rb [18]).

Here we study the spin textures created with two initial, uniform spin textures: $\zeta = (0, 1, 0)^{\mathrm{T}}$ and $\zeta = (0, 0, 1)^{\mathrm{T}}$, corresponding to the polar and ferromagnetic phases, respectively.

Under the field sweep process, the local spinors of the condensate rotate in the same manner as $\vec{s}$ in equation (2), resulting in

$$\zeta_{\text{polar}}(r,\phi) = \exp(-\mathrm{i}\mathbf{F}\cdot\hat{n}\beta)\begin{pmatrix}0\\1\\0\end{pmatrix} = \begin{pmatrix}-\frac{1}{\sqrt{2}}\mathrm{e}^{-\mathrm{i}\phi}\sin\beta(r)\\ \cos\beta(r)\\ \frac{1}{\sqrt{2}}\mathrm{e}^{\mathrm{i}\phi}\sin\beta(r)\end{pmatrix} \tag{4}$$

and

$$\zeta_{\text{ferro}}(r,\phi) = \exp(-\mathrm{i}\mathbf{F}\cdot\hat{n}\beta)\begin{pmatrix}0\\0\\1\end{pmatrix} = \begin{pmatrix}\mathrm{e}^{-\mathrm{i}2\phi}\sin^2\frac{\beta(r)}{2}\\ \frac{1}{\sqrt{2}}\mathrm{e}^{-\mathrm{i}\phi}\sin\beta(r)\\ \cos^2\frac{\beta(r)}{2}\end{pmatrix}, \tag{5}$$

where $\hat{n}(\phi) = -\hat{x}\sin\phi + \hat{y}\cos\phi$ is the axis of the local field rotation and we omit the precession angle $\gamma(r)$ that is not important for characterizing the spin textures. Because of the ϕ dependence of the rotation axis, the Berry phase factor of $\mathrm{e}^{\mathrm{i}(m_{\mathrm{F}}-m_z)\phi}$ [19] develops, leading to the phase winding numbers of (−1,0,1) and (−2, −1,0) for the $|m_z = +1, 0, -1\rangle$ components in the polar ($m_{\mathrm{F}} = 0$) and ferromagnetic ($m_{\mathrm{F}} = -1$) phases, respectively. The total angular momentum of the condensate is preserved to be zero for the polar phase but, in contrast, changes for the ferromagnetic phase [20].

Although these two final states are identical to each other in terms of spin pattern, their topological characteristics are fundamentally different. The symmetry of the order parameter space of the polar phase is $M_{\text{polar}} = (U(1)\times S^2)/\mathbb{Z}_2$ where $U(1)$ is for the gauge symmetry of the superfluid phase, S^2 is for the rotational symmetry of the spinor and $\mathbb{Z}_2$ comes from the invariant symmetry under $\vec{n}\to-\vec{n}$ and $\vartheta\to\vartheta+\pi$ [21]. Since the second homotopy group $\pi_2(M_{\text{polar}}) = \mathbb{Z}$ is not trivial, topologically stable 2D Skyrmions exist in the polar phase, so ζ_{polar} represents a 2D Skyrmion excitation [22]. On the other hand, the order parameter of the ferromagnetic phase has $SO(3)$ symmetry and the second homotopy group $\pi_2(SO(3)) = 0$, meaning that the Skyrmion spin texture is not topologically protected [23]. The spin excitation ζ_{ferro} in the ferromagnetic phase is referred to as the Anderson–Toulouse vortex [24]. When $\beta(r\to\infty) = \pi/2$, we refer to ζ_{polar} as a coreless spin vortex because it has only a spin flow with no net mass flow [23] and ζ_{ferro} as the Mermin–Ho vortex [25]. The Anderson–Toulouse and Mermin–Ho vortices have been studied in superfluid He-3 systems [26, 27]. Recent theoretical studies showed that these coreless vortex states are the ground states of ferromagnetic spinor condensates under slow rotation [28, 29].

3. Experimental results

3.1. The creation of Skyrmion spin textures in trapped condensates

We perform the spin texture imprinting experiments with $F = 1$ ^{23}Na condensates as described in [22]. A pancake-shaped, quasi-pure condensate is prepared in a 1064 nm optical dipole trap with trapping frequencies of $\omega_{x,y,z} = 2\pi\times(3.5, 4.6, 430)$ Hz. With a typical atom number of $\approx 1.2\times10^6$, the transverse Thomas–Fermi radii of the trapped condensate are $(R_x, R_y)\approx(150, 120)\,\mu$m and the atomic peak density $n\approx 1.2\times10^{13}\,\mathrm{cm}^{-3}$. The spin healing length $\xi_{\mathrm{s}} = \hbar/\sqrt{2mcn}\approx 6.4\,\mu$m ($a_2 - a_0 \simeq 5.7a_{\mathrm{B}}$ and a_{B} is the Bohr radius [30]) is much larger than the thickness of the condensate $\approx 1\,\mu$m, so our sample is an effective 2D spin system.

The condensate is initially generated in the $|m_F = -1\rangle$ state [31]. For the study of the spin textures of the polar phase, a full population transfer to the $|m_F = 0\rangle$ state is made before applying a spin texture imprinting process, using an adiabatic Landau–Zener RF sweep at a uniform bias field of $B_z = 20\,\mathrm{G}$, where the quadratic Zeeman shift is about 0.1 MHz.

The magnetic field for the spin texture imprinting is provided by three pairs of coaxial coils: one is for the quadrupole field and the others are for the uniform bias field to the $\pm z$-directions, respectively. We adiabatically turn on the quadrupole field to $B' = 7\,\mathrm{G\,cm^{-1}}$ in 3.5 ms with $B_z = 2\,\mathrm{G}$ and rapidly ramp the axial bias field to $B_z < -1\,\mathrm{G}$ at a variable rate $\dot{B}_z$. Then we switch off the quadrupole field within $150\,\mu$s and stabilize the bias field to $B_z = -500\,\mathrm{mG}$ within $100\,\mu$s. The quadrupole field provides an additional, transverse (anti-)trapping potential to atoms in the $|m_z = -1(1)\rangle$ state, so it would induce breathing-mode excitations for the field sweep process. To reduce this deleterious effect, we shortened the turn-on time of the quadrupole field as much as possible without losing the adiabaticity of the field change. During the imprinting process, the radial size of the condensate initially prepared in the $|m_z = -1\rangle$ state was observed to change by less than 3%, so the mechanical perturbation was negligible.

The density distributions $n_{0,\pm1}$ of the $|m_z = 0, \pm1\rangle$ components are measured by taking an absorption image after the Stern–Gerlach separation [22]. After the field sweep, we switch off the optical trap and apply a magnetic field gradient for 6 ms to spatially separate the spin components in the x-direction. An absorption image is taken using the $|F = 2\rangle \rightarrow |F' = 3\rangle$ cycling transition after pumping the atoms into the $|F = 2\rangle$ state. For a 15 ms time-of-flight, the condensate expands by about 10% in the transverse direction.

In order to characterize the spin textures, we reconstruct the distribution of the tilt angle $\beta(x, y)$ from the measured density distributions using the relations $\cos^2\beta = n_0/(n_1 + n_0 + n_{-1})$ and $\cos\beta = (n_1 - n_{-1})/(n_1 + n_0 + n_{-1})$ for the polar and ferromagnetic phases, respectively (see equations (4) and (5)). Figure 2 displays the typical spin textures observed in the condensates. The tilt angle clearly shows radial symmetry and monotonically increases from the center to the boundary of the condensate as expected. The tilt angle at the sample boundary could be controlled with the field sweep rate and we observed 2D Skyrmions and the coreless spin vortex states with the polar phase, and the Anderson–Toulouse and Mermin–Ho vortex states with the ferromagnetic phase. The phase winding nature of the spin textures has been confirmed in previous experiments by measuring the quadrupole oscillation frequencies [9], observing the splitting of a doubly charged vortex core [14] and matter wave interference patterns between the spin components [22].

3.2. Characterization of the spin texture imprinting method

The magnetic field sweep was performed very rapidly within a few hundreds of μs. Since this time scale is too short for the dynamics due to atom–atom interactions to be involved, we expect that the spin tilt angle $\beta(x, y)$ might be fully determined by the local adiabaticity $\eta(x, y)$ of the field rotation, which we found to be the case. Figure 3 shows $\cos^2\beta(\eta)$ obtained by azimuthally averaging $\cos^2\beta(x, y)$ and $\cos\beta(x, y)$ of the polar and ferromagnetic spin textures, respectively. We estimate the local adiabaticity as $\eta(r) = (\mu_B/2)B'^2(\kappa r)^2/\hbar|\dot{B}_z|$ with $\kappa = 0.9$ to account for the transverse expansion due to the time-of-flight, which is an oversimplification of the expansion dynamics. Remarkably, the data from the four different spin textures, regardless of the phase of the sample, overlap nicely and, furthermore, show good quantitative agreement with the numerical calculation for a single spin. This observation clearly demonstrates that with

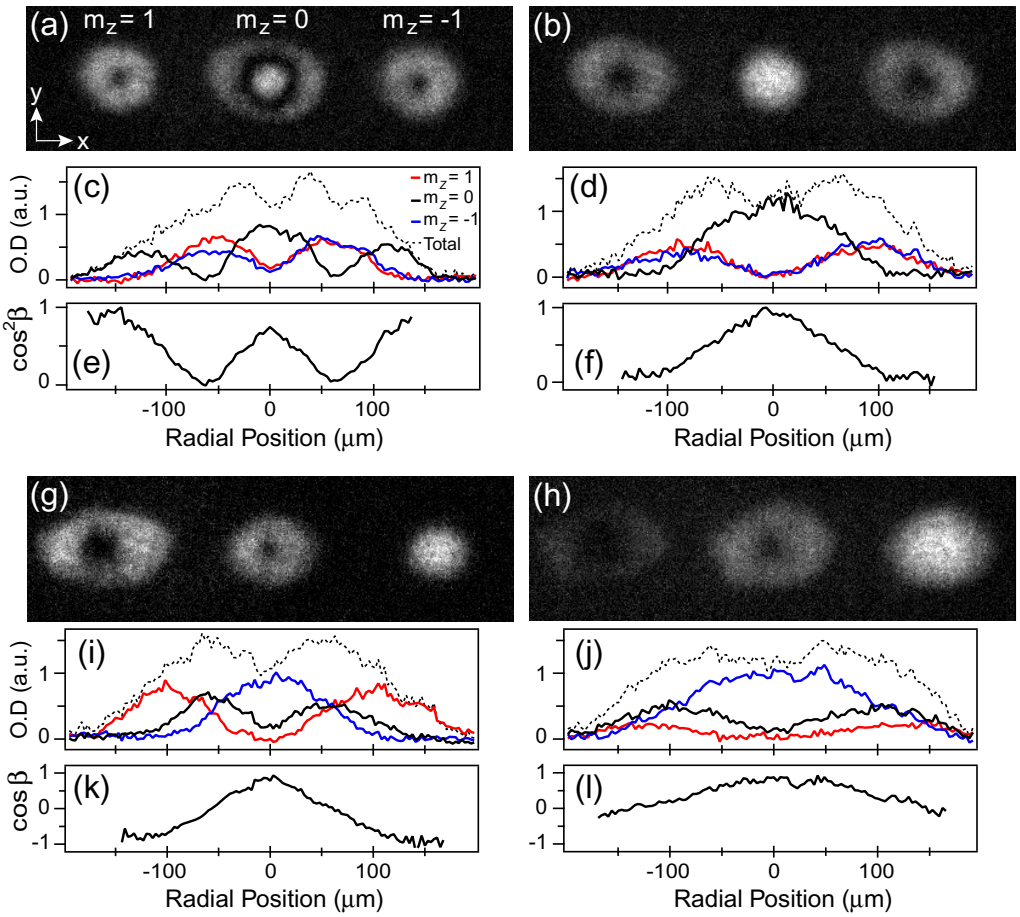

Figure 2. Skyrmion spin textures in spin-1 Bose–Einstein condensates. Skyrmion spin textures were imprinted with the field rotation method in trapped condensates that were initially prepared in (a, b) the $|m_z = 0\rangle$ (polar) or (g, h) $|m_z = -1\rangle$ (ferromagnetic) state. Density distributions of the three spin components, measured after a Stern–Gerlach spin separation, represent (a) a 2D Skyrmion, (b) a coreless spin vortex, (g) the Anderson–Toulouse vortex and (h) the Mermin–Ho vortex. The quadrupole field gradient was $B' = 7\,\mathrm{G\,cm^{-1}}$ and the field ramp rate was (a) $|\dot{B}_z| = 10$, (b) 46, (g) 10 and (h) $35\,\mathrm{G\,ms^{-1}}$. Panels (c, d, i, j) display the central cuts of the optical densities of the spin components along the x-direction and (e, f, k, l) show the corresponding tilt angle distributions $\beta(x)$ (see text). The field of view in the images is $1.3\,\mathrm{mm} \times 390\,\mu\mathrm{m}$.

this field rotation method the spin textures are generated in a controllable and deterministic manner. We infer that the expansion dynamics during the time-of-flight does not significantly modify the spin textures in our experimental conditions, ensuring that the measured density distributions adequately reveal the *in situ* distributions.

3.3. The creation of highly charged Skyrmions

One can envisage the creation of highly charged, i.e. $Q > 1$, Skyrmion spin textures by applying the imprinting process multiple times to a trapped sample. We explored this possibility with

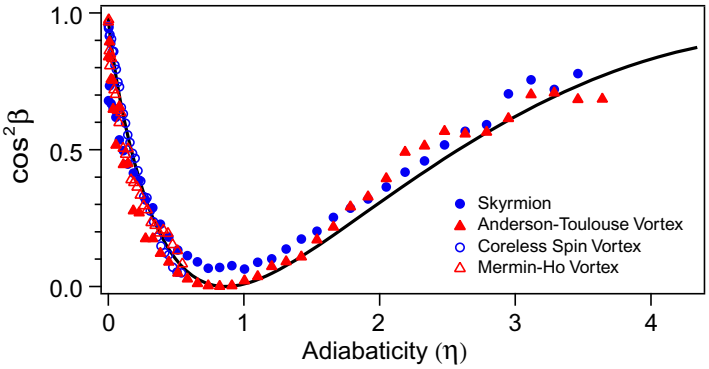

Figure 3. Spin tilt angle versus adiabaticity of the field rotation. The data points are obtained from the four different spin textures: the 2D Skyrmion (solid circle), the Anderson–Toulouse vortex (solid triangle), the coreless spin vortex (open circle) and the Mermin–Ho vortex (open triangle). The solid line is from the numerical calculation.

an experimental sequence with two consecutive field sweeps as described in figure 4. It is important to note that the additional tilt angle β_2 from the second field sweep depends not only on the adiabaticity of the field sweep but also on both the initial tilt angle β_1 and the azimuthal angle γ after the first field sweep. Moreover, γ keeps evolving in the interim between the two field sweeps. Although we know that it is possible to trace the evolution of the spin texture for a short time scale, precise control of the trajectory of the magnetic field would be technically demanding.

Reasoning that the dependence of β_2 on γ decreases when β_1 is close to zero or π, we adopted a more reliable scheme where the ratio of the local adiabaticities of the two field sweeps $\eta_2/\eta_1 \ll 1$ so that the first Skyrmion spin texture would be almost intact for the second field sweep process. In other words, the second field sweep creates an additional spin bending structure in the outer region of the first Skyrmion. Figure 4(a) illustrates the control sequence of the magnetic field. First, we imprinted a Skyrmion spin texture with $B' = 9.4\,\mathrm{G\,cm^{-1}}$ and $|\dot{B}_z| = 12\,\mathrm{G\,ms^{-1}}$ [$\eta(R_x) = 7.3$] in a polar condensate, resulting in a small, but distinguishable density-depletion ring in the $|m_z = 0\rangle$ component (figure 4(c)). Within 5 ms, we abruptly changed the field direction and applied the second field sweep with $B' = 7.0\,\mathrm{G\,cm^{-1}}$ and $|\dot{B}_z| = 40\,\mathrm{G\,ms^{-1}}$ [$\eta(R_x) = 1.2$]. Figure 4(d) shows the final spin texture where a double-ring structure is observed in all the spin components, indicating $Q > 1$.

4. Summary and outlook

In conclusion, we have investigated the magnetic field rotation method for imprinting Skyrmion spin textures in spin-1 Bose–Einstein condensates and demonstrated the creation of 2D Skyrmions and various coreless vortices in the polar and ferromagnetic phases. The spatial distributions of the spin textures show good quantitative agreement with the local single-spin description, where the spin tilt angle is fully determined by the local adiabaticity of the field rotation. This observation indicates that deterministic imprinting of spin textures is possible using this field rotation method. Furthermore, we have demonstrated the first creation of $Q > 1$ Skyrmion spin textures by consecutively applying the imprinting process multiple times to a trapped condensate.

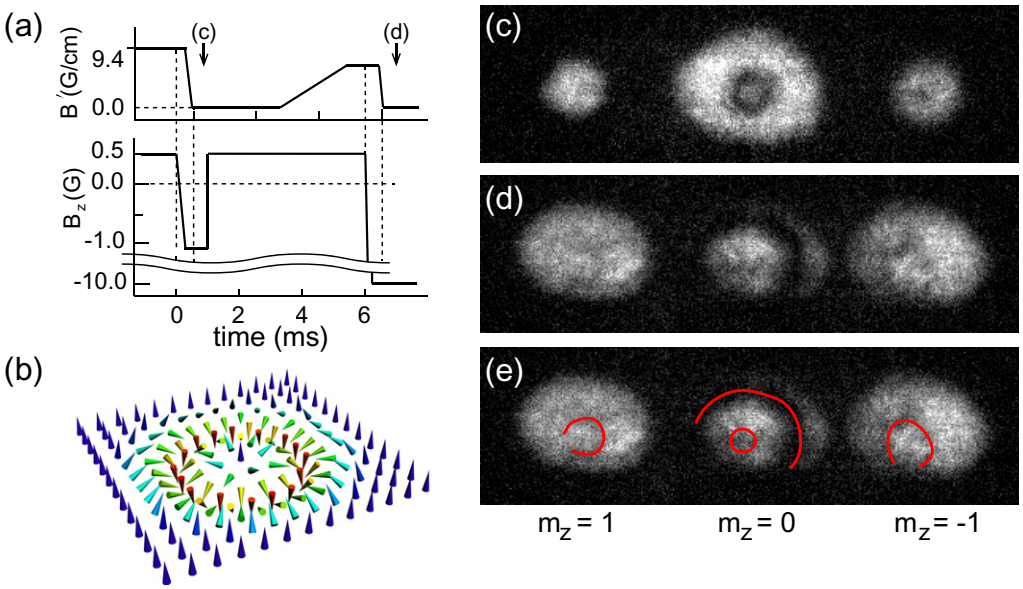

Figure 4. The creation of highly charged Skrymions in a spinor condensate. A Skyrmion spin texture with $Q > 1$ is generated by consecutively applying the imprinting process twice. (a) The control sequence of the magnetic field. (b) 3D illustration of a $Q = 2$ Skyrmion spin texture. Density distributions of the spin components after (c) the first and (d) the second field sweep, respectively. (e) The same as (d) with guidelines for the density-depleted regions.

Since the sample is kept in the optical trap after the spin texture imprinting process, our current experimental setup provides immediate opportunities to study the dynamic stabilities of the 2D Skyrmions and the coreless vortices. Recent theoretical studies showed that the Anderson–Toulouse and Mermin–Ho coreless vortices are dynamically unstable toward vortex splitting and phase separation [32]. We expect that this technique can be extended to engineer 3D topological excitations with timely control of the magnetic field. It has been proposed that knots [4] or Dirac monopole structures [5] can be generated by placing the zero-field point of a quadrupole field in a 3D condensate.

Acknowledgments

This work was supported by the National Research Foundation of Korea (NRF) grants funded by the Korean Government (MEST) (numbers 2010-0010172, 2011-0017527, 2008-0062257 and WCU-R32-10045). JC acknowledges support from a Global PhD Fellowship.

References

[1] Leonhardt U and Volovik G E 2000 How to create an Alice string in a vector Bose–Einstein condensate *JETP Lett.* **72** 46

[2] Khawaja U A and Stoof H 2001 Skyrmions in a ferromagnetic Bose–Einstein condensate *Nature* **411** 918

[3] Ruostekoski J and Anglin J R 2003 Monopole core instability and Alice rings in spinor Bose–Einstein condensates *Phys. Rev. Lett.* **91** 190402

[4] Kawaguchi Y, Nitta M and Ueda M 2008 Knots in a spinor Bose–Einstein condensate *Phys. Rev. Lett.* **100** 180403
[5] Pietilä V and Möttönen M 2009 Creation of Dirac monopoles in spinor Bose–Einstein condensates *Phys. Rev. Lett.* **103** 030401
[6] Madison K W, Chevy F, Wohlleben W and Dalibard J 2000 Vortex formation in a stirred Bose–Einstein condensate *Phys. Rev. Lett.* **84** 806
[7] Matthews M R, Anderson B P, Haljan P C, Hall D S, Wieman C E and Cornell E A 1999 Vortices in a Bose–Einstein condensate *Phys. Rev. Lett.* **83** 2498
[8] Andersen M F, Ryu C, Cladè P, Natarajan V, Vaziri A, Helmerson K and Phillips W D 2006 Quantized rotation of atoms from photons with orbital angular momentum *Phys. Rev. Lett.* **97** 170406
[9] Leanhardt A E, Görlitz A, Chikkatur A P, Kielpinski D, Shin Y, Pritchard D E and Ketterle W 2002 Imprinting vortices in a Bose–Einstein condensate using topological phases *Phys. Rev. Lett.* **89** 190403
[10] Bretin V, Rosenbusch P, Chevy F, Shlyapnikov G V and Dalibard J 2003 Quadrupole oscillation of a single-vortex Bose–Einstein condensate: evidence for Kelvin modes *Phys. Rev. Lett.* **90** 100403
[11] Coddington I, Engels P, Schweikhard V and Cornell E A 2003 Observation of Tkachenko oscillations in rapidly rotating Bose–Einstein condensates *Phys. Rev. Lett.* **91** 100402
[12] Neely T W, Samson E C, Bradley A S, Davis M J and Anderson B P 2010 Observation of vortex dipoles in an oblate Bose–Einstein condensate *Phys. Rev. Lett.* **104** 160401
[13] Freilich D V, Bianchi D M, Kaufman A M, Langin T K and Hall D S 2010 Real-time dynamics of single vortex lines and vortex dipoles in a Bose–Einstein condensate *Science* **329** 1182
[14] Shin Y, Saba M, Vengalattore M, Pasquini T A, Sanner C, Leanhardt A E, Prentiss M, Pritchard D E and Ketterle W 2004 Dynamical instability of a doubly quantized vortex in a Bose–Einstein condensate *Phys. Rev. Lett.* **93** 160406
[15] Leanhardt A E, Shin Y, Kielpinski D, Pritchard D E and Ketterle W 2003 Coreless vortex formation in a spinor Bose–Einstein condensate *Phys. Rev. Lett.* **90** 140403
[16] Leslie L S, Hansen A, Wright K C, Deutsch B M and Bigelow N P 2009 Creation and detection of Skyrmions in a Bose–Einstein condensate *Phys. Rev. Lett.* **103** 250401
[17] Stenger J, Inouye S, Stamper-Kurn D M, Miesner H-J, Chikkatur A P and Ketterle W 1998 Spin domains in ground-state Bose–Einstein condensates *Nature* **396** 345
[18] Chang M S, Hamley C D, Barrett M D, Sauer J A, Fortier K M, Zhang W, You L and Chapman M S 2004 Observation of spinor dynamics in optically trapped ^{87}Rb Bose–Einstein condensates *Phys. Rev. Lett.* **92** 140403
[19] Berry M V 1984 Quantal phase factors accompanying adiabatic changes *Proc. R. Soc.* A **392** 45
[20] Isoshima T, Nakahara M, Ohmi T and Machida K 2000 Creation of a persistent current and vortex in a Bose–Einstein condensate of alkali-metal atoms *Phys. Rev.* A **61** 063610
[21] Mukerjee S, Xu C and Moore J E 2006 Topological defects and the superfluid transition of the $s = 1$ spinor condensate in two dimensions *Phys. Rev. Lett.* **97** 120406
[22] Choi J, Kwon W J and Shin Y 2012 Observation of topologically stable 2D Skyrmions in an antiferromagnetic spinor Bose–Einstein condensate *Phys. Rev. Lett.* **108** 035301
[23] Ueda M and Kawaguchi Y 2010 Spinor Bose–Einstein condensates arXiv:1001.2072
[24] Anderson P W and Toulouse G 1977 Phase slippage without vortex cores: vortex textures in superfluid ^{3}He *Phys. Rev. Lett.* **38** 508
[25] Mermin N D and Ho T-L 1976 Circulation and angular momentum in the a phase of superfluid helium-3 *Phys. Rev. Lett.* **36** 594
[26] Salomaa M M and Volovik G E 1987 Quantized vortices in superfluid 3He *Rev. Mod. Phys.* **59** 533
[27] Blaauwgeers R, Eltsov V B, Krusius M, Ruohio J J, Schanen R and Volvik G E 2000 Double-quantum vortex in superfluid 3He-A *Nature* **404** 471
[28] Mizushima T, Machida K and Kita T 2002 Mermin–Ho vortex in ferromagnetic spinor Bose–Einstein condensates *Phys. Rev. Lett.* **89** 030401

[29] Martikainen J P, Collin A and Suominen K A 2002 Coreless vortex ground state of the rotating spinor condensate *Phys. Rev.* A **66** 053604

[30] Burke J P, Greene C H and Bohn J L 1998 Multichannel cold collisions: simple dependences on energy and magnetic field *Phys. Rev. Lett.* **81** 3355

[31] Heo M S, Choi J and Shin Y 2011 Fast production of large ^{23}Na Bose–Einstein condensates in an optically plugged magnetic quadrupole trap *Phys. Rev.* A **83** 013622

[32] Takahashi M, Pietilä V, Möttönen M, Mizushima T and Machida K 2009 Vortex-splitting and phase-separating instabilities of coreless vortices in $F = 1$ spinor Bose–Einstein condensates *Phys. Rev.* A **79** 023618

Appendix I

Gauge potential for neutral atoms in a magnetic quadrupole field

This appendix includes a reprint of Ref. : Yong-il Shin and Jae-yoon Choi. *"Gauge potential for neutral atoms in a magnetic quadrupole field"* Journal of the Korean Physical Society **63**, 951 (2013).

Journal of the Korean Physical Society, Vol. 63, No. 4, August 2013, pp. 951∼956

Gauge Potential for Neutral Atoms in a Magnetic Quadrupole Field

Yong-il SHIN* and Jae-yoon CHOI

Center for Subwavelength Optics and Department of Physics and Astronomy, Seoul National University, Seoul 151-747, Korea

(Received 25 February 2013, in final form 19 March 2013)

We consider a spinor Bose-Einstein condensate of neutral atoms in a magnetic quadrupole field and investigate the gauge potential derived from the spatially-varying magnetic field. We discuss the critical condition for a singular, quantized vortex state being energetically favored in the spinor condensate and find that it is necessary under experimentally realistic conditions to use atoms with hyperfine spin $F > 1$ and/or a more spatially-varying magnetic field, *e.g.*, hexapole or octopole fields. Finally, we show that a spinor condensate in a ring geometry is beneficial for observing the gauge potential effects.

PACS numbers: 67.85.-d, 03.75.Mn, 03.65.Vf
Keywords: Spinor condensate, Berry phase, Quantized vortex
DOI: 10.3938/jkps.63.951

I. INTRODUCTION

Ultracold atomic gases are highly controllable, clean quantum many-body systems, and have enabled the study of a broad range of quantum phenomena including Bose-Einstein condensation, Mott-insulator transitions, high-temperature fermionic superfluidity, and Anderson localization [1]. One of the frontiers in current quantum gas research is exploring quantum Hall physics, which was initiated by observing the integer and the fractional quantum Hall effects in two-dimensional(2D) electron systems [2,3]. This requires an artificial magnetic field for neutral atoms, which can induce a force like the Lorentz force for a charged particle in a magnetic field.

Early works in this pursuit investigated rotating atomic gases, where the Coriolis force in a rotating frame played the role of the Lorentz force in a magnetic field [4, 5]. Quantized vortices were observed in a rotating Bose-Einstein condensate (BEC) [6,7], and BECs in the lowest Landau level were created with fast rotation [8]. However, if the quantum Hall regime is to be reached, the rotation frequency needs to be extremely close to the deconfinement limit for the trapping potential [9], which remains technically challenging. Recently, new methods based on the light-induced Berry phase have been demonstrated to generate artificial magnetic fields for neutral atoms [10]. Quantized vortices were observed in BECs in spatially-engineered Raman laser fields [11], and a staggered magnetic field was generated using Raman-assisted tunneling in an optical lattice [12].

An alternative way to exploit the Berry phase for creating a gauge potential is using an inhomogeneous magnetic field. Because of the spin-gauge symmetry, a particle carrying a non-zero spin acquires a Berry phase when its spin makes a cyclic adiabatic evolution in the Hilbert space for the spin [13]. Thus, when the particle moves in a spatially-varying magnetic field, it will experience an effective magnetic field as its spin follows the direction of the local magnetic field. This spin-gauge effect has been actively studied for many decades in spintronics [14]. The underlying mechanism for the light-induced gauge potentials can be understood in a similar manner by regarding the dressed states in the Raman laser fields as pseudo-spin states.

In this paper, motivated by our recent experiments where we created skyrmion spin textures in quasi-2D spinor Bose-Einstein condensates by using a magnetic quadrupole field [15, 16], we study the gauge potential for atoms in the inhomogeneous magnetic field. Here, we describe the superfluid state of the spinor condensate by estimating the gauge potential derived from the magnetic field and discuss the critical condition for a singular, quantized vortex state being energetically favored.

II. EFFECTIVE GAUGE POTENTIAL

In this section, we present a brief description of the effective gauge potential present in an inhomogeneous magnetic field. Let us consider a neutral atom of mass m and hyperfine spin $F = 1$ in a spatially non-uniform magnetic field $\vec{B}(\vec{r})$. The local field direction is denoted by $\hat{b}(\vec{r}) = \vec{B}/|\vec{B}| = (\sin\beta\cos\alpha, \sin\beta\sin\alpha, \cos\beta)$, where $\alpha(\vec{r})$ and $\beta(\vec{r})$ are the azimuthal and the tilt angles of the field direction with respect to the $+z$-direction, re-

*E-mail: yishin@snu.ac.kr

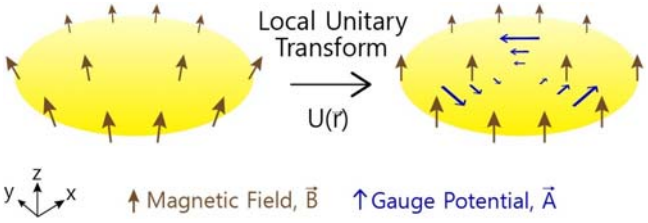

Fig. 1. (Color online) Under a local unitary transformation $U(\vec{r})$, the system in a spatially-varying magnetic field is mapped to an effective system where the magnetic field direction is uniform, introducing a gauge potential $\vec{A}(\vec{r}) = -iU\nabla U^{\dagger}$.

spectively. The Hamiltonian of the system is

$$\begin{aligned} H &= \frac{\vec{p}^2}{2m} - g\mu_B \vec{F}\cdot\vec{B}(\vec{r}) \\ &= \frac{\vec{p}^2}{2m} - g\mu_B(\vec{F}\cdot\hat{b}(\vec{r}))|\vec{B}|, \end{aligned} \tag{1}$$

where g is the g-factor of the atom, μ_B the Bohr magneton, and $\vec{F}$ the hyperfine spin operator with $F_x = \frac{1}{\sqrt{2}}\begin{pmatrix} 0&1&0\\1&0&1\\0&1&0\end{pmatrix}$, $F_y = \frac{i}{\sqrt{2}}\begin{pmatrix} 0&-1&0\\1&0&-1\\0&1&0\end{pmatrix}$, and $F_z = \begin{pmatrix} 1&0&0\\0&0&0\\0&0&-1\end{pmatrix}$. In this representation, the state of the atom is described by a three-component spinor $|\Psi\rangle = (\psi_1, \psi_0, \psi_{-1})^{\mathrm{T}}$, where $\psi_{0,\pm1}$ are the wavefunctions of the $m_z = 0, \pm1$ spin components of the atom, respectively.

Now, we take a local unitary transformation $U(\vec{r})$ which rotates the reference axis for the spin, which is uniformly set to $+\hat{z}$, to the local magnetic field direction $\hat{b}$, *i.e.*, transforms the eigenstates of $\vec{F}\cdot\hat{b}$ to the eigenstates of F_z. The transformed Hamiltonian is given by

$$\begin{aligned} H' &= UHU^{\dagger} \\ &= \frac{1}{2m}U\vec{p}^2U^{\dagger} - g\mu_B U(\vec{F}\cdot\hat{b})U^{\dagger}|\vec{B}| \\ &= \frac{1}{2m}(\vec{p} - i\hbar U\nabla U^{\dagger})^2 - g\mu_B F_z|\vec{B}|, \end{aligned} \tag{2}$$

where $\hbar$ is the Planck constant h divided by 2π. Under this transformation, the system is mapped to an effective system in a magnetic field whose direction is spatially uniform (Fig. 1), introducing a gauge potential $\vec{A}(\vec{r}) \equiv -iU\nabla U^{\dagger}$. This gauge potential is referred to as the Berry connection.

To present an explicit form of the gauge potential, we set the local unitary transformation to be a rotation around $\hat{n} = (\hat{b}\times\hat{z})/|\hat{b}\times\hat{z}| = \sin\alpha\hat{x} - \cos\alpha\hat{y}$ by the tilt angle β:

$$\begin{aligned} U &= e^{-i\beta\hat{n}\cdot\vec{F}} \\ &= \begin{pmatrix} \cos^2\frac{\beta}{2} & \frac{\sin\beta}{\sqrt{2}}e^{-i\alpha} & \sin^2\frac{\beta}{2}e^{-i2\alpha} \\ \frac{-\sin\beta}{\sqrt{2}}e^{i\alpha} & \cos\beta & \frac{\sin\beta}{\sqrt{2}}e^{-i\alpha} \\ \sin^2\frac{\beta}{2}e^{i2\alpha} & \frac{-\sin\beta}{\sqrt{2}}e^{i\alpha} & \cos^2\frac{\beta}{2} \end{pmatrix}. \end{aligned} \tag{3}$$

When we expand $\vec{A} = -iU\nabla U^{\dagger} = \vec{A}_x F_x + \vec{A}_y F_y + \vec{A}_z F_z$, this choice of the unitary transformation gives

$$\begin{aligned} \vec{A}_x &= \cos\alpha\sin\beta\nabla\alpha + \sin\alpha\nabla\beta, \\ \vec{A}_y &= \sin\alpha\sin\beta\nabla\alpha - \cos\alpha\nabla\beta, \\ \vec{A}_z &= (1-\cos\beta)\nabla\alpha. \end{aligned} \tag{4}$$

Note that the components of $\vec{A}$ are matrices that do not commute with each other and that the gauge potential represents an example of a non-Abelian gauge potential.

Here, we restrict our interests to the adiabatic regime in which the atom in a spin eigenstate remains in the same eigenstate with respect to the local reference axis. This means that there is no spin flips when the atom travels between two spatial points. The off-diagonal elements in H' account for the spin transitions, so ignoring them, we obtain the adiabatic Hamiltonian

$$\begin{aligned} H'_{\mathrm{ad}} &= \frac{1}{2m}(\vec{p} + \hbar\vec{A}_z F_z)^2 - g\mu_B F_z|\vec{B}(\vec{r})| \\ &+ \frac{\hbar^2}{2m}(1 - \frac{1}{2}F_z^2)\big((\nabla\beta)^2 + \sin^2\beta(\nabla\alpha)^2\big), \end{aligned} \tag{5}$$

and the resulting adiabatic gauge potential for the $|m_F\rangle$ state is $\vec{A}_{\mathrm{ad}} = m_F\vec{A}_z$, where $|m_F\rangle$ denotes the spin eigenstate with a quantization axis parallel to the local magnetic field. The last term is the scalar potential from $(\vec{A}_x F_x + \vec{A}_y F_y)^2$, which has different magnitudes for $|m_F = 0\rangle$ and $|m_F = \pm1\rangle$.

The Hamiltonian for a charged particle in a magnetic field $\vec{B}$ is $H_{\mathrm{B}} = \frac{1}{2m}(\vec{p} - q\vec{A}_{\mathrm{B}})^2$, where q is the electric charge of the particle and $\vec{A}_B$ is the vector potential with $\vec{B} = \nabla\times\vec{A}_{\mathrm{B}}$. The comparison between H'_{ad} and H_{B} shows that the neutral atom in the spatially-varying magnetic field experiences an effective magnetic field $\vec{B}^* = -\frac{\hbar}{q}\nabla\times\vec{A}_{\mathrm{ad}}$. The vector field $\vec{\Omega}(\vec{r}) \equiv \nabla\times\vec{A}_{\mathrm{ad}}$ is referred to as the Berry curvature, which is gauge-invariant, *i.e.*, independent of $U(\vec{r})$. The Berry curvature can be shown to be directly related with the spatial curvature of the field direction $\hat{b}$ as

$$\begin{aligned} \vec{\Omega} &= m_F\nabla\times\big((1-\cos\beta)\nabla\alpha\big) \\ &= m_F\frac{\epsilon_{ijk}}{2}\big(\hat{b}\cdot(\partial_i\hat{b}\times\partial_j\hat{b})\big)\hat{k}, \end{aligned} \tag{6}$$

where i, j, k are spatial coordinates. This relation is, indeed, valid for a particle with an arbitrary spin number F.

III. SPINOR CONDENSATE IN A QUADRUPOLE MAGNETIC FIELD

Figure 2(a) shows a schematic diagram of the experiment setup for our recent works [15,16], where an oblate spinor condensate in an optical trap is exposed to a three-dimensional magnetic quadrupole field. The condensate is placed in the center of the $z = 0$ plane, and the axis of

the quadrupole field is aligned to that of the condensate. The magnetic field distribution is given by

$$\vec{B}(r,\theta,z) = B'(r\hat{r} - 2z\hat{z}) + B_z\hat{z}, \tag{7}$$

where B' is the radial field gradient and B_z is an external bias field along the axial direction. The z-position of the zero-field center of the quadrupole field is $z_0 = B_z/2B'$.

The two angles describing the magnetic field direction $\hat{b}(\vec{r})$ are

$$\begin{aligned} \alpha(r,\theta,z) &= \theta, \\ \beta(r,\theta,z) &= \tan^{-1}\left(\frac{r}{2z'}\right), \end{aligned} \tag{8}$$

with $z' = z_0 - z$. From Eqs. (4) and (6), the gauge potential and the Berry curvature for an atom in the $|m_F\rangle$ state are given, respectively, by

$$\vec{A}_{\rm ad}(r,z') = m_F\frac{\sqrt{r^2+4z'^2}-2z'}{r\sqrt{r^2+4z'^2}}\hat{\theta}, \tag{9}$$

$$\vec{\Omega}(r,z') = m_F\frac{-2r\hat{r}+2z'\hat{z}}{(r^2+4z'^2)^{3/2}}. \tag{10}$$

Then, the Hamiltonian for the atom in the $z = 0$ plane reads

$$H_{\rm s} = \frac{1}{2m}\left(\vec{p} + \hbar\vec{A}_{\rm ad}(r,z_0)\right)^2 + V(r), \tag{11}$$

where

$$\begin{aligned} V(r) =& \frac{1}{2}m\omega_r^2 r^2 - \frac{\mu_B}{2}m_F B'\sqrt{r^2+4z_0^2} \\ &+ \frac{\hbar^2}{2m}(1-\frac{1}{2}m_F^2)\frac{5r^2+8z_0^2}{(r^2+4z_0^2)^2}, \end{aligned} \tag{12}$$

including the harmonic potential of the optical trap, the Zeeman energy with $g = -1/2$, and the scalar potential derived from the off-diagonal gauge potentials.

Next, we investigate the state of the condensate in this gauge potential. The kinetic momentum of the atom is $\vec{\Pi} = \vec{p} + \hbar\vec{A}_{\rm ad}$, containing the gauge potential; thus, the superfluid velocity in the condensate is given by $\vec{v}_s = \frac{\hbar}{m}(\nabla\phi + \vec{A}_{\rm ad})$, where ϕ is the superfluid phase. In this case, the quantization of the superfluid circulation is expressed as

$$\oint(\vec{v}_s - \frac{\hbar}{m}\vec{A}_{\rm ad})\cdot d\vec{l} = \frac{h}{m}q_v, \tag{13}$$

where q_v is an integer representing the winding number of the superfluid phase along the closed path [17]. When we prepare the condensate in the $|m_F = \pm 1\rangle$ state with a uniform superfluid phase, the condensate contains a non-zero superfluid circulation of $\vec{v}_{s0}(r) = \vec{A}_{\rm ad}(r,z_0)$ in the lab frame, which is along the azimuthal direction. Therefore, the spinor condensate is, indeed, rotating in the magnetic quadrupole field. This is a coreless vortex state having a finite angular momentum without a density-depleted core.

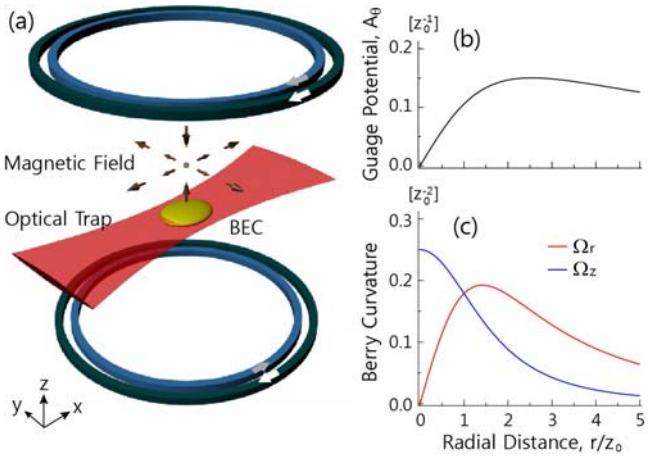

Fig. 2. (Color online) (a) Schematic of the experimental setup where a quasi-2D spinor condensate is prepared in an optical trap and a magnetic quadrupole field is applied by using pairs of current-carrying coils. The axis of the quadrupole field is aligned along that of the condensate. (b) Adiabatic gauge potential $\vec{A}_{\rm ad}(r) = m_F A_\theta\hat{\theta}$ (see text for the corresponding unitary transformation) and (c) Berry curvature $\vec{\Omega}(r) = m_F(-\Omega_r\hat{r} + \Omega_z\hat{z})$ for the $F = 1$ spinor condensate in the $z = 0$ plane. $z_0(>0)$ denotes the z-position of the zero-field center of the magnetic field.

It is pedagogically helpful to express the order parameter Ψ of the spinor condensate in the coreless vortex state with the spin quantization axis along the z-direction. Let us consider a situation where, for example, a condensate with a uniform superfluid phase is initially prepared in the $|m_z = -1\rangle$ state for $B' = 0$ and $B_z > 0$, and the field gradient is adiabatically ramped up to $B' > 0$. The initial order parameter is described by $\Psi_i = \sqrt{n(r)}e^{i\phi}(0,0,1)^{\rm T}$, where $n(r)$ is the superfluid density. As the zero-field point moves from $z = +\infty$ to z_0 with increasing B', the local atomic spin adaptively follows the rotating magnetic field. Then, the final order parameter Ψ_f is given by

$$\Psi_f(r,\theta) = U^\dagger\Psi_i = \sqrt{n(r)}e^{i\phi}\begin{pmatrix}\sin^2\frac{\beta(r)}{2}e^{-i2\theta}\\ \frac{-\sin\beta(r)}{\sqrt{2}}e^{-i\theta}\\ \cos^2\frac{\beta(r)}{2}\end{pmatrix}, \tag{14}$$

where we neglect the change of $n(r)$ due to the modification of the external potential.

This description shows that by applying the quadrupole field, the atoms initially populated in the $|m_z = -1\rangle$ state are coherently transferred to the $|m_z = 0, +1\rangle$ states which have orbital angular momenta of $-\hbar$ and $-2\hbar$, respectively. The total angular momentum of the system is

$$\begin{aligned} L_z &= \int[-\hbar n_0(r) - 2\hbar n_{+1}(r)]2\pi r dr \\ &= -2\hbar\int n(r)\sin^2\frac{\beta(r)}{2}2\pi r dr, \end{aligned} \tag{15}$$

where $n_{+1,0}$ are the densities of the $m_z = +1, 0$ components, respectively. This is identical to the total angular momentum estimated from the superfluid velocity for the $|m_F = -1\rangle$ state; *i.e.*, $L_z = \int dr\, 2\pi r n(r)\hat{z}\cdot[\vec{r}\times m\vec{v}_{s0}(r)]$. It is remarkable that the change of the angular momentum as the zero-field point is approached can be understood to be a result of an effective electromotive force induced by the increasing effective magnetic field, *i.e.*, the Berry curvature. This force is termed the spin-motive force.

IV. VORTEX GROUND STATE

Quantized vortices are the characteristic response of a superfluid system to rotation and are typically observed with density-depleted cores containing superfluid phase singularity [6, 7]. The Hamiltonian for a particle in a reference frame rotating with angular velocity $\vec{\omega} = \omega\hat{z}$ is given by $H_R = \frac{\vec{p}^2}{2m} - \vec{\omega}\cdot\vec{r}\times\vec{p} = \frac{1}{2m}(\vec{p} - m\vec{\omega}\times\vec{r})^2 - \frac{1}{2}m\omega^2 r^2$, which shows that a uniform Berry curvature $\vec{\Omega}$ can be considered to be an effective rotation of $\vec{\omega} = \frac{\hbar}{2m}\vec{\Omega}$. In this section, we discuss the experimental condition for having a quantized vortex state with a singular core as the ground state of a spinor condensate.

For a condensate trapped in a three-dimensional harmonic potential, the critical rotation frequency for generating a quantized vortex is estimated to be $\omega_c = \frac{5\hbar}{2mR^2}\ln\frac{0.67R}{\xi}$ [18], where R is the Thomas-Fermi radius and ξ is the healing length of the condensate, representing the vortex core radius. When $\omega > \omega_c$, the energy of the vortex state in the rotating frame is lower than that of the non-vortex state. In our case, the magnitude of the Berry curvature at the trap center is $\Omega_0 = 1/(4z_0^2)$,so one might simply expect a singular vortex state to be energetically favored when $\Omega_0 > \Omega_c = \frac{2m}{\hbar}\omega_c$. This criterion was applied in Ref. [19], where the authors considered a $F = 2$ condensate trapped in a Ioffe-Pritchard magnetic trap. However, we note that the variation of the Berry curvature over the condensate is not negligible, so it must be taken into account.

We estimate the energy difference ΔE between the coreless vortex state Ψ_f and the singular, singly-charged vortex state Ψ_v which we define as $\Psi_v(r,\theta) = \Psi_f \times \sqrt{s(r)}e^{i\theta}$, where $s(r)$ represents the shape of the density profile of the singular vortex core in an infinite system. The superfluid velocity in the singular vortex state is given by

$$\vec{v}_{s,v}(r) = \frac{\hbar}{m}\left(\vec{A}_{\rm ad} + \frac{\hat{\theta}}{r}\right) = \frac{\hbar}{mr}\cos\beta(r)\hat{\theta}. \tag{16}$$

In the hydrodynamic regime, *i.e.*, $\xi \ll R$, the energy difference of the two vortex states is given by

$$\Delta E \approx \pi n(0)\frac{\hbar^2}{m}\ln\frac{1.46b}{\xi} + \int_b^R \frac{mn(r)}{2}[v_{s,v}^2(r) - v_{s0}^2(r)]2\pi r dr, \tag{17}$$

where the first term is the energy of a singly-charged vortex in the center region for $r < b$ ($\xi \ll b \ll R$) [20] and the second term corresponds to the kinetic energy of the superfluid in the region for $r > b$. In a harmonic potential approximation, $n(r) = n(0)[1 - V(r)/V(R)] \approx n(0)(1 - r^2/R^2)$, we obtain

$$\frac{m\Delta E}{\pi\hbar^2 n(0)} \approx \ln\frac{1.46b}{\xi} + \int_b^R \left(1 - \frac{r^2}{R^2}\right)\frac{4z_0 - \sqrt{r^2+4z_0^2}}{r\sqrt{r^2+4z_0^2}}dr \approx \ln\frac{2.41R}{\xi} - \frac{2}{t^2}(\sqrt{1+t^2}-1) + 2\ln\frac{2}{1+\sqrt{1+t^2}}, \tag{18}$$

where $t = \tan\beta(R) = R/2z_0$ and terms of higher order in b/R are neglected. As $t \to 0$, *i.e.*, in the limit of no quadrupole field, $\Delta E = \frac{\pi\hbar^2 n(0)}{m}\ln\frac{0.89R}{\xi}$, equivalent to Eq. (33) in Ref. [18].

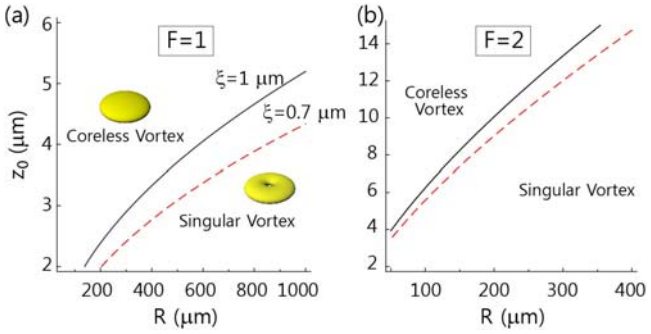

Fig. 3. (Color online) Phase boundary of the singular-vortex ground state of a quasi-2D spinor condensate of hyperfine spins (a) F=1 and (b) F=2 in a magnetic quadrupole field. R is the radius of the condensate, and ξ is the healing length, representing the characteristic size of the vortex core.

In Fig. 3, we display the critical curve of $\Delta E = 0$ in the z_0-R plane, showing the existence of a large-t region in which the singular vortex state becomes energetically favored over the coreless vortex state. However, it seems to be experimentally demanding to fulfill the condition. For example, for $R = 100$ μm, the zero-field point of the quadrupole field needs to be placed less than a few μm away from the condensate. This requires tight confinement of the condensate along the z-direction, as well as extremely stable control of the magnetic field.

The ground state of an infinite superfluid system in a uniform Berry curvature Ω is well know to be a vortex lattice state with an areal vortex density of $\Omega/2\pi$. Here, one might consider a quantized vortex to be accompanied by a Berry curvature flux of 2π. In our case, the flux Φ

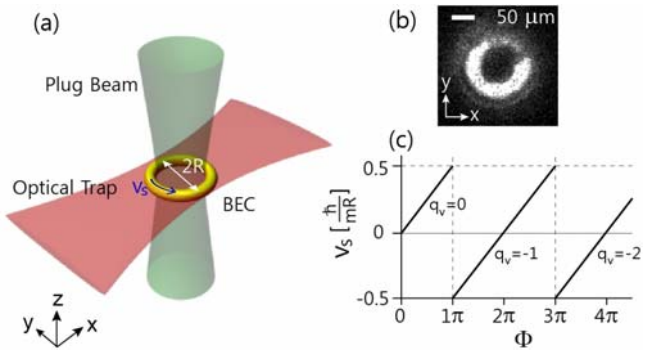

Fig. 4. (Color online) Spinor condensate in a ring trap. (a) A toroidal potential is formed by applying a repulsive optical potential (a blue-detuned plug beam) in the trap center. (b) Absorption image of a BEC trapped in the potential. (c) Superfluid velocity v_s in a ring of radius R versus Berry curvature flux Φ in the ring. v_s shows a sawtooth-like behavior as Φ increases, where transitions between vortex states occur at $\Phi = (2|q_v| - 1)\pi$. q_v denotes the winding number of the superfluid phase for the vortex state.

through the condensate is given by

$$\Phi = \int \vec{\Omega} \cdot d\vec{a} = \oint \vec{A}_{\rm ad} \cdot d\vec{l} = 2\pi[1 - \cos\beta(R)], \quad (19)$$

and the condition $\Phi = 2\pi$ is marginally satisfied when $\beta = \pi/2$. This qualitatively explains the results of our numerical calculation, suggesting that using atoms of higher hyperfine spin and/or a more spatially-varying magnetic field, *e.g.*, hexapole or octopole fields might be necessary to observe a singular-vortex ground state in experiment. Note that the flux Φ is the Berry phase acquired for one adiabatic circulation along the boundary of the condensate. We performed a similar analysis of the $F = 2$ case and verified that $F = 2$ condensates provide a favorable condition for the vortex ground state [Fig. 3(b)].

Another route for observing the generation of singular vortices as a spin-gauge effect is employing a BEC in a ring trap (Fig. 4). The superfluid velocity in the singular vortex state diverges as $v_{s,v} \propto 1/r$ in the center region whereas $v_{s0} \propto r$ in the coreless vortex state. Therefore, the relative energy cost of the singular vortex state can be alleviated by suppressing the density in the center region. For example, when a $F = 1$ condensate is trapped in a ring of radius R, the criterion $\Delta E < 0$ is reduced to $|v_{s,v}| < |v_{s0}|$, which is satisfied in a broad range of the experiment parameters with $\beta(R) > \pi/3$, *i.e.*, $z_0 < R/2\sqrt{3}$. At the critical point, the Berry curvature flux Φ in the ring is π. It is straightforward to extend this discussion to multiply-charged vortex states where the superfluid velocities are $v_s(q_v) = \frac{\hbar}{mR}(\Phi/\pi + q_v)$. For a minimum supercurrent in the ground state, the superfulid velocity will show a sawtooth-like behavior as Φ increases [Fig. 4(c)]. Superfluid flow in a ring geometry has been investigated in recent experiments with BECs in toroidal traps, and persistent currents [21] and quantized behavior of superfluid flow [22, 23] have been observed. In our experiment setup, a ring geometry was achieved by superposing a repulsive optical potential, *i.e.*, a plug beam in the center of the optical trap [Fig. 4(b)] [24].

V. CONCLUSIONS AND OUTLOOKS

In conclusion, we have presented an overview of the gauge potential derived from a spatially-varying magnetic field, and described $F = 1$ spinor condensates in a magnetic quadrupole field. We have investigated the critical condition for having a singular-vortex ground state, suggesting that using atoms with hyperfine spin $F > 1$ and/or a more spatially-varying magnetic field, *e.g.*, hexapole or octopole fields might be necessary to observe the vortex ground state in experiment. Finally, we have considered a spinor condensate in a ring trap, and found that it provides a more favorable condition for observing spin-gauge effects. Because the artificial gauge potential originates with the Berry phase in the multi-dimensional Hilbert space for the atomic spin, it is naturally non-Abelian [25], resulting in a spin-dependent effective Lorentz force. Spinor condensates in spatially-varying magnetic fields should allow the study of spin-dependent transport phenomena such as spin Hall effects [26]. Furthermore, this gauge potential couples the motional state of the atom to its internal spin state, providing a new setting for the study of spin-orbit coupling effects [27], which is one of the hot topics in current condensed matter physics.

ACKNOWLEDGMENTS

This work was supported by the NRF of Korea funded by MEST (Grants No. 2011-0017527 and No. 2008-0062257). Y. S. and J. C. acknowledge support from the T. J. Park Science Fellowship and the Global PhD Fellowship, respectively.

REFERENCES

[1] I. Bloch, J. Dalibard and W. Zwerger, Rev. Mod. Phys. **80**, 885 (2008).
[2] D. C. Tsui, H. L. Stormer and A. C. Gossard, Phys. Rev. Lett. **48**, 1559 (1982).
[3] R. B. Laughlin, Phys. Rev. Lett. **50**, 1395 (1983).
[4] N. R. Cooper, Advances in Physics **57**, 539 (2008).
[5] A. L. Fetter, Rev. Mod. Phys. **81**, 647 (2009).
[6] K. W. Madison, F. Chevy, W. Wohlleben and J. Dalibard, Phys. Rev. Lett. **84**, 806 (2000).
[7] J. R. Abo-Shaeer, C. Raman, J. M. Vogels and W. Ketterle, Science **292**, 476 (2001).

[8] V. Schweikhard, I. Coddington, P. Engels, V. P. Mogendorff and E. A. Cornell, Phys. Rev. Lett. **92**, 040404 (2004).
[9] N. R. Cooper, N. K. Wilkin and J. M. F. Gunn, Phys. Rev. Lett. **87**, 120405 (2001).
[10] J. Dalibard, F. Gerbier, G. Juzeliūnas and P. Öhberg, Rev. Mod. Phys. **83**, 1523 (2011).
[11] Y.-J. Lin, R. L. Compton, K. Jiménez-Garcia, J. V. Porto and I. B. Spielman, Nature **462**, 628 (2009).
[12] M. Aidelsburger, M. Atala, S. Nascimbène, S. Trotzky, Y.-A. Chen and I. Bloch, Phys. Rev. Lett. **107**, 255301 (2011).
[13] M. V. Berry, Proc. R. Soc. London A **392**, 45 (1984).
[14] T. Fujita, M. B. A. Jalil, S. G. Tan and S. Murakami, J. Appl. Phys. **110**, 121301 (2011).
[15] J. Choi, W. J. Kwon and Y. Shin, Phys. Rev. Lett. **108**, 035301 (2012).
[16] J. Choi, W. J. Kwon, M. Lee, H. Jeong, K. An and Y. Shin, New J. Phys. **14**, 053013 (2012).
[17] Y. Kawaguchi and M. Ueda, Phys. Rep. **520**, 253 (2012).
[18] E. Lundh, C. J. Pethick and H. Smith, Phys. Rev. A **55**, 2126 (1997).
[19] T. L. Ho and V. B. Shenoy, Phys. Rev. Lett. **77**, 2595 (1996).
[20] V. L. Ginzburg and L. P. Piatevskii, Sov. Phys. JETP **7**, 858 (1958).
[21] C. Ryu, M. F. Anderson, P. Cladé, V. Natarajan, K. Helmerson and W. D. Phillips, Phys. Rev. Lett. **99**, 260401 (2007).
[22] A. Ramanathan, K. C. Wright, S. R. Muniz, M. Zelan, W. T. Hill III, C. J. Lobb, K. Helmerson, W. D. Phillips and G. K. Campbell, Phys. Rev. Lett. **106**, 130401 (2011).
[23] S. Moulder, S. Beattie, R. P. Smith, N. Tammuz and Z. Hadzibabic, Phys. Rev. A **86**, 013629 (2012).
[24] M.-S. Heo, J. Choi and Y. Shin, Phys. Rev. A **83**, 013622(2011).
[25] F. Wilczek and A. Zee, Phys. Rev. Lett. **52**, 2111 (1984).
[26] M. Taillefumier, E. K. Dahl, A. Brataas and W. Hofstetter, Phys. Rev. B **80**, 020407(R) (2009).
[27] Y.-J. Lin, K. Jiménez-Garcia and I. B. Spielman, Nature **471**, 83 (2011).

Appendix J

Observation of a Geometric Hall effect in a Spinor Bose-Einstein Condensate with a Skyrmion Spin Texture

This appendix includes a reprint of Ref. : Jae-yoon Choi, Sang Won Seo, and Yong-il Shin. *"Observation of a Geometric Hall effect in a Spinor Bose-Einstein Condensate with a Skyrmion Spin Texture"* Physical Review Letters **111**, 245301 (2013).

Observation of a Geometric Hall Effect in a Spinor Bose-Einstein Condensate with a Skyrmion Spin Texture

Jae-yoon Choi, Seji Kang, Sang Won Seo, Woo Jin Kwon, and Yong-il Shin*

Center for Subwavelength Optics and Department of Physics and Astronomy, Seoul National University, Seoul 151-747, Korea

(Received 30 September 2013; published 10 December 2013)

For a spin-carrying particle moving in a spatially varying magnetic field, effective electromagnetic forces can arise due to the geometric phase associated with adiabatic spin rotation of the particle. We report the observation of a geometric Hall effect in a spinor Bose-Einstein condensate with a Skyrmion spin texture. Under translational oscillations of the spin texture, the condensate resonantly develops a circular motion in a harmonic trap, demonstrating the existence of an effective Lorentz force. When the condensate circulates, quantized vortices are nucleated in the boundary region of the condensate and the vortex number increases over 100 without significant heating. We attribute the vortex nucleation to the shearing effect of the effective Lorentz force from the inhomogeneous effective magnetic field.

DOI: 10.1103/PhysRevLett.111.245301 PACS numbers: 67.85.−d, 03.65.Vf, 03.75.Kk, 05.30.Jp

When a particle with a spin slowly moves in a spatially varying magnetic field and its spin adiabatically follows the field direction, the particle acquires a quantum-mechanical phase known as the Berry phase [1]. This phase originates from the geometrical properties of the parameter space of the system, and in the Hamiltonian description, it can be represented as a gauge potential [2]. Just like the vector potential for a charged particle, the gauge potential generates forces from its spatial and temporal variations [3], and the geometric forces act like magnetic and electric forces on the spin-carrying particle.

Emergent electromagnetism of this spin origin can lead to novel spin transport phenomena. In magnetic materials, because of the coupling of a spin current to magnetization, a noncoplanar spin texture of magnetization gives rise to an effective internal magnetic field, leading to the intrinsic anomalous Hall effect [4,5]. Recently, the topological Hall effects were observed in chiral magnets with Skyrmion lattice spin textures [6–8]. Since the Berry phase is proportional to the spin value, effective electromagnetic forces are intrinsically spin dependent and, thus, they have been actively investigated for spintronics applications [9–11]. In recent experiments with ultracold neutral atoms, artificial magnetic and electric fields were synthesized using atom-light interaction [12,13], presenting a new opportunity for exploring quantum many-body phenomena in gauge fields. This experimental technique is based on the Berry-phase effect from the pseudospin texture of light-dressed atoms [14].

In this Letter, we report the observation of a geometric Hall effect in a spin-polarized atomic Bose-Einstein condensate, where a rigid spin texture of Skyrmion configuration is imposed by a spatially varying external magnetic field. We investigate the condensate dynamics under translational oscillations of the spin texture and observe that a circular motion of the condensate is resonantly induced from the translational drive. This directly manifests the existence of the effective Lorentz force acting on the condensate. Furthermore, we observe that quantized vortices are dynamically nucleated in the circulating condensate, which we attribute to the inhomogeneity of the effective magnetic field.

This work presents an alternative method for generating an artificial gauge field for neutral atoms, in particular, without using light. Based on spatial and temporal control of the real atomic-spin texture, this method does not suffer from atom loss and heating associated with spontaneous scattering of light [14,15], and thus enables us to study superfluid dynamics in a gauge field in a more dissipation-free condition [16].

We consider a neutral atom with hyperfine spin F moving in a spatially and temporally varying magnetic field $\mathbf{B}(\mathbf{r}, t)$. The system's Hamiltonian is given as $H = \mathbf{p}^2/2m - g_F \mu_B \mathbf{F} \cdot \mathbf{B}$, where m is the atomic mass, g_F is the Landé g factor, μ_B is the Bohr magneton, and $\mathbf{F}$ is the spin operator. If we take a local unitary transformation $U = \exp(-i\beta\hat{n} \cdot \mathbf{F})$ that rotates the quantization axis for the spin from a fixed axis $\hat{z}$ to the local magnetic field direction $\hat{b} = \mathbf{B}/|\mathbf{B}|$, where β is the tilting angle of $\hat{b}$ from $\hat{z}$ and $\hat{n} = (\hat{b} \times \hat{z})/|\hat{b} \times \hat{z}|$, then the Hamiltonian is transformed to $H' = (\mathbf{p} + \hbar\mathcal{A})^2/2m + V - g_F \mu_B F_z |\mathbf{B}|$, with a gauge potential $\mathcal{A}(\mathbf{r}, t) = -iU\nabla U^\dagger$ and a scalar potential $V(\mathbf{r}, t) = -i\hbar U \partial_t U^\dagger$, where $\hbar$ is the Planck constant h divided by 2π. In the adiabatic regime where the atom keeps its spin in the m_F state for the quantization axis along $\hat{b}(\mathbf{r}, t)$, the atom feels effective magnetic and electric fields [17,18]:

$$\mathbf{B}_i^e = -m_F \frac{\hbar}{2} \epsilon_{ijk} \hat{b} \cdot (\partial_j \hat{b} \times \partial_k \hat{b}), \tag{1}$$

$$\mathbf{E}_i^e = -m_F \hbar \hat{b} \cdot (\partial_i \hat{b} \times \partial_t \hat{b}), \tag{2}$$

where i, j, k are spatial coordinates and ϵ_{ijk} is the Levi-Cività symbol. The corresponding charge value of the atom is set to be unity.

Our system consists of a Bose-Einstein condensate of ^{23}Na atoms in the $|F = 1, m_F = -1\rangle$ state. We prepare a nearly pure condensate in a pancake-shaped optical dipole trap with trapping frequencies of $\omega_{x,y,z} = 2\pi \times (3, 3.9, 370)$ Hz and adiabatically ramp-up a three-dimensional magnetic quadrupole field

$$\mathbf{B} = \frac{B_q}{2}(x\hat{x} + y\hat{y} - 2z\hat{z}) - B_x\hat{x} + B_z\hat{z}, \tag{3}$$

with $B_q = 7.6$ G/cm. The position of the zero-field center is controlled by external bias fields B_x and B_z as $\mathbf{r}_m = (x_m, y_m, z_m) = (2B_x/B_q, 0, B_z/B_q)$ and initially placed above the condensate at $\mathbf{r}_m = (0, 0, 36)$ μm [Fig. 1(a)]. In the $z = 0$ plane, the tilt angle β of $\hat{b}$ increases with radial position $r'_\perp = \sqrt{(x - x_m)^2 + (y - y_m)^2}$ as $\tan\beta = r'_\perp/2z_m$ and the magnetic field imposes a spin texture of two-dimensional Skyrmion configuration on the condensate [19]. The Zeeman energy $E_Z = -g_F\mu_B|\vec{B}|$, with $g_F = -\frac{1}{2}$, provides an additional but dominant radial trapping potential. The radial trapping frequency is estimated

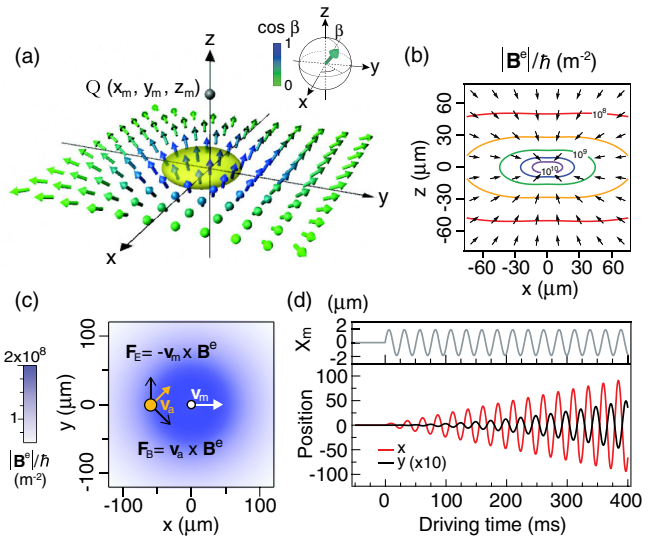

FIG. 1 (color online). Geometric Hall effect for a neutral atom moving in a three-dimensional magnetic quadrupole field. (a) The zero-field center of the magnetic field is indicated by a point Q. The atom (yellow ellipsoid) is in the $|m_F = -1\rangle$ spin state for the local field direction denoted by an arrow. (b) Effective magnetic field $\mathbf{B}^e$ for the atom. (c) When the atom and the zero-field center move with velocities $\mathbf{v}_a$ and $\mathbf{v}_m$, respectively, an effective Lorentz force $\mathbf{F}_B = \mathbf{v}_a \times \mathbf{B}^e$ and an effective electric force $\mathbf{F}_E = -\mathbf{v}_m \times \mathbf{B}^e$ occur on the atom. (d) The Hall response of the atom to sinusoidal oscillations of the zero-field center [Eq. (6) for $\omega_m = \omega_r$ and $X_m = 2$ μm]. A y-directional motion emerges from the x-directional modulation of Q.

to be $\omega_r = \sqrt{\omega_{x,y}^2 + (\mu_B B_q/8mz_m)} \approx 2\pi \times 40.3$ Hz at the trap center. For the typical atom number of $N \approx 3.3 \times 10^6$, the Thomas-Fermi radius of the condensate is $R_{\mathrm{TF}} \approx 44$ μm.

For the spin-polarized condensate in the $|m_F = -1\rangle$ state, the gauge potential and the effective magnetic field are given as

$$\mathcal{A}(\mathbf{r}) = -\frac{\sqrt{r'^2_\perp + 4z'^2} + 2z'}{r'_\perp\sqrt{r'^2_\perp + 4z'^2}}\hat{\theta}, \tag{4}$$

$$\mathbf{B}^e(\mathbf{r}) = -\frac{2\hbar}{(r'^2_\perp + 4z'^2)^{3/2}}\mathbf{r}', \tag{5}$$

where $\hat{\theta}$ is the unit vector of the azimuthal direction with respect to the $+z$ axis and $\mathbf{r}' = \mathbf{r} - \mathbf{r}_m$ [20]. We can associate the effective magnetic field $\mathbf{B}^e$ with a monopole located at $\mathbf{r}_m$ which carries effective flux of $\oint \mathbf{B}^e \cdot d\boldsymbol{\sigma} = -2h$ [Fig. 1(b)] [21,22]. The magnetic flux passing through the condensate is $\Phi_B^e/h = 0.13$, which is much smaller than the critical value for having a singular vortex ground state [17,20,23].

We study a Hall response of the system under translational oscillations of the spin texture, $\mathbf{r}_m(t) = X_m \sin\omega_m t\hat{x}$, which is driven by sinusoidal modulation of the external bias field B_x. The temporal variation of the spin texture generates an effective electric field $\mathbf{E}^e = -\dot{\mathbf{r}}_m \times \mathbf{B}^e$ [Eq. (2)], perpendicular to the driving direction $\hat{x}$. This field can be understood as an induced electric field from the moving magnetic monopole with velocity $\mathbf{v}_m = \dot{\mathbf{r}}_m$ [Fig. 1(c)]. Including the restoring force from the magnetic trapping potential, the equation of motion for a single atom in the $z = 0$ plane is given as

$$m\frac{d^2\mathbf{r}'_\perp}{dt^2} = -m\omega_r^2\mathbf{r}'_\perp + \frac{d\mathbf{r}'_\perp}{dt} \times B_z^e(r'_\perp)\hat{z} + m\omega_m^2 X_m \sin\omega_m t\hat{x}, \tag{6}$$

where $\mathbf{r}'_\perp = (x - x_m, y)$ and $B_z^e(r'_\perp) = 2\hbar z_m/(r'^2_\perp + 4z_m^2)^{3/2}$ from Eq. (5) [24]. In the reference frame of the spin texture, this describes a driven harmonic oscillator under a static magnetic field. When we start with an atom at rest, the atom will undergo forced oscillations along the x direction and its transverse motion will be induced by the effective Lorentz force [Fig. 1(d)]. This is a geometric Hall effect arising from the noncoplanar spin texture.

In our experimental condition, the cyclotron frequency $\omega_c = |\mathbf{B}^e|/m \leq \hbar/4mz_m^2$ is 3 orders of magnitude smaller than the trap frequency ω_r, implying that it would be experimentally challenging to directly detect the Lorentz force by examining an atom's motion. However, the effects of the effective Lorentz force can be amplified through resonant behavior of the system because the trapping frequencies for the x and y directions are same.

When $\omega_m = \omega_r$ in Eq. (6), the x-directional amplitude linearly increases as $(\omega_r X_m/2)t$, leading to a quadratic amplification of the y-directional motion as $(\omega_c \omega_r X_m/8m)t^2$. For $\omega_c/\omega_r \sim 10^{-3}$, the y-directional amplitude is expected to become comparable to the modulation amplitude X_m within 0.5 s [Fig. 1(d)].

We investigate the center-of-mass motion of the condensate by taking its *in situ* absorption images for various driving times t_m and $X_m \approx 2$ μm [25]. The condensate position was determined from a 2D Gaussian fit to the images. Figures 2(a)–2(d) display the temporal evolutions of the displacement of the condensate from its initial position for various driving frequencies ω_m near the resonance. The initial increasing rate of the x-directional amplitude is measured to be about 2.3×10^{-4} m/s, which is close to the estimated value of $\omega_r X_m/2 = 2.5 \times 10^{-4}$ m/s, and discernible y-directional motion appears after a few 100 ms. In the peak response at $\omega_m = 2\pi \times 39.2$ Hz, we observe that a circular motion with almost zero ellipticity develops for $t_m > 600$ ms [Fig. 2(e)].

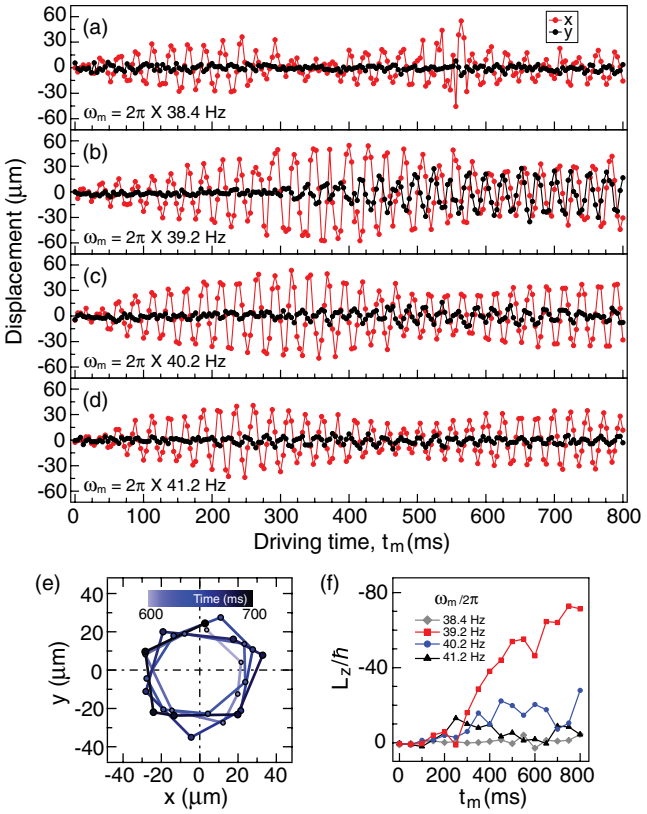

FIG. 2 (color online). (a)–(d) Temporal evolution of the condensate position under translational oscillations of the spin texture for various driving frequencies ω_m. The condensate position was measured for every 4 ms and each data point was obtained from a single measurement. (e) Trajectory of the condensate in the x-y plane for $\omega_m = 2\pi \times 39.2$ Hz. (f) External angular momentum L_z per atom in the condensate. The condensate velocity was determined from the position data, and L_z is displayed with 50 ms binning.

The radius of the trajectory is about 30 μm, corresponding to external angular momentum $L_z \approx -80\hbar$ per atom. The emergence of a circular motion under the translational drive characterizes the geometric Hall effect in our system.

We observe that the circulation direction of the condensate is always clockwise, giving negative L_z [Fig. 2(f)]. Numerical simulation of the single-particle dynamics predicts circulation in the opposite direction for large negative detuning of the driving frequency, $(\omega_m - \omega_r)/2\pi < -1$ Hz [24]. However, in our experiment for $\omega_m < 2\pi \times 38.5$ Hz, there is no detectable y-directional motion and even the development of x-directional oscillation seems to be strongly suppressed [Fig. 2(a)]. Full accounting for the condensate dynamics requires a superfluid hydrodynamics description including the interplay between the spin texture and the internal mass current [26,27]. In the gauge field, the superfluid velocity $\mathbf{v}_s$ is required to satisfy the Mermin-Ho relation $\nabla \times \mathbf{v}_s = -\mathbf{B}^e/m$ [17], and therefore the condensate always has an internal rotational motion. Note that the initial state of the condensate is a coreless vortex state with $\mathbf{v}_s = (\hbar/m)\mathcal{A}$ due to the Skyrmion spin texture [28–30]. We speculate that the external circulation of the condensate might be rectified by its internal rotational motion.

Recently, the dynamics of a spinor condensate with a Skyrmion spin texture was theoretically investigated [31–33]. In the study of a rigid spin texture case [33], it was shown that the spin texture can precess around the center of the condensate and its precession direction is determined by the chirality of the spin texture. In terms of the relative motion between the rigid spin texture and the condensate center, the circulation direction observed in our experiment is consistent with the theoretical prediction. However, their direct comparison is limited because our system is an externally driven system.

Another remarkable observation in the condensate dynamics is the nucleation of quantized vortices. Figure 3 shows time-of-flight images of the condensate for various driving times t_m, where quantized vortices are detected with density-depleted cores. The condensate first deforms into an elliptical shape, and after a few 100 ms quantized vortices start to appear in its boundary region. Eventually, the condensate becomes packed with many vortices. For 2 s relaxation in a stationary trap, vortices form a triangular lattice [Figs. 3(f)–3(j)], indicating that they are of the same sign [34]. For $\omega_m = 2\pi \times 39.2$ Hz, the vortex number N_v almost linearly increases for $t_m < 1$ s and becomes saturated to $N_v > 100$ within 3 s [Fig. 3(k)]. There is no significant heating during the process and the condensate fraction decreases by less than 20% [24].

We attribute the vortex nucleation in the circulating condensate to the inhomogeneity of the effective magnetic field $\mathbf{B}^e(\mathbf{r})$. The effective Lorentz force $\mathbf{F}_B = \mathbf{v}_s \times \mathbf{B}^e$ has $\nabla \times \mathbf{F}_B = -(\mathbf{v}_s \cdot \nabla)\mathbf{B}^e \neq 0$ for uniform $\mathbf{v}_s$ and, thus, it can play as a shearing force to deform the condensate

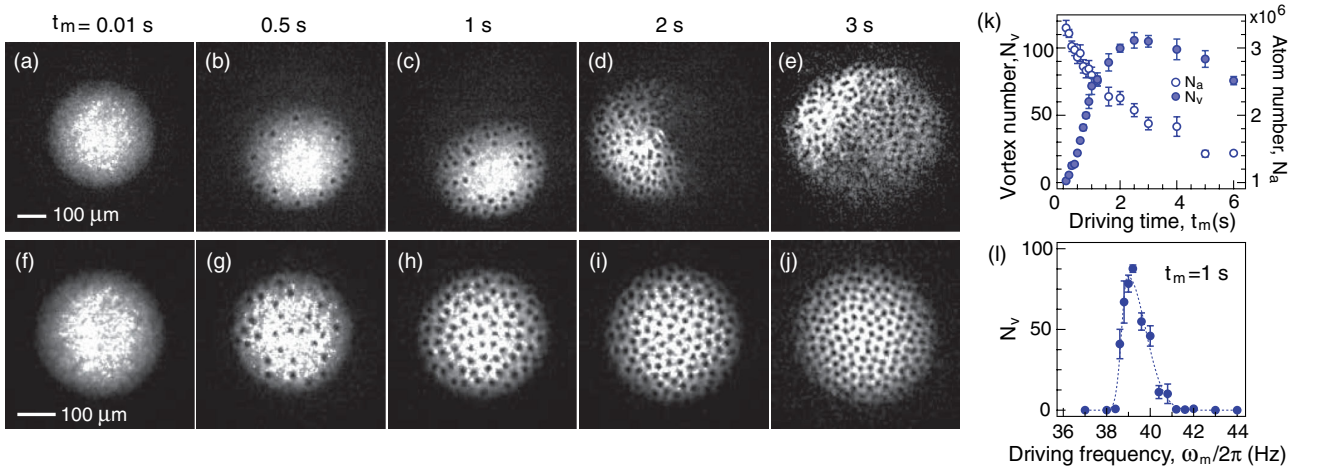

FIG. 3 (color online). Vortex nucleation in the spinor condensate circulating around the Skyrmion spin texture. (a)–(e) Absorption images after 15 ms time of flight for $\omega_m = 2\pi \times 39.2$ Hz and various driving times t_m. The condensate deforms into an elliptical shape and quantized vortices are nucleated in its boundary. (f)–(j) Images after 2 s relaxation in a stationary trap [24]. (k) Temporal evolution of the vortex number N_v (solid circles) and the atom number N_a (open circles). (l) N_v for $t_m = 1$ s versus $\omega_m/2\pi$. The dashed line is an asymmetric Gaussian curve fit to the data, giving the center frequency at 39.2 Hz, and the left and right $1/e^2$ linewidths of 0.4 and 1.2 Hz, respectively. Each data point was obtained from at least eight measurements.

and consequently lead to the dynamical nucleation of quantized vortices in the boundary region. We observed that the vortex nucleation is affected by the axial trapping frequency ω_z [24], implying that a three-dimensional description including the coupling between the axial and transverse motions might be necessary to explain the vortex nucleation dynamics.

In our experiment, we observe that the nucleated vortex number shows similar asymmetric dependence on the driving frequency ω_m to that observed in the amplification rate of the y-directional motion [24]. This suggests that the vortex nucleation rate Γ_v can be used as a quantitative measure for the geometric Hall effect in our superfluid system. We measure Γ_v for various values of the effective magnetic flux Φ_B^e by changing the distance z_m of the zero-field center from the condensate [Fig. 4]. Here, we set $\omega_m = 2\pi \times 35$ Hz and adjust the radial trapping frequency $\omega_r \propto \sqrt{B_q^2/B_z}$ with B_q and B_z to obtain a maximum Hall response for a given $z_m = B_z/B_q$. The vortex nucleation rate Γ_v was determined from a linear fit of $\Gamma_v(t_m - t_0) \times \theta(t_m - t_0)$ to $N_v(t_m)$ for $t_m \leq 1$ s [Fig. 4, inset], where $\theta(t)$ is the Heaviside step function. We find that Γ_v monotonically increases with Φ_B^e. The onset time $t_0 = 390 \pm 50$ ms, showing no clear dependence on Φ_B^e.

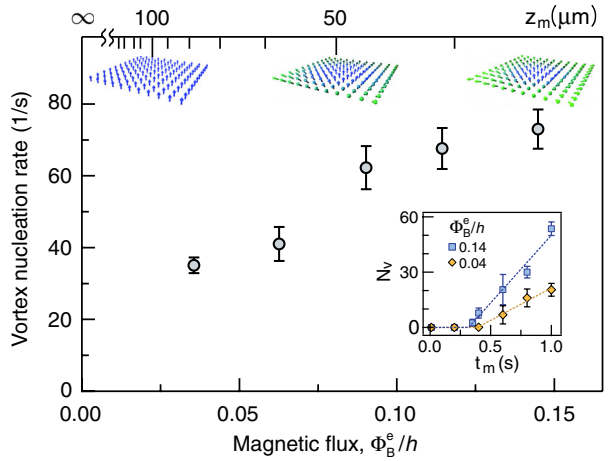

FIG. 4 (color online). Vortex nucleation rate Γ_v versus effective magnetic flux Φ_B^e passing through the condensate. The inset displays the vortex number N_v as a function of driving time t_m, and Γ_v is determined from a linear fit (dashed line) to the data. The data were acquired with condensates containing about 2.3×10^6 atoms for $\omega_m = 2\pi \times 35.0$ Hz and $X_m = 2.8$ μm.

In conclusion, we have observed the geometric Hall effect in a spinor Bose-Einstein condensate with a Skyrmion spin texture and presented the first study of superfluid dynamics in an inhomogeneous gauge field. We expect the spin-texture oscillation method to be extended to spin mixture systems for studying spin-dependent transport phenomena such as spin drag [35] and spin Hall effects [36,37]. Employing nanofabricated ferromagnetic structures might be envisaged to achieve a strong effective magnetic field [38].

This work was supported by the NRF of Korea funded by MSIP (Grants No. 2011-0017527, No. 2008-0061906, and No. 2013-H1A8A1003984).

*yishin@snu.ac.kr

[1] M. V. Berry, Proc. R. Soc. A **392**, 45 (1984).
[2] A. Shapere and F. Wilczek, *Geometric Phase in Physics* (World Scientific, Singapore, 1989).

[3] A. Stern, Phys. Rev. Lett. **68**, 1022 (1992).
[4] Y. Taguchi, Y. Oohara, H. Yoshizawa, N. Nagaosa, and Y. Tokura, Science **291**, 2573 (2001).
[5] N. Nagaosa, J. Sinova, S. Onoda, A. H. MacDonald, and N. P. Ong, Rev. Mod. Phys. **82**, 1539 (2010).
[6] M. Lee, W. Kang, Y. Onose, Y. Tokura, and N. P. Ong, Phys. Rev. Lett. **102**, 186601 (2009).
[7] A. Neubauer, C. Pfleiderer, B. Binz, A. Rosch, R. Ritz, P. G. Niklowitz, and P. Böni, Phys. Rev. Lett. **102**, 186602 (2009).
[8] Y. Li, N. Kanazawa, X. Z. Yu, A. Tsukazaki, M. Kawasaki, M. Ichikawa, X. F. Jin, F. Kagawa, and Y. Tokura, Phys. Rev. Lett. **110**, 117202 (2013).
[9] S. E. Barnes and S. Maekawa, Phys. Rev. Lett. **98**, 246601 (2007).
[10] P. N. Hai, S. Ohya, M. Tanaka, S. E. Barnes, and S. Maekawa, Nature (London) **458**, 489 (2009).
[11] S. A. Yang, G. S. D. Beach, C. Knutson, D. Xiao, Q. Niu, M. Tsoi, and J. L. Erskine, Phys. Rev. Lett. **102**, 067201 (2009).
[12] Y. J. Lin, R. L. Compton, K. Jiménez-García, J. V. Porto, and I. B. Spielman, Nature (London) **462**, 628 (2009).
[13] Y. J. Lin, R. L. Compton, K. Jiménez-García, W. D. Phillips, J. V. Porto, and I. B. Spielman, Nat. Phys. **7**, 531 (2011).
[14] J. Dalibard, F. Gerbier, G. Juzeliūnas, and P. Öhberg, Rev. Mod. Phys. **83**, 1523 (2011).
[15] V. Galitski and I. B. Spielman, Nature (London) **494**, 49 (2013).
[16] L. J. LeBlanc, K. Jiménez-García, R. A. Williams, M. C. Beeler, A. R. Perry, W. D. Phillips, and I. B. Spielman, Proc. Natl. Acad. Sci. U.S.A. **109**, 10 811 (2012).
[17] T.-L. Ho and V. B. Shenoy, Phys. Rev. Lett. **77**, 2595 (1996).
[18] T. Fujita, M. B. A. Jalil, S. G. Tan, and S. Murakami, J. Appl. Phys. **110**, 121301 (2011).
[19] J. Choi, W. J. Kwon, and Y. Shin, Phys. Rev. Lett. **108**, 035301 (2012).
[20] Y. Shin and J. Choi, J. Korean Phys. Soc. **63**, 951 (2013).
[21] V. Pietilä and M. Möttönen, Phys. Rev. Lett. **103**, 030401 (2009).
[22] P. Milde *et al.*, Science **340**, 1076 (2013).
[23] E. Lundh, C. J. Pethick, and H. Smith, Phys. Rev. A **55**, 2126 (1997).
[24] See Supplemental Material at http://link.aps.org/supplemental/10.1103/PhysRevLett.111.245301 for details on the experimental setup, the single-particle dynamics including the anharmonicity of the magnetic trapping potential, and the vortex nucleation rate for various experimental conditions.
[25] In order to reduce the optical density of the sample, we applied a 100 μs pulse of a resonant light to the sample just before imaging. The modulation amplitude X_m was checked to be in the linear-response regime in terms of vortex nucleation [24].
[26] A. Lamacraft, Phys. Rev. A **77**, 063622 (2008).
[27] Y. Kawaguchi and M. Ueda, Phys. Rep. **520**, 253 (2012).
[28] A. E. Leanhardt, Y. Shin, D. Kielpinski, D. E. Pritchard, and W. Ketterle, Phys. Rev. Lett. **90**, 140403 (2003).
[29] P. Zhang, H. H. Jen, C. P. Sun, and L. You, Phys. Rev. Lett. **98**, 030403 (2007).
[30] J. Choi, W. J. Kwon, M. Lee, H. Jeong, K. An, and Y. Shin, New J. Phys. **14**, 053013 (2012).
[31] X.-Q. Xu and J. H. Han, Phys. Rev. A **86**, 063619 (2012).
[32] C.-C. Huang and S.-K. Yip, Phys. Rev. A **88**, 013628 (2013).
[33] J. Armaitis, H. T. C. Stoof, and R. A. Duine, Phys. Rev. Lett. **110**, 260404 (2013).
[34] A. L. Fetter, Rev. Mod. Phys. **81**, 647 (2009).
[35] R. A. Duine and H. T. C. Stoof, Phys. Rev. Lett. **103**, 170401 (2009).
[36] M. Taillefumier, E. K. Dahl, A. Brataas, and W. Hofstetter, Phys. Rev. B **80**, 020407(R) (2009).
[37] M. C. Beeler, R. A. Williams, K. Jiménez-García, L. J. LeBlanc, A. R. Perry, and I. B. Spielman, Nature (London) **498**, 201 (2013).
[38] P. Bruno, V. K. Dugaev, and M. Taillefumier, Phys. Rev. Lett. **93**, 096806 (2004).

초 록

극저온 양자기체계는 외부환경과 잘 고립이 되어 있고 전자기장을 통해서 조작이 용이하며 양자 현상을 직접적으로 관측할 수 있어 다양한 양자 다체계현상을 연구 할 수 있는 시스템이다. 우리는 ^{23}Na(나트륨) 원자 기체를 이용하여 이차원 초유체의 성질을 연구하는 것을 목표로 하였고, 이를 위해 원자기체를 극저온 상태로 냉각 시켜 보즈-아인슈타인 응집체(Bose-Einstein condensate, BEC) 상태로 만들어 줄 수 있는 레이저 시스템과 진공 시스템을 구축하였다. 우리가 만든 BEC 기계는 광자기 포획(magneto-optical trap) 을 통해 원자들을 1차적으로 냉각하고 이후 사중극 자기장 우물에서 라디오 주파수를 통한 증발 냉각으로 약 10^7 개의 순수한 응집체를 17 초 안에 만들 수 있었다.

낮은 차원 (1차원 혹은 2차원) 물리현상의 대표적인 특징은 열적 요동이 먼 거리 질서도를 파괴하여 질서 변수가 정의 되지 않는다는 점이다. 그럼에도 불구하고 상전이 현상이 2차원에서 존재할 수 있음이 Berezinskii-Kosterlitz–Thouless (BKT)에 의해 연구되었는다. 이들은 대칭성의 깨짐과 그로 인한 질서 변수의 발생이라는 기존의 상전이 현상과 달리 2차원에서는 양자 쌍 소용돌이(quantum vortex pair)의 생성과 분해에 의해서 위상학적으로 다른 두 상이 매개됨을 보였다. 최근 연구에 의하면 원자기체를 충분히 납작하게 만들어 주면 조화 우물에서도 BKT 정상-초유체 상전이 현상이 일어남을 보였고 이를 통해 임계온도 근처에서 일어나는 다양한 현상들이 보고 되었다. 하지만 2차원 초유체상에 존재하는 위상요동의 열적 의존성이나 양자 쌍 소용돌이의 직접적인 관측은 이루어지지 않았고 우리는 이를 위해 하나의 준 이차원 광트랩을 만들어 실험을 진행하였다.

위상요동의 측정을 위하여 우리는 시료를 가두고 있던 광트랩을 갑자기 꺼 일정 시간동안 자유 팽창을 허락하였고, 이후 생기는 밀도 분포의 변화를 분석하였다. 시료에 있던 위상 요동은 자유 팽창을 거치면서 간섭을 하게 되어 밀도 분포에 반영이 되었고, 정량적인 분석을 위해 밀도 분포의 파워 스펙트럼을 구하였다. 관측된 스펙트럼은 파수에 대해 진동하는 모습을 보였으며, 이는 근접장 회절현상의 예인 탈봇(Talbot) 현상으로 이해될 수 있다. 재 규격화된 스펙트럼의 세기를 통해 위상 요동의 열적 의존성을 살펴볼 수 있었으며, 본 실험에서는 온도가 감소할수록 세기가 감소하는 양상을 보여 위상 요동의 근원이 열적 에너지임이 규명되었다. BKT-초유체의 가장 큰 특징은 열적 요동에 의한 양자 쌍소용돌이이다. 양자 소용돌이의 핵근처에는 강한 원심력으로 인해 원자가 존재할 수 없고 따라서 사진을 찍게 되면 구멍으로 보인다. 그러나 구멍의 크기가 너무 작아 보통 시료를 팽창을 시킨뒤에 사진을 찍게 되는데, 이차원의 경우 위상요동이 밀도 분포에 변화를 주어 소용돌이 핵을 정확히 찍을 수 없다. 우리는 이런 제약을 피하기 위해 자유팽창하기 전에 준비된 시료를 3 차원으로 가져가서 위상요동 중 소리알 (phonon) 을 완화 시켜주었고, 이후 팽창을 통해 소용돌이의 핵을 관측 할 수 있었다. 관측된 소용돌이의 공간적 분포를 통해 두 양자 소용돌이가 강한 상관관계를 갖고 있음을 알 수 있었고, 이는 BKT 초유체의 특성을 잘 뒷받침하는 실험이다. 뿐만 아니라, 온도를 달리하면서 양자 소용돌이의 공간적 분포를 통해 유한한 크기의 이차원 보즈 기체가 보이는 BEC-BKT 교차현상을 볼 수 있었다.

원자는 스핀을 갖고 있어 파동함수의 질서변수 다양체(order parameter manifold)가 스칼라의 파동함수보다 더 다양한 위상 여기구조를 가질 수 있다. 2 차원 스커미온 구조는 스핀들이 분수 형태로 나가는 모양인데 스핀-1의 반자성

스피너 응집체의 경우 이구조가 위상학적으로 독특한 구조가 된다. 우리는 앞선 광트랩에 담긴 원자기체를 사중극자 트랩을 이용하여 위상학적으로 안정한 2차원 스커미온을 구현하였고 이 구조의 동역학적 변화를 살펴보았다.

스커미온 구조는 위상학적 특성 외에 스핀들이 같은 평면상에 놓여 있지 않기 때문에 베리(Berry) 곡률이 유한한 값을 같는다. 따라서 중성 원자가 스커미온 스핀 구조를 갖는다면 원자는 기하학적인 전자기력을 받을 수 있다. 우리는 사중극 자기장을 이차원 원자 위에 놓음으로서 중성 원자에게 기하학적 자기력을 가하였고, 조화우물에 갇힌 원자의 조화운동을 공명시켜 홀(Hall) 효과를 관측하였다.

주요어 : 보즈-아인슈타인 응집현상, 베레진스키-코스털리츠-사울리스 상 전이 , 열적 위상 요동, 양자 소용돌이, 스커미온, 베리 위상.

학 번 : 2009-20433

감사의 글

대학교 4학년 2008년 여름, 케번디쉬 연구소에 연구 참여 학생으로 일하면서 막연하게 갖고 있었던 실험을 경험 할 수 있었고 이를 통해 2009년 서울대 대학원에 입학하였다. 지난 과거를 회상해 볼 때 결코 짧지 않았던 학위과정이었고 또 버티기 힘든 기간도 몇 번 있었던 것 같다. 학위과정을 겪으며 나 자신에 대해 좀 더 잘 알 수 있었고 때로는 한심한 모습에 실망과 좌절도 했지만 그런 과정 속에서 더욱 성숙할 수 있었던 것 같다. 아직도 여러 가지 부족한 면이 보이지만 다행히 2014 년 졸업하게 되는데 이는 주변에 있는 수많은 사람들의 아낌없는 도움과 격려가 있었기에 가능했다. 이에 부족하지만 감사의 글로나마 보답을 하고 싶다.

무엇보다 이제 막 학부를 졸업하고 아무것도 모르는 학생을 처음으로 받아 인내로 졸업까지 이끌어주신 지도교수님께 감사를 드립니다. 실험실에 처음에 갔을 땐 아무것도 없는 빈 공간이었지만 교수님과 함께 하나하나 기계를 조립하고 늦음 밤까지 남아서 실험실을 구축했던 경험은 어디에서도 얻을 수 없는 소중한 자산으로 남을 것입니다. 늘 학생들을 실험동료로서 여겨주시며 이를 통해 연구원으로 성장하는 강한 동기 부여를 해주셨을 뿐만 아니라 실험결과에 대한 다양한 해석과 이를 토대로 한 앞으로의 실험 지도는 연구를 진척하는데 결정적인 도움이 되었습니다. 또한, 그룹 내에서 자유롭게 토의 할 수 있는 분위기를 형성해 주시고

연구에 관련된 일은 아낌없이 지원해주셔서 짧은 기간 동안 다양한 연구를 할 수 있었습니다. 무엇보다도, 실험 물리학자로서 물리를 바라는 모습과 끊임없이 배우려는 자세는 본인이 졸업을 하고 앞으로 과학자로 성장 하는데 있어서 반드시 닮아야 할 모습이 될 것입니다. 논문 심사를 맡아 격려의 말씀과 좋은 지적을 해주시는 제원호 교수님, 강병남 교수님, 민홍기 교수님께 감사를 드립니다. 바쁘신 와중에도 시간을 내주셔서 날카로운 지적과 조언을 해주신 문종철 박사님께도 고맙다는 말씀을 전합니다. 또한 비록 짧은 시간이었지만 다양한 양자 다체계 현상을 강의해주신 전건상 교수님께 감사드립니다.

연구실에서 함께 동거 동락했던 친구들이 있어 실험실 생활을 보다 즐겁게 할 수 있었다. 실험을 하는 도중 미쳐 내가 생각하지 못한 점과 물리적으로 맞지 않는 해석들을 지적해주어 나 스스로에게도 자극이 되었다. 또한 나의 계획을 믿고 같이 실험하며 그러다 밤늦게까지 붙잡혀 집에도 못가 고생했던 우진, 상원, 세지에게 너무나 감사하다. 같이 많은 실험을 하지는 못했지만 재미있는 실험 결과나 혹은 연구 결과가 발표되면 같이 나누고 토론하며 모르는 점을 같이 고민한 민식이, 민석이, 무송이, 정호에게도 고맙단 말을 전하고 싶다. 연구에 몰두할 때 뿐 아니라 가끔 같이 게임을 하기도 하고 뭉쳐서 다른 랩 사람들과 농구나 축구도 하며 혹은 몇 일 동안 스키장에서 같이 스키도 타고 휴식도 취하면서 실험 때문에 힘들고 지친 심신을 달랠 수 있었고 그로인해 실험을 다시 하려는 의지가 생겼던 것 같다. 생각해보면 연구실 구성원 모두가 독특하지만 조화를 이루어 더 재미있는 양자 기체 연구실이 아니었나 싶다. 치킨맨과 같은 외모로 우리를 즐겁게한 민식이. 무엇보다 외모에 대한 강력한 자신감으로 무장하며 우리 연구실에서 개그를 담당하고 다른 친구들을 몸으로 사랑하며 무엇보다 중요한 실험 장비인 *프린터*를 관리해주는 장인정신을 보여준 우군. 일찍이 큰 연구비를 받아

한 달에 한 번씩 우리들에게 맛있는 음식을 사주고 해박한 역사 지식 덕에 모두가 (한 사람을 제외하고) 재밌었던 경험을 안겨준 상원이, 독특한 걸음법으로 우리를 즐겁게 해주는 세지와 선배들의 사랑을 새로 받고 있는 정호. 우군의 사랑을 많이 받아서 인지 종종 알 수 없는 소리를 내기도 하지만 꾸준히 노력하는 무송이와 반응을 예측 할 수 없지만 늘 나와 함께 주말에도 연구실을 지킨 민석이. 좋은 동료들 덕에 지난 5 년을 버틸 수 있었던 것 같다. 좋은 일이 있으면 서로 축하해주고 어려울 때는 같이 힘들어 하고 서로를 위하며 다시 앞으로 나갈 수 있는 모습이 앞으로도 계속 지속되길 바란다.

실험실 동료 외에도 다른 분들에게도 감사의 말을 전하고 싶다. 짧은 석사과정동안 인연을 맺어 지속적으로 만나 서로의 이야기를 나눈 창우, 정운이, 종원이 그리고 모도영. 모두 나의 좋은 친구들이다. 학위과정을 시작할 때 여러 좋은 말씀들로 격려와 조언을 아끼지 않고 해주신 명선형 그리고 용희형. 같이 축구도 하며 친목을 다진 지현이형, 완희형, 결이형 그리고 다현이형. 비슷한 분야를 연구하며 이야기를 나누었던 준기와 문주형 성삼이형. 모두에게 고맙다는 말을 전하고 싶다. 또한 매주 좋은 설교 말씀들로 격려를 해주신 대학교회 김동식 목사님과 형제회라는 모임을 통해 서로의 안부를 묻고 즐거운 시간을 보낸 재용형, 바우형, 노아형, 재홍형, 재훈이에도 특별히 감사의 말을 전하고 싶다. 무엇보다 5년이라는 시간을 늘 나와함께 해주며 바쁜 대학원 생활을 인내해주고 함께 해준 소희에게도 고맙다는 말을 전하고 싶다. 정해지지 않은 나의 일정에 희생해주어 너무 고맙고 덕분에 내가 연구에만 몰두 할 수 있었다. 마지막으로 사랑하는 나의 가족들에게도 감사의 말을 전하고 싶다. 집안의 장남이 되어 물리학과를 가려고 했을때에도 격려의 말씀을 주시고 앞으로의 일에 신경을 써주신 아버지 어머님 덕분에 지금 내가 있을 수 있었다.